Solid Freeform Fabrication Proceedings

September, 1992

The breadth of Solid Freeform Fabrication as an important and totally integrated approach to design, materials processing and manufacturing is contained in this proceedings of the SFF Symposium held in Austin, Texas on August 3-5, 1992.

SFF Topics covered in the Symposium include:

Computer Sectioning
Machine Design
Materials Processing:
Metals
Ceramics
Polymers
Waxes
Composites
Applications

Harris L. Marcus, Joseph J. Beaman,
Joel W. Barlow, David L. Bourell,
and Richard H. Crawford, Editors

Table of Contents

PREFACE

This Proceedings of the Third Solid Freeform Fabrication Symposium, held at The University of Texas in Austin on August 3-5, 1992, again demonstrates the very active interest in this fully integrated approach to design, materials processing, and manufacturing. The active participation of speakers and attendees from industry that uses SFF, SFF machine manufacturers, universities, and government gives a clear indication of the importance that SFF in its many variants has in the future of manufacturing. As SFF extends itself into structurally sound parts made of polymers, metals, ceramics and their composites, the number of people and institutions involved will continue to grow exponentially. The organizers look forward to this growth and the continued availability of the Solid Freeform Fabrication Symposium to serve as a source of technical exchange among the researchers involved in the area.

The Symposium was organized in a manner to allow the multi-disciplinary nature of the SFF research to be presented coherently. To avoid parallel sessions a poster session was organized. The initial session emphasized the computer interfacing required for SFF. This was followed by a session associated with materials related research on SFF. Two sessions were offered describing the latest techniques and modifications of SFF. These sessions were highlighted by a spirited panel discussion led by Robert L. Brown, Emanuel Sachs, and Joel Barlow, on "where is SFF going?." The final session concentrated on machine issues in SFF. The written versions of the presented papers are incorporated into these Proceedings. The editors would like to thank the speakers for their prompt delivery of the manuscripts that allows the timely publication of these Proceedings. The constantly changing state of the SFF art as represented by these Proceedings will serve both the people presently involved in this fruitful area as well as new researchers and users coming into Solid Freeform Fabrication.

The editors would also like to extend a warm thank you to Carolyn Medina for her extensive efforts in the detailed handling of the logistics of the meeting and the Proceedings. We would also like to thank the organizing committee, the speakers, the session chairmen, panel members, and the attendees for their enthusiastic contributions. We look forward to the continued close cooperation of the SFF community in organizing the Symposium. We also want to thank ONR and DARPA for co-sponsoring the Symposium and DTM Corporation for hosting the reception.

The editors

Organizing Committee:

Dick Aubin, United Technologies
Joel Barlow, The University of Texas at Austin
Joseph J. Beaman, The University of Texas at Austin
David L. Bourell, The University of Texas at Austin
Robert L. Brown, The Gillette Company
William Coblenz, DARPA
Richard Crawford, The University of Texas at Austin
Samuel Drake, University of Utah
Steven Fishman, Office of Naval Research
Harris L. Marcus, The University of Texas at Austin
Fritz Prinz, Carnegie Mellon University
Emanuel Sachs, Massachusetts Institute of Technology
Greg Sanders, General Motors Corporation
Peter R. Sferro, Ford Motor Company
Ralph Wachter, Office of Naval Research
Michael Wozny, Rennselaer Polytechnic Institute

SYSTEMS ISSUES IN SOLID FREEFORM FABRICATION

Michael J. Wozny
Rensselaer Design Research Center
Rensselaer Polytechnic Institute
Troy, New York 12180

Abstract

This paper is concerned with the systems aspects of the Solid Freeform Fabrication (SFF) technology, i.e., the issues that deal with getting an external geometric CAD model to automatically control the physical layering fabrication process as directly as possible, regardless of the source of the model. The general systems issues are described, the state of systems research is given, and open research questions are posed.

1. INTRODUCTION

Prototyping requirements today, and general manufacturing requirements in the future, call for the rapid, fabrication of one-of-a-kind, structural strength parts driven directly by computer-sensible geometric data. The general class of Solid Freeform Fabrication (SFF) systems, where material is added layer by layer, has the potential to become the dominant prototyping technology in the near term, and even a key manufacturing technology in the future.

Solid Freeform Fabrication deals with the problem of fabricating, under computer control, a CAD description of a desired part by selectively solidifying or bonding one or more raw materials into a thin layer, representing a horizontal slice of the desired part; and then fusing the successive thin layers into a 3D solid object. The material may be a gas, liquid, powder or a thin solid sheet, while the solidification process may be polymerization, sintering, chemical reaction, plasma spraying or gluing. The geometry data may be CAD geometry, CAT or MRI imaging data, or special forms like contour slices. Only CAD geometry is assumed in this paper, since it is the dominant source of data for SFF today.

General references on various aspects of the technology are [Marcus, et. al. 91, Bjorke 91, Kruth 91, Arline 91, Bourell et. al. 90, Deckard 86]. Other references can be found in the proceedings of the annual symposia on Solid Freeform Fabri   ion at the University of Texas at Austin, and the annual conferences at the University of D&   (Ohio). Current events are published in the monthly newsletter [Cohen].

A high-level systems view of the overall SFF process is shown in Fig. 1.1. The computer-sensible geometric CAD model describes the desired final shape of the physical part. The information processing subsystem converts this input geometric model into a form suitable for controlling the solidification process. The physical solidification process subsystem creates the actual physical part. (The term solidification is used because it is the dominant processing technology today.) The physical process parameters depend upon the characteristics of the material(s), the solidification process, the environment in the solidification chamber, as well as precision, fabrication speed, and geometric shape.

As we shall see, the control strategy is basically feedforward control, since modeling of the solidification process is still a very active research area, and adequate sensor technology is lacking. Most progress in research has been in the manipulation of geometric shapes.
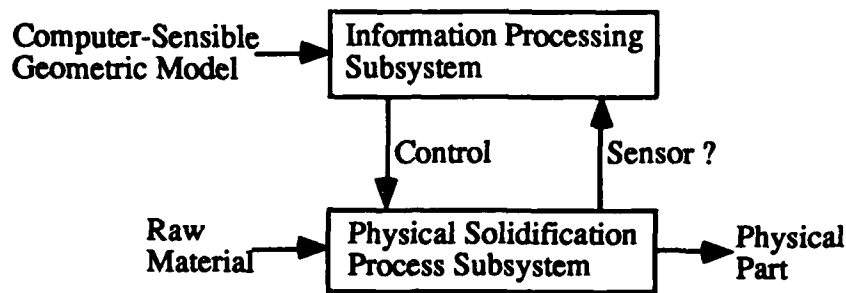
Figure 1.1 Major Subsystems

2. PHYSICAL LIMITATIONS ON SHAPE

The input geometric model represents the desired shape of the physical part. In order to develop an appropriate control strategy the ideal geometry must first be sliced into layers.

2.1 Slices of Finite Thickness. Since the layers of the physical material must have finite thickness, we are faced with the volume sampling problem shown in Fig. 2.1. This 3D aliasing effect limits the accuracy of the final physical part.
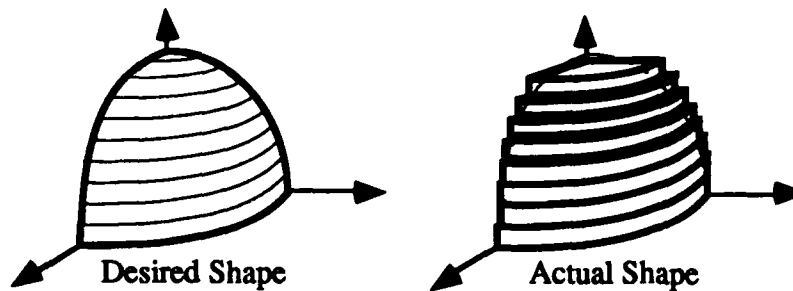
Fig. 2.1 Finite Layers

From a systems point of view, layer thickness is primarily influenced by the trade-off shown in Fig. 2.2. However, physical characteristics such as depth of solidification, density and desired strength are also key considerations.
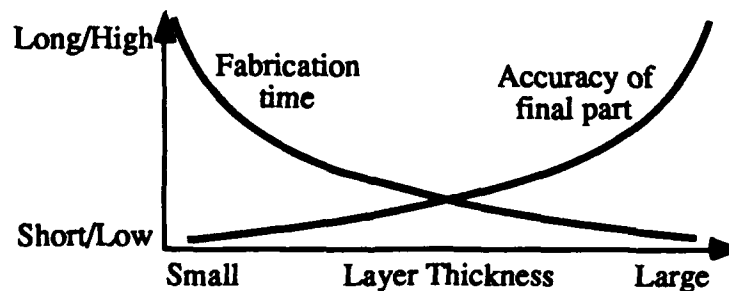
Fig. 2.2 Trade-off in Layer Thickness

One means for reducing the effect of volume sampling, for layers of constant thickness, is to choose the extent of each layer so that it best fits the enclosed solid slice. Fig. 2.3 illustrates one

approach for a solid of revolution where the radius of each layer depends on the ratio of the layer volume to the part volume. Criteria other than equal volumes can be chosen. Also, the calculation becomes much more difficult for parts which are not solids of rotation. This subject requires further study.
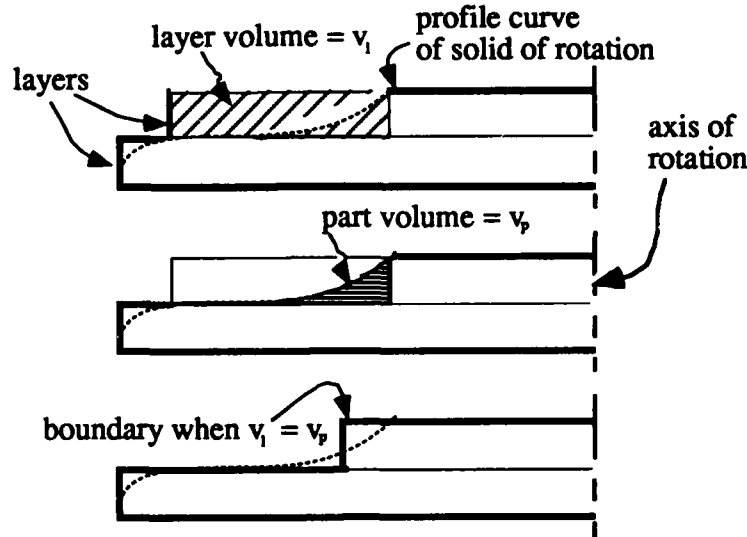
Fig. 2.3 Reducing Volume Aliasing Effects in Solids of Rotation

In a recent study, 3D anti-aliasing can also be achieved by varying thickness of the slice (sometimes called adaptive slicing). The thickness of the slice has been related to local surface curvature, number of contours in each slice, and distance between line segments in different slices [Dolenc et. al. 92].

The above method contributes to the reduction of the 3D aliasing, but does not eliminate it. Aliasing can be further reduced only by taking advantage of physical phenomena.

2.2 Scan Vectors of Finite Thickness. There is also an aliasing effect due to the finite thickness of scan lines on each layer, as shown in Fig. 2.4. From a systems point of view, compensation techniques such as overlapping and multi-directional scan lines, and tracing the final boundary can be used to minimize the effects of sampling. (Scanning strategies for efficiency are discussed in Section 9.) However, the ultimate accuracy depends on the beam size and beam energy cross-section. These and other sources of error were studied by [Bjorke 91].

Desired Shape   Actual Shape
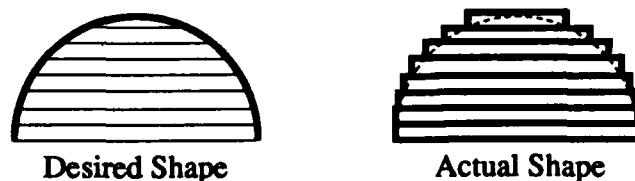
Fig. 2.4 Scan Line Aliasing

The next section describes cases where apparently harmless solid models and modeling techniques, severely impact the fabrication of physical parts.

3

3. PHYSICAL IMPLICATIONS OF CAD SOLID MODELS

Regardless of field, models are developed to answer specific questions. If the models are extended to new contexts, then all assumptions must be carefully re-examined. This is the case with CAD geometry models which now are being extended to directly drive the layered fabrication process. Solid models created for purposes of visue'ization or analysis are not necessarily appropriate for SFF.

3.1 Coincident Surfaces. The following example illustrates a problem which occurs when a solid model with coincident surfaces is used to fabricate a part [Aubin 92]. Such a model is perfectly adequate for visualization or volume analysis, but fails for SFF.

Suppose a solid model is created in which the coincident (inner) surfaces of adjoining constituent solid elements are not removed. This tactic is commonly used when transitioning between different solid sections. The resulting fabricated physical object may exhibit deformations or poor strength characteristics in the region of the coincident surface. Fig. 3.1 illustrates this problem.

internal concident surface
not removed from final
solid model

scan lines abut,
causing problems
in physical part

Cross section of two
adjoining solid objects
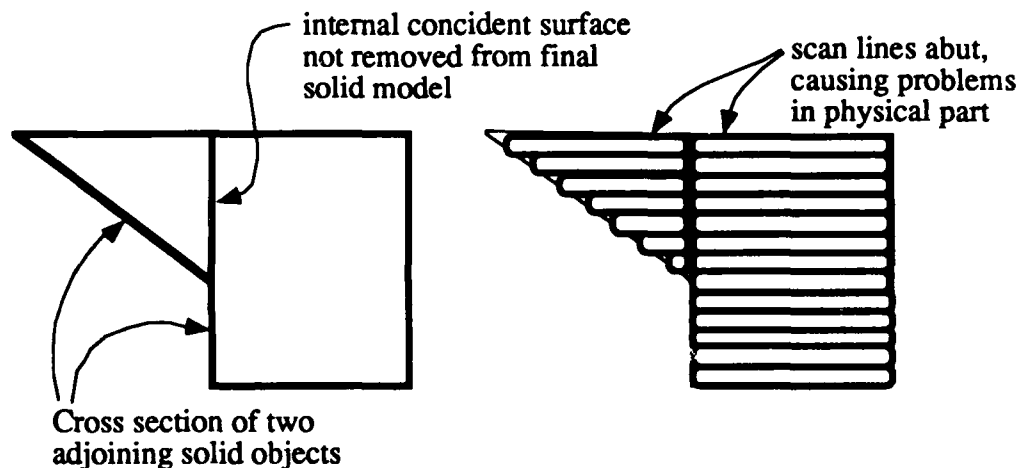
Fig. 3.1 Concident Surfaces

What other situations exist where improperly (for SFF) generated CAD models may result in undesired physical characteristics? In another case, abutting solids can also result in non-manifold topology [Weiler 86] conditions where there is ambiguity of what constitutes the interior or exterior of the final object [Rock 91, Bøhn 92 & Wozny 92]. Such cases need to be identified and studied. We must understand the resulting physical manifestation implicit in the geometric model. A rule base may be needed to evaluate troublesome cases when validating solid models (more later).

Next, suppose the user discovers an anomaly in the geometric solid while fabricating a physical part. It would be useful to send this anomalous data back to the CAD system and modify the existing geometric data without having to return to the original model in the CAD system. What associativity information is needed so that models which have been already sliced and scanned can easily be modified in a global sense? This is also an open question.

3.2 Postprocess geometry in the CAD System. The situation in the previous paragraph leads to the question of where should the processing of solid models into scan lines take place? One could postprocess in the CAD system, geometric part data directly into scan vectors suitable to

4

control the physical fabrication process. The CAD system has a common geometric representation and, therefore, can generate exact slices and scan vectors.

Although this approach may be efficient for a specific CAD/SFF device combination, transferring scan vectors has its drawbacks. The approach requires extensive low level knowledge about the SFF device, such as internal timing and control mechanisms. Errors can be very costly, since there is minimal error protection and recovery. The scan line files will be extremely large for real problems. Verification of the data would not be easy, as well as compensating for SFF idiosyncrasies such as shrinkage.

This situation is similar to plotting a curve on an XY-plotter, where the curve is subdivided into short straight line segments in the CAD system, and then the segments are sent to the plotter in the proper sequence and timing. Using another analogy, it's like programming in assembly language rather than a high level language like C or Pascal. Although it may work very well in specialized situations, it does not appear to be strategic. The high level descriptions change most slowly and remain more modularized than low level data and descriptions.

3.3 Processing Geometry in the SFF Device. The strategic approach is to accept high level 3D geometry descriptions from the CAD environment and perform all subsequent slicing, scanning and other related processing in the SFF device. This approach, in principle, allows a general fabrication capability which can accept data from any CAD system, making the SFF device independent of the CAD environment.

High level geometric descriptions permit general procedures for the validation, orientation and nesting of parts, increasing accuracy and machine utilization. Questions such as part placement for optimal fabrication including part build time, scanning efficiency, part surface finish, and accuracy on critical dimensions need to be investigated. Such investigations will likely find ties to other research in tolerancing and feature-based modeling. Since most parts use only a portion of the maximum allowable part fabrication volume, they can be nested to increase machine thruput. This nesting problem requires nontrivial extensions of two-dimensional nesting concepts to three-dimensions. Physical process properties may also be incorporated in such algorithms to account for part shrinkage and proximity to adjacent parts.

If such operations are to be performed in the SFF device, then the device must maintain maximum flexibility by accepting a high level geometric description from any CAD system, regardless of math form and representation. Attacking the problem of proliferating of math forms is discussed next.

4. COMMON MATHEMATICAL FORM

Unfortunately, many different mathematical forms have been developed to model the extensive range of part geometries A subset of these forms is illustrated in Fig. 4.1. Each mathematical form requires its own set of slicing, scanning, and other algorithms, and there-in lies the problem. It is impractical for SFF devices to support this range of input models.
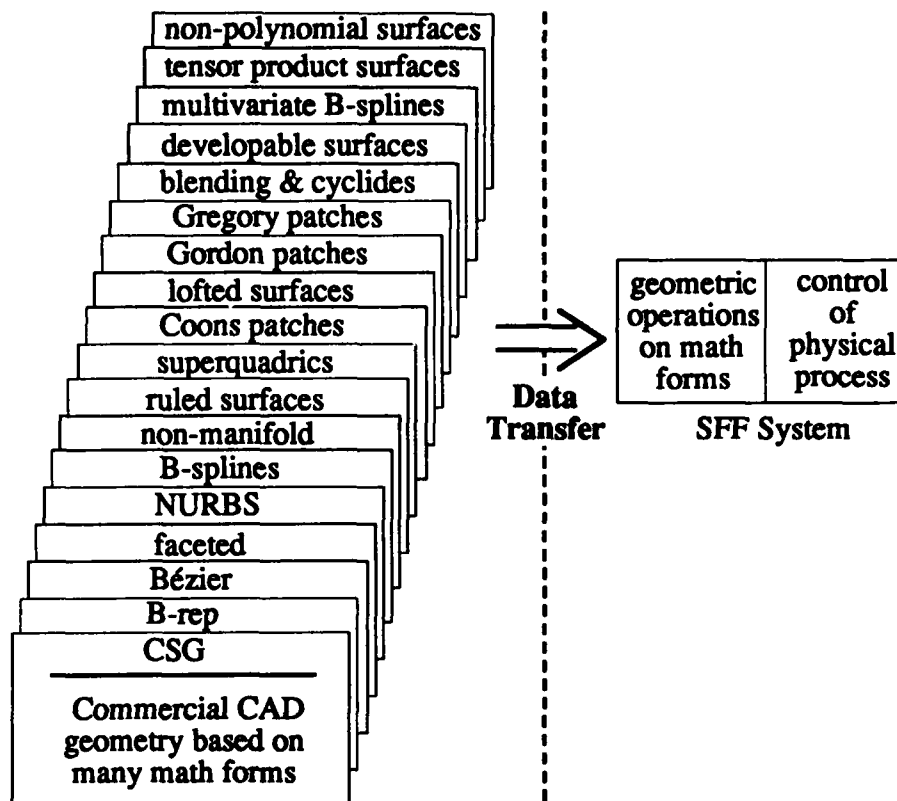
Fig. 4.1 Many Math Forms for Geometric CAD Parts

The strategic approach is to settle on one, or at most a few, common mathematical forms and require that all geometric models be approximated with the chosen common forms. Accepting this premise, the next question is, which forms are the most appropriate? Should the simplest possible form of planar triangular facets be chosen, or a reasonably general form such as non-uniform rational B-splines (NURBS)? Clearly, using a low degree polynomial surface element to approximate a given geometric model will require more elements to achieve a given precision, than would a high degree polynomial surface element. On the other hand, low degree elements involve simpler algorithms for slicing and scanning, implying faster computation. A study of these trade-offs, illustrated in Fig. 4.2, for a class of representative part models would be enlightening.
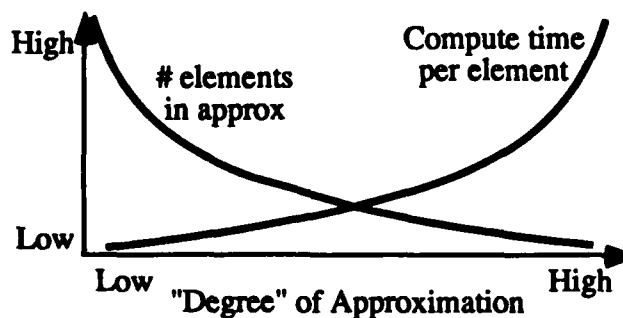
Fig. 4.2 Trade-off in Compute Time and Complexity

6

Although a NURBS surface element (patch) is relatively general, and can represent the majority of real parts, it could be overkill if most of those parts consist primarily of simple geometries, implying unnecessary computations, and overhead.

Today the de facto industry standard [Stereolithography Interface Specification] is faceted representations, i.e., the approximating surface element is a planar triangle. Unfortunately, the number of triangular facets needed to maintain high precision in complex parts becomes prohibitive. Higher degree polynomial and rational polynomial approximations are necessary to maintain precision. Fortunately, a precedent has been set in the evolving CAD data exchange standards, IGES, and STEP ["ISO CD 10303 - 42]. Since the purpose of these evolving standards is to exchange CAD data (e.g. geometry) among different CAD environments, as well as applications, without revealing proprietary internal data representations, then SFF devices should also accept these geometric forms, which includes NURBS surfaces. Consequently, slicing and scanning algorithms need to be developed only for the STEP math forms. Although the general mathematics for general surface-surface intersections, including NURBS, has been developed, no reliable experimental package is widely available.

A note of caution. If a CAD model was originally created entirely with NURBS surfaces, then the above CAD exchange standards guarantee that the model can be sent to a SFF device essentially intact. However, if a geometric CAD model is of a different math form which must be approximated with NURBS patches, including continuity conditions, then the problem becomes extremely difficult. Subsequent sections will show that even the simple planar patch approximation spawns a whole host of nontrivial problems. All of these problems become orders of magnitude more difficult for NURBS patch approximations. The advantage of NURBS is that most models will be originally generated in this representation, eliminating the need for approximations.

The next section examines some of the problems which arise when creating facet approximations.

5. FACET APPROXIMATION

Unfortunately, many commercial tessellation algorithms used by CAD vendors today are not robust, creating polygonal approximation models having: gaps (cracks, holes, punctures), i.e., missing facets; incorrect or inconsistent normals; non-manifold topology [Weiler 86] conditions, where three or more facets share a common edge or two solids are tangent along a common boundary; edge and point degeneracies consisting of equal or collinear edges; and self-intersections [Bøhn & Wozny 92]. The underlying problem is due, in part, to the difficulties in tessellating trimmed surfaces, surface intersections, and controlling numerical error. A surface intersection anomaly which results in a gap is shown in Fig. 5.1.
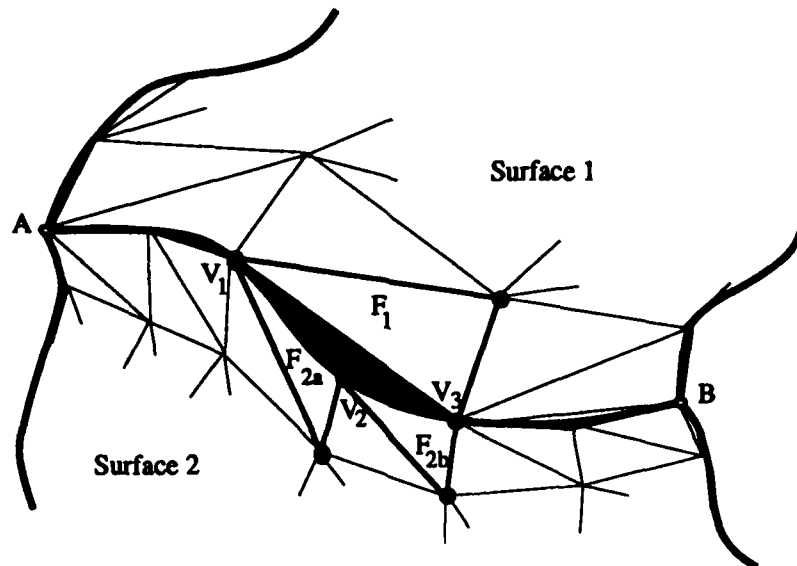
Fig. 5.1 Gaps Due to Missing Facets

The missing facet in the geometry model means that the SFF device has no defined stopping boundary on a given slice, and processes material right to the physical limit of the device, creating a stray physical solid line and ruining the part. This is an example of an invalid model.

Although a number of anomalies in tessellated models have been identified, they are by no means well understood. The more interesting problem, described next, is how to repair these invalid models.

6. VALIDATION OF GEOMETRY AND REPAIR

A basic requirement of the CAD geometric model is that it must realize a valid physical part from the SFF process. A model which meets this requirement is called valid. How does one ensure, *á priori*, that the CAD model is valid? The first step in validation deals with having a closed shell, i.e., no missing facets. (Model validation can be described in terms more general than tessellated models, for example, NURBS.)

If the model is invalid, then procedures must be developed to repair it. If a tessellated model is found to have gaps, then it must be repaired, i.e., the gaps must be filled with a "suitable" approximation of triangular facets. Since we only have a sampled surface available, i.e., the model is "correct" only at discrete points All the data which defined the original surface is not available. In addition, if some of the discrete points are also missing, then even the original faceted surface cannot be restored.

The model validation and repair problem for tessellated models can be stated as follows: Given a facet model, i.e., a set of triangles defined by their vertices, in which there are gaps, i.e., missing one or more sets of polygons, generate a "suitable" triangular surface which "fills" the gaps.

Preliminary research has shown the repair problem is difficult and not at all obvious [Rock 91]. Non-manifold edges must be resolved such that each facet has only one neighboring facet along each edge, i.e., reconstructing a topologically manifold surface. The problem of cracks requires the identification of the bounding edges and their sets of closed hole-boundary loops. Vertices can be eliminated from this loop by forming new triangular facets with neighboring vertices until the hole-boundary disappears. Finally, the problem of possible self-intersections resulting from the

8

earlier (possibly numerically imprecise) operations must be resolved.

An integral part of the above solution is to ensure a correct surface orientation for all facets. If the original facet orientations cannot be trusted, then it cannot be assured that a CAD-model with internal voids and solids can be correctly repaired. See [Bøhn & Wozny 92] for recent results on the repair problem.

7. EFFICIENT SLICING

After validating and conditioning, the geometric model is first sliced into layers, and each layer converted into scan lines as shown in Fig. 7.3. The scan lines determine the toggle points (on/off points) for the laser beam controller. The slicing or surface-plane intersection algorithms are very computation intensive. As a result it is important to make these algorithms as efficient as possible.

| 3Dmodel | Slice 3D model into 2D planar layers | Convert each 2D layer into 1D scan lines | To Laser Controller |
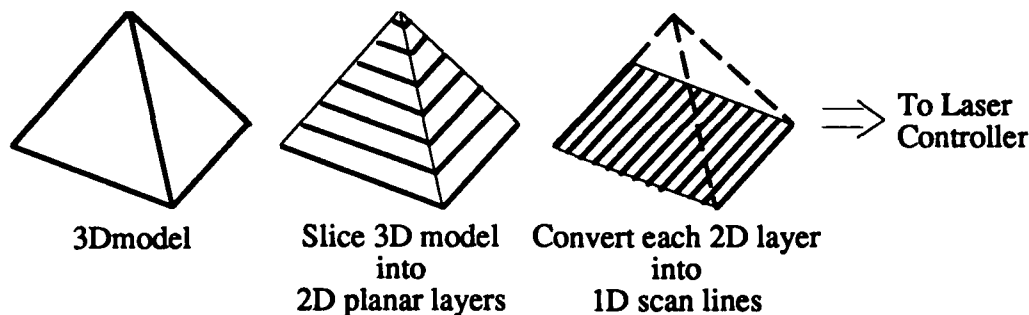
Fig. 7.1 Geometric Slicing Operations to Create Scan Lines.

To gain efficiency, topology information about the facets is needed. Using topology to incrementally intersect each triangle at a given vertical level as the algorithm marched around the facets proved to be a very efficient technique. Details are given in [Rock 91, Rock & Wozny 91b].

Other techniques, such as ray-tracing, were aimed at generating scan lines directly from the 3D model, but in general, such methods proved to be very computation intensive and thus slower [Rock 91]. Slicing NURBS surfaces is significantly more computation intensive than the polygonal marching algorithm above, as expected.

8. FILE-FORMATS

The current *de facto* SFF input file-format standard, STL, was developed by 3D Systems, Inc. [Stereolithography Interface Specification]. It consists of an unordered list of triangular facets without any topological information other than the orientation of each facet (i.e., which side of the facet is the material-side). Consequently, it is not always obvious how to mate neighboring facets, nor is it a trivial matter to determine which facets are neighbors due to numerical imprecision.

A majority of the problems encountered with the STL file format is the lack of topological information. The redundancy in storing duplicate vertices and edges is shown in Fig. 8.1. An algorithm for generating topological information is given in [Rock 91, Rock & Wozny 92].

STL Format: 12 Verticies
(36 doubles)

RPI Format: 5 Verticies
(15 doubles, 12 pointers)
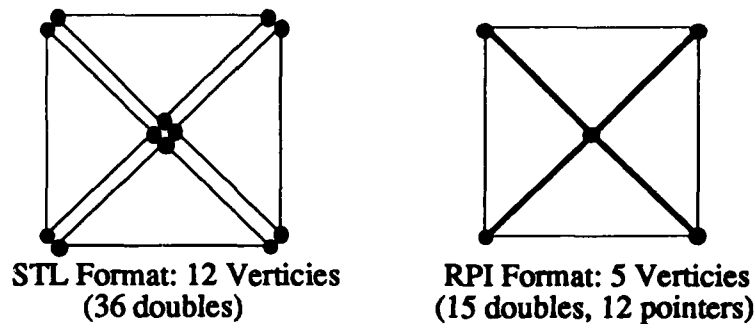
Fig. 8.1 Edge and Vertex Redundancy in STL Format

A new file format, called the RPI format, [Rock 91, Rock and Wozny 91a] is significantly more compact than the STL format, eliminates the redundancy in STL, maintains topological information, and simplifies the task of ensuring that a model is valid, i.e., no missing facets, etc. The RPI format is derivable from STL format data. It is extensible, represents facet solids, and includes information about facet topology. Topological information is maintained by representing each facet solid entity with indexed lists of vertices, edges, and faces. Instead of explicitly specifying the vertex coordinates for each facet, a facet can reference them by index number, reducing redundancy. The RPI format file is composed of a collection of entities, each of which internally defines the data it contains, and conforms to the syntax defined in the syntax diagram shown in Fig. 8.2.

Each entity is composed of an entity name, record count, schema definition, schema termination symbol, and the corresponding data. The data is logically subdivided into records which are made up of fields. Each record corresponds to the definition provided by the schema. Each field corresponds to one variable type in the Type Definition. Entity definitions have been developed for specifying facet solids, CSG solids, operations and transformations on these solids, as well as process specific data [Rock 91].
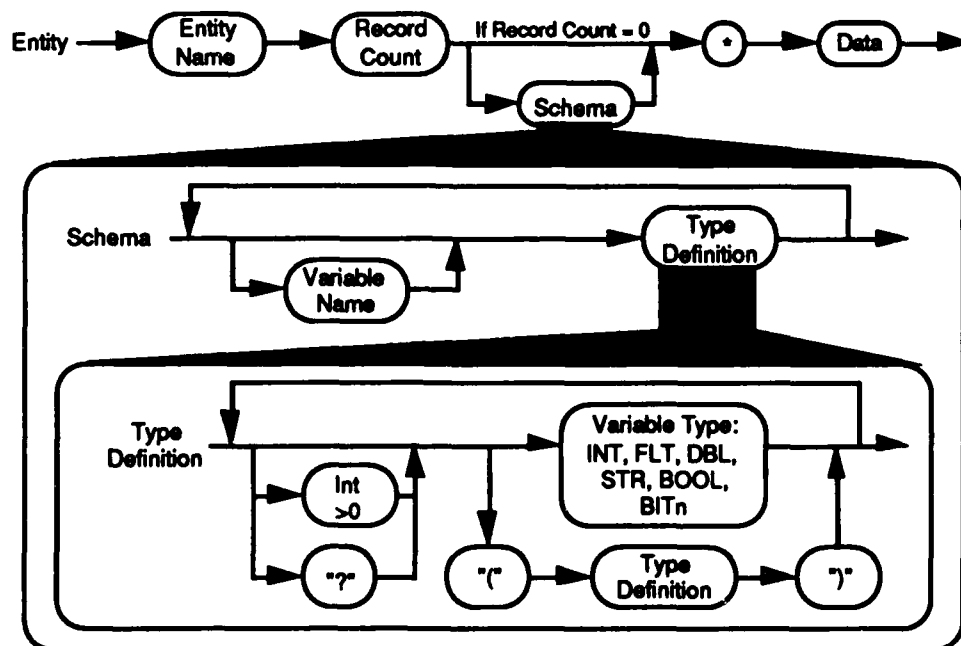
Fig. 8.2 RPI Format Entity Syntax Diagram, from [Rock 91]

10

9. INTELLIGENT SCANNING

It is not clear that the standard raster scan is the best scanning strategy for SFF. For example, experiments have shown that tracing the boundary of a part provides a better edge definition. This section, based on preliminary research by [Sankauratri 92], describes several strategies that are derived from the geometric shape of a polygonal slice.

9.1 Longest Edge Scan. In this case the scanning is done parallel to the longest edge of the polygon. Fig. 9.1 illustrates the advantage of this strategy. It results in longer uninterrupted active periods of processing material.

Raster
Scan
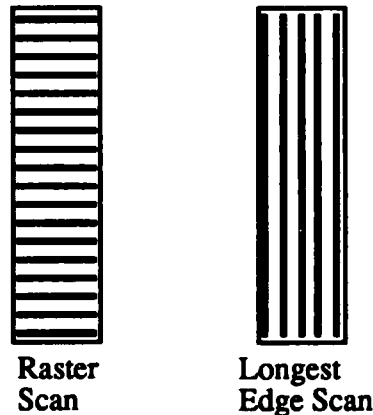
Longest
Edge Scan

Fig. 9.1 Advantage of Longest Edge Scanning

This strategy can be achieved simply by rotating the physical part or the laser to achieve the proper orientation, and raster scanning.

9.2 Adaptive Longest Edge Scan. In this case the scan proceeds perpendicular to the longest edge until a transition (i.e., a vertex) is reached. Then all the remaining edges, including the new ones formed during the scanning are searched to find the current longest edge. The scan proceeds perpendicular to the new longest edge until another transition is reached. This approach, illustrated in Fig. 9.2, minimizes the number of toggle points.
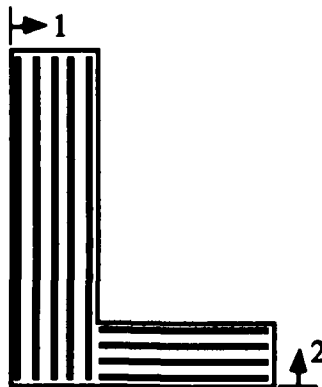
Fig. 9.2 Adaptive Longest Edge Scanning

In this approach and the following one, the changes in scanning direction will effect the physical characteristics of the part. This aspect requires further investigation.

1 1

9.3 Spiral Scan. In spiral scanning, the center of the spiral is placed at the centroid of the polygonal slice. Equi-angular rays are extended from this point. The scanning is incrementally generated from one ray to the next. An advantage of this approach is that the part is fabricated from the inside toward the outer boundary. This allows expansion due to the heat of the fabrication process to constantly move toward the unprocessed material. It appears that more accurate parts could be obtained in this manner. From a geometrical point of view, spiral scanning produces one long scan line for convex polygons.
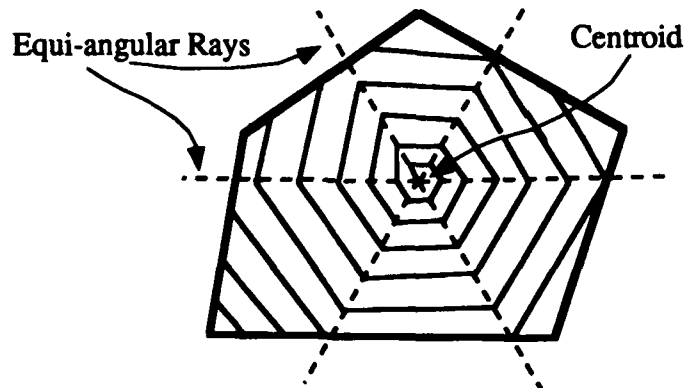
Fig. 9.3 Spiral Scanning

9.4 Medial Axis as a Scanning Strategy. If one extends spiral scanning to polygons with holes or to scanning about internal lines rather than centroids, the analogy to the medial axis [Prinz] is uncanny. Geometrically, the medial axis is the locus of centers of circles of various radii whose circumferences touch the object boundary at two points. Intuitively, of one thinks of the 2D polygon as an area which burns (yes, fire) uniformly, then the medial axis is the set of lines to which the object eventually burns when the boundary (including hole boundaries) is set on fire. The medial axis for a rectangular slice is shown in Fig. 9.4.
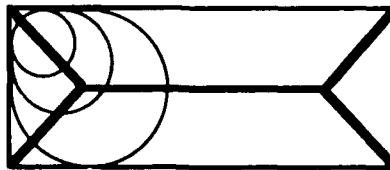
Fig. 9.4 Medial Axis for Rectangle

Unfortunately, the medial axis itself is not symmetrical enough to generate a continuously increasing spiral with equi-angular rays. But the concept does point toward a type of symmetry that is needed to support this type of scanning strategy. More research is needed to develop a uniform theory of scanning strategies, based on object symmetries.

10. INTELLIGENT CONTROL

For reasons of specificity, this section is concerned with the laser sintering process. The last section described an intelligent scanning strategy for controlling, for example, the laser beam. However, the overall goal is not simply intelligent scanning, but intelligent sintering. Intelligent sintering closes the feedback loop around the entire physical process, as illustrated in Fig. 10.1.
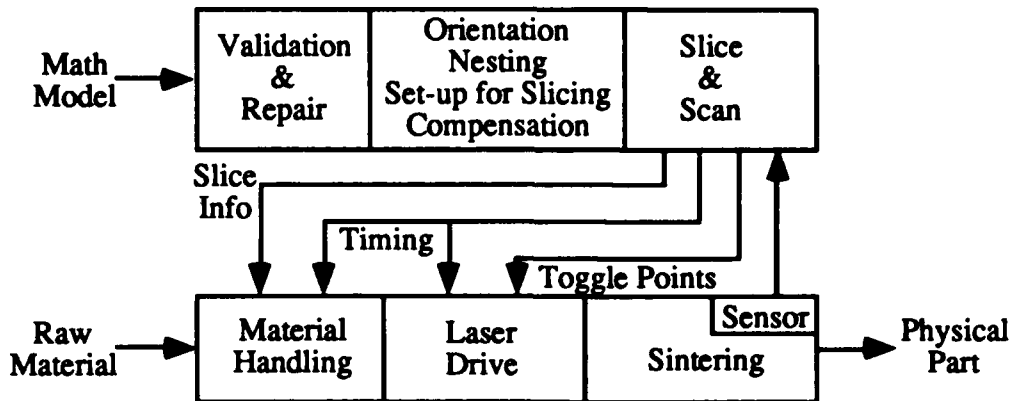
Fig.10.1 Block Diagram Showing Feedback

Research issues consist of modeling the physical process as the plant dynamics in the control loop, and developing the appropriate sensor technology to feed back the proper signals.

11. CONCLUSIONS AND FUTURE TRENDS

Although the technology is still in its infancy, it has the potential to be a dominant technology in data driven rapid prototyping, and ultimately in data driven fast, flexible, lot-size-of-one, manufacturing.

The major systems problem today deals with data transfer, namely, what should be the standard interface specification for the SFF system so that it can accept geometric data from any CAD system. The adoption of the STL format represented an appropriate approach in the early stages of the commercial technology in 1988, but now needs a major revision. The RPI format is a big step in this new direction. It is also clear that the technology must move beyond tessellated geometric models and deal with precise geometry. The evolving ISO STEP/PDES data exchange standard, especially the geometrical aspects, will have a major role in determining the data interface of future SFF systems.

The next major thrust will most likely be in efficient slicing and scan conversion for precise models. Questions which deal with part orientation, nesting, and intelligent scanning, have yet to be addressed in the open literature.

SFF systems, when viewed as lot-size-of-one manufacturing machines will provide an advanced capability where manufacturing, design, and materials all come together into a meaningful whole. This will change our design methodologies as well as eliminate or radically change traditional manufacturing procedures, such as, planning, tooling, and fixturing.

This work focused on systems and geometric issues. But it is clear that in the future CAD will extend beyond the predominate geometric volume considerations, and integrate more material characteristics. Instead of building strength into parts by adding bulk (geometric volume), SFF

13

allows the possibility of changing material properties to achieve strength. One can also consider changing surface material to increase wear characteristics. The issue of blending from one material to another needs to be investigated, as well as a range of new applications, such as smart materials and devices developed in layers. Finally, we need to incorporate material characteristics into our CAD systems and download such characteristics directly to SFF machines.

12. ACKNOWLEDGMENTS

13. REFERENCES

Arline, J., "A User Survey of Problems with Rapid Prototyping Systems," *Rapid Prototyping Report,* vol. 1, no. 6, November 1991, pp. 7-8.

Aubin, Dick, Private Communication, May, 1992.

Bjorke, O., "How to Make Stereolithography into a Practical Tool for Tool Production," *Annals of the CIRP*, vol. 40/1/, 1991.

Bøhn, J. H. and M.J. Wozny, "Automatic CAD-Model Repair: Shell-Closure," *Solid Freeform Fabrication Symposium 1992*, Published by the University of Texas at Austin, 1992.

Bourell, D.L., Beaman, J.J., Marcus, H.L., and J.W. Barlow, "Solid Freeform Fabrication An Advanced Manufacturing Approach," *Solid Freeform Fabrication Symposium 1990*, Published by the University of Texas at Austin, 1990.

Cohen, A.L., eds., *Rapid Prototyping Report.*, The newsletter of the desktop manufacturing industry, CAD/CAM Publishing, Inc., 841 Turquoise St., Suites D&E, San Diego, CA 92109-1159.

Deckard, C.R., "Part Generation by Layerwise Selective Sintering," M.S. Thesis, Department of Mechanical Engineering, University of Texas at Austin, 1986.

Dolenc, A., Mäkelä, I., and R. Hovtun, "Better Software for Rapid Prototyping with INSTANTCAM", IFIP Transactions B. *Human Aspects in Computer Integrated Manufacturing*, G.J. Olling and F. Kimura, eds. Elsevier Science Publishers B.V. (North-Holland), 1992.

"ISO CD 10303 - 42. Product Data Representation and Exchange - Part 42: Integrated Resources: Geometrical and Topological Representation," ISO Subcommittee 4, *Industrial Data and Global Manufacturing Programming Languages*. Secretariat: National Institute of Standards and Technology, Gaithersburg, MD, 1991.

Kruth, J.P., "Material Incress Manufacturing by Rapid Prototyping Techniques," *Annals of the CIRP* , vol. 40/2/, 1991.

Marcus, H.L., Beaman, J.J., Barlow,. J.W., Bourell, D.L., and Crawford, R.H., eds., "*Solid*

Rock, S. J., "Solid Freeform Fabrication and CAD System Interfacing," MS Thesis, (also RDRC Technical Report 91036) Rensselaer Design Research Center, Rensselaer Polytechnic Institute, Troy, NY, December 1991. [1991]

Prinz, F., Carnegie Mellon University, unpublished paper, 1988-1992.

Rock, S.J., and M.J. Wozny, "A Flexible File Format for Solid Freeform Fabrication," *Solid Freeform Fabrication Symposium 1991*, Marcus, Beaman, Barlow, Bourell, and Crawford, eds., Published by the University of Texas at Austin, August 1991. [1991a]

Rock, S.J., and M.J. Wozny, "Utilizing Topological Information to Increase Scan Vector Generation Efficiency," *Solid Freeform Fabrication Symposium 1991*, Marcus, Beaman, Barlow, Bourell, and Crawford, eds. , Published by The University of Texas at Austin, August 1991. [1991b]

Rock, S.J., and M.J. Wozny, "Generating Topological Information from a "Bucket of Facets'" *Solid Freeform Fabrication Symposium 1992*, Published by the University of Texas at Austin, August 1992.

Sankauratri, Sridhar. "Intelligent Scanning", unpublished preliminary version of M.S. Thesis. Rensselaer Polytechnic Institute, Troy, N.Y., August, 1992.

"Stereolithography Interface Specification," 3D Systems, Inc., June 1988.

Weiler, K., "Topological Structures for Geometric Modeling," Ph.D. Thesis, Rensselaer Polytechnic Institute, Troy, NY, August 1986. (Also RDRC Technical Report 86032)

Process Control System for a High Temperature Workstation performing the Selective Laser Sintering Process

Suman Das, Graduate Research Assistant
Richard H. Crawford, Assistant Professor
J.J. Beaman, Professor
Department of Mechanical Engineering
The University of Texas at Austin

Abstract

This paper describes the design and implementation of a Computer Process Control System for a High Temperature Workstation performing Selective Laser Sintering of metal and ceramic powders. As compared to our previous machine [1], the increased complexity and sophistication of the new workstation [2] requires a variety of measurement and control devices which are interfaced to a process control computer. Among these are a gas analyzer, a data logger, a step motor controller and a CNC controller. This process control system incorporates a XView (a X Window System Toolkit) based Graphical User Interface which allows the user to set and change process parameters on-line as well as receive graphical feedback on the process.

Introduction

The Selective Laser Sintering (SLS) Process has made much progress since its first demonstration in 1986 [3]. With the objective of sintering metals and ceramics, the Solid Freeform Fabrication group at the University of Texas at Austin acquired a 1.1 kW CO_2 laser in September 1991. Design and Fabrication work on a High Temperature Workstation (HTW) to serve as the testbed for SLS of metals and ceramics was begun in June 1991 [2,4]. The construction of the first version of the HTW was completed in Fall 1991 and experimental tests on a variety of metal powders and ceramics were initiated in November 1991. This sintering chamber incorporated a powder delivery system and a work area for the laser scanning. A second chamber has been constructed to continue work towards the next stage of research (i.e. high temperature, high laser power sintering) . This chamber incorporates a powder heating and temperature control system and a strict environment control system [5]. This paper describes the Computer Process Control System that runs the SLS process on the HTW .

Design Objectives

Platform
In contrast with our previous SLS machine, called "Bambi", which uses an IBM PS-2 running MS-DOS as its process control computer, the SFF group decided to adopt the Unix Operating System for process control in the High Temperature Workstation. This choice is justified by several reasons. First, it provides us with multitasking capabilities, standard networking and file-transfer protocols and X as the Window system. This choice was also dictated by the desire to have two similar computing environments, one to be used for SLS software development and the other to be used purely to run the HTW.

Process Control
One of the design objectives at the start of the Selective Laser Sintering project was to design a fully automated machine which could be used for rapid part fabrication. The operation of this machine should require minimum human intervention and expertise. With

16

this goal in mind, the function of the Process Control System is to automate all aspects of the operation of the High Temperature Workstation, including geometry data processing, laser and scanning system, powder feed and leveling system, temperature data logging, monitoring sintering chamber enviroment composition and pressures, and safety procedures such as machine shutdown in the event of abnormal conditions.

Graphical User Interface

Another design objective of the Process Control System for the HTW was to present the user with a simple menu-driven graphical user interface to operate the machine. This user-interface should allow the user to enter process parameters such as part side drop and feed side rise, delay between successive scans and repetition of layers. The interface should also allow the user to interrupt the process, change process parameters and continue the process. The interface should include process monitoring faetures that provide the user with a graphical feedback on the status of the process. The graphical feedback should include a display of the current layer scanned on screen, reporting of various sintering chamber temperatures obtained from a datalogger and the composition of the chamber's environment obtained from a Residual Gas Analyser.

Design Features

Platform

A Sun Sparcstation IPC was chosen as the Process Control Computer. This choice provided binary compatibility as well as file sharing capability with the Sun Sparcstation 2GX being used for software development and testing purposes.

Process Control

The process control computer functions as a system integrator by handling all communication with the various control and measurement devices. This design centralizes the feedback from these devices and allows user control over them via a menu-driven interface. Figure 1 shows a schematic of the Process Control System in the High Temperature Workstation.
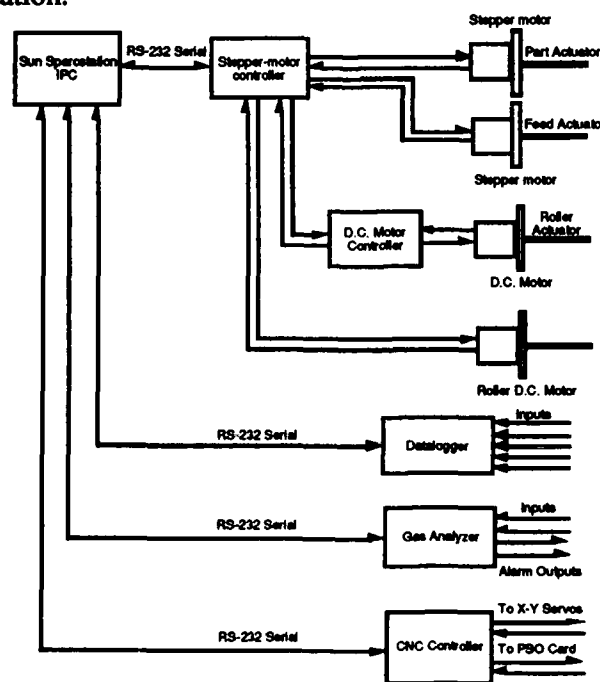
Fig. 1 A schematic of the HTW Process Control System

17

Laser Scan Control by CNC

The scanning system for the 1.1kW Everlase CO_2 laser on the HTW consists of a set mirrors mounted on a pair of X-Y linear motion tables. The motion of the X-Y tables is controlled by an Aerotech Unidex-21 CNC controller with a position accuracy of 0.001" over a travel of 12" in either direction. The motion tables are capable of scan speeds of upto 20 inches/sec. In order to perform raster scans, the CNC controller incorporates a Position Synchronous Output mechanism that ties the laser beam switching to the linear position encoders of the motion tables. The scan data is expressed in the form of a sequence of laser-off and laser-on distances (expressed in microns) for each scan-line. The scan data is sent from the process control computer to the CNC controller on a layer-by-layer basis. The CNC is interfaced to the process control computer via a serial RS-232 interface.

Powder Delivery and Leveling System

The powder delivery and leveling system consists of a pair of cylinders, a pair of pistons and a leveling roller (Figure 2). The pistons are actuated by a linear-actuator/stepper-motor combination. The roller is mounted on a linear-actuator that traverses the length of the powder bed . Rotational motion is delivered to the roller by a D.C. motor through a set of bevel gears and a flexible shaft. The leveling sequence consists of a sequence of motions of the piston actuators, the roller actuator and roller rotation, and is controlled by a stepper-motor controller and a set of relays. The stepper-motor controller receives commands from the process control computer via a serial RS-232 interface.
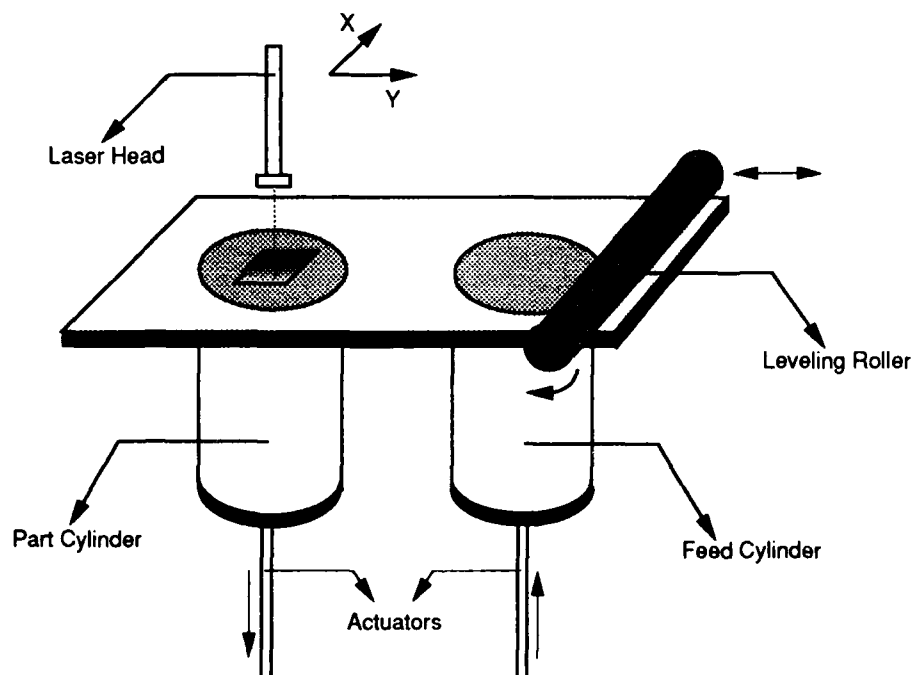
Fig 2. A schematic of the Powder Delivery and Leveling System

Gas Analyzer

Selective Laser Sintering of metals and ceramics requires monitoring the gaseous composition of the sintering chamber for two reasons. First, Oxygen content must be monitored for safety purposes, to prevent the possibililty of explosive reactions. Second, the gaseous composition must be known during layer-wise gas-phase materials processing which is a future possibility. A Residual Gas Analyzer is employed for these purposes. The Gas Analyzer has an alarm output that goes high when a preset oxygen concentration is exceeded and sets on a relay which closes the shutter in the laser, thereby preventing the

18

laser beam from reaching the powder bed. The gas analyzer receives commands from the process control computer and sends data back to the computer via a serial RS-232 interface.

Datalogger

High-temperature high laser-power selective laser sintering of metals and ceramics necessitates the monitoring of temperatures at various points in the chamber, on the powder bed and at the heater surface, to provide a uniform temperature distribution across the powder bed [5]. A datalogger is used for this purpose. This datalogger used for this purpose is capable of receiving sixteen analog inputs and four digital inputs as well sending 16 digital alarm outputs. The datalogger reports the various temperatures to the process control computer via a serial RS-232 interface. Along with the temperature, the data sent by the datalogger also indicates whether a preset temperature limit has been exceeded for each channel.

Graphical User Interface

On start-up, the process control software displays a base window with two pull down menus. The menu named "Process" has several submenus pertaining to process related items (Figure 3). The menu named "Simulation" has submenus that allow the user to view the geometry data associated with the part to be created without actually performing any sintering (Figure 4).
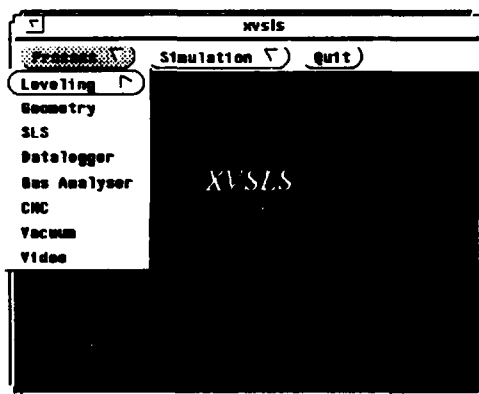
Fig 3. The Process Menu
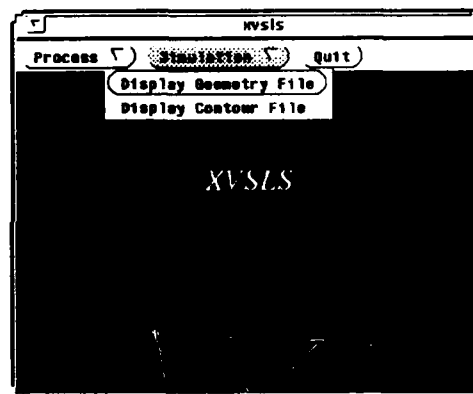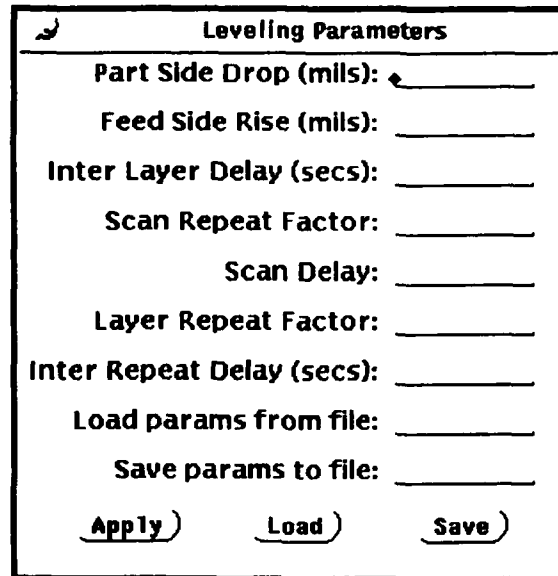
Fig 4. The Simulation Menu

Leveling Parameters

The leveling submenu has two subselections, "Leveling" and "Dummy Layers" .
Selecting "Leveling" raises a "Leveling Parameters" popup window (Figure 5). This window has a number of input text fields into which the user must enter his preferred parameters. Apart from supplying Part Side Drop and Feed Side Rise in mils, the user may also supply the value of following parameters:

Inter Layer Delay: A time delay in seconds before scanning of the next layer is initiated.

Scan Repeat Factor: Scan the same layer more than once without depositing fresh powder.

Scan Delay: A time delay between successive scans when the value of the above variable is greater than one.
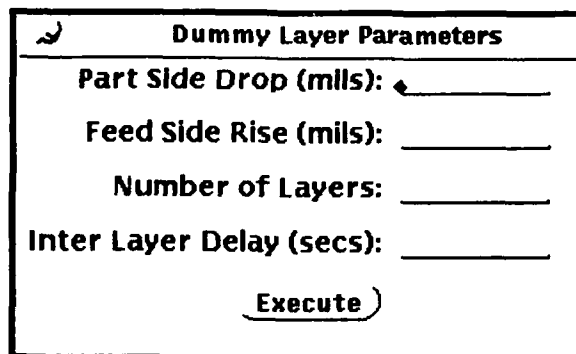
Layer Repeat Factor:	Each layer may be repeated. This is useful in scaling a part.
Load Parameters from File:	The user may load the above parameters from file into which these values were previously stored.
Save Parameters to File:	The user may save the entered parameters into a file for future retrieval.

```
┌─────────────────────────────────┐
│ ↲        Leveling Parameters     │
├─────────────────────────────────┤
│   Part Side Drop (mils): ◆_____ │
│                                   │
│    Feed Side Rise (mils): _____ │
│                                   │
│ Inter Layer Delay (secs): _____ │
│                                   │
│      Scan Repeat Factor: _____  │
│                                   │
│             Scan Delay: _____   │
│                                   │
│      Layer Repeat Factor: _____ │
│                                   │
│ Inter Repeat Delay (secs): _____ │
│                                   │
│    Load params from file: _____ │
│                                   │
│     Save params to file: _____  │
│                                   │
│   Apply )    Load )    Save )     │
└─────────────────────────────────┘
```

Fig. 5 The Leveling Parameters popup Window

Selecting "Dummy Layers" raises a "Dummy Parameters" popup window (Figure 6). This window has input text fields into which the user enters part side drop, feed side rise and the number of dummy layers that are to be deposited (i.e. layers with no scanning). This feature is useful when one wishes to level the powder bed before starting the actual process of making a part.

```
┌─────────────────────────────────┐
│ ↲      Dummy Layer Parameters    │
├─────────────────────────────────┤
│  Part Side Drop (mils): ◆_____ │
│                                   │
│   Feed Side Rise (mils): _____  │
│                                   │
│     Number of Layers: _____     │
│                                   │
│ Inter Layer Delay (secs): _____ │
│                                   │
│          Execute )                │
└─────────────────────────────────┘
```

Fig. 6 The Dummy Layers Parameters popup Window

Geometry Parameters

Selecting the Geometry submenu raises a "Geometry Parameters" popup window (Figure 7). This popup allows the user to enter the name of the geometry data file

associated with the part to be made. The geometry data file contains the scan information for all layers of the object. Upon entering the file name and clicking on the "Open" button, the process control software counts the number of layers in the geometry file and reports it to the user. The user can now enter the starting layer (default is 1) and the number of layers to be processed (default is All). Clicking on the "Apply" button saves these parameters into geometry parameters file which is used by the process control software. Clicking on "Close" closes the currently open geometry file allowing the user to open another geometry file.

```
┌──────────────────────────────────────────────────┐
│  ↵            Geometry Parameters                 │
├──────────────────────────────────────────────────┤
│      HTW Geometry File ●_____           │
│                                                    │
│      Total Layers in File: _____                  │
│                                                    │
│          Set to Layer #: 1____                     │
│                                                    │
│  Layers to process (0-all): 0____                  │
│                                                    │
│      Open )        Apply )        Close )          │
│                                                    │
└──────────────────────────────────────────────────┘
```

Fig. 7 The Geometry Parameters popup Window

SLS Parameters

Selecting the SLS submenu raises the "SLS Parameters" window (Figure 8). This window has text input fields for the CNC program that is to be run and the desired scale factor on the part. There are two checkbox choices also; one allows the user to by-pass the leveling action and the other allows the user to invoke a display of layer scans on screen. This display is synchronized with the actual scanning of the laser as the part is being built. The "Start" button initiates the execution of the SLS process. Three other buttons "Interrupt", "Continue" and "Stop" allow the user to interrupt an ongoing scan for any reason, to continue the process after an interrupt and to stop the process respectively.

```
┌──────────────────────────────────────────────────┐
│  ↵              SLS Parameters                     │
├──────────────────────────────────────────────────┤
│  Bypass Leveling Sequence _│ Yes ✓ No             │
│                                                    │
│     Display Layer Scans _│ Yes ✓ No               │
│                                                    │
│       CNC program file: ●_____            │
│                                                    │
│          Scale Factor: _____              │
│                                                    │
│  Start )   Interrupt )   Continue )   Stop )       │
│                                                    │
└──────────────────────────────────────────────────┘
```

Fig. 8 The SLS Parameters popup Window

Datalogger

Selecting the Datalogger submenu raises the "Datalogger" popup window (Figure 9). This window has 20 text output fields that display the value of each channel of the datalogger. A slider is provided to adjust the frequency with which the data is reported. Pressing the "Connect" button establishes a connection with the datalogger. Pressing

"Start" initiates the reading data from the datalogger. A checkbox choice provides the user with the option of saving the received data to a file.

```
┌──────────────────────────────────────────────────────┐
│  ┌─┐                    Datalogger                    │
│  └─┘                                                   │
│    DL Channel 0: _____          │
│    DL Channel 1: _____          │
│    DL Channel 2: _____          │
│    DL Channel 3: _____          │
│    DL Channel 4: _____          │
│    DL Channel 5: _____          │
│    DL Channel 6: _____          │
│    DL Channel 7: _____          │
│    DL Channel 8: _____          │
│    DL Channel 9: _____          │
│   DL Channel 10: _____          │
│   DL Channel 11: _____          │
│   DL Channel 12: _____          │
│   DL Channel 13: _____          │
│   DL Channel 14: _____          │
│   DL Channel 15: _____          │
│   DL Channel 16: _____          │
│   DL Channel 17: _____          │
│   DL Channel 18: _____          │
│   DL Channel 19: _____          │
│  Interval between Reads (secs) 5____ 5  ├───────  388  │
│  Save Data to File _⌐ Yes ☑ No                        │
│  Save to File: _____                         │
│   ⎛Connect⎞  ⎛Start⎞  ⎛Stop⎞  ⎛Disconnect⎞            │
└──────────────────────────────────────────────────────┘
```

Fig. 9 The Datalogger popup Window

Gas Analyzer

Selecting the Gas Analyzer submenu raises the "Gas Analyzer" popup window (Figure 10). This window has a text field that displays a preset Oxygen concentration threshold in terms of partial pressure (Torr) . There are six text output fields that display the peak values of the each of the six channels of the Residual Gas Analyser. Pressing "Connect" establishes a connection between the process control computer and the Gas Analyzer. Pressing "Start" initiates reading the peak partial pressures from the Gas Analyzer. A slider allows the user to set the frequency at which the Gas Analyzer output is sampled. A checkbox choice provides the user with the option of saving the pressure data to a file. The gases currently being monitored are Oxygen, Nitrogen and water vapor.

Fig. 10 The Gas Analyzer popup Window

Geometry File Display

Selecting the "Display Geometry File" submenu under the "Simulation" menu raises a "Geometry File" popup window (Figure 11). This window has three buttons labeled "Draw" , "Clear" and "Quit" respectively and a viewport (canvas) in which the graphics are displayed. Pressing "Draw" raises a popup (Figure 12) which has a textfield for the name of the geometry file to be displayed. Upon entering the file name and pressing "Open", the software counts the total number of layers in the file and reports it to the user. The user can now select the starting layer, ending layers and a time delay between the display of successive layers. Selecting "Start" initiates the display. The user may interrupt the display at any time by pressing "Interrupt", continue the display after an interrupt by selecting "Continue" or stop the display altogether by selecting "Stop".
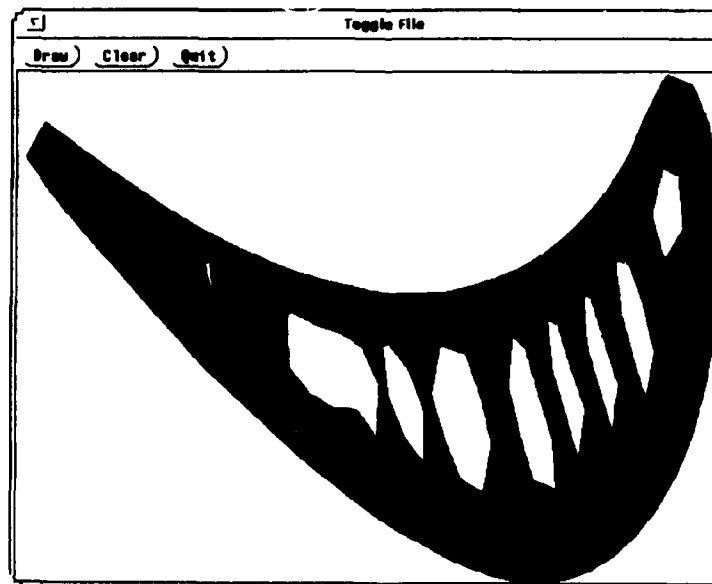
Fig. 11 The Geometry File Display

23
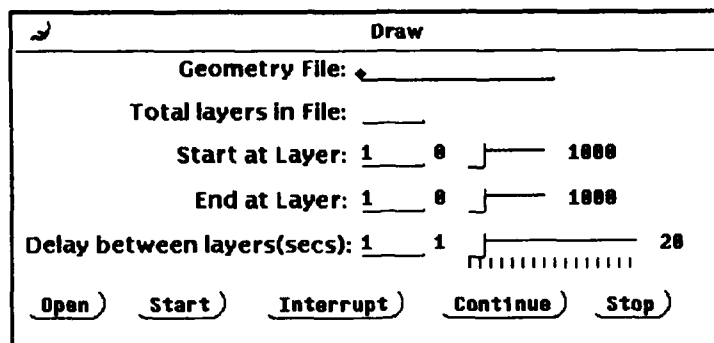
Fig. 12 The Draw popup window

Future Work

Features to be incorporated in future versions of this Process Control Software are:

1. A time history plot of various temperatures logged from the datalogger.

2. A time history plot of the partial pressures read in from the gas analyzer.

3. An interface to the temperature controller for the heater.

4. Real time control of laser power through software.

5. Tracing of part boundaries prior to raster scanning, which may improve part quality and surface finish. A polygonal contour representing the boundary of a layer may be used to approximate the actual boundary by several cubic splines joined together.

6. A display of contour files used in 5 above.

7. A Video popup window that shows the actual process captured through a video camera positioned above the part cylinder.

Conclusion

The first version of process control software for the High Temperature Workstation has been tested and used successfully to make test parts [6]. This design successfully meets the objectives established for implementing an integrated process control environment for the Selective Laser Sintering Process. This design is modular and provides room for enhancements, improvements and changes as the requirements of the ongoing research on the High Temperature Workstation become more stringent.

References

1. Forderhase, Paul A. *Design of a Selective Laser Sintering Machine Intended for Academic Use.* Master's Thesis, The University of Texas at Austin , May 1989.

2. Das, S., McWilliams, J., Wu, B., and Beaman J. J., *Design of a High Temperature Workstation for the Selective Laser Sintering Process,* Solid Freeform Fabrication Symposium, The University of Texas At Austin, Aug 12-14, 1991.

3. Deckard, C. R., *Part generation by Layerwise Selective Sintering*, Master's Thesis, The University of Texas at Austin, May 1986.

4. Das, S., Crawford R.H., and Beaman, J.J., *Software Testbed for Selective Laser Sintering,* Solid Freeform Fabrication Symposium, The University of Texas at Austin, Aug 12-14, 1991.

5. Hysinger, C., McWilliams, J., and Beaman J.J., *Design of a High Temperature Sintering Chamber for the Selective Laser Sintering Process*, Solid Freeform Fabrication Symposium, The University of Texas at Austin, Aug 3-5, 1992.

6. Zong, G., Wu, Y. and Marcus, H.L., *Liquid Phase Selective Laser Sintering of High Temperature Materials*, Solid Freeform Fabrication Symposium, The University of Texas at Austin, Aug. 3-5, 1992.

A PARALLEL SLICING ALGORITHM FOR SOLID FREEFORM FABRICATION PROCESSES

C. F. Kirschman, C. C. Jara–Almonte
Center for Advanced Manufacturing
Mechanical Engineering Department
Clemson University, Clemson, SC

ABSTRACT

Slicing can account for more than 60% of the time to prepare a part for building on a stereolithographic apparatus. To improve the preparation time, a parallel slicing algorithm was developed. The algorithm was run on a Butterfly GP1000 using 2, 4, 8, 16, and 32 processors and superlinear speedup was observed due to high memory requirements. The parallel algorithm can reduce slice times by up to 92% on 16 concurrent processors as compared to a single processor.

INTRODUCTION

Stereolithography is one of several different Solid Freeform Fabrication (SFF) technologies available today (Ashley, 1991). The most common stereolithography apparatus (SLA) is the SLA 250 from 3D Systems (Valencia, CA). Because of its popularity, the initial software development described in this paper was aimed at this machine; however, it is believed that the concepts can be extended to any of the technologies.

The preparation of a part, detailed by 3D Systems (1989), begins in a CAD system. A solid model is created to represent the part. The part is then converted to a stereolithographic format (stl) file. This file contains a set of triangles which define the surface of the part and the outward pointing normals to these triangles.

Next, this faceted representation is preprocessed for building in the SLA. First the part is supported, and then it is sliced by another computer. Then the files containing the layers are sent to a third computer for merging, preparation, and reconstruction in the SLA. The parts are built layer–by–layer from the bottom up in layers 0.0025 to 0.030 inch thick.

One of the biggest complaints of the users of this technology is that the preparation time before building is too long. Slicing in particular can account for 60% or more of the time between the CAD system and the SLA. Because of this, efforts are underway to reduce the slicing time. This paper discusses techniques for improving the slicing speed by employing parallel architectures.

SLICING

The slicing process is depicted in Figure 1. A solid model is designed in CAD, and then is tessellated. Each of the resulting triangles is then segmented, and the segments for each z–level are joined to form a contour. The contours define the shape of the part to be built.

Currently, slicing at Clemson University is done by a simple geometric algorithm (Chalasani, 1991). The algorithm is shown in Figure 2. First, the stl file is read in. Next, the coordinates of the vertices of the triangles are multiplied by a large number, usually about 5000. This converts the
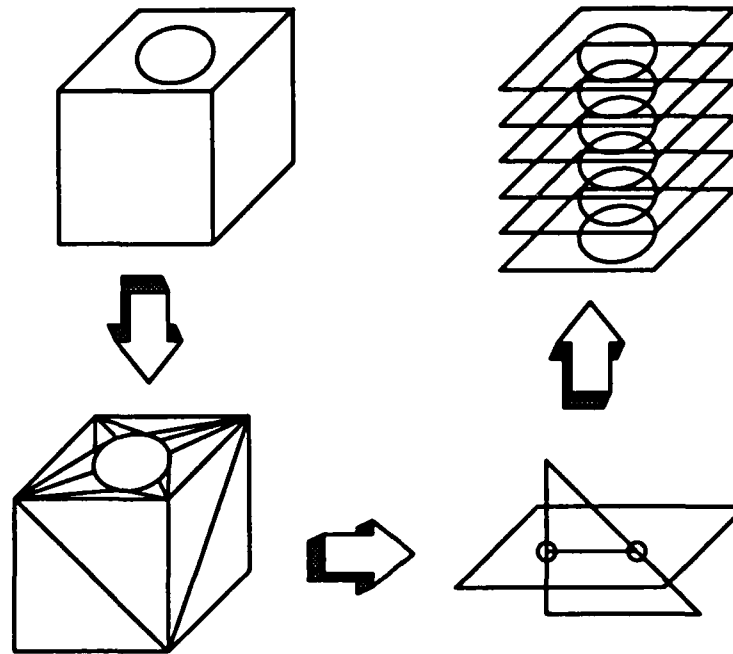
Figure 1. The Slicing Process

coordinates to integers, which computers can process faster. Then all flat triangles are separated and identified as the skin fills on the top and bottom of the part.

Then, for each z layer, each remaining triangle is checked to see if it passes through a plane parallel to the platform at that height, using equations such as those in Wolstenholme (1971). If it does, the intersections of the triangle and the plane make up a line. Once all of the triangles have been checked, the resulting list of lines is sorted in a head–to–tail fashion. This leads to a complete contour of the part at this level. The area defined by this contour is then hatched in a reasonable pattern, depending on the application; often squares or triangles are used. Hatching algorithms are discussed in Foley et al. (1990). These layers are then stacked up and written to a file, and the memory is freed. This sliced file is sent to another computer for the merging process. The merged file then is used to drive the SLA.

It is not necessary for the part to be completely solidified in the SLA, so the boundaries are drawn and hatched in a honeycomb manner and the part is built encapsulating liquid. The "green" part is then postcured in an ultraviolet (UV) oven until completely solid (3D Systems, 1989). This reduces wear on the laser, which has a finite life.

ARCHITECTURE

The slicing algorithm shown in Figure 2 was run on both serial and parallel computers and compared for slicing speed. Although the different computers do not employ the same processors, they represent typical machines available today. The parallel and serial algorithms were kept as similar as possible, but certain modifications had to be made for different platforms.

Serial Computer

The serial computer used for this work was a Sun Microsystems SparcStation 1+ running SunOS 4.1.1. It uses a Sun 4/65 processor running at 25 MHz with a 25MHz floating point processor, capa-

27
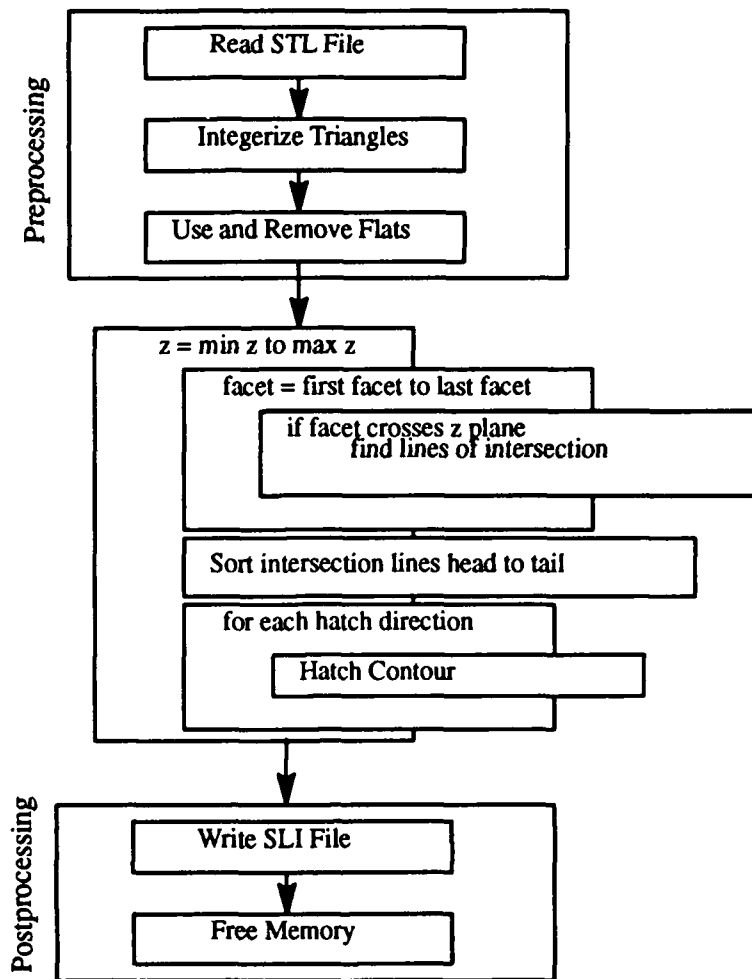
Figure 2. Geometric Slicing Algorithm.

ble of 15.7 MIPS. The particular machine has sixteen megabytes of memory and 100 megabytes of swap space. The machine was completely unloaded when testing was done.

Parallel Computer

The parallel computer used for this work was the Butterfly GP1000 running the MACH 1000 operating system, which is UNIX–like. It has 94 nodes, each one comprised of a Motorola 68020 processor with a floating point unit (FPU) and memory management unit (MMU). It is a physically distributed, logically shared memory machine as shown in Figure 3. The butterfly architecture is used because all of the processors are the same distance from the memory, and therefore the communication cost is constant. This provides better results when the algorithm is run on larger numbers of nodes. The actual program was run on clusters of 1, 2, 4, 8, 16, and 32 nodes of this machine.

TEST CASES

There were four test data sets for the algorithms, detailed in Table 1 below. There are two parameters which are important to the speed: number of triangles and number of layers. It was found that the layers were the controlling factor in problem size, so a formula was devised to represent problem size as a function of these two numbers. It was arbitrarily decided that the layers accounted for 75%

28
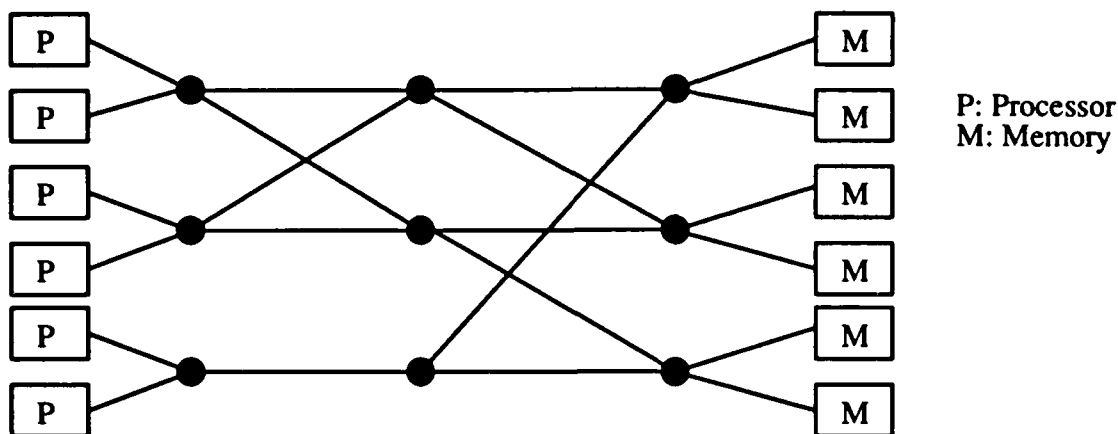
Figure 3. Simple Butterfly® Multistage Switch Connection.

of the running time and the number of triangles accounted for 25%. But, the number of triangles is about an order of magnitude greater than the number of layers, so this it was scaled by dividing by 10. A measure of problem size is given by:

$$\text{size} = 0.25\frac{N_{tri}}{10} + 0.75N_{layer} \tag{1}$$

where N_{tri} = Number of Triangles
N_{layer} = Number of Layers.

Table 1. Problem Sizes.

Problem Size	152	180	184	292
Number Triangles	40	2450	1008	9386
Number Layers	201	159	211	76
Slicing Time*(min)	5:23	6:05	9:21	13:48

*Sliced using 3D System's slicing algorithm on NEC 386/16, standard isohatch, no skin fills.

PARALLELIZATION OF THE ALGORITHM

The next step in the process was to parallelize the slicing algorithm. The Butterfly uses a "Uniform System" to support its parallel functions. It uses a "host" which sends jobs to the nodes in the cluster. This provides an easy method for the programmer to access the parallel power of the architecture. Essentially, the host serves as a manager, which passes out the tasks to each processor as it finishes its current task. This can lead to a bottleneck if many processors are waiting in the queue for jobs.

The essential differences between the serial and parallel programs are in the areas of variable management. Even though it is a shared–memory architecture, certain things must be declared global if the other nodes are to see them. The global declaration consists of a macro that informs all nodes in the cluster of the location of the memory, and allocation routines to gain space for these variables. Also, any data to be accessed through global pointers must be declared in the shared memory, which is also accessed through calls to the Uniform System.

Global variables are necessary due to the minimal nature of the calling routines for parallel node utilization. These allow the user to call a function with the only passed variable being the current index. Therefore, any other necessary information must be maintained globally. This creates a communication cost problem when too much information must be accessed from the global store or several processors need to write to memory on the same processor.

RESULTS

Serial Algorithm

The serial version of the algorithm was run on the SparcStation, and the computational times are in Table 2 below. The SparcStation uses a much newer and faster microprocessor, so the times are faster than the concurrent processors and the 3D Systems algorithm (Table 1). However, they show the possibilities for speed when better processors are used in parallel. The variations in these numbers are as great as 15%, with problem 184 varying by 5 seconds over 6 runs.

Table 2. Serial Algorithm Times.

Problem Size	152	180	184	292
Time (sec)	10	27	58	50

Parallel Algorithm

For parallel algorithms, it is useful to define certain measures of performance. From Fox et al. (1988), define T_{seq} to be the time elapsed on a single or sequential processor of the parallel machine. $T_{conc}(N)$ is then defined to be the elapsed time on N concurrent processors. Now, the concurrent speedup, S(N), can be defined by:

$$S(N) = \frac{T_{seq}}{T_{conc}(N)}$$

(2)

If S(N) = N, it is called *linear speedup*, which means that the algorithm is twice as fast on two processors as one, and twice as fast on four as on two. Generally, linear speedup cannot be attained because of *communication costs*, which is the time it takes for one processor to communicate with other processors. Other factors affecting performance can be found in Fox et al. (1988). A second measure of the performance is the efficiency, ε, defined by:

$$\varepsilon = \frac{S(N)}{N}$$

(3)

Efficiency is optimally 100%, but again other factors can influence this. Both efficiency and speedup depend on the performance on a single processor of the parallel machine.

This algorithm parallelized well. The times for each run are shown in Figure 4, and the speedup and efficiencies are shown in Figures 5 and 6. The speedup is actually superlinear and the efficiencies are greater than 100% for the 184 and 292 cases. This is due to the amount of memory these large cases require. For a single processor, the memory requirements exceed the locally available memory, so the CPU must access slower memory, either on another node or on disk as swap space. This makes the single processor case slower, which then skews the speedup so that it seems to be

superlinear when in fact it is not. The small case, 152, shows this since it does not approach linearity or peak efficiency.
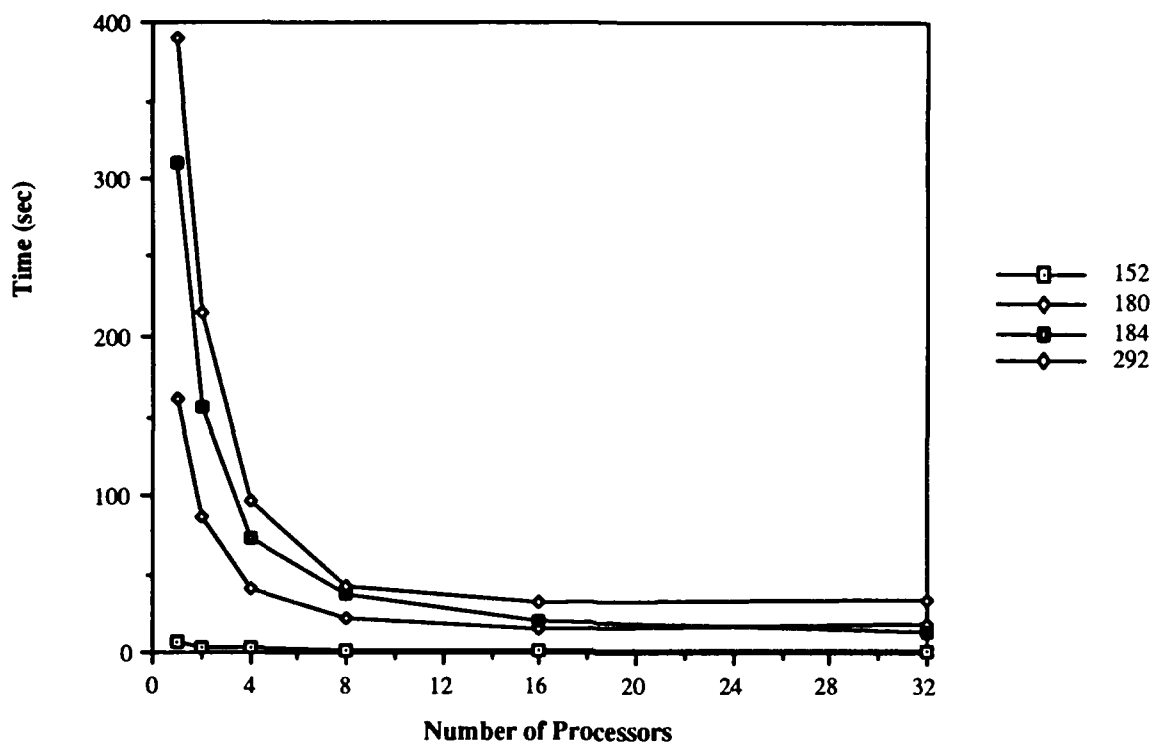
Figure 4. Time vs. Number of Processors for Parallel Algorithm.
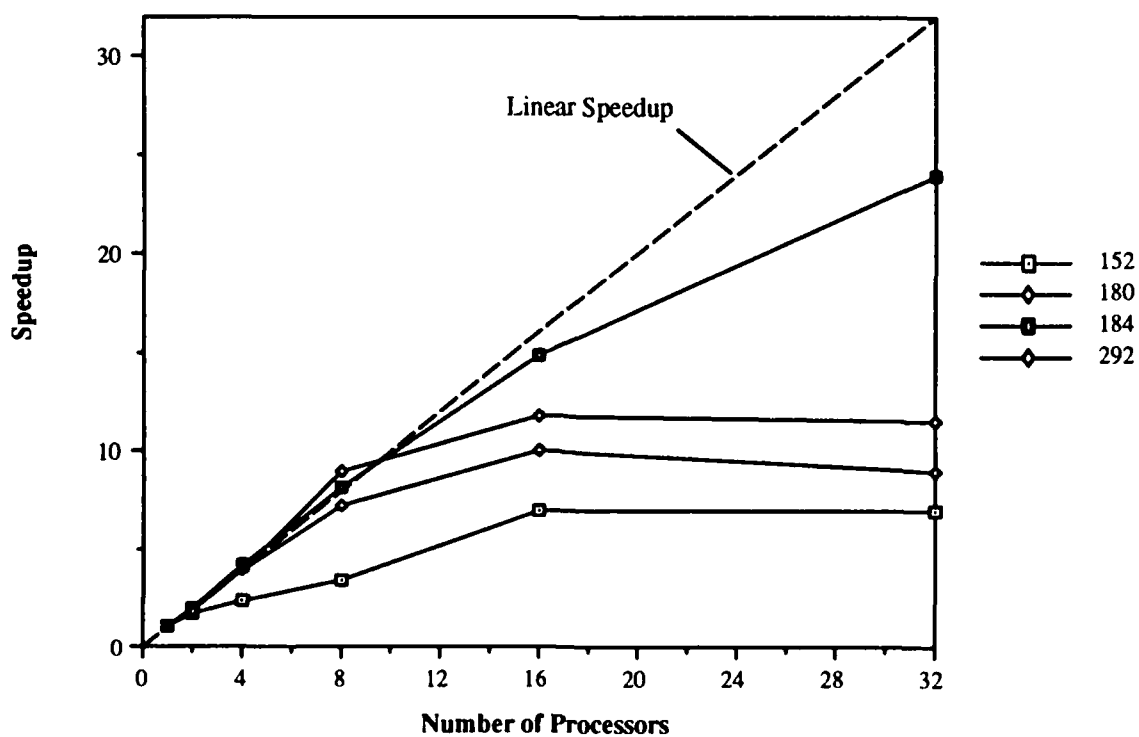
Figure 5. Speedup for Algorithm 1.

31
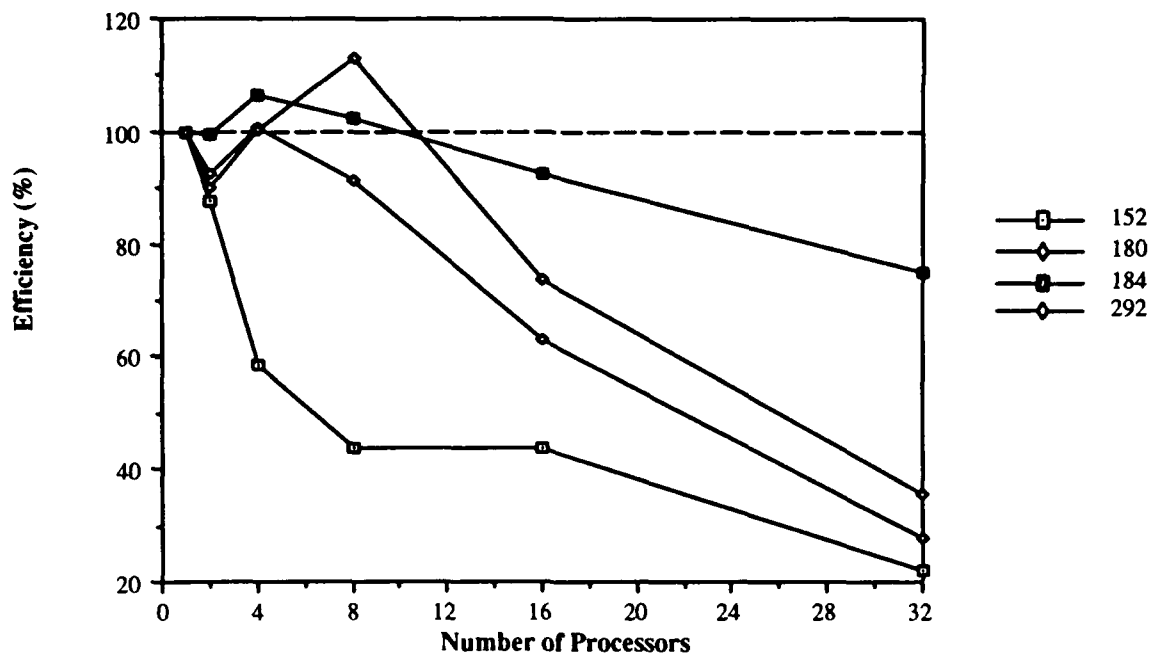
Figure 6. Efficiency for Algorithm 1.

The small case also suffers greatly from communication cost as the number of processors increase. Due to the small size, each processor has a minimal amount of work to do for each function call. This means that it will finish quicker and request another job from the Uniform System. However, with many nodes finishing quickly, the host will be unable to send them jobs sufficiently rapidly and a queue will form. This applies to larger problems when utilizing many processors. A solution would be to send more work to each node, perhaps several layers at once.

It is believed that the actual speedup is close to linear, but not actually superlinear. The efficiency is close to 100% with up to 8 processors, but drops off for 16 and 32 processors as communication cost increases.

CONCLUSIONS

The algorithm is a good implementation to exploit the power of the Butterfly. Superlinear speedups were recognized due to the large memory requirements. Even greater speed might be gained by a parallelizing smaller parts of the already parallel routines; this is known as *fine grain parallelization*. However, communication may become prohibitive if this is done. Other improvements could be gained by passing multiple laye s to each processor when the number of processors becomes large. This will increase the work load on each processor, and reduce the queue at the host.

Furthermore, this algorithm can be implemented on a distributed memory machine. These machines, such as the NCUBE/10 hypercube, use a similar host to the Butterfly. However, the memory is not shared, so all necessary information must be sent to the node and returned to the hosts; this may increase communication costs. These machines are more common, and often employ faster processors than the Butterfly.

The time to slice a part on the Butterfly in serial is much greater than on the sequential SparcStation, due to the much slower processors employed by the parallel machine. However, when four

or more processors are used, the parallel machine is faster than the serial machine. This shows promise for improving slicing speed by using faster concurrent processors.

The concurrent algorithm shows promise for reducing the preparation time for parts built on the SLA. With four processors, the slicing time was reduced as compared to the single, faster Sun processor. The improvements are small for small cases, but it is believed that the very large cases, which can take hours to slice, can benefit greatly from this algorithm. Furthermore, it is believed that the addition of skin fills to the algorithm will simply offset the curves by a fixed amount. All SFF technologies can benefit from increased slicing speed.

ACKNOWLEDGEMENTS

REFERENCES

3D Systems, Inc. (Valencia, CA), 1989, SLA–250 Users Reference Manual, 1989.

S. Ashley, "Rapid Prototyping Systems", *Mechanical Engineering*, April 1991, pp. 34–43.

J. D. Foley, A. van Dam, S. K. Feiner, J. F. Hughes, Computer Graphics: Principles and Practice (2nd Ed.), Addison–Wesley 1990.

G. Fox, M. Johnson, G. Lyzenga, S. Otto, J. Salmon, and D. Walker, Solving Problems on Concurrent Processors: Volume 1, Prentice Hall, 1988.

K. L. Chalasani, B. N. Grogan, A. Bagchi, C. C. Jara–Almonte, A. A. Ogale, and R. L. Dooley, "An Algorithm to Slice 3D Shapes for Reconstruction in Prototyping Systems", *Proceedings of 1991 ASME Computers in Engineering Conference*, pp. 209–216, August 1991.

Wolstenholme, E. OE., Elementary Vectors, 2nd. edition, Pergamon Press, 1971.

IMPROVED QUALITY OF SFM-PROCEDURES
BY SYSTEMATIZED OPERATIONAL PLANNING

D. Kochan
TU Dresden, Germany

Introduction

The ability to create 3D-physical objects directly from 3D-CAD-data marks a new stage in the entire scientific technological development. The scientific spiral as a symbol for continuously higher developments of advanced production-technology demonstrates the new reached developmental level (see figure 1).

In the mid-fifties the amalgamation of 1) computer technology, 2) electronics (later microelectronics), and 3) machine tools led to the new quality in flexible manufacturing technology in kind of NC-technology. The resulting necessity for rational determination of tool movements, process sequences, and others with algorithmic approaches leads to many kinds of computer applications for geometrical and technological decision support. All practical applied CAP, CAM, CAD/CAM, CAE-systems are the evidence for algorithmic based solutions.

Now in the new developmental stage we have to consider some more and very difficult to determine influence factors from different aspects (see figure 2). The current amalgamation of 1) powerful NC-technology, 2) advanced computer technology in different kinds, 3) new physics principles like laser technology etc., and 4) the inclusion of new materials leads to new problem areas.

It can be emphasized that the traditional approach based on algorithmic solution for problem solving and decision support in connection with SFM for reliable process-determination and control seems restricted. Especially the exact determination of material properties and the material behavior under determined conditions are very difficult to solve in an algorithmic approach. The inclusion of specific object and process related knowledge seems necessary. Before these aspects will be discussed, a proposal for unified terminology will be briefly explained.

Justification of the Term "Solid Freeform Manufacturing"

Based on the interesting fact that scientists and researchers of different disciplines have developed the new technologies, and now the application ranges are also very many-sided, a lot of various terms are created. It is interesting to remark that this was not the case for example with NC-technology, laser technology, etc.

Only the main used terms are included in table 1. The comments on the right side are characterizing the restriction of most of the introduced terms. On the other hand, it seems clear that not only for international understanding, but also for conversation in every enterprise, a unified term is necessary. Normally such a term has to reflect kernel points on the determined content. This is given by 1) solidification as a typical feature of different procedures; 2) freeform as the feature for geometrical objects of any complexity; 3) manufacturing, because all kinds of procedures are prior manufacturing processes. The term fabrication was only justified during the first years, because it is also used for Invention. I do hope we all can find an agreement for the best suitable term: "Solid Freeform Manufacturing."
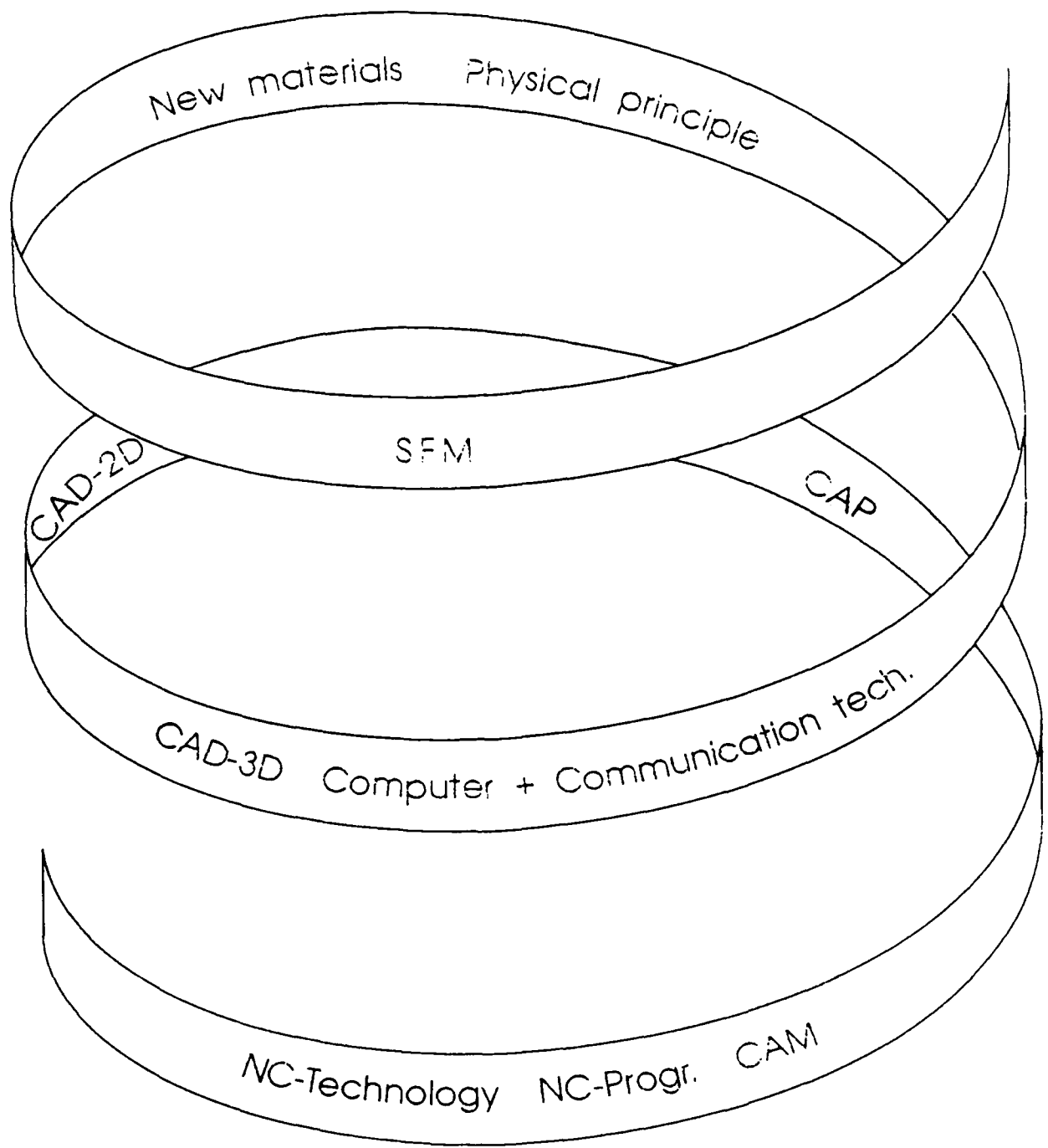
FIG.1: General developmental trends starting from NC-Technology
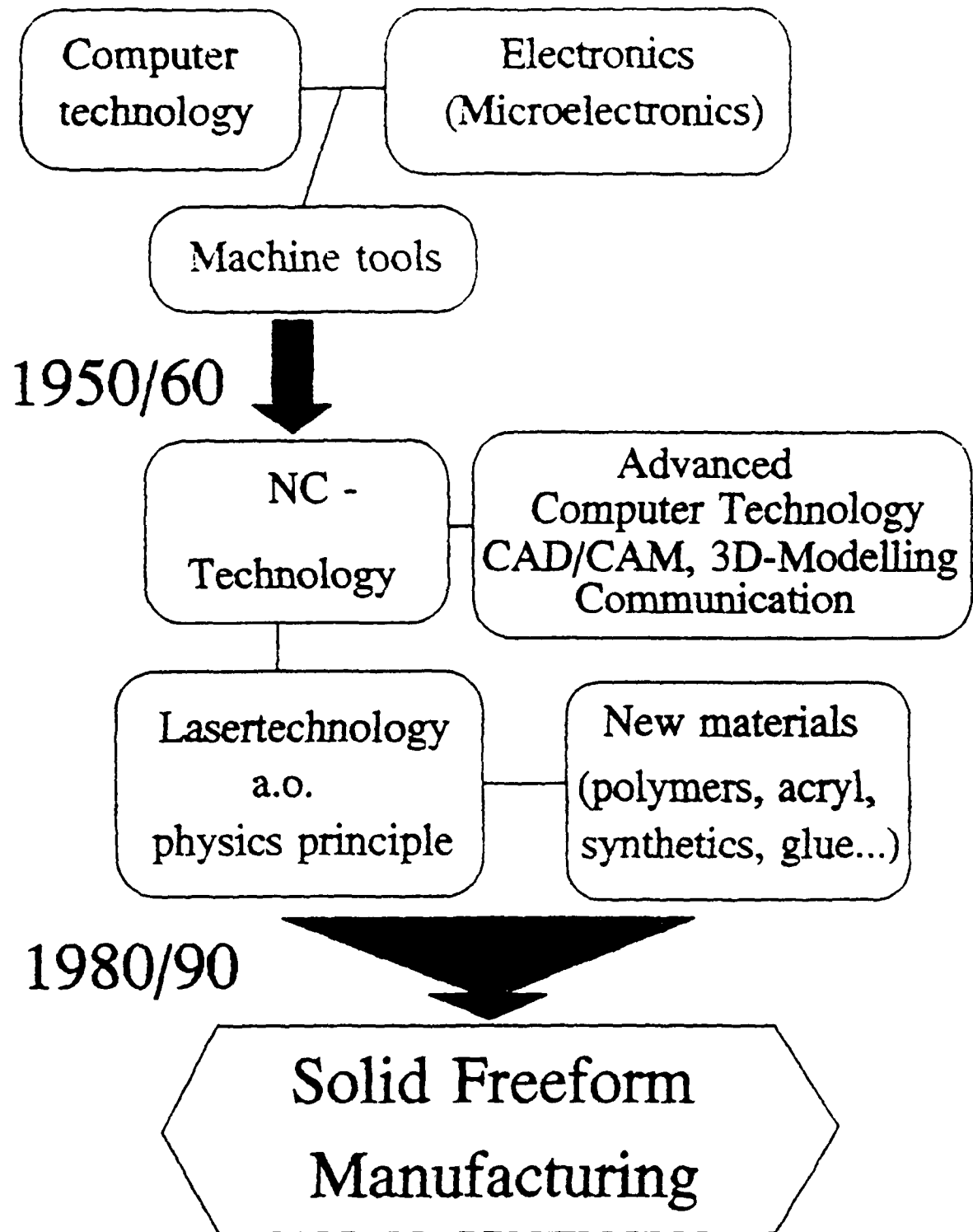
FIG 2: Developmental steps in advanced manufacturing technology

Term	Comments
CAD oriented Manufacturing	Not only CAD oriented (every manufacturing technology has to be customer oriented!)
Direct CAD Manufacturing	See above
Desktop Manufacturing	Not general to accept; the desk could be only a very small facility for manufacturing
Instant Manufacturing	In every manufacturing process will be produced "instant" parts
Layer Manufacturing	Characterized most, but not all of the new principles
Material Deposit Manufacturing	Includes the geometrical, not the physical aspects
Material Addition Manufacturing	see above (MDM)
Material Incress Manufacturing	Good explanation also from the geometrical aspect; difficult to translate
Solid Freeform Fabrication Solid Freeform Manufacturing	Both terms includes the aspect of solidification and the geometrical complexity of the manufacturing procedure
3D Printing	Printing is only one possibility
Rapid Prototyping	Widely used, but also in computer technology with other content

Table 1. Essential Terms for
Solid Freeform Manufacturing.

General Requirements Concerning Systematized Operational Planning

The general task of operational planning consists of transforming of geometrical information into specific process information for building real objects in a reliable kind. The general SFM-process sequence of transferring 1) input data; 2) checking these data; 3) making evaluations concerning producibility; 4) preparing of building parameters for positioning and stepwise manufacturing under consideration of given possibilities (equipments) and specific restrictions required for process-accompanied documentation. The most customer deliver special recommendation for specific building parameters, shrinkage factors etc.

For making the entire process-chain transparent and reproducible, some additional information is necessary. In general the following aspects have to be considered:

1) In agreement with European and International (ISO) Quality-standards every element and requirement - especially also for process planning - have to be documented in a systematic and orderly manner in the form of written policies and procedures (ISO 9000).

2) The application engineer, who is responsible for the further input-data preparation (starting from 3D-data) has to oversee the entire process realization. Because of the many-sided influence-factors, he needs some systematic support.

3) Also the CAD-designer who intends to use SFM-techniques needs at least some basic principles which have to be considered in the design phase. This aspect is related to the requirements of Concurrent or Simultaneous Engineering in connection with necessary information feedback about producibility.

4) Every interested customer has to know what kind of processes for specific part requirements are suitable. It could be useful if suitable information is available for specific benchmark-tests for evaluation of different SFM-systems depending on part or factory specific requirements.

For all mentioned requirements, a suitable part classification seems to be a useful aid.

Part Classification for SFM Technology

The available classification methods and schemes for mechanical part manufacturing are not suitable for SFM-procedures, because the typical application ranges for this principle are restricted to a higher degree of complexity. Most simple part classes are not suitable for generation with SFM-procedures. A specific part classification was therefore proposed.

Main aspects for a suitable subdivision and classification scheme for SFM-procedures are:
1) similarities for specific rules for building procedures - dependent on the determined principle;
2) consideration of typical application ranges for different SFM-processes;
3) as a first approach, general classification independent of other essential influence factors like materials, measurements (sizes), accuracy, etc. (these have to be considered additionally).

38

It can be emphasized that the SFM-technologies have only a few restrictions concerning part classes. But based on the materials used (fluids, powder, solid), and the specifics of different building procedures, it seems very necessary to take into consideration specific requirements concerning the external and internal shapes, respectively, the general part structures. This request results from the different material behavior during and after the building processes, especially related to aspects of accuracy, stiffness, distortion, curling, etc. For this widely applied principle of Stereolithography, a lot of tests and measurements were made with specific test parts, but the results cannot be generalized because every part-structure leads to other behaviors (1, 2).

For solving this problem as a first approach the philosophy of Group Technology can be used in modified kind. That means a classification of typical part-structures with similar features could be possible and helpful. A proposal is shown in figure 3.

Application of Knowledge Based Methods

In the frame of the general part classification, a further detailed subdivision for every part class is possible depending on:

1) materials corresponding to different applications;
2) measurements (part sizes). The part sizes and part structures are mostly related to shrinkage, distortions, curling effects. Therefore specific experience has to be acquired and included into the necessary rule-system. Such rule-systems are necessary for every kind of material (resins, etc.) and every specific SFM-procedure.
3) accuracy, tolerances. These aspects are closely related to the same influence factors as mentioned above for measurements. Therefore the necessary rule-system has to consider these influence factors in complex kind.
4) surface quality, especially smoothness.

The surface quality of plans is standardized by ISO 1302, whereas for freeform shapes there does not exist any standard till now. Essential features are also: form deviations, position deviations, measurement deviations, and roughness and combinations. The surface quality depends on: material, building procedure (especially possible layer-thickness), necessity of support-structures. These influence factors have also to be considered in the specific rule-system.

It can be emphasized that all laser-lithography-procedures, which require support-structure, have to take into consideration specific requirements for the positioning and building procedure. Whereas the part classes 7 and 8 are extremely difficult from the points of accuracy, smoothness on both sides, and stability (respectively curling and distortion) for laser lithography principles; on the other side, these part classes are well suited for the LOM-principle.

With this example, it can be characterized that the different procedures have specific advantages and disadvantages related to the different part classes. A general differentiated rule base system can therefore be helpful for good work-division between different companies, service bureaus, and customers.

In general, it has to be emphasized that the highly sophisticated technology cannot be exactly determined like classical mechanical procedures. The many-sided influence factors request rule based methods for including specific experiences and knowledge. The acquisition of specific knowledge is mainly possible by careful application of suitable operational sheets.

Curling
Warping
distursion

stiffnes
stability

Measurements
(part sizes)

Part structure
(Configuration)

Material

Shrinkage
(dimensional
accuracy)

Surface
quality
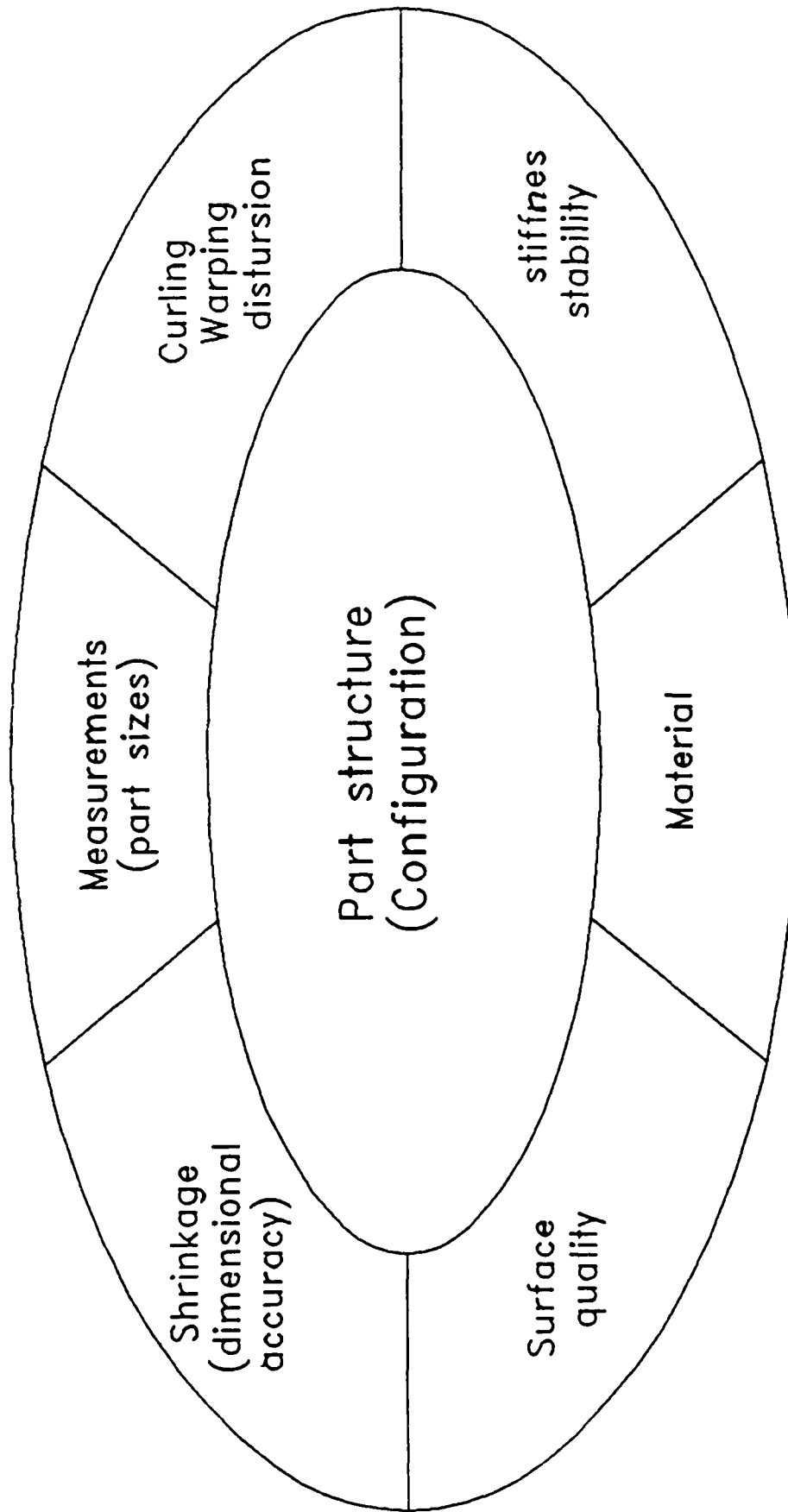
FIG 3 : Object related influence factors for quality
justified SFM-procedures

40

Operational Planning Tasks and Methodical Aids
by a Unified Operational Sheet

General Tasks

The SFM-operational planning tasks result by the logical sequence of the entire information flow and necessary decision steps. The main steps in the general process chain for the different SFM-procedures can be characterized as follows:

1) checking of the prepared 3D object input data
2) computer aided preparation of the building procedure (including positioning, slicing, preparation of support structures, if necessary) and if available, use of simulation techniques
3) controlling and supervising of the building procedure
4) postcuring (if necessary)
5) cleaning
6) finishing.

For evaluation of the results of manufactured parts under consideration of quality, costs, and time, all working steps have to be considered. Therefore, a suitable process accompanied documentation needs some more information as the detailed building parameters. In agreement with the experiences of traditional operational planning systems, the following aspects have to be considered:

1) identification of input data, media, responsible persons
2) determination of the geometrical objects, the building possibilities, spatial assortments, arrangements with other parts, necessary support structures, slice parameters
3) determination of technological parameters (cure depth, laser power, respectively other physics parameters).
4) software-handling, user-support, dialogue mode, graphical aids
5) recommendations for postcuring, cleaning, finishing

Unified Operational Sheet

It will be endeavored that the operational planning system can be used for all SFM-techniques. This request can be fulfilled if a general operational sheet will be completed by specific recommendation depending on determined requirements by the different procedures. Based on these general requirements, a unified operational plan is proposed which has to be prepared and used by the application engineer (SLA-user) for every part, also in case of repetition. For practical usage the following aspects and remarks have to be considered. The key point of the proposed operation sheet I is the relation to the aspects of FMEA (failure mode and effect analysis). That means that in addition to the necessary object-specific facts, which are included in the operational sheet, all essential comments and evaluation of results are most important. The operational sheet I covers the entire process chain. The operational sheet II is fully identical to the specific recommendation of a determined equipment and used specific materials and includes only the building process.

Utilization of Information Content of Operational Sheets

There are given different possibilities for utilization of the information content:

1) Basis for exact time and cost calculation for every object manufactured by the determined SFM-equipment.

2) Basis for time and cost estimation for carefully selected parts (based on the proposed part classification and part analysis at the determined company).

3) Using of these time and cost-elements as a realistic basis for qualified Benchmark tests.

4) Basis for knowledge and rule acquisition in the given part-class-related frame, including the opportunity for continuous qualification of the rule system ("knowledge source").

As was emphasized in the introduction, the material properties and the changing physical parameters (i.e., laser-power, laser-beam diameter, etc.) in relation to different part-structures do not allow any algorithmic determined approach. Therefore, such human oriented adaptive learning seems necessary.

Expected Results and Advantages

The proposed method for operational planning is based on the currently available experiences primarily suitable for laser-lithography procedures. But it depends on more detailed knowledge about other SFM-techniques like Cubital "Solid Ground Curing" or DTM "Selective Laser Sintering," or Helisys "Fused Deposition Materials," or any other commercially available systems, a modification seems very easy. It can be pointed out that with a permissible additional expenditure, some important results are possible:

1) Methodical support for a systematically guided operational planning by the responsible application engineer.

2) It allows a systematized acquisition of rules and knowledge, which can be collected to reuse.

3) The quality of the reached results can be improved. That leads to an increased success-rate and to reduction of waste.

4) The exact determination of process-data and times is the basis for exact economical calculations.

5) The learning phase for part preparation can be shortened.

By the proposed methodical approach, a first startpoint and general frame is given. The rule system especially concerning the shrinkage factors has to be completed depending on included different part classes. In this connection, it can be emphasized that depending on specific application requirements and frequency in a determined part class, a further subdivision is possible. But under consideration of user-friendly handling of the proposed method, the general subdivision in ten part classes seems most suitable.

Summary and Conclusion

First approaches were made on selected parts. In this connection the principle suitability of the proposed method was confirmed. A consequent broad application and further development is planned in cooperation with the German NC-Society.

Acknowledgment

providing worthwhile experiences and support. Practical tests were also supported by BIBA, Bremen (Prof. Hirsch and his colleagues) and 3D-Systems, Darmstadt. By the companies: Cubital/Germany; Dormier/Germany; CMET/Japan; EOS/Germany, some informative material was delivered and interesting discussion provided. Many thanks also for this useful cooperation.

References

1. P.F. Jacobs and J. Richter, "Advances in Stereolithography Accuracy," in *Proceedings of Solid Freeform Fabrication Symposium 1991*, The University of Texas at Austin, pp. 138-157.

2. B.E. Hirsch and H. Muller, "Stereolithography - Fields of Application and Factors Influencing the Accuracy," in *Proceedings of the IFIP WG5.3 Working Conference on Process Planning for Complex Machining with AI-Methods* (27-29 Nov. 1991, Gaussig, Germany), North-Holland-Elsevier Science Publishers.

An Experimental Study of the Relationship between Microstructure and Mechanical Properties of a Ceramic Composite Fabricated by Selective Laser Sintering

Uday Lakshminarayan*

and

H.L.Marcus

Center for Materials Science and Engineering

University of Texas, Austin, TX 78712.

ABSTRACT

Alumina-ammonium phosphate powder blends were processed with Selective Laser Sintering. Ammonium phosphate with a melting point of 190°C, acts as a binder when processed with a laser and holds the alumina (m.p. 2300°C) particles together to form a "green" body. When the green body is heat treated at 850°C for 6 hours, ammonium phosphate decomposes evolving ammonia and water vapor. Residual P_2O_5 reacts with alumina to form aluminum phosphate. This results in a composite of unreacted alumina with a coating of aluminum phosphate around the alumina particles. The variation of compressive strength of these low density ceramic composites was investigated in terms of the particle size distribution the amount of binder in the initial blend. It was observed that the strength depends on the relative density and initial blend composition and the critical flaw size. A constitutive equation was formulated to characterize the influence of the relative density, binder composition and the critical flaw size on the strength of the composite.

INTRODUCTION

The concept of Solid Freeform Fabrication (SFF) to generate parts directly from the CAD data without part-specific tooling has been described earlier [1]. Selective Laser Sintering (SLS), one of the Solid Freeform Fabrication (SFF) techniques being investigated at the University of Texas was first described by Deckard and Beaman [2]. The SLS process employs a focused laser beam scanned on the surface of the powder bed to induce selective particle - particle bonding in a thin layer of powder. The part is generated by sintering appropriate cross-sections on layers of powder stacked on top of each other. The unsintered powder in each layer remains in the powder bed during processing to support overhangs and other structures in subsequent layers.

---

* Now with DTM Corp., Austin, Texas.

The absence of part-specific tooling in SLS makes the process economical in small-scale production runs where the fabrication of tools for conventional processes constitute a substantial fraction of the cost of the parts. Initial applications for SLS include design verification models made with engineering plastics such as polycarbonate or nylon and wax patterns for investment casting. In these applications, surface finish and dimensional accuracy are of primary importance and strength is of secondary importance. However, the application of SLS to generate ceramic and metal parts for functional applications requires a detailed understanding of the factors affecting the strength of the part. In this paper, the effect of initial particle size, the composition of the precursor powder and the intrinsic defects on the fracture behavior of the composite is considered.

POWDER PROCESSING BY SLS

The processing of alumina - ammonium phosphate powder blends by SLS was described in detail in references [3] and [4]. During laser processing, ammonium phosphate with a melting point of 190°C melts and holds the alumina particles (m.p. 2300°C) in the desired shape. A Nd:YAG laser (wavelength = 1.06µm, Q-switched at 40KHz) focused to a beam diameter of 0.5mm was used as the energy source to melt ammonium phosphate. Laser energy was maintained at 20W and the scan speed was 4cm/s. The distance between scans was 0.5mm. The layer thickness was 125µm. The bed biasing temperature was room temperature.

The "green" part from the SLS processing equipment was fired at 850°C for 6 hours. During the secondary heat treatment the temperature was ramped up at 2°C/min with an intermediate soak at 450°C to drive off reaction products. After firing, the parts were cooled in the furnace [3]. During heat treatment, ammonium phosphate decomposed evolving ammonia and water vapor as by-products. Residual phosphorus pentoxide reacted with the alumina to form aluminum phosphate. Thus a composite of alumina and aluminum phosphate capable of withstanding intermediate temperatures was obtained in a net-shape by SLS using a blend of alumina and ammonium phosphate as the precursor powders.

Compressive strength of the samples was measured on specimens having nominal measurements of 0.5"x1"x1". The specimens were oriented during SLS processing such that the build plane was parallel to the 1"x1" cross-section. The samples were ground flat and subjected to compressive stresses in an Instron Universal Testing Instrument with a cross-head speed of 1 mm/s. The loads were applied perpendicular to the build plane.

INITIAL POWDER ANALYSIS

X-ray powder diffraction analysis of the as-received precursor powders indicated that the alumina was in its α-form and the ammonium phosphate was in its tetragonal form. Preliminary investigation indicated that a 95.0% pure alumina absorbed laser radiation at 1.06μm better than the purer form (99.9%). Hence, the research work reported in this paper was confined to the less pure form of alumina. The major impurities in 95 % pure alumina are[1]:

TiO_2-2.91%, SiO_2-0.71%, Fe_2O_3-0.35%, MgO-0.14%.

Three different alumina particle sizes were tested during our experiments. The mean and standard deviation of the particle size distribution of the coarse, medium and fine alumina are shown in Table. 1. The ammonium phosphate particle size was maintained below 44μm throughout our experiments.

Manufacturer's Designation	Average Size (μm)	Standard Deviation (μm)
Duralum 150	80.0	11.8
Duralum 220	69.0	9.2
Duralum 400	8.7	5.0

Table 1. Mean particle size and standard deviation of alumina particles used in experiments.

RESULTS AND DISCUSSION

The compressive strength of a porous ceramic composite depends on three microstructural factors: 1. porosity (or relative density), 2. binder content and 3. crack size. Each of these factors is considered briefly here.

In general, it has been observed that the strength of a porous material decreases as its porosity increases [5,6,7]. As porosity increases the load bearing area decreases resulting in a reduction of the strength of the material. Balshin [5] and Knudsen [6] have proposed equations 1 and 2 respectively to relate the strength of the composite to its porosity.

$\sigma = \sigma_0 (1-P)^m$ ---- (1)

$\sigma = \sigma_0 e^{(-bP)}$ ---- (2)

where σ = Strength of porous solid

σ_0 = Strength of a fully dense solid (P = 0.0)

P = Porosity of solid

---

[1] Analysis supplied by Washington Electro-Minerals Niagara, NY.

46

b and m are constants.

Both equations are based on the reduction of strength due to a reduction in load bearing area. Rice [7] on the other hand proposed an equation of the form

$$\sigma = (\pi/2)(\eta/\tan\eta)^{1/2}(E\gamma/(R+L))^{1/2} \quad \text{---- (3)}$$

where $\eta = \pi R/(R+\lambda)$

σ=Strength of porous material

R=Pore radius

E=Young's modulus of material

γ=Surface fracture energy

L=Fraction of the grain size

λ=Pore spacing=$4R(1-P)/3P$ for evenly distributed spherical pores

to relate the effect of porosity on the strength of the material in terms of the stress concentration induced at the tip of the pores. From equations 1-3 it can be generalized that a decrease in the load bearing area and stress concentration at pore tip reduce the strength of the material.

Eqn. 4 relates the effect of the binder content to the strength of the composite [8]. The $G^{-0.5}$ term in Eqn. 4 is derived from the Griffith crack criterion for the fracture of brittle materials. Here it is assumed that the crack size controlling the strength of the material is equal to the grain size. The $(V_b/V_p)^{0.75}$ term accounts for the energy spent by the intergranular crack to propagate through the binder. As is evident in Eqn. 4, as the amount of binder increases, the strength of the composite increases.

$$\sigma = k(V_b/V_p)^{0.75}(\gamma E/G)^{0.5} \quad \text{---- (4)}$$

where σ=Strength of porous material

k=Constant

V_b=Volume content of binder in composite

V_p=Volume content of primary phase in composite

γ=Surface fracture energy

E=Young's modulus

G=Grain size.

The effect of a surface flaw (length a) or an internal flaw (length 2a) on the strength of a brittle material is given by the Griffith's crack criterion (Eqn. 5).

$$\sigma = Y(E\gamma/a)^{0.5} \quad \text{---- (5)}$$

where σ=strength of porous solid

Y=Geometrical factor

E=Young's modulus

γ=Surface fracture energy

a=crack size

As shown in Eqn. 5, strength varies in an inverse square relationship with the crack length. As a first approximation, it is reasonable to assume that the crack size equals grain size [8]. Based on this assumption, Knudsen [6] formulated Eqn. 7 combining the effects of the pore size and the porosity on strength in one equation.

$$\sigma = kG^{-a}e^{-bP} \quad ---- (6)$$

where σ=strength of porous solid

G=Grain size

P=Porosity of solid

k, a and b are constants.

Based on the discussion thus far, it is inferred that the strength of the alumina - aluminum phosphate composite depends on its relative density, the binder content and the flaw size. The increase in density with alumina particle size and the amount of binder in the initial powder blend was discussed in an earlier report [1]. Fig. 1 shows the variation of the compressive strength of the alumina - aluminum phosphate composite fabricated by SLS with the binder content and the alumina particle size. It is seen that at a composition (i.e. 35%), the strength of the material increases with the alumina particle size. This is attributable to two reasons. As the alumina particle size decreases, the relative density of the material decreases [9]. In addition, as will be discussed later, very large cracks were observed in compacts with fine alumina ($9\mu m$). The presence of large cracks lowers the strength of the material.

In Fig. 2, the strength of composite is plotted against its relative density showing its linear dependence. Considering composites at a particular relative density, specimens fabricated with the finest alumina had the highest strength. It was pointed out in an earlier report [4] that the composites using fine alumina required a higher binder content than when using coarse alumina to get the same relative density. The presence of a large binder content results in a stronger material. From the preceding paragraphs, it is clear that the strength of the alumina-aluminum phosphate composites depends on its relative density, binder content and the crack size.

To predict the relationship between the strength of an alumina / aluminum phosphate composite and its porosity, composition and crack size, an equation was formulated (Eqn.7).

$$\sigma = B(1-P)a^{-0.5}(V_b)^p \quad ---- (7)$$

σ=Strength of the porous alumina - aluminum phosphate composite.

B and p are constants

a=Crack size

P and V_b have been defined earlier.
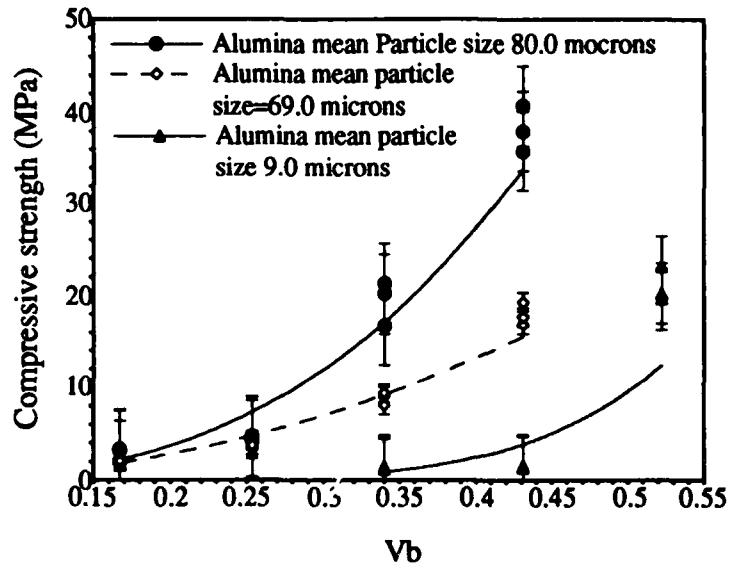
Fig. 1. Compressive strength of alumina - aluminum phosphate composites fabricated by SLS using different alumina particle sizes and varying amounts of aluminum phosphate in the composite.
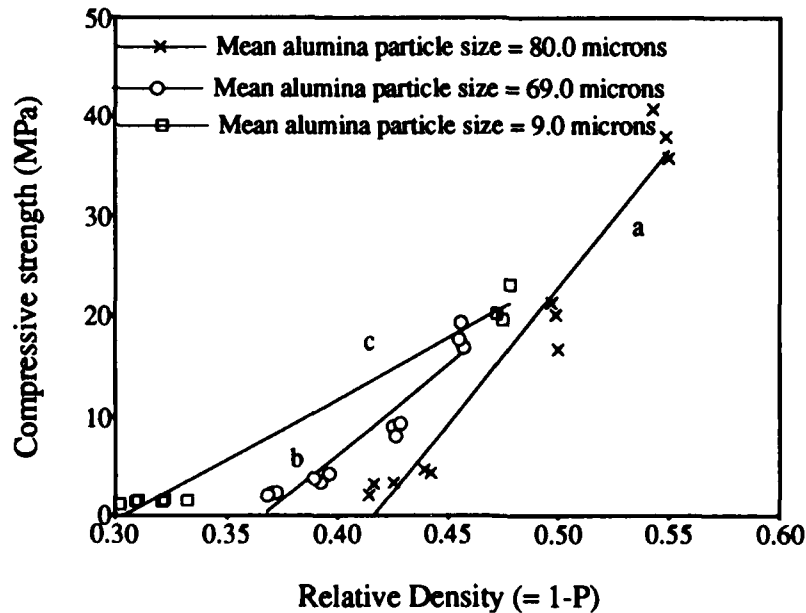
Fig. 2. Variation of the compressive strength of the alumina - aluminum phosphate composites with their relative densities and alumina particle sizes.

49

In equation 7, the term (1-P) accounts for the dilution in the strength of the composite due to porosity. The exponent of the (1-P) term was assumed to be 1 based on the experimental observation in Fig. 2. V_b accounts for the area of the aluminum phosphate through which the crack has to propagate. The $a^{-0.5}$ term is introduced to characterize the influence of the surface crack size on the material strength. The exponent of the crack length is -0.5 for mixed mode fracture that occurs during compressive loading [10]. B and p are constants. Assuming that the material is completely dense (P=0) and V_b=1, Eqn. 7 reduces to

$$\sigma = B * a^{-0.5} \quad \text{---- (8)}$$

From Eqn. 8, it can be inferred that B should correspond to the fracture toughness of a pure aluminum phosphate specimen with no pores under compressive loading. No data for the fracture toughness of aluminum phosphate is available in the literature. However, the mode I (K_{IC}) fracture toughness of alumina is between 3 - 5 MPa√m [10].

As a first approximation, assume that for the coarsest alumina (80μm) grain size equals the crack size. By plotting $\ln(V_b)$ vs $\ln(\sigma * \sqrt{a}/(1-P))$, B and p were determined to be 5.0MPa/√m and 2.6 respectively . These values were then substituted in Eqn. 7 to calculate the strength of the composites containing 69.0μm and 9.0μm alumina powder assuming that the crack size in each composite equals the alumina grain size (Figs. 3 and 4).

Comparing the actual and calculated strengths of the alumina-aluminum phosphate composites in Figs 3 and 4, it can be inferred that equation 7 predicts the trends in the strength behavior of the composites accurately. However, the calculated values of the strength of the composite assume that the flaw size equals the average alumina grain size. But as seen in Table 1, there is a size distribution for the alumina particles. Hence the intrinsic crack size is greater than the average alumina particle size. This results in an overestimation of the composite strength if we assume that the grain size equals flaw size in the material (Figs. 3 and 4). Processing flaws as large as 400μm have been observed on surface of composites made with fine alumina powder (9μm). If a flaw size of 400μm is used in Fig. 4, then the agreement between calculated and measured values improves. Further microstructural analysis is essential to understand the effect of material and processing parameters on the flaw size in the material.
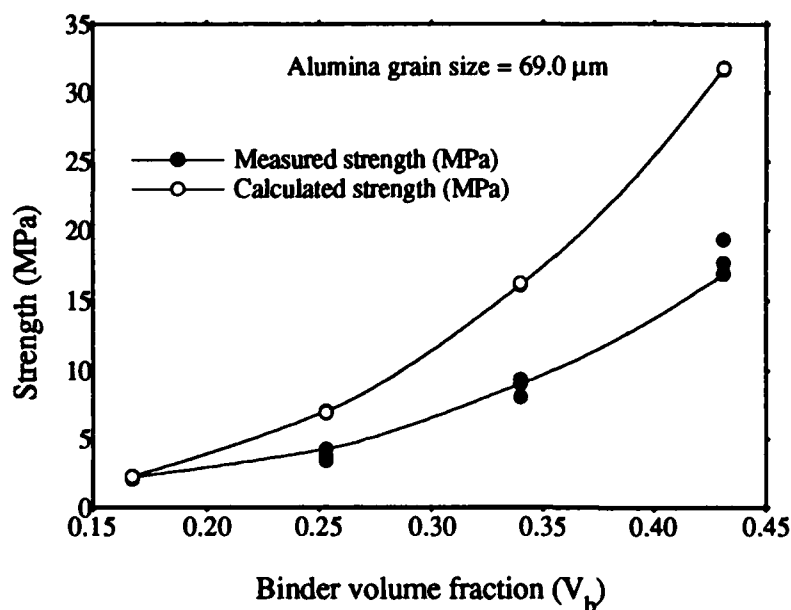
Fig. 3. Measured and calculated compressive strength of alumina - aluminum phosphate composites fabricated by SLS. Eqn. 7 was used in calculating the strength. It was assumed that the crack size = alumina particle size = 69μm, B = 5.0MPa√m and p = 2.6.
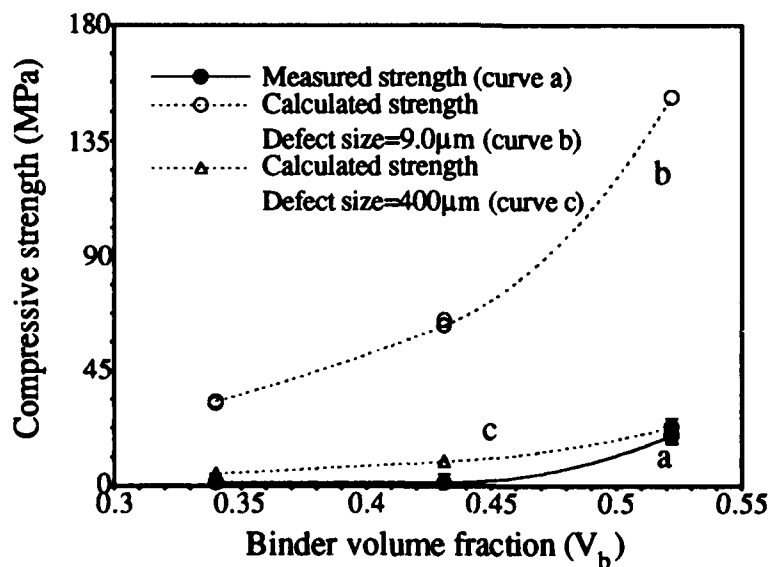
Fig. 4. Calculated and measured compressive strength of alumina - aluminum phosphate ceramic composites fabricated by SLS. The calculated values were determined

using B=5.0MPa√m and p=2.6 in Eqn. 7. Curve b assumes a crack size of 9.0 μm (alumina particle size in initial blend) and curve c assumes a crack size of 400 μm.

CONCLUSIONS

The compressive strength of the alumina - aluminum phosphate composites fabricated by SLS was studied as a function of the porosity, binder content and the surface flaw size. The strength of the composite increases as the binder content increases and as the porosity and defect size decrease. Hence factors such as alumina particle size and binder content which influence the microstructure have a strong effect on the strength of the composites. A constitutive equation was formulated to relate the effects of the microstructural factors on the strength of the composite. While the equation predicted the general trends in the variation of the strength with microstructural factors, more detailed investigation into the crack size controlling the strength of the material is required in order to use the constitutive equation as a predictive tool.

REFERENCES

1. Proceedings of the Solid Freeform Fabrication Symposium, Aug. 11-14, 1991, University of Texas, Austin, Eds. J.J.Beaman, H.L.Marcus, D.L.Bourell and J.W.Barlow.
2. C.R.Deckard and J.J.Beaman, "Solid Freeform Fabrication and Selective Laser Sintering", Proc. of the 15th Conference of North American Manufacturing Research, Bethlehem PA, May 27 29, 1987, pp 636 - 640.
3. U.Lakshminarayan, S.Ogrydiziak and H.L.Marcus, "Selective Laser Sintering of Ceramic Materials", in Ref. 1.
4. U.Lakshminarayan and H.L.Marcus, "Microstructural and Mechanical Properties of Al2O3/P2O5 and Al2O3/B2O3 Composites Fabricated by Selective Laser Sintering", Proceedings of the Solid Freeform Fabrication Symposium, Aug. 3 - 4, 1991, University of Texas, Austin, Eds. H.L.Marcus, J.J.Beaman, J.W.Barlow and D.L.Bourell.
5. M.Yu.Bal'shin, "Relations on the Mechanical Properties of Powder Metals and their Porosity and the Ultimate Properties of Porous Metal Ceramic Materials ", Doklady Akademi Science, USSR, 67 [5], 831 - 834.
6. Knudsen, "Dependence of Mechanical Strength of Brittle Polycrystalline Specimens on Porosity and Grain Size", Journal of Ceramic Society, 42 (8), 1959, pp 376 - 389.
7. R.W.Rice, "Microstructure Dependence of Mechanical Behavior of Ceramics", Treatise on the Materials Science and Technology, Vol. 11, 1977, Academic Press, New York.
8. Bache H.H. Journal of American Ceramic Society, 53 (12), 1970, pp 654 - 658.

9. U.Lakshminarayan, Ph.D. Dissertation, University of Texas, Austin, May 1992.

10. A.R.Ingraffeas and H.Y.Ko, "Determination of the Fracture Parameters for Rock", Mixed Mode Crack Propagation, (Eds) G.C.Sih, P.S.Theocaris, Sijthoff and Noordhoff, (1981).

11. R.Hertzberg, Deformation and Fracture Mechanics of Engineering Materials, 3rd Edition, John Wiley and Sons, 1989, pp 412.

ACKNOWLEDGMENTS

Project MAXWELL:
Towards Rapid Realization of Superior Products

Deba Dutta
Noboru Kikuchi
Panos Papalambros

Department of Mechanical Engineering
& Applied Mechanics
The University of Michigan
Ann Arbor, MI 48109

and

Fritz Prinz
Lee Weiss

Engineering Design Research Center
Carnegie Mellon University
Pittsburgh, PA 15213

Abstract

We describe a new methodology for the design and manufacture of mechanical components. The methodology is a synergism of a new, mathematically rigorous procedure for the concurrent design of shape and material composition of components, and a new manufacturing process called MD* for their realization. The concurrent design strategy yields information about the global shape of the component and its material composition. The fabrication of such designs with novel microstructural configurations require unconventional manufacturing processes. MD* is a shape deposition process for the free-form fabrication of parts from single or composite materials and is ideally suited for realizing the aforementioned designs. Project MAXWELL, therefore, promotes the use of layered manufacturing beyond prototyping tasks and offers the possibility of their integration into the mainstream product development and fabrication process. .

1. INTRODUCTION

Project MAXWELL proposes a methodology that is a synergism of a new mathematically rigorous procedure for the concurrent design of material composition and shape of components, and a new manufacturing process for their realization. At the University of Michigan (U-M), a methodology has been developed for designing the *form and material composition* of mechanical and structural components based only on a description of the loading conditions and packaging requirements. At Carnegie Mellon University (CMU), a new manufacturing process has been developed for the free-form fabrication of parts from *single or composite materials* by thermal spray shape deposition. Project MAXWELL aims at integrating these two novel technologies, for realizing strategic benefits rooted in the rapid realization of novel mechanical and

54

structural components. Furthermore, the design methodology illustrates the importance of layered manufacturing techniques such as MD* beyond prototyping tasks.

The project hypothesis is the existence of an integrated methodology for the rapid realization of mechanical and structural components that could not have been designed and/or manufactured before. Such parts will possess superior structural and mechanical properties (*e.g.*, lower weight to stiffness ratio), and will satisfy packaging and other manufacturing requirements (*e.g.*, ease of assembly). The project goal is proof of concept through design, manufacture, and testing of actual parts.

The current application domain is in automobile design and manufacture and includes sheet metal/composite panels, brackets and suspension components, and special structures for side impact energy absorption. The process is also suitable for the design and manufacture of prosthetic devices in bioengineering applications.

In this paper, we first motivate the concurrent design of form and material in the context of structurally superior products. Next, we provide an overview of the relevant methodologies developed at U-M and CMU respectively. Finally, we describe the current status and future goals of project MAXWELL.

2. CONCURRENT DESIGN OF STRUCTURE AND MATERIAL

2.1 Design of the Global Structure Using the Homogenization Method

A fundamental approach to the thermo-mechanical characterization of general composite materials was first put forth by James Clerk Maxwell (1831-1879) and was later generalized as the theory of mixtures to provide a rigorous foundation for studying the mechanics of *composite materials* (*see, e.g.*, [FUN65]). Project MAXWELL aims at transforming those early ideas into engineering reality.

Necessity of topological design in addition to size and shape design is widely recognized by structural engineers. If topological changes are not allowed, size and shape optimization procedures can improve a design by approximately 5~15%. Topological modifications can often yield 30~50% improvement. An example illustrates this. The beam in Figure 1 is subjected to a bending moment. A hollow beam is more effective than a solid beam. For the same amount of material, the beam design on the right, which involves topological changes, is better than the one on the left, which is derived by shape optimization.
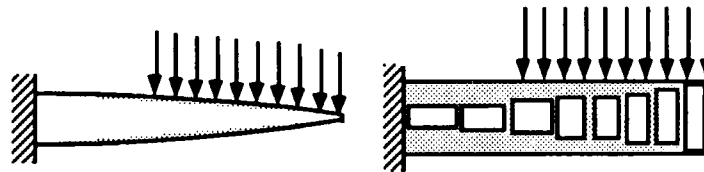
Figure 1: Shape Design and Topology Change of a Structure

The homogenization method is based on the above observation. The topology and shape problem is formulated as a new optimization problem *involving material distribution*. Given a solid with a prescribed volume, we generate *microscale voids* in design domains where a solid structure is *not* required for supporting loads. Therefore, instead of designing the shape and physical dimensions of the cross section of a structure, we generate infinitely many microscale voids within the configuration wherever the stress is small. If a portion in the domain is highly stressed the homogenization method prevents the creation of microscale holes and that portion remains solid. Furthermore, the

orientation of a non-circular void has a significant effect on the overall material response. Therefore, in the new optimization problem, the design variables are the density of microscale voids and their orientation over a specified domain. By removing material completely from portions of the domain densely packed with voids, the optimum shape of the structure is identified, while its topology is determined by accounting for the number of "global" holes (see also Figure 2)
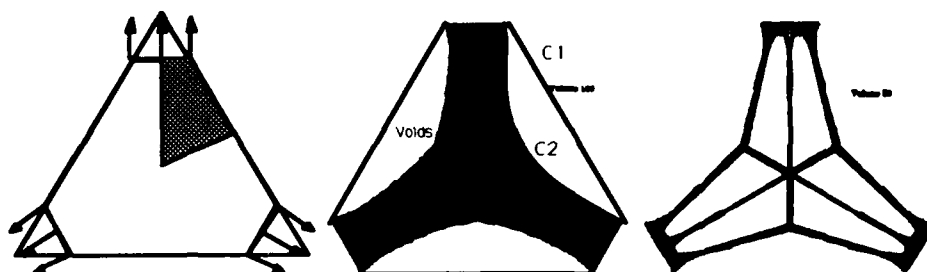
Figure 2: Identification of the Shape and Topology

This intuitive method of "shaping and drilling" a structure is based on the theory of homogenization -- a mathematically rigorous method developed in the mid-1970s for the study of mechanics of composite materials. Most composite materials possess a fine scale microstructure composed of fibers, whiskers, inclusions, and matrices. Applied mathematicians in France, Italy, and the former Soviet Union [LUR84, SAN80, TAR77] developed the homogenization theory to derive the constitutive equation of a composite material, i.e., to evaluate the average stress-strain relation of the structure. Since we are interested in generating infinitely many microscale holes to form a possibly perforated structure, the stress analysis of such a structure requires the derivation of an equivalent effective average stress-strain relation. A homogenization approach enables the design of topology and shape without using spline functions. Difficulties in geometric modeling are avoided, and stress analysis iterations are performed on a fixed finite element mesh.

2.2 Introduction of Microstructure

Although the optimization process permits the perforation of the domain, the resulting optimum configuration is often a homogeneous solid. In our design optimization scheme, we consider the domain to be a very specialized, fictitiously constructed, composite material consisting of solids and voids. In order to determine the best microstructure, we allow the design domain to include other composite materials, e.g., ones that can improve strength, toughness, vibrational characteristics, acoustics, impact resistance and impact energy absorption.

High Bending Rigidity   Low Bending Rigidity

Figure 3: Benefits of Composites

Non-homogeneous composite materials result in significant improvements in thermo-mechanical properties without increase in weight. For example, while bending rigidity of a beam or shell-like structure is proportional to Young's modulus of the material, it is also

56

proportional to the *cube* of its thickness. Therefore, a design criterion such as bending rigidity can be daramatically improved by using composites with a stronger material in the outer surfaces and weak and lighter materials in the inner core, Figure 3. Composite structures can also improve vibrational characteristics without increasing weight or changing the overall configuration. If large dumping is desired, a material with high dumping characteristics can be inserted.

For crashworthiness, an important issue in automobile panel design, complex microstructures must be introduced. Plastic deformation or destruction of the fine microstructure can absorb large amounts of energy. In front- or rear-end crash situations, the need for fine scale microstructures is often eliminated by building simple reinforcing frames that absorb crash energy in the available space. For side impact, however, space for design is much more limited and use of fine scale structures may be very advantageous.

Use of such structures has not been realized in practice due to the lack of an attractive manufacturing process that delivers non-homogeneous and anisotropic materials. For example, it is impossible to create internal voids within a component (such as in Fig. 2) by conventional NC machining. Instead, one has to build voids in the workpiece material prior to machining. As a result, the void orientation which often has a significant impact on overall material response cannot be handled explicitly. In MAXWELL, we propose to use CMU's MD[*] process where a the component is built up layer by layer, allowing the possibility of creating and orienting the voids as desired. Therefore, MD* enables serious consideration of these unusual and highly efficient structures for the first time.

3. OPTIMIZATION MODELS FOR CONCURRENT DESIGN OF MACRO- AND MICRO-STRUCTURES

3.1 A Simple Formulation of the Optimization Model

Relating microstructure to global shape requires a new approach to design optimization and is enabled by homogenization. Concurrent design optimization can be performed to obtain the best microstructure in addition to optimal shape and topology.

Let f be the objective function, such as the total weight, cost, or other scalar quantitity. Suppose g is a vector function representing the set of design constraints introduced by mechanical and manufacturing requirements. Then the design problem can be posed as the following optimization problem

$$\min_{d} \quad f(d,u)$$
$$g(d,u) < 0$$

where d is the set of design variables and u is the state variable vector describing the thermo-mechanical behavior of the structure defined by the state equation

$$L_d(u) = 0$$

The operator L_d of the state equation is a function of the design variables.

The overall formulation is similar to standard optimization except for the design variables. For the layout design described in the previous section, design variables are the size of a rectangular hole in the unit cell characterizing the microstructure and its angle of rotation. If two different materials are considered, the design variables might

define the constitution of the unit cell. For example, if we consider three different microstructures, Figure 4, we might choose to design the layout of the lamination, the mixture, or the fiber density of the resulting composite material.
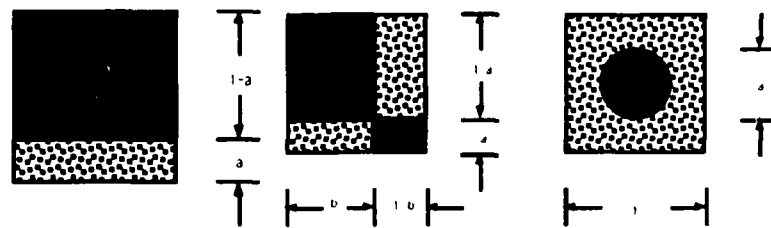
Figure 4: Design Variables at the Microstructure Level

This approach allows inclusion of material composition in the model, but is insufficient for concurrent material and structural design, since the configuration of the microstructure is specified *apriori* (although the designer has considerable flexibility in choosing the size of the lamination, mixture, and fiber). Clearly, the chosen microstructural configuration need not be the optimum. Therefore, we must derive the optimal microstructure and optimal global layout for the structure concurrently.

Applied mathematicians at Courant Institute, University of Paris, and in the former Soviet Union, have conducted research on optimal composition, without considering global structural configuration; see [KOH86] for a survey. These methods concentrate on finding the lower bound on the complementary energy of a generalized mixture of two different materials. Typically, sequential lamination is used to yield a closed-form homogenized effective stress-strain relation. These elegant theoretical developments have not led to substantive engineering applications. Furthermore, these studies have primarily concentrated on optimum composite structure independent of the stress field generated in the structure. Namely, material constitution is obtained in its ideal setting independent of the true stress field. That is not acceptable for structural configurations carrying thermo-mechanical loads.

3.2 An Optimization Model for Concurrent Macro-Micro Layout

To overcome these limitations, we formulate a new design problem that optimizes both the microstructure and the global structural configuration. We consider minimizing an objective function that represents the complementary energy of the unit cell consisting of two materials. The constraints are the equilibrium equations and the periodic boundary conditions. We further require that the average stress over a unit cell is equal throughout the global structure under a specified volume fraction of the two materials forming the composite. To minimize this objective function defined over the unit cell, we apply the same method as in layout optimization of the global structure. That is, the microstructure is designed by using a *refined* microstructure; see Figure 5.

Thus, two microstructures are introduced, one to determine the layout of a global structure and the other to define the optimum material layout in the microstructure. This allows designing a possibly non-homogeneous, anisotropic, composite structure, optimal with respect to topology, shape and material.

In contrast to the applied mathematics approach, our choice of objective function in material design need not be restricted to the complementary energy. If we wish to design a structure and its material such that it can absorb, say, crash energy the objective function may be defined as the integration of the complementary strain energy over the period of crash. There has been limited research in structural optimization with nonlinear state equations. Methods for linear state equations must be extended for history-

58

dependent nonlinear state equations, in order to meet challenges such as side impact energy absorption in automotive body design.
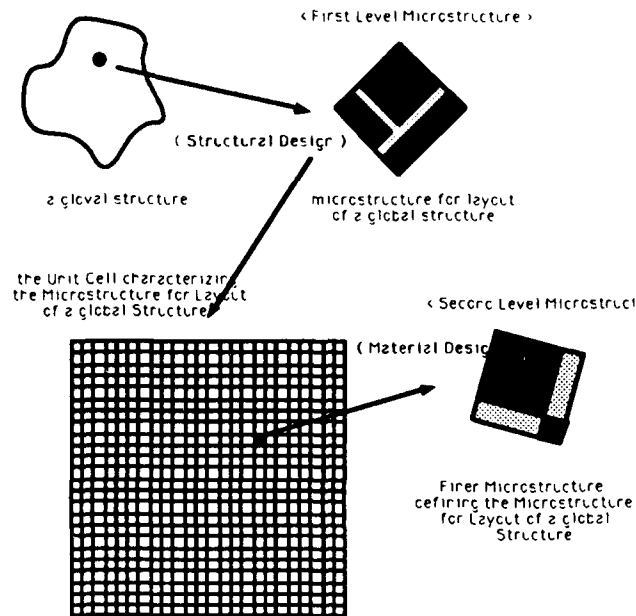
Figure 5: Concurrent design of Structure & Material using a two-level microstructure

The true benefits of deriving such optimal topologies and microstructures in a rigorous fashion can only be measured after the designs are transformed into physical products and tested. However, conventional manufacturing such as NC milling and truing are insufficient for the realization of such designs, since it is not possible to affect the "inner core" of the object being machined. On the other hand, layered manufacturing techniques are ideally suited for such fabrication tasks since they can create internal voids and complicated external geometries simultaneously. Therefore, our design method in MAXWELL promotes the use of layered manufacturing *beyond* prototyping tasks into the mainstream product development and fabrication phase. In MAXWELL, we use the MD* process, a layered manufacturing technique developed at CMU, for the realization of designs resulting from the homogenization method.

4. FABRICATION BY THE MD* PROCESS

In the MD* (recursive Mask and Deposit) process developed at CMU, parts are manufactured by successively spraying cross-sectional layers. Each layer may contain several different materials. The geometry of the part is not constrained and its shape and material composition can be changed continuously during fabrication. To create a part, its geometric model is first sliced into cross-sectional layers, typically 0.001 to 0.005 inches thick. For each material in a layer, a disposable mask is made that exposes the area where that material occurs. The mask is placed upon the top layer of the growing part shape and a robotically manipulated thermal spray gun traverses the areas exposed by the mask. Masks are made from paper stock cut with a laser. Several alternative strategies are feasible for creating support structures for the part as it grows, including retaining a part of the mask or spraying the support material in place after the primary materials are deposited.

Deposition of more demanding materials, such as steel, is feasible. However, support material is required to act as a surface to which the sprayed material will adhere and to "release" the part when completed. Low-melt alloys, such as tin-based compositions, satisfy these requirements for arc sprayed steel. The sprayed steel bonds locally to a tin/bismuth composition by superficially melting and abrading a very thin layer of the low-melt alloy, which is melted away when the part is fully completed. After a layer of steel is deposited, using pressure sensitive paper masks to expose the areas where steel is to be sprayed, the mask is removed. Finally, the steel is masked off with a complementary mask and the support materials sprayed down.

Selective material deposition is also feasible with the MD* approach. Building composite structures with several different materials within a layer can be accomplished by using multiple masks to form each layer. This enables the capability to create integrated electromechanical devices, e.g., mechanical structures with embedded electronics and unique composite, multi-material structures as elaborated in Section 3. Availability of the MD^* manufacturing process provides the requisite technology for the realization of novel designs (at the macro- and micro-structure level) generated by the homogenization method.

In the context of Project MAXWELL, MD* is particularly relevant since it addresses another current manufacturing challenge -- robust processes for forming and joining *composite structures*. While the material properties of composites dramatically expands the possibilities for new product designs, current composite manufacturing technologies severely limit the possible geometries. MD^* has the potential to create *dense* composite and laminate structures of arbitrary geometric complexity, while masking also enables selective material deposition. Therefore, different regions within a layer can be composed of different materials. For example, integrated electro-mechanical assemblies are feasible such as encapsulated computer packages with embedded electronics.

5. CURRENT STATUS AND FUTURE GOALS OF PROJECT MAXWELL

Project MAXWELL is a synergistic integration of two novel research efforts, one in design and the other in manufacturing, for the purpose of establishing of a sound methodology for the rapid realization of superior products. Basic research directly relevant to MAXWELL has been ongoing at the participating institutions for over three years. The U-M results to date can be summarized as the development of a three phase prototype system for the concurrent design of superior structural components.

Phase I: Based on the specified boundary conditions (type and magnitude of loads) and designable space (packaging specifications) the homogenization method is applied to derive a grey scale image representation of the material composition and distribution that is optimal relative to desired structural performance measures.

Phase II: Using computer vision and geometric modeling techniques this image is interpreted and translated into a realistic structure, e.g., a radically new perforated or multi-material composition reminiscent of biological structures.

Phase III: A parametric optimization model based on finite element analysis is formulated and solved to determine a complete dimensional and material description of the structure.

Ongoing research at CMU directly relevant to MAXWELL can be summarized as the development of MD* process for the rapid manufacture of single or multi-material components. Therefore, in MAXWELL we have

Phase IV: The manufacture of the Phase III output (*i.e,* discrete parts of arbitrary geometry and possibly varying material composition) using the MD^* process.

Currently the U-M system can deal with 2D and 2.5D components (sheet metal panels, brackets, beams, etc.). The capability of MD^* includes the manufacture of most designs developed at U-M. Therefore, current efforts in MAXWELL are geared towards enabling the fabrication and testing of some sample 2D/2.5D parts produced in Phase III.

Phase V: The final phase in MAXWELL is the testing phase, where the Phase IV products will be subjected to various mechanical tests. Qualitative indices of performance in Phase V will include measures such as weight to stiffness ratio, impact energy absorption rates and fatigue life.

Based on the test results in Phase V, iterations through Phases II, III, and IV may be necessary. During the iterations, in Phase IV, the manufacturing process could now include a conventional metal removal process (*e.g.,* milling) in addition to MD^* depending on the suggested changes to geometry (shell interior or exterior) in Phase II. Ongoing work focuses on three dimensional components and extensions to all five phases of MAXWELL are envisioned.

ACKNOWLEDGEMENTS

REFERENCES

[ASH91] Ashley, S., "Rapid Prototyping Systems" *Mechanical Engineering,* 113(4), 34-43 (1991)

[BEN86] Bennet, J.A and Botkin, M.E., *The Optimum Shape: Automated Structural Design,* Plenum Press, New York 1986

[BEN88] Bendsoe, P.M., and Kikuchi, N., "Generating Optimal Topologies in Structural Design Using a Homogenization Method", *Comp. Meth. Appl. Mech. Eng.,* Vol 71, 197-224, 1988

[BOT85] Botkin, M.E. and Bennet, J.A., "Shape Optimization of Three Dimensional Folded Plate Structures", AIAA J,, 23(11) 1804-1810, (1985)

[BOU90] Bourell, D.L., Beaman, J.J., Marcus, H.L. and Bralow, J.W., in *Proceedings Solid Freeform Fabrication Symposium,* The University of Texas at Austin, Texas, 1-7, August 1990

[BRE91] Bremicker, M., Chirehdast, M., Kikuchi, N., Papalambros, P. Y., "Topology and Shape Optimization in Structural Design", *J of Mechanics of Structures and Machines,*

[CHO83] Choi, K.K. and Haug, E.J., "Shape Design Sensitivity Analysis of Elastic Structures", *J of Structural Mechanics,* 11(2) 231-269 (1983)

[ESP85] Esping, B.J.D, *The OASIS Structural Optimization System,* Report No. 85-3, The Royal Institute of Technology, Stockholm, 1985

[ESP87] Esping, B.J.D, Holm, D., Isby, R., and Larsson, M., *Shape Optimization of A Suspension Arm using OASIS,* Report No. 87-8, The Royal Institute of Technology, Stockholm, 1987

[FLE86] Fleury, C., and Braibant, V., "Structural Optimization: A New Dual Method Using Mixed Variable", *Int. J Num. Methods in Eng,* Vol 23, 409-428, 1986

[FUN65] Fung, Y.C., *Foundations of Solid Mechanics,* Prendice-Hall, Englewood Cliffs, NJ, 1965.

[GAL73] Gallagher, R.H. and Zienkiewicz (ed.) *"Optimal Structural Design: Theory and Applications",* John Wiley, Chichester, 1973

[GAL84] Gallagher, R.H., Atrek, E., Ragsdell, K.M., and Zienkiewicz, *"New Directions in Optimal Structural Design",* John Wiley, New York, 1984

[HAU81] Haug, E.J., and Cea, J., (ed.) *"Optimization of Distributed Parameter Structures, Vols 1, 2"* Sijthoff & Noordhoff, Alphen aan den Rijn, 1981

[HAU87] Hauber, D., "Automated fabrication of net shape microcrystalline and composite metal structure without molds", in *Proceedings of NSF 14th Conference on Production Research and Technology,* University of Michigan, 461-66, Oct. 1987

[HER91] Herman, H. and Sampath, S., in *Proceedings of 2nd Plasma-Technik Symposium,* Luzern, Switzerland, May, 1991

[KIK86] Kikuchi, N., Chung, K.Y., Torigaki, T., and Taylor, J.E., "Adaptive Finite Element Methods for Shape Optimization of Linearly Elastic Structures", *Comp. Meth. Appl. Mech. Eng.,* Vol 57, 67-91, 1986

[KOH86] Kohn, R.V., and Strang, G., "Optimal Design and Relaxation of Variational Problems", *Comm. Pure Appl. Math.,* Vol 39, 1-25 (Part I) 139-182 (Part II) 353-377 (Part III), 1986

[LEV 81] Lev, O.E., (ed.) *Structural Optimization - Recent Developments,* ASCE, 1981

[LUR84] Lurie, K.A, and Cherakev, A.V., "Exact estimates of conductivity of composites formed by two isotropically conducting media taken in prescribed proportion", *Proc. Royal Soc. Edinburgh,* 99A, 71-78, 1984

[MER91] Merz, R., Prinz, F.B. and Weiss, L. E., *"Planning.Mask Cutting For Thermal Spray Spray Deposition,"* Tech Report EDRC 24-73-91, Carnegie Mellon Univ, 1991

[MOR82] Morris, A.J., (ed.) *Foundations of Structural Optimization: A Unified Approach,* John Wiley, Chichester, 1982

[MOT87] Mota Soares, C.A., (ed.) *"Computer Aided Optimal Design: Structural and Mechanical Systems"* Springer Verlag, Berlin, 1987

[OLH83] Olhoff, N, and Taylor, J.E., "On Structural Optimization", J. *Appl. Mech.,* Vol. 50, 1134-1151, 1983

[PAP90] Papalambros, P.Y., and Chirehdast, M. "An Integrated Environment for Structural Configuration Design", *J of Eng. Design,* Vol 1, No. 1, 73-96, 1990

[SAN80] Sanchez-Palencia, E., "Non-homogeneous media and vibration theory", Springer Lecture Notes in Physics, Berlin, 1980

[SCH79] Schanck, E., "An Optimization Procedure for Stress Concentration by the Finite Element Technique", *Int. J Num. Meth. Eng.,* Vol. 14, 115-124, 1979

[SPU71] Spunt, L., *Optimal Structural Design,* Prentice Hall, 1971

[TAR77] Tartar, L., "Estimation de coefficients homogeneises, *Springer Lecture Notes in Mathematics,* Berlin 364-373, 1977

[WEI91] Weiss, L. E., Prinz, F. B. and Siewiorek, D. P, "A Framework for thermal spray shape deposition in the MD* system" in *Proceedings of Solid Freeform Fabrication Symposium,* The University of Texas At Austin, August, 1991

[WEI90] Weiss,L., Gursoz, E.L., Prinz, F.B., Fussell, P.S., Mahalingham, S. and Patrick, E.P., "A Rapid Tool Manufacturing System Based on Stereolithography and Thermal Spraying", *Manufacturing Review,* 3(1), 40-48 (1990)

Selective Laser Sintering and Reaction Sintering of Ceramic Composites

P. Kamatchi Subramanian, Guisheng Zong and H.L. Marcus
Center for Materials Science and Engineering
The University of Texas at Austin
Austin, TX 78712.

Abstract

Selective Laser Sintering and Reaction Sintering (SLS and SLRS) are used as methods of forming composites and preforms. Al_2O_3/Al and SiC/Al were studied as model systems. Ceramic and metallic powders are mixed and locally sintered using SLS and SLRS. Post processing heat treatment was also employed. Wettability and residual stress aspects of this process are discussed.

Introduction

Composite materials consisting of a polymer or a metal matrix reinforced with a strengthening phase started developing in the early 1960's. The reinforcement can be as particulate or as fibers. While these composite materials show great promise of improved strength and stiffness, fabrication of parts from the metal and ceramic matrix composites has limited their application .

One of the methods of overcoming the processing difficulties is to form preforms from the reinforcing phase in the required shape and then to infiltrate the preforms with matrix material. Selective Laser Sintering (SLS) and Selective Laser Reaction Sintering (SLRS) offer the possibility of forming netshape preforms which could then be infiltrated. In the SLS or SLRS of preforms or composites described here, the reinforcing ceramic phase, is mixed with the metal and locally sintered under the laser beam. The metal melts and binds the ceramic together into a porous composite. In SLRS part of the metal powder reacts with the oxygen in the atmosphere to form an oxide. Prior work on the Selective Laser Sintering of ceramics at University of Texas involved binding the ceramic with a low melting temperature inorganic binder [1,2]. The issues involved in SLS and SLRS of metal and ceramic composites are examined in this paper. The material systems examined in this work are Al_2O_3 /Al and SiC/Al .

Experimental

Al_2O_3 /Al

Powders of Al_2O_3 (15μ spherical)and Al (20μ spherical)were mixed in various ratios by weight and sintered in a SLS system[3,4] under the 100W Nd:YAG laser (1.06μm) modulated at 20KHz. Single layer tests were conducted on these powders using various power levels and scan speeds. From these measurements the scanning speeds and power levels used in the study were determined. Multilayered parts were made using the powder delivery and leveling systems in the SLS chamber[3,4]. No powder bed biasing temperature was employed during the process. Three compositions containing 15%, 25% and 35% by weight of Al were made and sintered.

During sintering under the laser beam of the Al_2O_3 /Al system, part of the Al melts and partially oxidizes as it binds the particles together. The untransformed Al is further

transformed to the oxide by means of a secondary heat treatment. The part was heated in a furnace under air to a temperature of $1050^\circ C$ for 18 hours and then furnace cooled.

SiC/Al

SiC powder (15μ) and Al powder ($20\ \mu$) were mixed in the ratio 3:1 and sintered in the 1.1kW CO_2 Laser ($10.6\mu m$) SLS system. This material system could not be sintered in the 100W SLS system because the laser power was not sufficient . The part was then fired at $1300^\circ C$ in air to partially oxidize the aluminum.

Results of SLS and SLRS of Al_2O_3/Al composites.

It was found that 30-35W of laser power is sufficient to sinter the 25 and 35 wt% of Al while about 43W of power was required to sinter the 15wt % of Al. In order to have a proper basis for comparison all specimens for density measurement were made with 43W of laser power and at a scan speed of 4.6 cm/sec.

Micro structure

Both the surface and cross-section of the Al_2O_3 /Al composite prior to secondary treatment were observed in a Scanning Electron Microscope (SEM). The molten Al has wet the alumina particles and is bonding the particles together (Fig.1). Regions appear as agglomerates of high density (Fig.2). The regions of high density are separated by regions where the particles are only loosely bound (Fig.3). In this region the Al_2O_3 particles are not completely wet by the Al.

The distance of separation between the agglomerates decreases as the percentage of metal in the powder mixture increases. This may be seen by comparing Fig.1 which is from a part made out of 85:15 Al_2O_3: Al mixture and Fig.4 . which is from a part of 65:35 mixture where the agglomeration covers most of the surface. The cross section of the specimen after firing in air has similar agglomeration (Fig.5). The agglomerated region is a fairly dense dispersion of the Al_2O_3 in the Al matrix. (Fig.6)

Density measurements

Specimens of 2.5cmX2.5cm cross-section with varied thickness of approximately 7 to 9mm were made and density was determined by a direct volume measurement both before and after firing. The variation in density with composition is shown in Fig.7. The density decreases with increase in the composition of Al. This is because of the lower density of Al. (Density of Al =2.7g/cc , density of Al_2O_3 = 3.97g/cc) This is modified by the fraction of Al that is reaction sintered. The fraction of full theoretical density of this composite always remained around 0.45 . A line corresponding to 45% of the theoretical density of the composite with weight percentage of Al is also plotted on Fig.7 . This seems to indicate that the composite density reflects the powder bed density.

Mechanical properties

25 Wt% Al specimens of   0.6cmx7.6cmx2.5cm were sintered and fired. Four point bend strength tests were conducted at room temperature in air at 0.2mm/min on these. The average bend strength for the 25 wt% Al composition was determined to be 3.6 ± 0.7 MPa (520 ± 100 psi) . Five samples were measured.

**Figure1. Surface of a composite containing 15 % Al.
Agglomerates and regions of low density may be seen.**
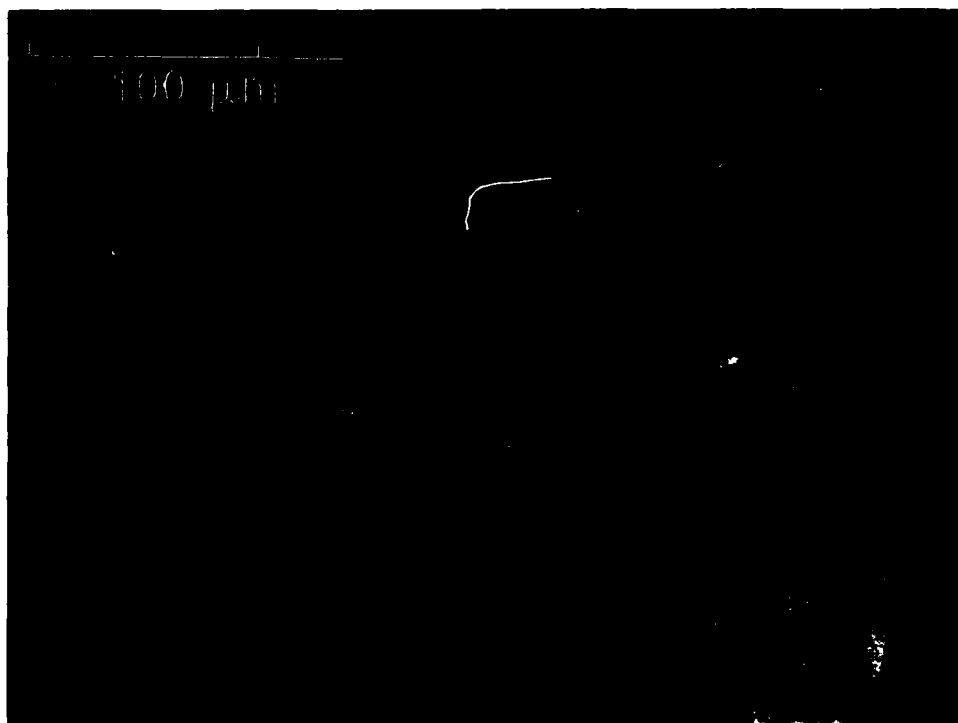
**Figure 2. An enlarged view of an agglomerated region.
It may be seen that these regions are very dense.**

Figure 3. A view of one of the low density regions
It may be seen that the powder particles are
not enveloped by a dense metallic layer.
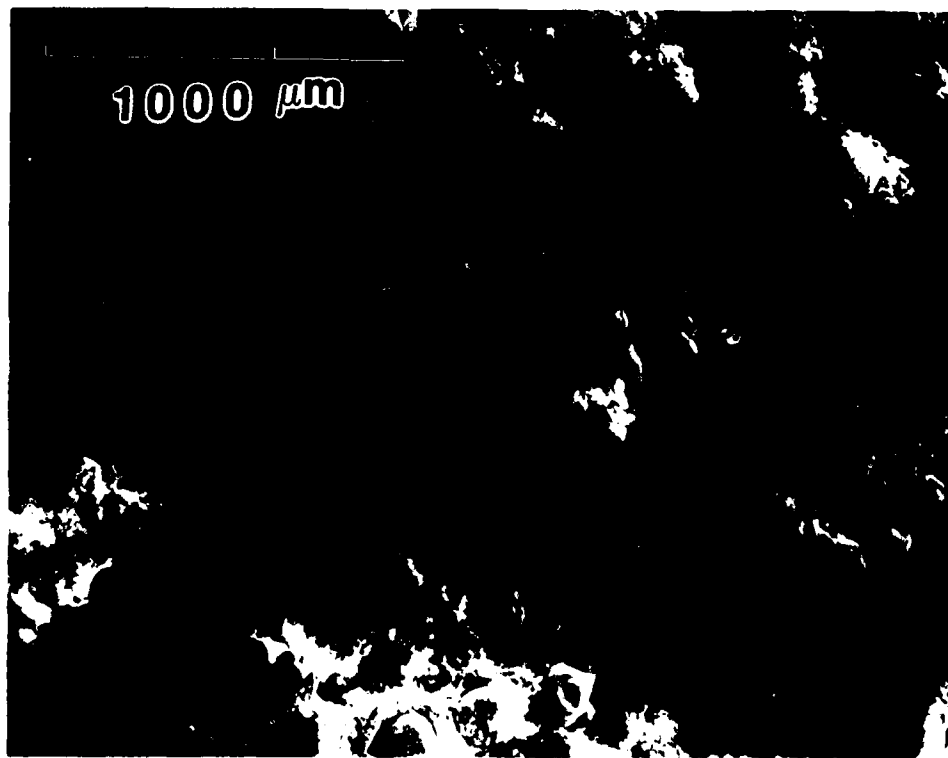
Figure 4. Surface of a composite containing 35% metal..
The denser agglomerates are closer spaced.

Fig. 5 Cross-section of a 75:25 specimen .
It is similar to the surface of the specimen.
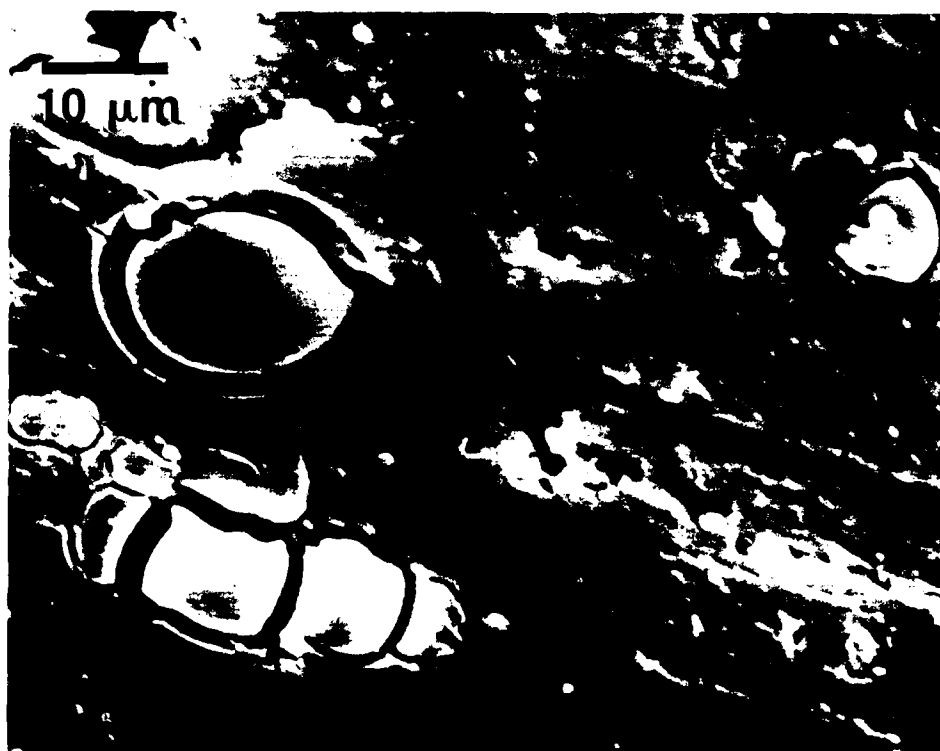
Figure.6. Cross-section through an agglomerate. The Alumina particles
are surrounded by a matrix of Aluminum.

67
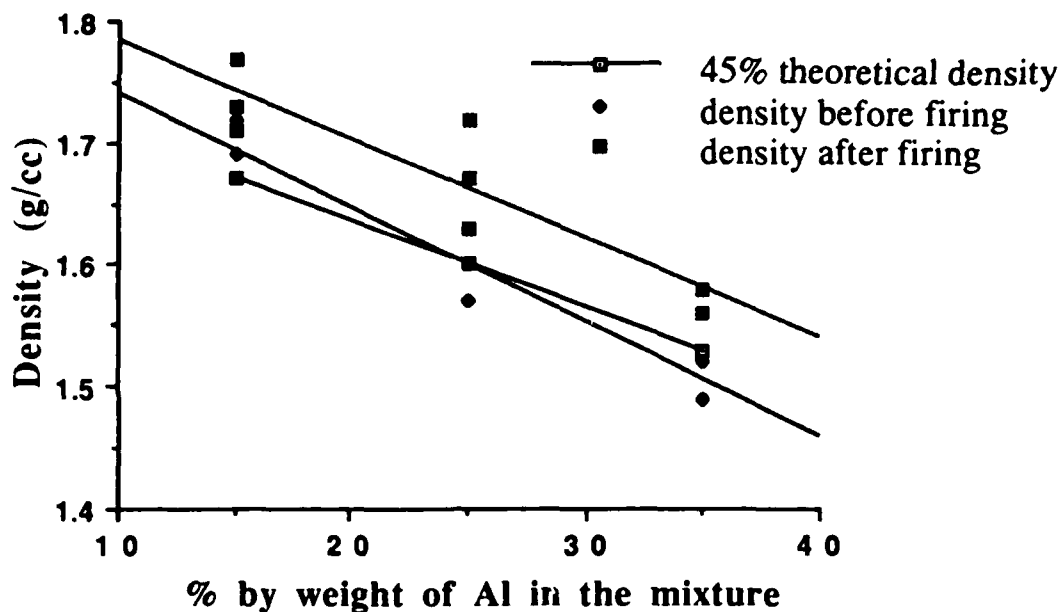
Figure 7. Variation of densiy with weight percentage of Aluminum.

Results of the SLS and SLRS of SiC/Al composites.

SiC powder (15μ) and Al powder (20 μ) were mixed in the ratio 3:1 and sintered in the high power workstation under the 1.1 kW CO_2 laser. A power level of 120W and a scan speed of 1.66cm/s was employed. The part was then fired at 1300°C in air for 18 hours and furnace cooled. The fired density was 1.3g/cc which is 0.42 of the theoretical density . X-ray diffraction shows that the phases present are SiC, Al and α-Al_2O_3. A picture of a part formed is shown in Fig.8. This shows that shapes of SiC/Al/Al_2O_3 can be made by this process.
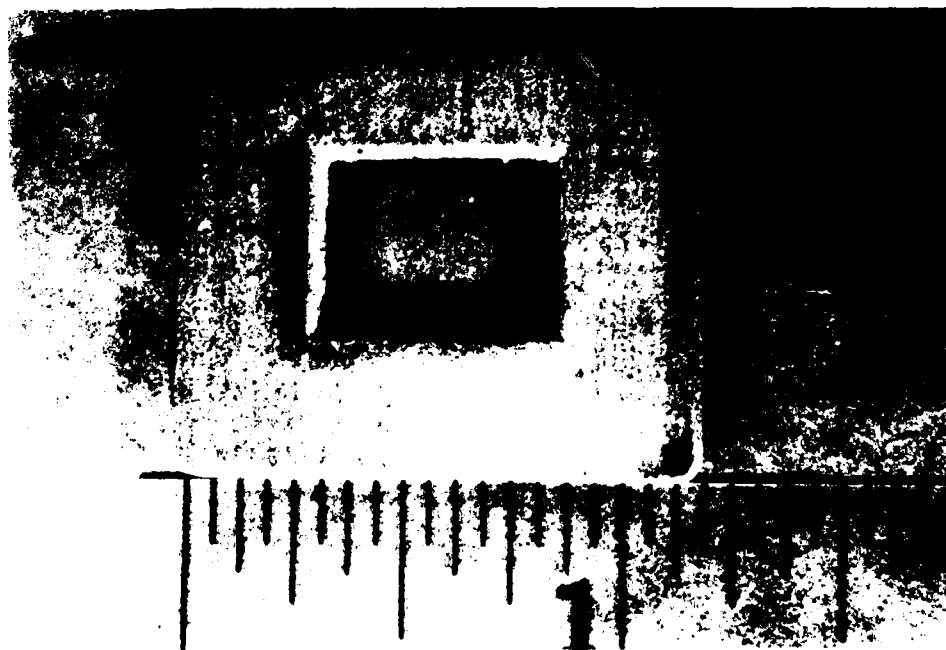
Figure.8. A SiC/Al part.

Discussion

The agglomerated regions in the Al_2O_3/Al composite are where the Al has completely wet the Al_2O_3. The wettability is normally characterized in terms of the wetting angle. Lower wetting angle implies better wetting of the ceramic by the metal phase. The wetting angle changes with temperature. In the case of Al_2O_3/Al the wetting angle changes with temperature as given by Table I[5]

Table I

Temperature	Contact angle
700	120
800	110
900	90
1000	75

Hence in order to obtain good binding between the Al_2O_3.ceramic and the Al matrix phase it is not only necessary to melt Al but also to heat it to a sufficiently high temperature to reduce the wetting angle. This would imply having a high power of the laser beam. Preheating the powder allows lower laser power to raise the temperature to aid wetting. Wetting agents may also be added. The effect of the wetting agents is to reduce the wetting angle and thus help in densification but none were added in this study.

In the case of SiC/Al systems the variation in wetting angle is given in Table II[6]. It can be seen that this requires the Al to be heated to a higher temperature than the Al_2O_3/Al system. Hence the higher power to sinter the SiC/Al system.

Table II

Temperature	Contact angle
725	150
900	130
1000	90

Residual stresses.

The powder in this process is at room temperature. When the laser scans the surface the metal is heated to a temperature of at least $660°C$ (the melting point of Al) and higher to get wetting. The metal melts, wets the Ceramic and binds it together. The composite also undergoes rapid cooling due to the surrounding cool material. The coefficient of thermal expansion of the Al $(23-33 \times 10^{-6})/°C$[7] over the temperature range 25 to 500°C is much greater than the SiC $(5 \times 10^{-6})/°C$[7] or Al_2O_3 $(7 \times 10^{-6})/°C$[7] causing it to shrink more than SiC or Al_2O_3 with cooling. The constraint on the shrinkage due to the ceramic results in development of very local residual stresses across the metal ceramic interface. Another cause of residual stress is the temperature gradient along the scan line. In this case the coefficient of exapnsion can be calculated by the rule of mixtures such that, $\alpha_{composite} = \alpha_{Al}V_{Al} + \alpha_{Al2O3}V_{Al2O3}$ where V_{Al} and V_{Al2O3} are the volume fractions of Al and Alumina respectively. The solid state cooling in the cold surrounding material leads to a more global residual stress pattern.

The problems associated with residual stress increases with increase in percentage of metal due to the increase in the coefficient of expansion . Increase in power has been observed to aggravate the residual stress probably due to the increased temperature gradient along the scan line. Fig.9 shows the debonding between SLS layers of the

Al_2O_3/Al composite when the penetration depth combined with the resulting residual stress is not taken into account.
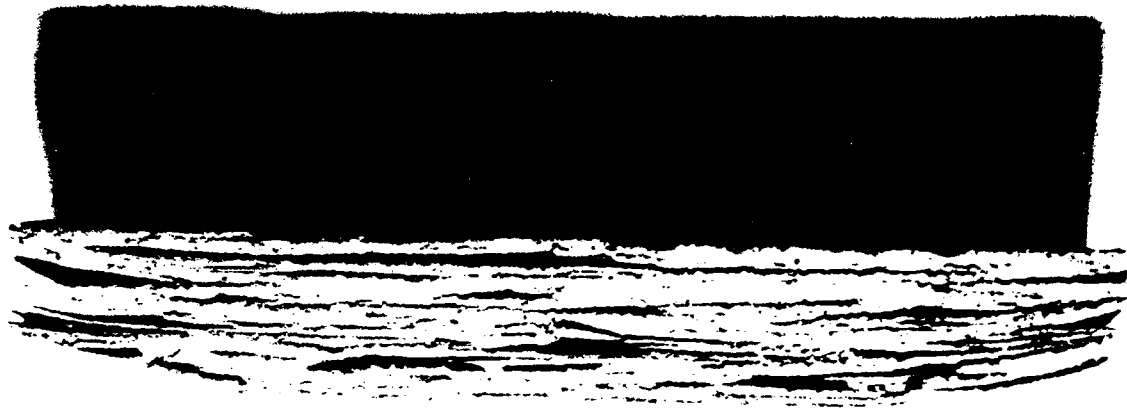
Figure 9. Cracks that occur in a specimen on account of residual stresses

Summary and Future Research.

Selective Laser Sintering and Reaction sintering show promise to be viable methods to form ceramic composites and preforms of Al_2O_3/Al and SiC/Al. Future work will be to determine the effects of varying particle size ratios and the effect of wetting agents. In addition the influence of preheating the powder on residual stress and mechanical properties will be studied.

References.

1. U. Lakshminarayan , S. Ogrydziak and H.L. Marcus, "Selective Laser sintering of ceramic materials ", Proceedings of the solid Freeform fabrication symposium , Ed. J.J. Beaman, H.L. Marcus, D.L. Bourell and J.W. Barlow, 1990, pp. 16 .

2. U. Lakshminarayan and H.L. Marcus, Microstructural and Mechanical properties of Al_2O_3 /P_2O_5 and Al_2O_3/B_2O_3 by Selective Laser Sintering", Proceedings of the solid freeform fabrication symposium, Ed. H.L. Marcus, J.W. Barlow, D.L. Bourell and R.H. Crawford, 1991, p.205

3. C. Deckard and J.J.Beaman, Proceedings, 15th conference on Production research and Technology, University of California at Berkeley, 1989, p.623

4. C. Deckard, Selective Laser Sintering, Ph.D. Dissertation , The University of Texas at Austin, December 1988.

5. D.A. Weirauch, Jr. "A reappraisal of wetting in the system Al-Al$_2$O$_3$ from 750 - 1000°C ", Ceramic micro structures 86 Role of interfaces edited by J. A. Pask and A. G. Evans p.329
6. C. A. Calow and A. Moor , in "Practical Metallic Composites " , The Institution of Metallurgists, London, 1974, p.B17.
7. CRC handbook of tables for applied engineering science, second edition, 1980, p.249.

Acknowledgement.

Direct Selective Laser Sintering of High Temperature Materials

G. Zong, Y. Wu, N. Tran, I. Lee, D. L. Bourell, J. J. Beaman, and H. L. Marcus

Center for Materials Science & Engineering
and
Department of Mechanical Engineering
The University of Texas at Austin, Austin, TX 78712

Abstract

Selective Laser Sintering (SLS) involving a coexisting liquid and particulate solid during the SLS processing can be used to produce freeform parts directly with high temperature materials. Factors such as scanning laser power density, residence time, scan line spacing, the interfacial energies between the liquid and solid phases, powder bed biasing temperature, and sintering atmosphere greatly affect the microstructure evolution in the SLS process. Direct SLS of high melting temperature mixed powder materials was demonstrated using a 1.1 kW CO_2 laser SLS system. The relationship between the microstructures and the process parameters will be described.

1. Introduction

Selective Laser Sintering is a pressureless sintering process used for Solid Freeform Fabrication (SFF). SLS has been used successfully to fabricate prototype parts and preforms with polymer, ceramic, or low melting temperature metallic materials [1-4]. A liquid phase is usually involved during the SLS processes. The atomic diffusion in the liquid phase is faster than that in the concurrent solid state process. The capillary force due to a wetting liquid is the driving force for rapid compact densification. The liquid also reduces the interparticle friction; thereby, aiding rearrangement of the solid particles. In addition, liquid dissolution of sharp particle edges and corners may allow more efficient packing. Thus, SLS processing control offers the opportunities for microstructure manipulations to optimize properties. With proper control of the above parameters, direct SLS of materials is possible. In this paper, direct SLS of high melting temperature mixed powder materials will be demonstrated using a 1.1 kW CO_2 laser SLS system.

2. Experimental

To perform selective laser sintering of high temperature materials, a high power laser selective sintering system was designed and assembled. There are four major components in the system: 1) a 1.1 kw CO_2 laser system with focusing optics and scanning mechanism; 2) a

72

Sun station and its interface to control the laser pattern generation; 3) a sintering chamber with a resistance plate heater in part cylinder and inert gas purging capability; and 4) a powder delivery and leveling system. Figure 1 shows schematic diagram of the sintering cell.

The initial materials studied were Cu-Ni and WC-Co-Ni mixed powders as well as stainless steel 304L powders. Additive powders were also used. Optical metallograph, SEM, AES, EDS, and XRD were employed to study the sintering behaviors.
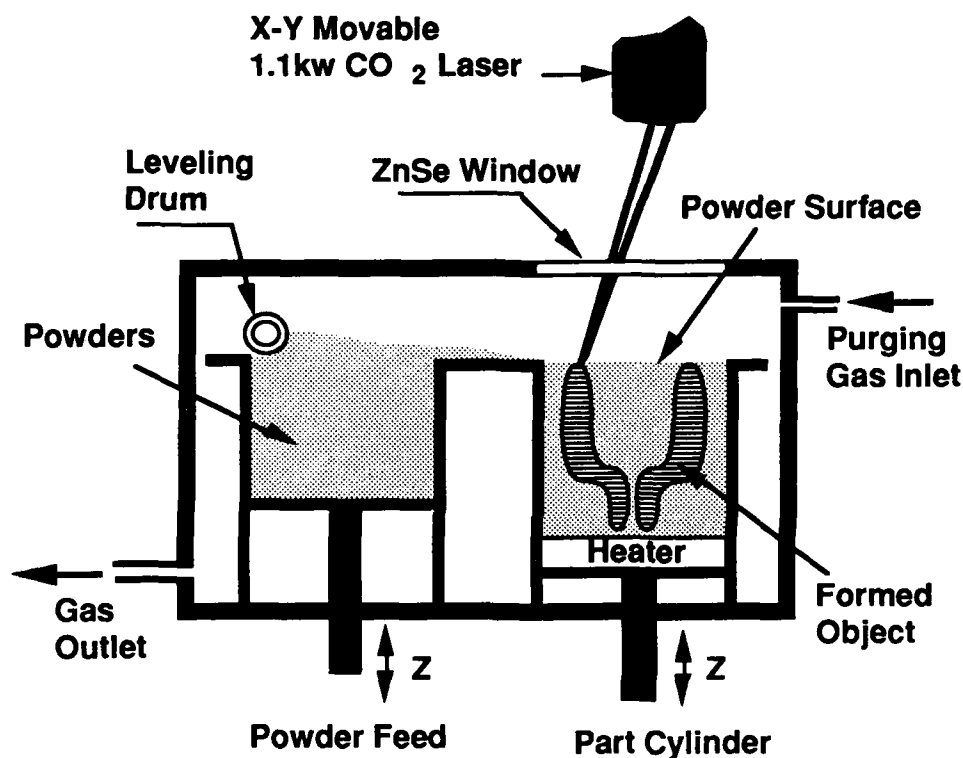
Figure 1   Sintering cell for high laser power SLS

3. Results and Discussions

The main SLS processing concerns are the properties of the starting powder, the laser parameter settings, and the atmosphere in which powder sintering occurs. These parameters and their interactions determine the SLS product quality. The initial results of the SLS of high temperature materials using the system described above will be presented with evaluation of laser parameter effects, role of additives, and sintering atmosphere effects.

3.1 Laser parameter effects in SLS

For a given SLS system, the laser parameters to be set in a typical SLS run are laser power density (P), scan speed (v), and scan spacing (S). Figure 2 shows the SLS sintering single layer thickness as a function of scan speeds and scan line spacing for 100 μm Cu powder. The sintered layer thickness decreases with increasing scan speeds due to shorter interaction (sintering) time. This thickness also decreases with decreasing scan line spacing. Since the laser beam diameter of 4.5 mm is larger than the scan line spacings studied (0.254, 0.508, 1.016, 1.270 mm), scan overlapping occurred in these tests. The smaller the scan line spacing, the more scan overlapping. Therefore, the sintered layer thickness decreases with increasing scan overlapping. This relationship can be explained by considering the fact that the thermal conductivity and reflectivity of the sintered solid are higher than those of the starting powder. The more the scan overlapping in a laser scan, the more laser energy will be transferred away by heat conducting through the sintered solid and reflected away by sintered solid surface. Thus the sintering layer thickness decreases.
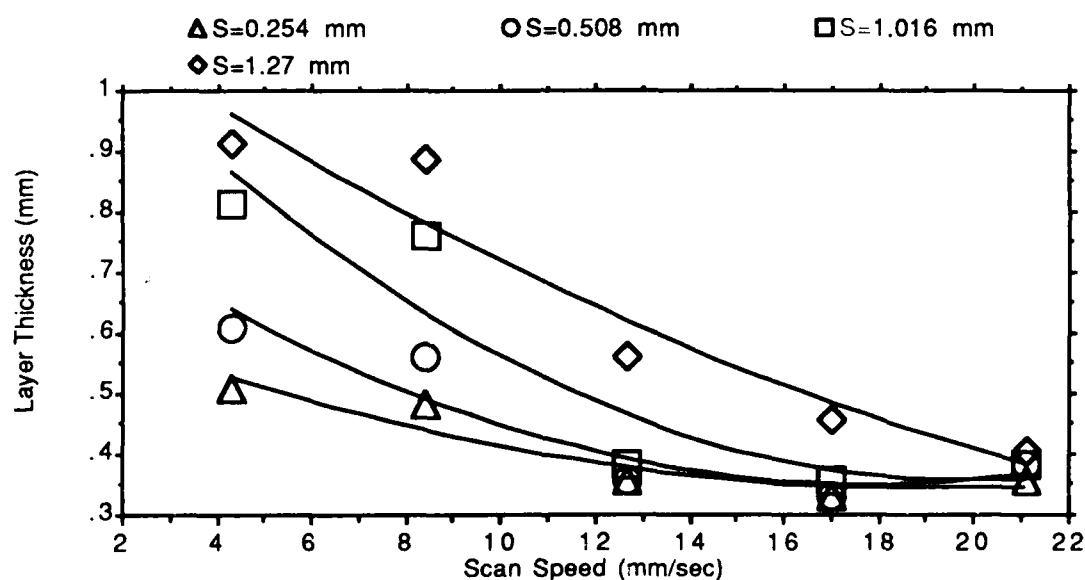
Figure 2 SLS sintering layer thickness as a function of laser scan speeds and scan line spacing. Laser power = 200w, beam size=4.5 mm, nitrogen flow rate = 60 *l* /min, no powder bed biasing temperature, for copper powder (~100μm) material.

To obtain a desired microstructure, sintering laser power (temperature) and scan speed (time) are the most important factors. The quality of the blend and analysis of the atmosphere also affect the microstructure. SLS tests and metallographic studies have been made to investigate the effect of laser power and scan speed on the sintering of a Bronze+Ni system. Figures 3 shows the typical sections of the SLS sintered part. These pictures show the strong effect of laser power and scan speed on the amount, size, and shape of residual porosity. The

sintered porosity is lower at higher laser power and lower scan speed. The pores become smaller and more rounded as the laser power increases and scan speed decreases because both sintering temperature and time are increased, more rearrangement [5] is involved during sintering. The metallographic study confirms the effect of laser power and scan speed. Figure 4 shows undersintered microstructure at conditions of Figure 3(a) and well sintered microstructure at conditions of Figure 3(c). Successful parts (Figure 5) with ~82% of theoretical density were obtained at laser power = 280w, beam size=4.5 mm, scan speed = 4.2mm/sec, scan line spacing =0.5mm, layer thickness=0.25mm, purging nitrogen flow rate = 60 l /min, powder bed biasing temperature=350 ^{0}C, for 60 wt% Bronze 9010 (~100μm)-30 wt% Ni (~100μm)-Cu3P (63μm) powder mixture.

During SLS process, laser heating causes temperature gradients that lead to the formation of residual stresses and strains throughout the sintered part. In the extreme case, these residual stresses will cause sintered layer curling. Laser power density and scan speed, together with scan path, part size, and powder bed biasing temperature, have strong effects on the generation of residual stresses in the sintered parts. Initial results showed that curling can be overcome or reduced by suitable setting these parameters. These results will not be discussed in detail in this paper.

3.2 Role of Cu3P in SLS of Cu-Ni materials

Tests have been carried out with several kinds of Cu-Ni and Bronze-Ni powders containing various amounts of Cu3P (0-10 wt%). These tests show that the present success of SLS of Cu-Ni powders is, to a large extent, dependent upon the addition of Cu3P. This section will discuss the role of Cu3P in SLS of Cu-Ni materials.

X-ray analysis of the starting powder mixture of 60 wt% Bronze-30 wt% Ni -Cu3P and its SLS sintered part indicated that Cu3P peaks showed up on the profile of the starting powder but not on the profile of SLS sintered samples (Figure 6). However, EDS analysis (Figure 7) showed that P is still in the sintered part. This phenomena can be explained by referring to the Cu-P equilibrium diagram [6] in Figure 8. The Cu-Cu3P partial system is a simple eutectic. The solubility of P in Cu is about 1.7 wt.% at the eutectic temperature of 714^{0}C. At the usual SLS sintering temperatures (above the melting point of copper, 1085 ^{0}C), Cu3P (melting point 1022^{0}C) will melt and there is considerable solubility of P in the molten copper. When Cu3P melted, P is diluted by the copper in bronze. Calculation indicates that total weight percentage of P in copper becomes 1.27%, about the solubility of P in copper at room temperature. Thus , after sintering, P is a solute in the Cu-P solution instead of forming Cu3P. Secondary electron micrograph and X-ray mapping of the fracture surface of the sintered 60 wt% Bronze-30 wt% Ni -Cu3P sample show P, Cu, and Sn elements appearing at same area of the sintered part, revealing P-Bronze solution (Figure 9). Figure 9 also shows that Ni remained solid during the sintering, as seen earlier in the optical microscopic studies (Figure 4).
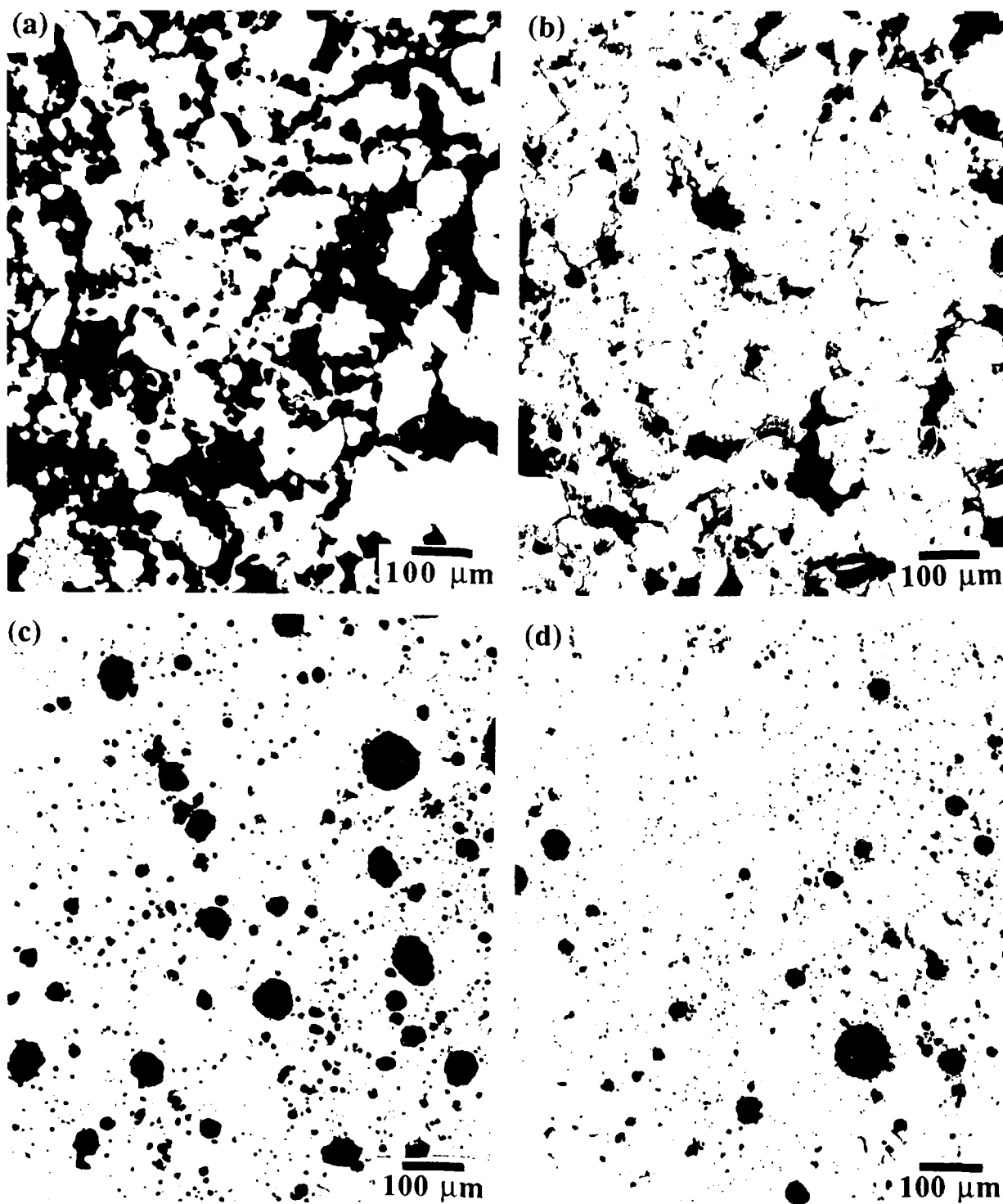
Figure 3 Microstructure of Bronze+Ni+Cu3P sintered at laser beam size=4.5 mm, scan line spacing =0.5mm, purging nitrogen flow rate= 60 *l* /min, no powder bed biasing tempe.ature, and (a) laser power = 200w, scan speed = 21.2mm/sec, (b) laser power = 200w, scan speed = 12.7mm/sec, (c) laser power = 280w, scan speed = 21.2mm/sec, (d) laser power = 280w, scan speed = 12.7mm/sec.
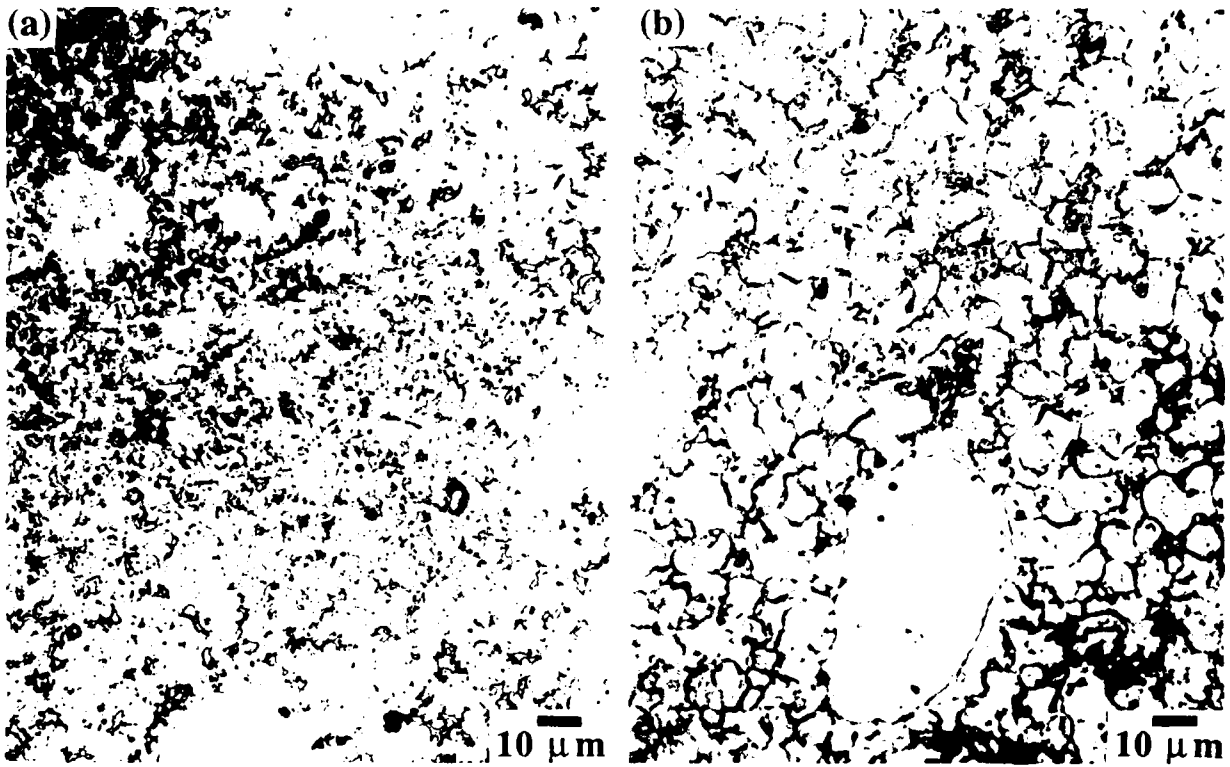
Figure 4 Microstructure of Bronze+Ni+Cu3P sintered at laser beam size=4.5 mm, scan speed = 21.2mm/sec, scan line spacing =0.5mm, purging nitrogen flow rate= 60 *l* /min, no powder bed biasing temperature, and (a) laser power = 200w, (b) laser power = 280w.

Figure 5 SLS Cu-Ni part.
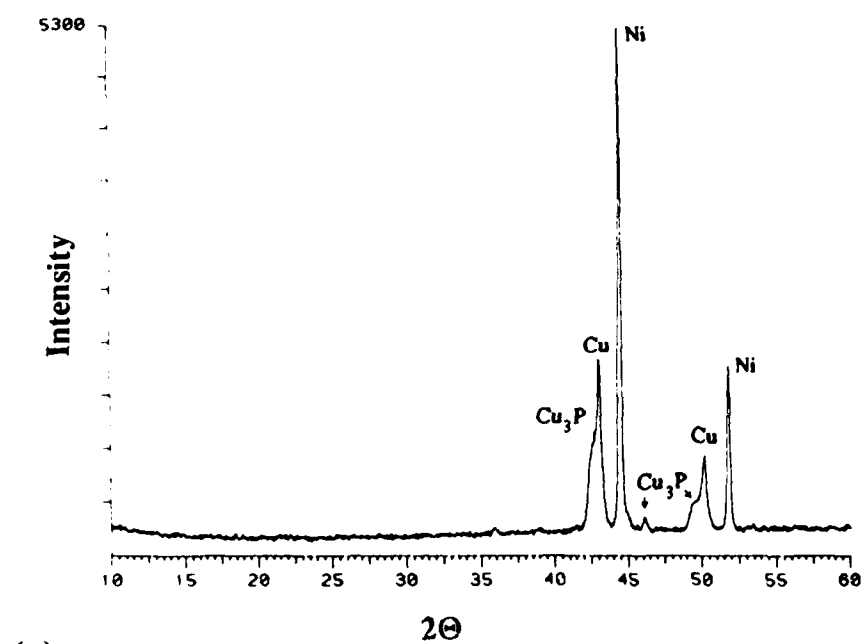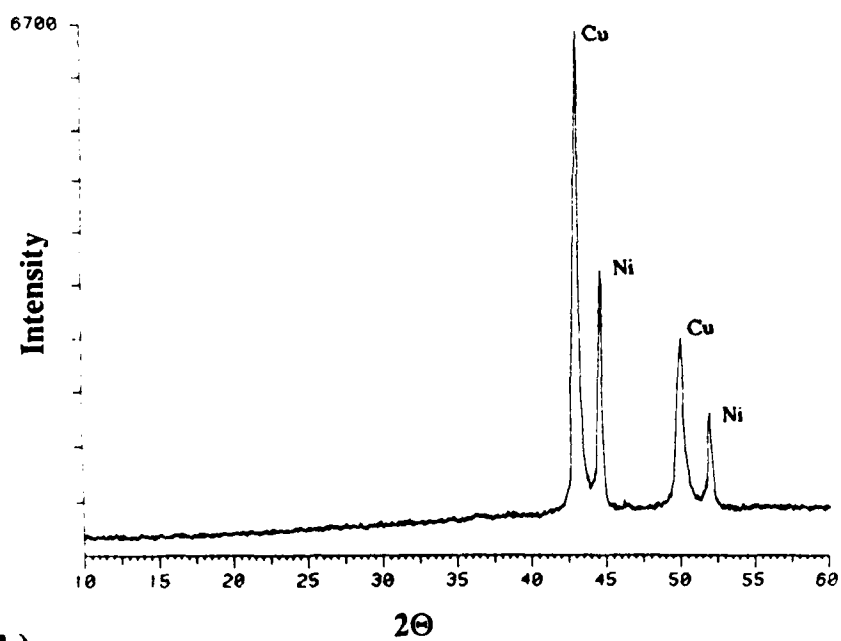
Figure 6 X-ray profiles of (a) starting powder mixture and (b) SLS sintered 60 wt% Bronze-30 wt% Ni -Cu3P.
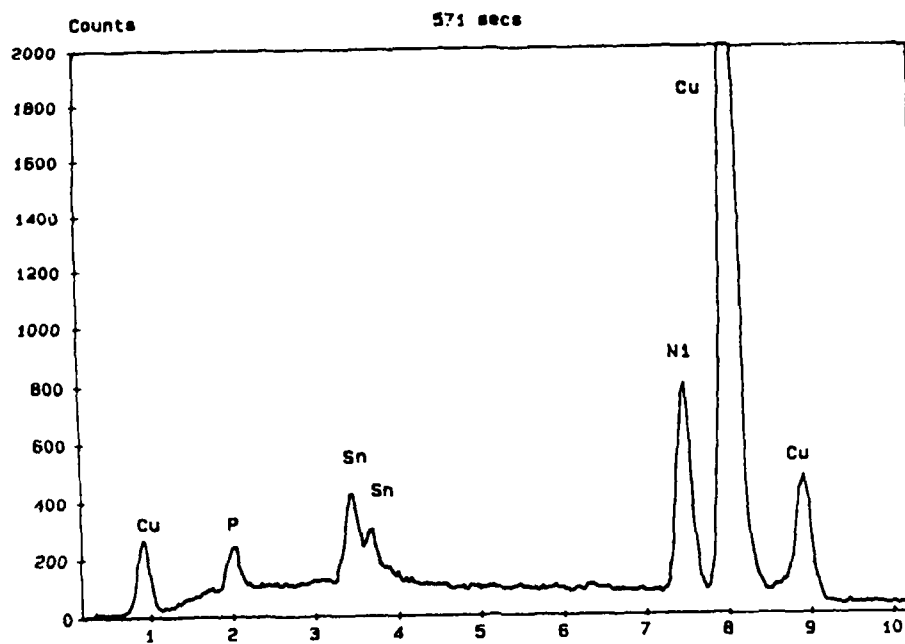
Figure 7 EDS analysis of SLS sintered 60 wt% Bronze-30 wt% Ni -Cu3P.
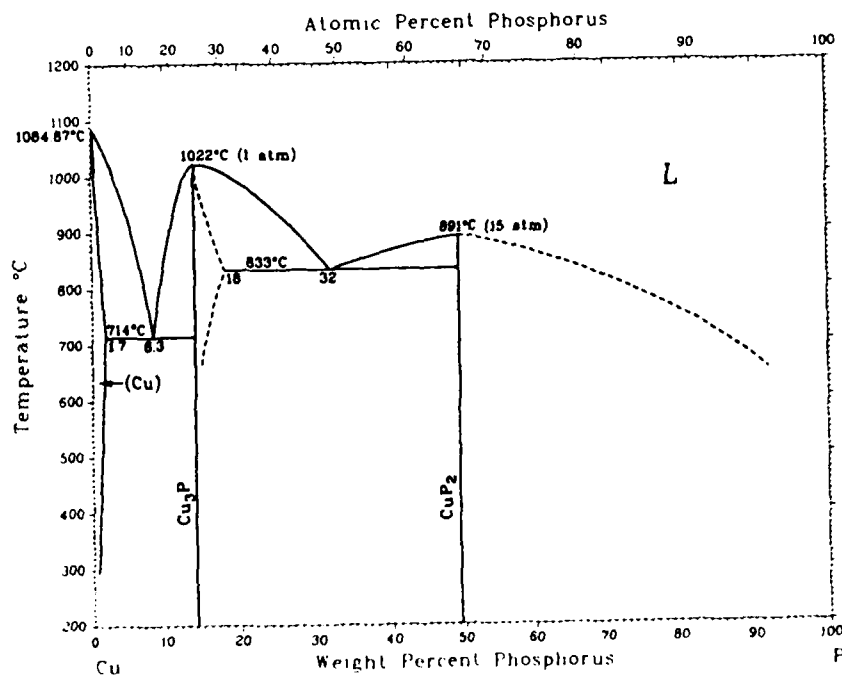
Figure 8 Cu-P equilibrium diagram [6].
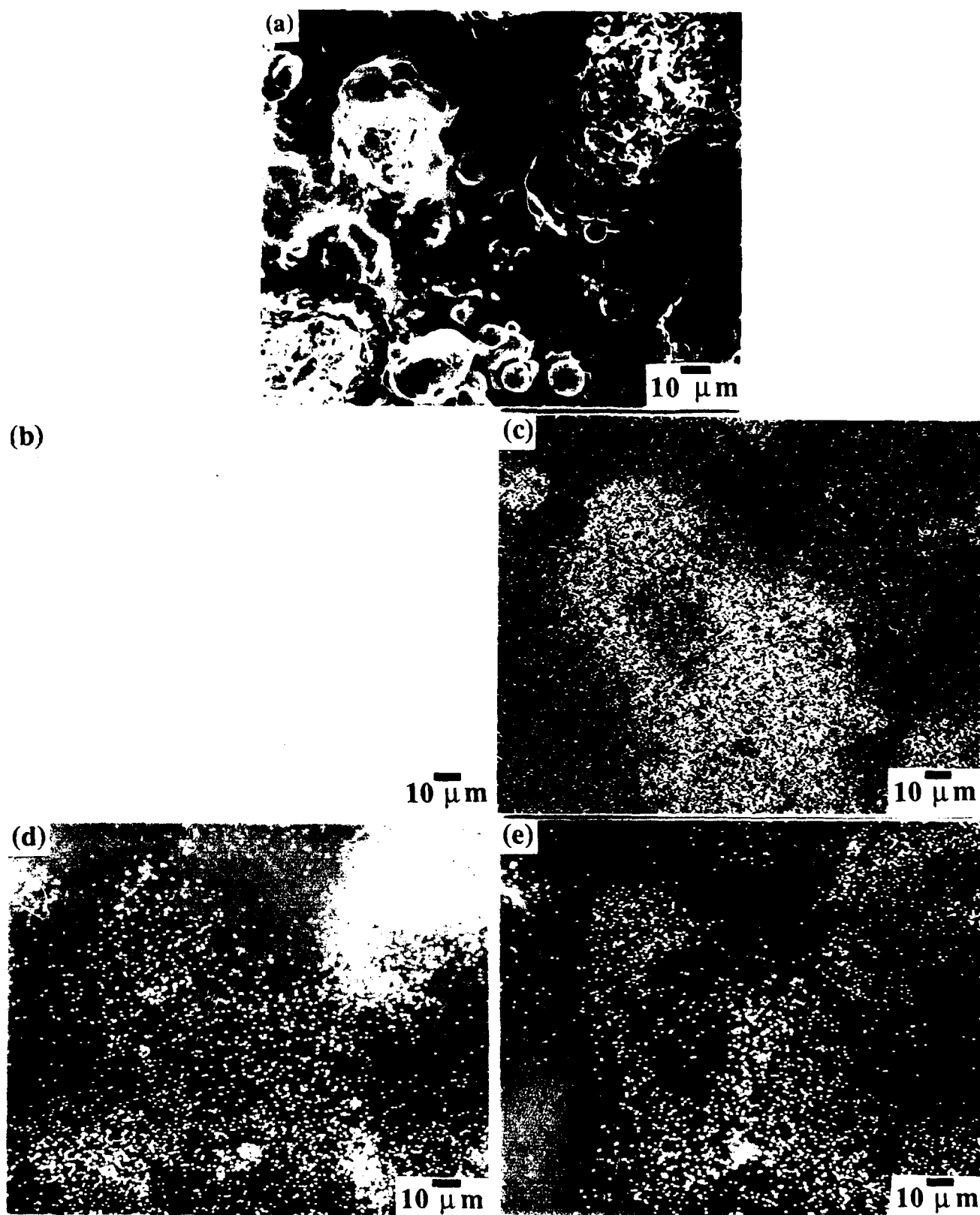
Figure 9 The secondary electron image (a) and X-ray element maps of (b) P, (c) Cu, (d) Sn, and (e) Ni form the fracture surface of the SLS sintered 60 wt% Bronze-30 wt% Ni -Cu3P.

Having located P in the sintered samples, we now discuss the role of P/Cu3P in the SLS process. Smooth sintering layers (less balling) can be obtained when Cu3P is added to the powder mixture. Therefore, the present of P in the SLS process may enhance sintering by improving the wettability of Cu-Ni system through reducing surface tension of liquid copper. Since the free energy of formation of P oxide is much smaller (more negative) than that of Cu and Ni, P may also act as a localized oxygen 'getter' and partially prevent the oxidations of Cu and Ni, thus enhance sintering. In-situ Auger fracture analysis of the fracture surface of SLS sintered 60 wt% Bronze-30 wt% Ni -Cu3P sample revealed strong oxidation and high P content in the oxide (Figure 10), though no wetting problems occurred during the sintering process. The carbon peak originates from the carbon on the free surface of the pores. This analysis supports the idea that P is a localized oxygen 'getter'. Systematic investigations into the effects of P and other wetting additions on the sintering behavior of Cu-Ni system in an oxygen clean environment are highly desirable.

3.3 Sintering atmosphere effects in SLS

The sintering atmosphere is one significant factor affecting selective laser sintering, especially high temperature SLS. The atmosphere protects against surface contamination during sintering. Additionally, a cleaning function is desired from the atmosphere to remove films (for example oxides) for rapid melt flow. The atmosphere plays an important role in reducing surface films which can alter the wetting angles. In conventional liquid phase sintering, best densification and properties can be achieved using vacuum sintering in many systems [5]. Residual atmosphere can be trapped in pores which seal during liquid flow. Such trapped atmosphere inhibits full densification. Sintering in an inert or insoluble atmosphere is most detrimental for this reason. The present SLS system uses an inert gas purging system to reduce the surface layer contamination. This section will address some problems associated with such an approach.

Residual gas analysis (RGA) was performed to analyze the gas in the working chamber. With 60 l /min nitrogen purging, which is the setting for all tests discussed in the paper, the N_2 to O_2 partial pressure ratio 5000:1 was measured. SLS of stainless steel 304L powder was unsuccessful using such an environment due to the oxidation problem.

SLS of WC-Co-Ni system produced strong parts with rough surfaces (Figure 11). Wetting angle of WC by both liquid Co in hydrogen and liquid Ni in vacuum at 1500°C is 0 [7]. However, the oxidation of Co and Ni causes poor wetting and thus balling. Auger surface analysis of sintered 70 wt.% (WC-12Co)-20 wt.% Co- Ni showed oxygen in the sample, as seen in Figure 12. For a sintered layer, balling occurs on the top of the layer, and the bottom of the layer shows good wetting. Optical studies of the bottom of the layers revealed expected composite microstructure (Figure 13a), and WC wets well by metal matrix Co and Ni. The

study implies that the oxidation of Co and Ni occurs only on the liquid surface during the SLS process. Figure 13b shows the fracture surface of the sintered WC-Co-Ni sample, where voids with liquid pools are obvious. These voids may be introduced by N2 gas trapped in liquid during liquid flow in SLS processing.
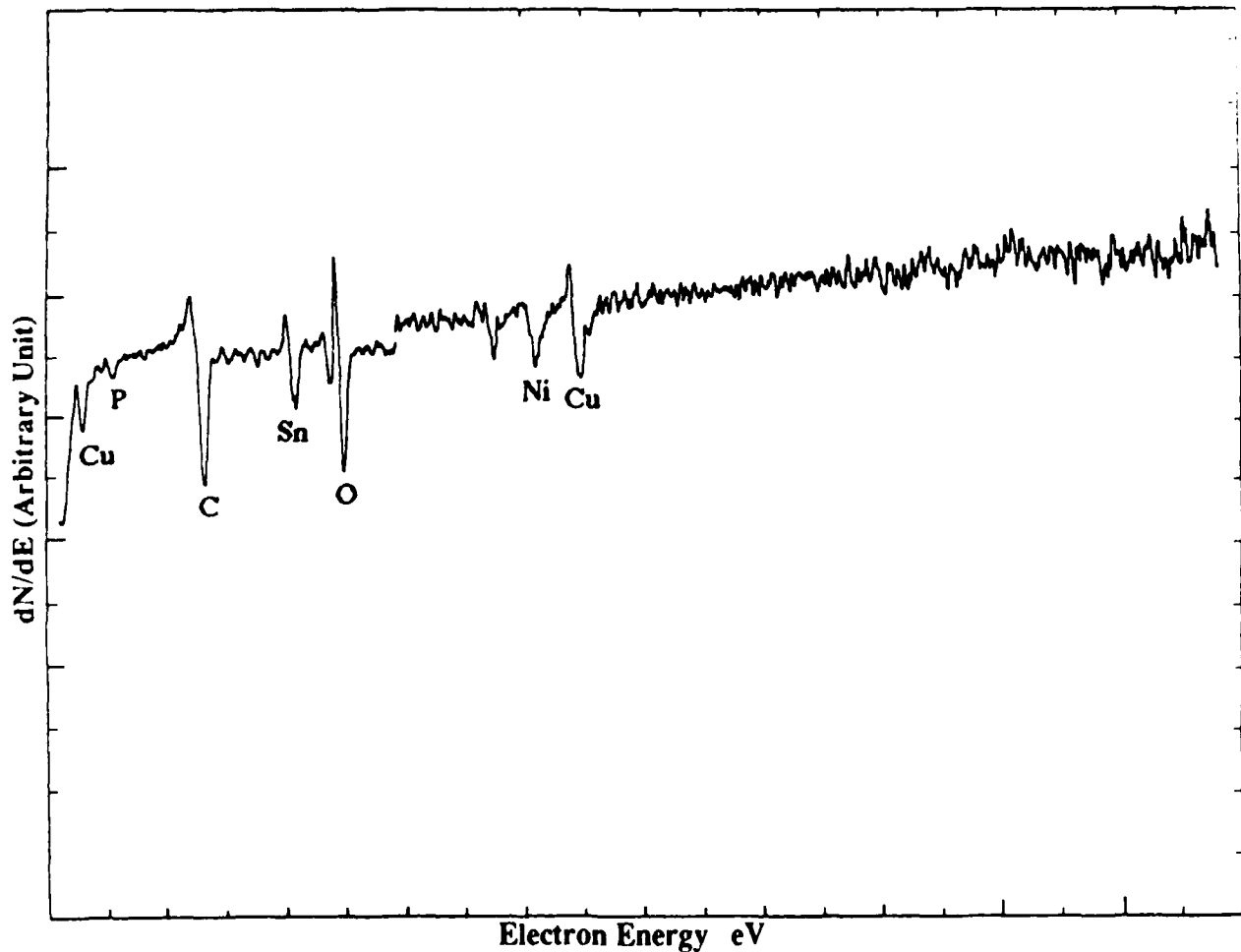
Figure 10 AES analysis of the in-situ fracture surface of the SLS sintered 60 wt% Bronze-30 wt% Ni -Cu3P.

4. Summary

Direct Selective Laser Sintering of high temperature powder mixtures has been demonstrated. Initial results indicate that SLS involving a coexisting liquid and particulate solid during the sintering can be used to produce freeform parts directly with high temperature materials. Many factors including scanning laser power density, residence time, scan line spacing, powder bed bias temperature, atmosphere, interfacial energies between the liquid and solid phases, and roles of additives are discussed in terms of the microstructure evolution.

These parameters and other factors such as solid phase solubility in the liquid, relative penetration of the liquid, particle size and distribution, powder leveling thickness and density are still to be studied.
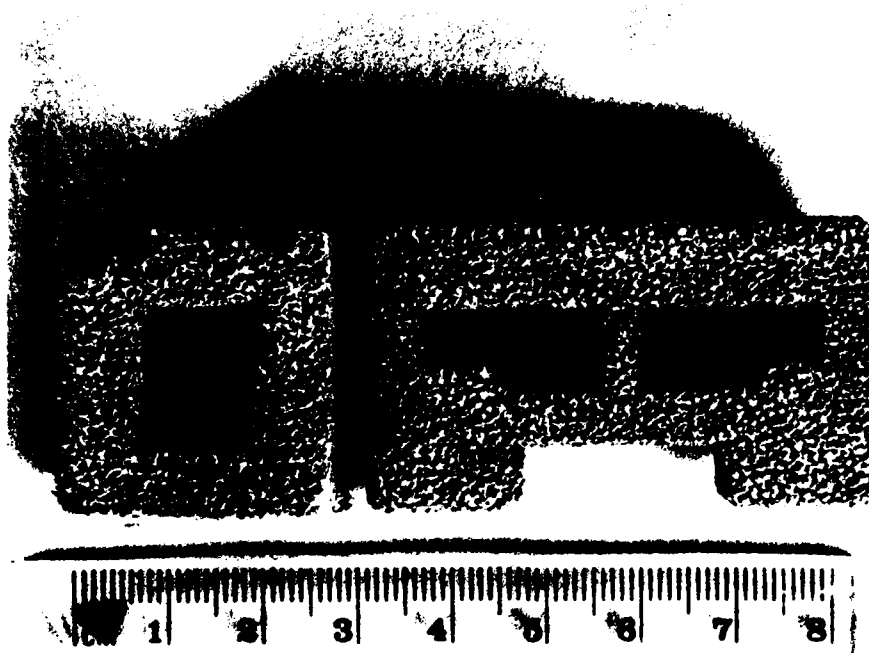
Figure 11   SLS fabricated WC-Co-Ni parts.
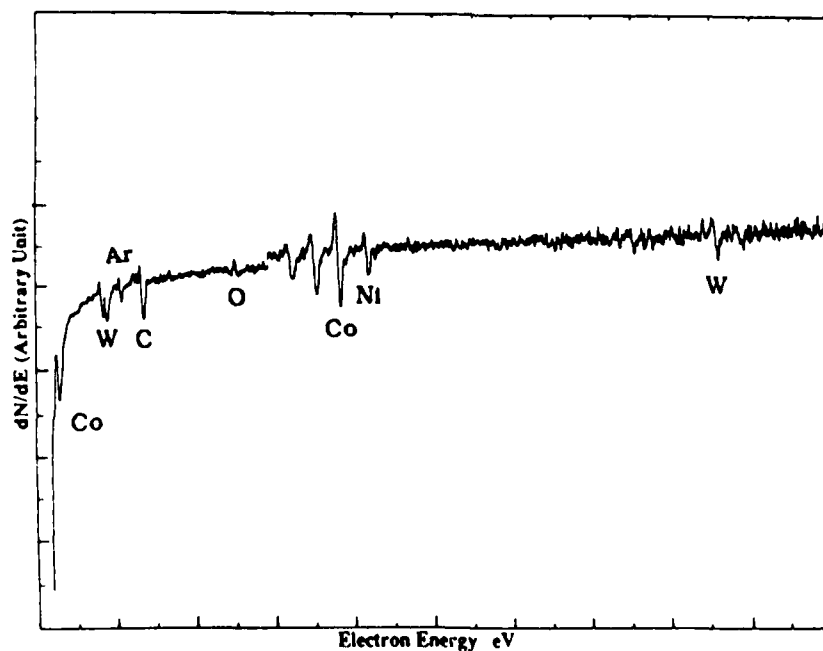
Figure 12   AES analysis of the (WC-12 wt.% Co)-20 wt.% Co-10 wt.% Ni sample, sputtering time = 6min.
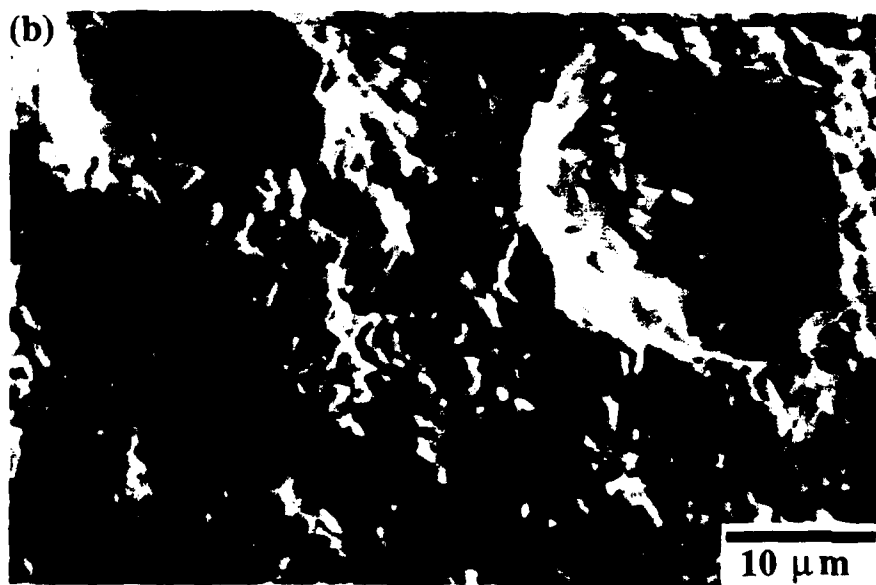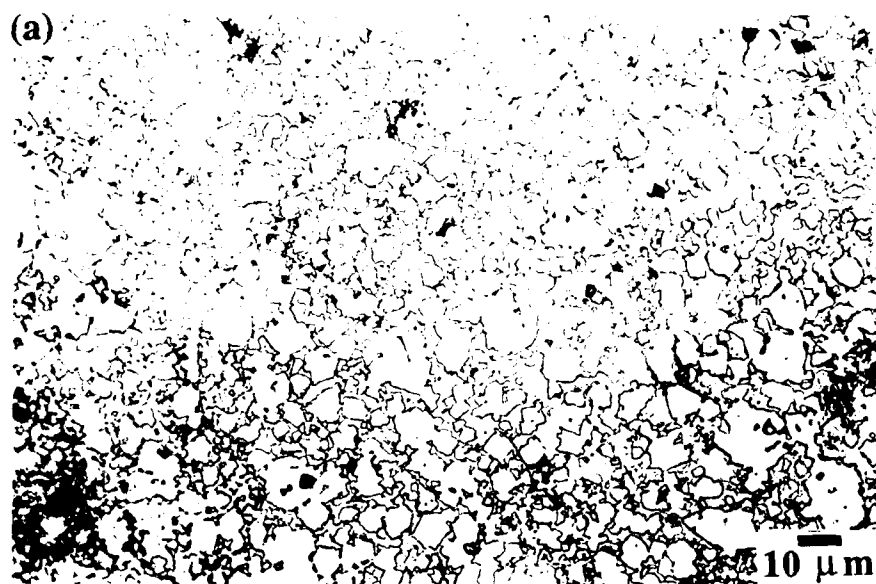
Figure 13 (a) Optical and (b) SEM micrographs of SLS sintered (WC-12 wt.% Co)-20 wt.% Co-10 wt.% Ni sample.

Acknowledgement

References

1. <u>1990 Solid Freeform Fabrication Symposium Proceedings</u>, Edited by J.J. Beaman, H.L. Marcus, D.L. Bourell, J.W. Barlow, 1990, The University of Texas at Austin, Austin, Texas.
2. <u>1991 Solid Freeform Fabrication Symposium Proceedings</u>, Edited by H.L. Marcus, J.J. Beaman, J.W. Barlow, D.L. Bourell, R.H. Crawford, 1991, The University of Texas at Austin, Austin, Texas.
3. H. L. Marcus, J. J. Beaman, J. W. Barlow, and D. L. Bourell, "Solid Freeform Fabrication: Powder Processing," *Ceramic Bulletin*, 69(6), 1990, 1030-31.
4. D. L. Bourell, H. L. Marcus, J. W. Barlow, and J. J. Beaman, "Selective Laser Sintering of Metals and Ceramics," to be published in the October 1992 issue of the *International Journal of Powder Metallurgy*.
5. Randall M. German, <u>Liquid Phase Sintering</u> (New York, NY: Plenum Press, 1985), 127-151.
6. "Binary Alloy Phase Diagrams," second edition, ASM International, 1990 Vol. 2, T. B. Massalski, editor-in-chief.
7. G. S. Upadhyaya, "Wetting of Ceramics by Melts - An Electronic Approach," <u>Sintered Metal-Ceramic Composites</u>, edited by G. S.. Upadhyaya, Elsevier Science Publishers B.V., Amsterdam 1984, p. 41.

Automatic CAD-model Repair: Shell-Closure

Jan Helge Bøhn and Michael J. Wozny

Rensselaer Design Research Center
Rensselaer Polytechnic Institute
Troy, New York 12180–3590
(518) 276–6751
bohn@rdrc.rpi.edu

Abstract

Shell-closure is critical to the repair of CAD-models described in the .STL file-format, the *de facto* solid freeform fabrication industry-standard. Polyhedral CAD-models that do not exhibit shell-closure, i.e. have cracks, holes, or gaps, do not constitute valid solids and frequently cause problems during fabrication. This paper describes a solution for achieving shell-closure of polyhedral CAD-models. The solution accommodates non-manifold conditions, and guarantees orientable shells. There are several topologically ambiguous situations that might arise during the shell-closure process, and the solution applies intuitively pleasing heuristics in these cases.

1 Introduction

It is critical that the CAD-models used in solid freeform fabrication (SFF) are robust to avoid failure during manufacturing. Unfortunately, CAD-models described in the .STL file-format [1], the *de facto* industry standard, frequently lack this robustness [2, 3, 4]. Typical problems include punctured shells, inconsistent facet-orientations, and internal walls and structures.

With the .STL file-format, the CAD-model solid is defined by its surface, i.e. the solid is defined by a closed shell enclosing its material. If this shell is punctured (i.e. open), then it can no longer properly contain the material, and this consequently causes the failures commonly associated with cracks, gaps, and holes (Figure 1.1). Similar problems arise when the facet-orientations across a shell are inconsistent. This too causes uncertainty regarding what side of the shell contains material. Finally, structural problems might arise from internal walls and structures within the solid. These internal features can create irregularities in the solidified material during the processing. For instance, with stereolithography [5] and selective laser sintering (SLS) [6], excess amounts of unsolidified material might get trapped inside the solidified matrix, and consequently result in uncontrolled shrinkage and surface warping (Figure 1.2).

The .STL file-format is capable of representing a robust, well-formed solid. Unfortunately, contemporary CAD-systems frequently fail to achieve this goal. There are two
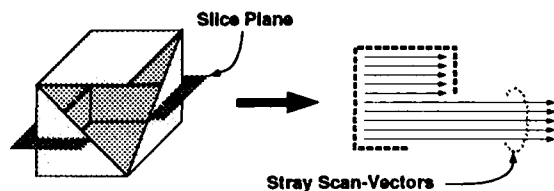
Figure 1.1 Shell-punctures causes the laser to produce stray scan-vectors.
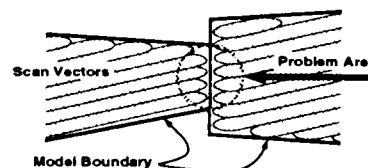
Figure 1.2 Internal walls cause structural discontinuities that can lead to excessive shrinkage.

design environments currently available for CAD; solid- and surface-modelers. Solid-modelers generally avoid punctured shells, but frequently generate needless internal walls and structures, and inconsistent orientations. In addition to these problems, surface-modelers frequently fail to properly mate adjacent surfaces; this results in punctured shells.

These problems are commonly resolved by the SFF-equipment operators prior to fabrication. The operator might attempt to edit the .STL file directly, or, if available, edit the original CAD-model to eliminate the problems. However, manual model repair becomes excessively expensive when the number of facets reaches 10,000 to 100,000+, and the number of errors run into the hundreds. This has lead to the development of automatic CAD-model repair.

Brock Rooney & Associates [7] perform limited CAD-model repair in their .STL translators, ensuring that their .STL output does not contain punctured shells. Their proprietary shell-closure solution is not complete. It does not handle orientability-problems satisfactorily, and it has limited success with certain simple structures. However, they report few problems in general with their .STL output when run on the software-robust stereolithography process of 3D Systems, Inc. In the rare cases where their shell-closure algorithms fails, the CAD-model must either be regenerated at the design-level, or be repaired manually as described above.

3D Systems, Inc. [8] provides its customers with a limited, proprietary model-repair facility. It too is intended to ensure that the model does not fail during fabrication, or if the repair fails, to provide indications to where it must be repaired manually. The program attempts to repair simple orientation problems, minor punctures, and facet-intersections, but leaves internal walls, and fails for large punctures and non-orientable shells. It performs the repair under the restriction of several user-specified parameters, and if these are set too conservatively, an intermediate result is generated. This output can be processed iteratively until a valid, though not necessarily correct result occurs.

The basic problem of CAD-model repair is that of inferring information that has been lost somewhere in the design process. While it might be easy in some cases to detect the presence of a problem, it is frequently impossible to determine with certainty what the correct solution is. This is especially true if the designer's intent is lost. Without it, an educated guess must be made whenever an ambiguity is encountered. The goal of our work is to match the quality of manual repair that is performed without the knowledge of the designer's intent.
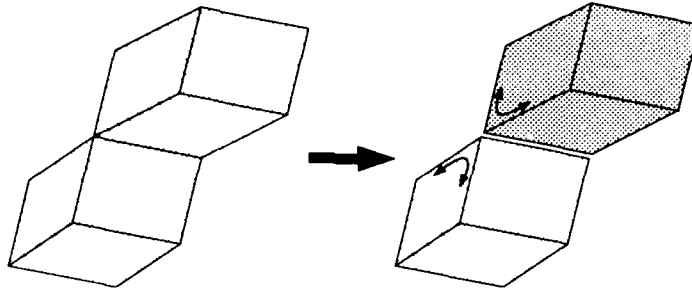
2 Shell-Closure

This paper presents a complete solution for shell-closure of polyhedral shells. In doing so, it also solves the orientability problems, and it simplifies the complexity of the model-topology for more efficient processing during fabrication. In particular, it ensures a pseudo two-manifold topological organization of the facets to facilitate high-speed slicing [4, 9]. This topological organization also simplifies the subsequent resolution of shell-intersection and shell-nesting problems, which are necessary for the removal of needless internal walls.

A (two-) manifold structure is homeomorphic to a two-dimensional disk at every point across its surface, i.e., each such point has a neighborhood that is topologically equivalent to a two-dimensional disk. A non-manifold structure violates this constraint; two cubes that touch along a common edge is one such example. However, if the facets at a non-manifold location are paired up properly, then this situation can be described as a set of (pseudo) two-manifold conditions [10] (Figure 2.1).

Our solution for shell-closure follows a three-stage strategy: First, we identify the lamina edges. Second, we combined these edges into closed, non-self-intersecting loops of boundary-curves; commonly known as directed Jordan curves. And finally, we create lids that fit these Jordan curves and that close the open shells.

3 Lamina Edges

A lamina edge is generally considered a special case of a non-manifold edge; it has only a single adjacent face [11]. Lamina edges are of interest because they make up the boundaries of the shell-punctures, and of the corresponding lids which we will create to close the shells. However, if the definition of a lamina edge is generalized, in particular generalizing the definition of a puncture, then we can expand the use of creating lids for shell-closure to also solve erroneous facet-orientations and complicated non-manifold conditions.

Expanded definition: A lamina edge exists along each face-edge that does not mate and pair properly this particular face with any other face along this edge. These lamina edges can be found as follows: Let all face-edges be candidates for lamina edges. Then, for each face-edge, attempt to find an adjacent face of compatible orientation such that

Surface Normal

a b

LEC = { a, b, ... }   **LEC = { ... }**
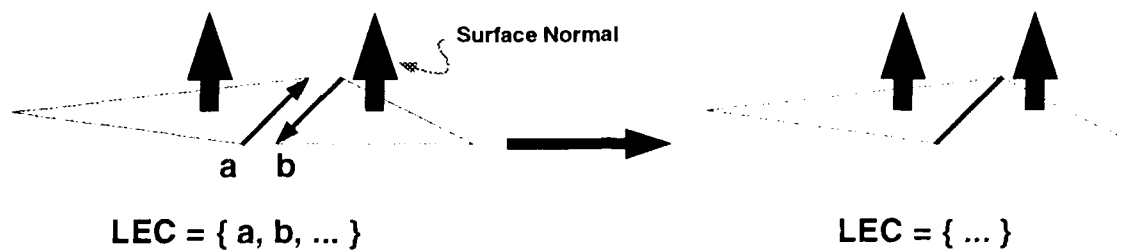
Figure 3.1 Two lamina edge candidates (a,b) are removed from the set of candidates (LEC) after a successful pairing of two faces about a common edge.

2D cut
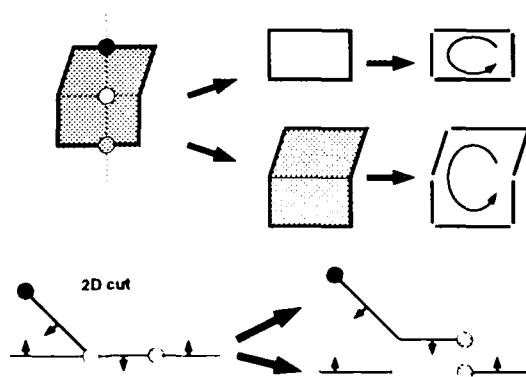
Figure 3.2 The orientability problem is solved by creating two sets of (partially) coincident lamina edges
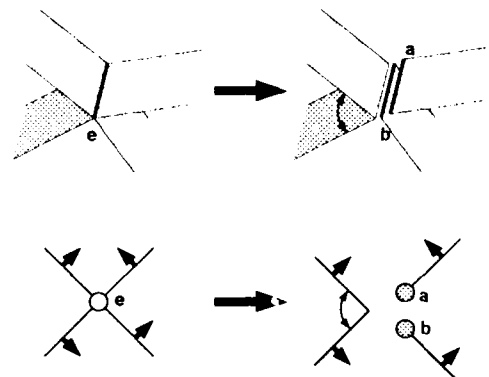
Figure 3.3 Two unpaired facets along a non-manifold edge yield two coincident lamina edges.

these two faces can be paired off and identified as adjacent about the common edge. Whenever this happens, the two coincident face-edges are removed from the set of lamina edge candidates (Figure 3.1). The face-edges that remain after this process is exhausted, are the lamina edges we seek.

The expended definition of lamina edges allows for the possibility of multiple, coinciding lamina edges along a single physical edge; this simply represents multiple shell-puncture boundaries partially or fully coinciding along this particular edge. In particular, Figures 3.2 and 3.3 illustrate the effect of this definition on areas with orientation and non-manifold problems. Note how allowing multiple coinciding lamina edges ensures that the boundary of a shell-puncture always forms a closed, directed non-self-intersecting loop, or more explicitly, a directed Jordan curve. These Jordan curves are essential for the subsequent lid-creation and shell-closure.

4 Directed Jordan Curves

The first step towards extracting directed Jordan curves from the set of lamina edge is to link the lamina edges into a set of non-intersecting boundary curve segments more precisely, arcs. Each arc is directional, is adjacent to a single shell, and is t
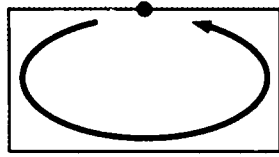
Figure 4.1 Simple, self-connecting loop (unambiguous).
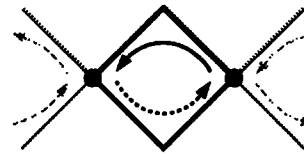
Figure 4.2 Linear combination (unambiguous).
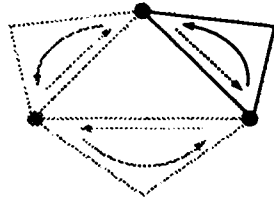
Figure 4.3 Cyclic with single direct returns.
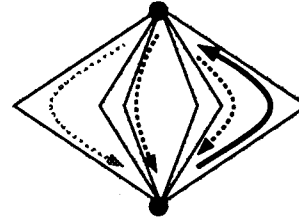
Figure 4.4 Cyclic with multiple direct returns.
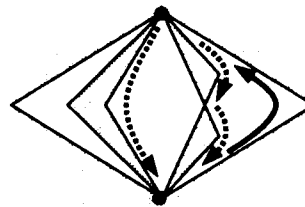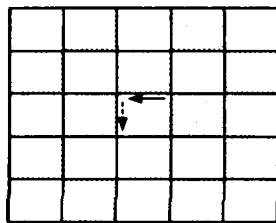
Figure 4.5 Trivial and nontrivial cases of cyclic with non-direct returns.

by two endpoints that might coincide. This can be achieved as follows: Initially, consider each lamina edge as an arc. Then, iteratively, for each vertex with only two adjacent arcs, merge those two arcs into a single arc, causing this vertex to no longer have an adjacent arc. The final set of arcs form a set of directed graphs (as defined in graph theory [12]) of various complexities that describe the shell-puncture boundaries, and these puncture-boundaries must be separated prior to lid-creation.

We have identified five classes of puncture-boundaries of increasing identification-complexity, which when combined, form the above mentioned sets of directed graphs. Among these classes, three occur in our industrial .STL test-suite, while the remaining two, the most complex classes, persist as unobserved possibilities: The most trivial class of all is the *simple* combination; a single self-connecting arc. It is unambiguous and trivial to detect, and it forms a complete puncture-boundary by itself (Figure 4.1).

The *linear* combination is also unambiguous; two arcs that are adjacent to the same shell and that form a closed loop. These arcs form a link between two separate subgraphs, each of which is less complex that their combination (Figure 4.2).

The remaining three classes are ambiguous because they offer multiple closed-loop alternatives, and because the Jordan curves are located in three-dimensional space rather than in a simplifying two-dimensional plane. Fortunately, one can make some reasonable,

basic assumptions that limit the number of loop-completion alternatives: For instance, we assume that, whenever it is an option, we should merge separate shells. This is based on the observation that the .STL file-format separates solids; consequently, all facets within a definition for a single solid should form a single shell. This dictates that, for the following three classes, two consecutive arcs may not be adjacent to the same shell prior to merging.

The class *cyclic with single direct return* is characterized by the formation of cyclic patterns by its punctures, and by the existence of a single returning arc for each of its arcs, once the option of connecting arcs along the same shell has been eliminated as described above (Figure 4.3). We have found this class to be rare, but present, in our industrial .STL test-suite.

The remaining two classes are theoretically feasible, though we have not yet encountered them: *Cyclic with multiple direct returns* is an inherently ambiguous problem (Figure 4.4); even after the elimination of one returning arc, multiple options remain. It must consequently be solved with additional heuristics, utilizing not only topological-, but also geometrical information. We choose to view it as a matching problem where the goal is to minimize the sum of the angles formed by the end-tangents of the connecting arcs. This heuristic finds the optimal choice in the planar case, and it has a graceful degradation as the situation becomes less planar and consequently more ambiguous. Furthermore, this problem can be solved as a *perfect matching with minimum weight* problem in $O(n!)$ time; specifically, in the case of two, three, and four arc-pairs, we end up with one, two, and six matching-combinations respectively: Relating back to the example in Figure 4.4, we observe the presence of six arcs (two upward arcs are not shown), yielding three arc-pairs. Once an arc is selected (solid black upward arc), the above shell-merger assumption eliminates one of the returning arcs (dotted gray downward arc) as an acceptable loop-forming match, leaving the other two returning arcs as possible matches to contend with. The selection of either returning arc will cause the merger of two shells, thus simplifying the remaining problem to the point where further loop-extraction is unambiguous. As a consequence, the overall problem has two possible combinations.

Finally, there is the class of *cyclic with non-direct returns*; these are combinations that require a sequence of more than two arcs to form a closed loop (Figure 4.5). Some of these cases can be solved trivially by incrementally merging arcs into longer parts, but one can also easily imagine cases that are more complex and ambiguous. One possible solution in the later case, is to project the arcs onto a suitable two-manifold structure, e.g. a plane, and resolve the matching-problem there.

More effort could clearly be invested in the loop-extraction from the more complex arc-combinations, but based on our industrial .STL test-suite, these problems appear to be few and far between. Instead, the central theme of our strategy is to identify the less complicated structures first, and extract their arcs from the original graph. This simplifies the remaining graph and will in general reveal additional unambiguous constructions. As a result, one can solve most complex graphs by solving trivial sub-problems.

91
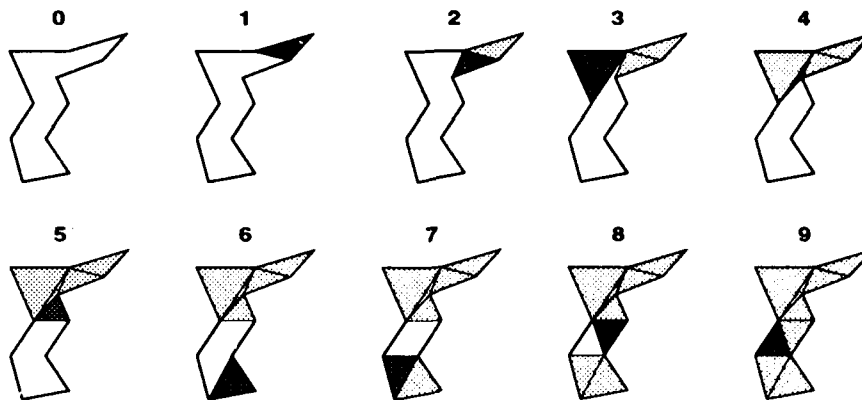
Figure 5.1 Lid-creation by iterative removal of the vertex with the smallest angle.
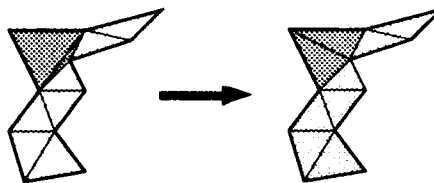
Figure 5.2 Iterative post-processing to improve the quality of the lid-surface.

5 Creating Lids

The task of creating lids is greatly simplified once the corresponding directed Jordan curves have been identified: The puncture is closed by an iterative algorithm that decrements the Jordan curve by eliminating one vertex at a time; the vertex is eliminated from further consideration by adding a facet that spans it and its two neighboring vertices along the shrinking Jordan curve. At each iteration, we remove the vertex along the Jordan curve that spans the smallest angle with its two neighboring vertices along the remaining, decremented Jordan curve (Figure 5.1). This avoids the clearly undesirable splitting of angles, and it will in general produce excellent results, especially for long narrow punctures which abound in industrial .STL files [7, 8].

However, this heuristic algorithm is not without drawbacks. It is a time-local algorithm in that it finds the best selection at any given time, without keeping the overall optimal solution in mind. An example of this is the selection of the third facet in Figure 5.1; it forces the subsequent undesirable creation of facet number four. Fortunately, such problems are easily rectified with a simple, inexpensive iterative post-processing step as illustrated in Figure 5.2: For each adjacent pair of lid-facets, flip their common diagonal edge if this increases their minimum facet-angle.

A more serious problem is the difficulty of finding the angles spanned about the vertices. While angles between vectors in 3D-space are in the range 0–180 degrees, it is clear, from the 2D-plane, that the angles between facet-edges are in the range 0–360 degrees. It turns out, however, that a conservative decision to assign the range 180–360 degrees to a vertex whenever there is a doubt to which half of the total range it belongs to, simply postpones its elimination. Eventually, one of the vertex's neighboring vertices

92
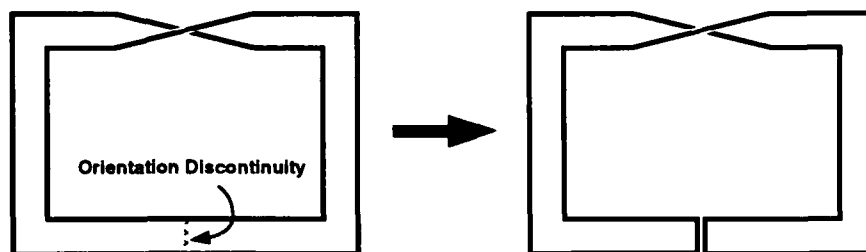
Figure 5.3 Cutting a non-orientable Möbius-strip along its orientation-discontinuity, results in a orientable panel.

will be eliminated, and its angles must be recomputed. Usually, this clarifies the situation, and the vertex might be assigned the range 0–180 degrees instead.

It is interesting to note that the above lid-creation algorithm is capable of creating a non-orientable shell if the open shell is non-orientable. An example of this would be the closure of a Möbius-strip. However, with our definition of lamina edges, non-orientable shells are cut such that they become orientable prior to lid-creation. In particular, the Möbius-strip becomes a simple panel (Figure 5.3). As a consequence, since the lid-creation algorithm maintains the directionality of the diminishing Jordan curves, we are guaranteed to maintain orientability throughout the shell-closure; and more importantly, the final closed shells are therefore always orientable.

6 Conclusions

This paper has presented a complete solution for shell-closure of polyhedral shells, the first step towards well-formed and manufacturable solids. The solution is based on topological principals, and consequently resolves orientability and non-manifold problems in addition to eliminating shell-punctures (i.e. cracks, holes, and gaps). As a result, the facet-model output consists entirely of closed, orientable shells, and the resulting facet-models can therefore be viewed as a set of two-manifold shells.

This topological organization simplifies the subsequent resolution of shell-intersection and shell-nesting problems, and it is a prerequisite for the detection and removal of zero-volume parts and other needless internal walls that create structural discontinuities in the fabricated parts.

7 Acknowledgments

References

[1] "Stereolithography Interface Specification," 3D Systems, Inc., June 1988.

[2] S. J. Rock and M. J. Wozny, "A Flexible File Format for Solid Freeform Fabrication," in: *Solid Freeform Fabrication Symposium Proceedings*, H. L. Marcus, J. J. Beaman, J. W. Barlow, D. L. Bourell, and R. H. Crawford (eds.), The University of Texas at Austin (Austin, TX), August 12-14 1991, pp. 1–12.

[3] J. Arline, "A user survey of problems with rapid prototyping systems," *Prototyping Report*, vol. 1, no. 6, November 1991, pp. 7–8.

[4] S. J. Rock, "Solid Freeform Fabrication and CAD System Interfacing," Master's thesis, Rensselaer Polytechnic Institute, Troy, NY, December 1991.

[5] R. A. Schubert, "StereoLithography," in: *NCGA '89 Conference Proceedings*, vol. 2, (Philadelphia, PA), April 17-20, 1989, pp. 182–186.

[6] C. R. Deckard, *Selective Laser Sintering (CAD/CAM)*. Ph.D. thesis, The University of Texas at Austin, 1989.

[7] B. Rooney. Private communication, Brock Rooney & Associates, Birmingham, MI, May 27, 1992.

[8] C. Alexander. Private communication, 3D Systems, Inc., Valencia, CA, May 29, 1992.

[9] S. J. Rock and M. J. Wozny, "Utilizing Topological Information to Increase Scan Vector Generation Efficiency," in: *Solid Freeform Fabrication Symposium Proceedings*, H. L. Marcus, J. J. Beaman, J. W. Barlow, D. L. Bourell, and R. H. Crawford (eds.), The University of Texas at Austin (Austin, TX), August 12-14 1991, pp. 28–36.

[10] M. Mäntylä, "Boolean Operations of 2-Manifolds through Vertex Neighborhood Classification," *ACM Transactions on Graphics*, vol. 5, no. 1, January 1986, pp. 1–29.

[11] K. J. Weiler, *Topological Structures for Geometric Modeling*. Ph.D. thesis, Rensselaer Polytechnic Institute, Troy, NY, August 1986. (RDRC-TR 86032).

[12] F. S. Roberts, *Applied Combinatorics*. Prentice-Hall, 1984.

A Method to Generate Exact Contour Files for Solid Freeform Fabrication

Sashidhar Guduri, Graduate Research Assistant
Richard H. Crawford, Assistant Professor
Joseph J. Beaman, Professor
Dept. of Mechanical Engineering
University of Texas at Austin

Abstract

Existing methods to create contour files generate a polygonal approximation of the contours instead of an exact representation. This paper presents a method to generate exact contours from Constructive Solid Geometry (CSG) representations. The method preserves the accuracy of the contour files provided the primitives used to generate the CSG tree are polygonal or quadric objects. Due to the inclusion of quadric objects into the primitive set an additional effort to solve for the intersection points between two quadric curves is required. The paper also presents a method to convert piecewise quadratic contours to toggle point files for raster scanning solid freeform fabrication processes.

Introduction

Computer software plays a major role in Solid Freeform Fabrication (SFF) techniques. The main aim of the computer software is to generate contour files at different cross sections of a given part geometry. These contour files can be rasterized to generate laser toggle point files.

Present methods for generating contour files use faceted representations of the part geometry. The contour files generated by these methods are polygonal approximations of the actual contours. This paper presents a method to generate exact contours, instead of polygonal approximations, by using a higher order geometric description of the part.

Description of the Method

Part Geometry Representation

The form of the geometric description of mechanical parts to be produced by SFF significantly affects the accuracy of the final part. The current state-of-the-art for most SFF technologies, consists of tessellating the surfaces of the geometric model into a mesh of non-overlapping triangular facets. The resulting geometry is transmitted in a standard file format, the so-called STL file format, established by 3D Systems, Inc. [1]. This format has been adopted by many CAD vendors, is readily available, and is considered adequate for most visualization applications. However, for producing accurate patterns and functional parts, the adequacy of the STL format is unclear [3]. There is a trade-off between the accuracy and the size of the geometric description. Highly non-linear surfaces, such as those found on turbine blades, manifolds, etc., must be tessellated into a large number of small facets, resulting in very large data files, and the accuracy of such descriptions is still suspect. For this reason richer geometric descriptions must be introduced to the SFF community.

Research at The University of Texas is aimed at using higher order geometric descriptions as input to the Selective Laser Sintering (SLS) process. Higher order geometric descriptions will increase the accuracy while reducing the file size. The research reported herein focuses on processing Constructive Solid Geometry (CSG), which represents the part geometry a binary tree whose leaf nodes are primitive solids (e.g. spheres, cylinders, cones etc.) and whose non-terminal nodes are the Boolean set operations union ($\cup$), intersection ($\cap$), and difference (–). In this work, processing for SFF proceeds in two stages: (1) slicing the input geometry to obtain the part's boundary curves in each scanning plane and (2) scan converting each contour to produce laser toggle points for raster scanning the part. Each of these stages is described below.

Slicing

The SLS process produces parts on a layer-by-layer basis. The part geometry is sliced by sintering planes (planes perpendicular to z axis) at regular intervals, typically 0.005-0.01 inches apart. Slicing the part geometry, represented by a CSG tree, at different cross sections involves slicing the primitives individually, and generating a slice for each primitive. The slice of a primitive is a collection of curves of degree two or less. Figure 1 shows the slices obtained by slicing a sphere and a cylinder having different orientations.

circle   rectangle   ellipse
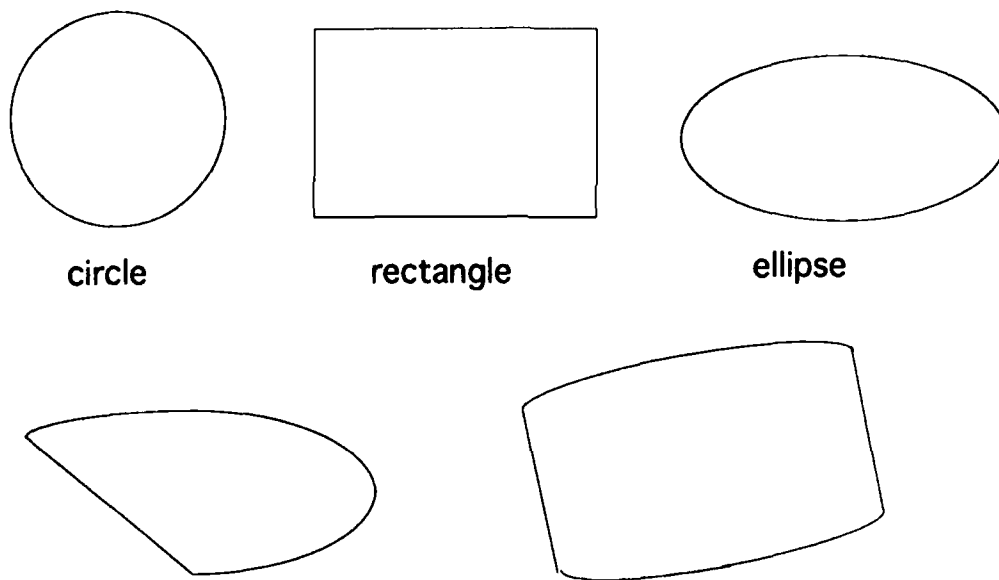
Figure 1. Slices obtained by slicing a sphere and a cylinder

Boolean operations

Once the slices for all the primitives are obtained, Boolean set operations are performed on them to generate the contour for that cross section. The process of applying the Boolean operations to simplify the binary tree is recursive. First, at the bottom level of the binary tree, the slices are generated by intersecting the current sintering plane with the primitives at the leaf nodes, producing contours for the primitives. Then the next higher level contours are generated by applying Boolean operations to the first level contours. This process is repeated recursively level by level to generate the final contour

96

for the current cross section. The process of applying a given Boolean operation to two given contours requires the calculation of the intersection points of the contours. An outline of the method to calculate the intersection points is given in Appendix A. After the calculation of all the intersection points, each contour is decomposed into curve segments whose end points are the intersection points. The curve segments of one contour are then classified with respect to the other contour, and vice-versa. The process of classification is described in the next section.

Classification

After the calculation of 'he intersection points, the curve segments must be grouped appropriately according to the Boolean operation (union, intersection or subtraction). This is done by classifying each curve segment on one contour with respect to the other contour. Classification is the process of determining if a particular curve segment is inside or outside the other slice. A ray casting algorithm is used for this classification [4]. According to this algorithm a point chosen on the curve segment is as the base point and an in-plane ray is generated. If the number of intersections of the ray with the other contour is even, then the point is outside the contour; otherwise, the point is inside. The special cases of tangency and vertex intersections are taken care by the software. After classification, the curve segments that form the new contour boundary are identified, based on the particular Boolean operation:

Operation ∪: Curve segments of both the contours that are classified as out.
Operation ∩: Curve segments of both the contours that are classified as in.
Operation –: Curve segments that are classified as out for the first contour and in for the second contour.

Figure 2 illustrates the steps in the classification and set operation application.

Toggle Point Generation

The process of toggle point generation for each layer is similar to rasterization in computer graphics image generation. The process generates discrete points on the contours at which the energy beam must be toggled on or off. The process consists of intersecting mathematical rays directed along each scan line in the contour plane with each curve segment of the contour and requires solving a second degree equation in one unknown. These intersections are then ordered in increasing order of the scan line coordinate direction. S 'al cases such as vertex intersection and ray tangency with the curve are taken care by . software. The output of the process is a binary file of toggle points.

Conclusions

Software for processing geometric data is an important factor in the development of Solid Freeform Fabrication techniques. This paper describes a method to generate exact contour files from CSG geometry for the SLS process. Future work focuses on expanding the variety of sources for geometric data, including development of a contour generation algorithm for rational bicubic parametric surfaces.

sphere1 : center at (0, 0, 0) and unit radius
sphere2 : center at (1, 0, 0) and unit radius
sphere3 : center at (0, 1, 0) and unit radius
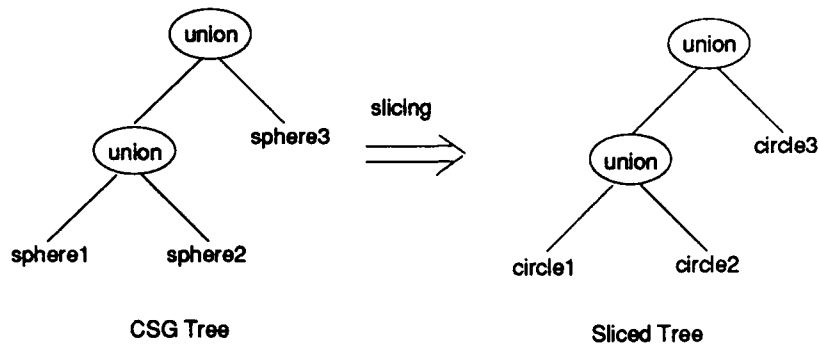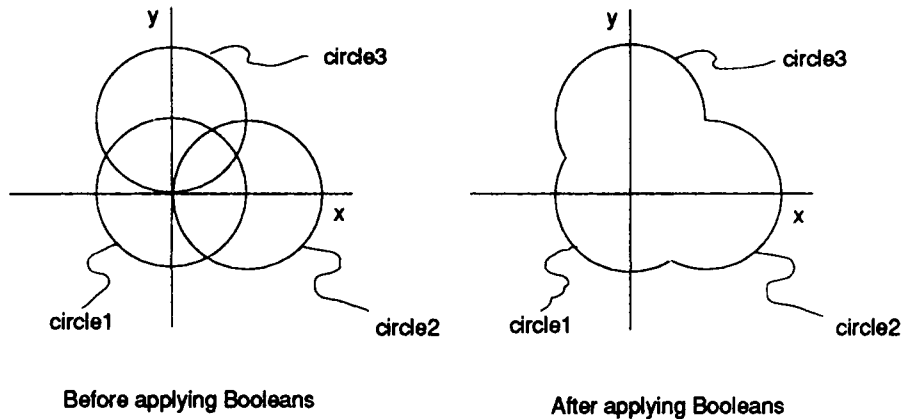
Figure 2. Contour classification and set operations.

Appendix A

Equation of a quadric curve in a plane can be written as

$$I(x,y) = ax^2 + by^2 + cxy + dx + ey + f = 0 \qquad \text{(eq. 1)}$$

Parametrization

The non-trivial case of parametrizing equation 1 is when a and b are non-zero. Otherwise the equation is already linear in one variable and expressible as a rational polynomial expression of the other, and hence a rational parametrization. To obtain the rational parametrization one has to make equation 1 non-regular in x or y. That is, eliminate the quadratic term in either x or y through coordinate transformation. Then one variable is linear and expressible as a rational polynomial expression of the other. The steps shown below describe an algorithm to eliminate the y^2 term.

98

(1) If equation 1 has a real root at infinity, a linear transformation of the type

$$x = a_1 x + b_1 y + c_1 \text{ and } y = a_2 x + b_2 y + c_2$$

will suffice. If equation 1 has no real root at infinity, one must use a fractional linear transformation of the type

$$x = (a_1 x + b_1 y + c_1) / (a_3 x + b_3 y + c_3) \text{ and}$$

$$y = (a_2 x + b_2 y + c_2) / (a_3 x + b_3 y + c_3)$$

(2) Points at infinity for equation 1 correspond to linear factors of the degree form (highest degree terms) of equation 1. For a quadric curve this corresponds to a real root at infinity if $c^2 > 4ab$. Otherwise both roots at infinity are complex. Furthermore, $c^2 = 4ab$ corresponds to a polynomial parametrization for the quadric curve, as the degree form is a perfect square.

(3) Applying a linear transformation for $c^2 \geq 4ab$ gives rise to

$$I(x,y) = I(a_1 x + b_1 y + c_1, a_2 x + b_2 y + c_2).$$

To eliminate the y^2 term, choose b_1 and b_2 such that

$$ab_1^2 + cb_1 b_2 + bb_2^2 = 0.$$

Here both the values of b_1 and b_2 can always be chosen to be real.

(4) After applying a homogeneous linear transformation for $c^2 < 4ab$, to eliminate the y^2 term, choose b_1, b_2 and b_3 such that they satisfy the homogeneous conic:

$$ab_1^2 + bb_2^2 + cb_1 b_2 + db_1 b_3 + eb_2 b_3 + fb_3^2 = 0.$$

The values of b_1 and b_2 are both real if $(cd - 2ae)$ is not less than the geometric mean of $4af - d^2$ and $4ab - c^2$.

(5) Finally, choose the remaining coefficients a_is and c_is, ensuring that the appropriate transformation is well defined.

The equations for two quadric curves are of the form

$$a_1 x^2 + b_1 y^2 + c_1 xy + d_1 x + e_1 y + f_1 = 0$$

$$a_2 x^2 + b_2 y^2 + c_2 xy + d_2 x + e_2 y + f_2 = 0$$

One of these equations can be parametrized using the method given above. For a detailed method refer to [2]. The parametric equations of x and y can be substituted in the second equation to give a polynomial of fourth degree in a single variable. The real roots of the polynomial can be obtained using the method described below.

Solutions of a fourth degree polynomial in one variable
A fourth degree polynomial can be written in the form

$$c_4 x^4 + c_3 x^3 + c_2 x^2 + c_1 x + c_0 = 0$$

When $c_4 = c_3 = 0$, the equation can be solved using the familiar quadratic formula. For the case when $c_4 = 0$, the equation reduces to a cubic that can be solved as follows:

(1) Divide the equation by c_3 to get the normal form

$$x^3 + Ax^2 + Bx + C = 0$$

(2) Substituting $x = y - \dfrac{A}{3}$ eliminates the quadratic term, yielding

$$y^3 + 3py + 2q = 0.$$

(3) Using Cardano's formula, the determinant is

$$D = q^2 + p^3 \text{ and } u, v = \sqrt[3]{-q \pm \sqrt{D}}$$

the roots of which are

$$y_1 = u + v \text{ and } y_{2,3} = -\frac{u+v}{2} \pm \frac{\sqrt{3}}{2}(u-v)i$$

Solving a quartic equation
Dividing the general equation of a quartic by c_4 yields the normal form:

$$x^4 + Ax^3 + Bx^2 + Cx + D = 0$$

Substituting $x = y - \dfrac{A}{4}$ eliminates the cubic term, resulting in:

$$y^4 + py^2 + qy + r = 0.$$

The resolvent cubic is then

$$z^3 - (p/2)z^2 - rz + (rp/2) - (q^2/8) = 0.$$

With z being the root of this equation, the roots of the quartic can be obtained by solving the two quadratic equations

$$y^2 \pm y\sqrt{2z-p} + z \mp \sqrt{z^2 - r} = 0$$

Resubstituting yields the correct values of x. For a detailed description of this method, refer to [5].

References

1. 3D Systems, Inc., "Stereolithography Interface Specification", 3D Systems, Inc., Valencia, CA, June 1988.

2. Abhyankar, S. S. and Bajaj, C., "Automatic Rational Parametrization of Curves and Surfaces I: Conics and Conicoids", Technical Report, Purdue University.

3. Darrah, J. and Wielgus, M., "A New CAD Model Format for SFF Machines?", *Proceedings of Solid Freeform Fabrication Symposium*, 1990, J. J. Beaman, H. L. Marcus, D. L. Bourell, and J. W. Barlow, eds., Austin, TX, August 6-8, pp. 121-125.

4. Foley J. D., van Dam, A., Feiner, S. K., and Huges, J. F., *Computer Graphics: Principles and Practice*, Addison-Wesley, Reading, MA, 2nd edition, 1990, pp 92-99.

5. Glassner, A. S, *Graphics Gems*, Academic Press, Boston, 1990, pp 404-406.

Parametric Analysis for Selective Laser Sintering of a Sample Polymer System

Xiaoming (Michael) Deng[1], Guisheng Zong[2], and Joseph J. Beaman[1&2]
1. Department of Mechanical Engineering
2. Center for Materials Science & Engineering
The University of Texas at Austin, Austin, TX 78712

Abstract

An experimental cross parametric relation evaluation and a parametric analysis effort were conducted to assess the effects of the major Selective Laser Sintering (SLS) process parameters on the quality of the SLS products using a sample powder system. The sintering results are discussed in terms of the major input parameters including laser power intensity, beam profile, scanning speed, and scanning path as well as powder packing density. The results indicate that increasing powder packing density is the most beneficial way to improve the SLS product quality.

1. Introduction

In a SLS process, a computer-controlled laser beam is used to heat the powder bed to cause localized sintering [1,2]. It is a complex process which involves many process parameters. The laser beam properties, such as laser beam profile, intensity, and wavelength, as well as its scanning speed and scanning path are very important parameters. In fact, these parameters together with powder material properties and sintering environment are key factors in a SLS process. An understanding of these parameters is very important to the successful SLS process control. Therefore, a cross parametric evaluation and a parametric analysis effort were conducted to assess the effects of the major process parameters, including laser power, beam scanning speed and powder packing densities, on the quality of the SLS products using a sample powder system in a single scan and single layer basis. The primary objective of this research is to determine the most effective factors for SLS part production qualitatively. It is focused on the investigation of the effect of the processing parameters on the sintering geometry definition, sintering depth, and sintering density. For simplification, the effects of environmental influences and materials were fixed. Machinery influences were neglected other than the powder packing density.

2. Experimental Approaches

2.1 Material Selection

Many powder materials can be used as the starting material for the SLS process. The sintering material for a SLS process is chosen by considering its sintering capability, mechanical property after sintered, and radiation stability of the material. Additionally, the melting point of the material

need to be considered for a given laser power. Polycarbonate powder was selected as a sample material for this experiment. It possesses good mechanical properties, good sintering capability and high radiation stability in polymers. The IR spectrum of polycarbonate indicates that the highest absorption rate is in the range of wavelength from $5.0\mu m$ to $11.0\mu m$.

2.2 Laser Selection

The choice of the laser is solely dependent on the selection of the powder material, its optical properties, thermal properties and the availability. Since polycarbonate powder had been chosen for this experiment, the CO_2 laser became a proper choice. Its wavelength is about $10.6\mu m$ which is in the best absorption rate range of polycarbonate.

The experimental CO_2 Laser has a frequency range of 50-400 Hz, TEMoo 95% purity of mode quality, and $\pm$ 5% of power stability (30sec. warm up time), and 3mm of output beam size. Laser beam profile was measured at surface of powder bed by using profilometer. Gaussian beam profile was observed with a beam waist of about 1.4 mm in 100% duty cycle. It was also noticed that a smooth Gaussian profile of the laser beam can be obtained only at the full duty cycle [3].

2.3 Experimental facilities

The experimental SLS machine, Bambi [4], was used in this experiment. A laser beam profilometer was used to measure the beam profile. JSM-35 Scanning Electron Microscope (SEM) was utilized to observe the sectional sintering geometry and analyze the changes of sintered microstructure. SEM has a much larger depth of field than the optical microscope and is useful for the observation of an uneven surface.

2.4 Sample preparation and measurement

Cross section of the sample was taken from the sintered layer as shown in Fig. 1. Sintering depth can be identified from a so-called sectional sintering geometry. Sectional sintering geometry is a section view of the sintered part (path). It is defined from sintered surface, along the direction of laser beam (Z-axis), to a region that sintering density appears obviously reduced(Fig.2). The sintering depth is defined within a solid sintering region. It is evaluated by means of the mean heights of the solid sectional sintered portions. The sectional sintering geometry can be clearly observed and measured using SEM.

The fractional density is defined as the area ratio of the solid sintered region to the void region within the average height of the sintering geometry.

3. Experimental Results and Parametric Analysis

3.1 Sectional sintering depth vs. laser power and scanning speed
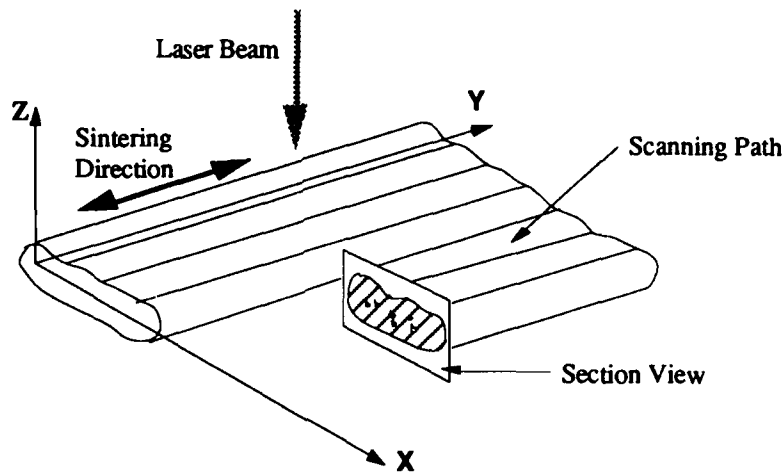
Fig. 1 Sample collection
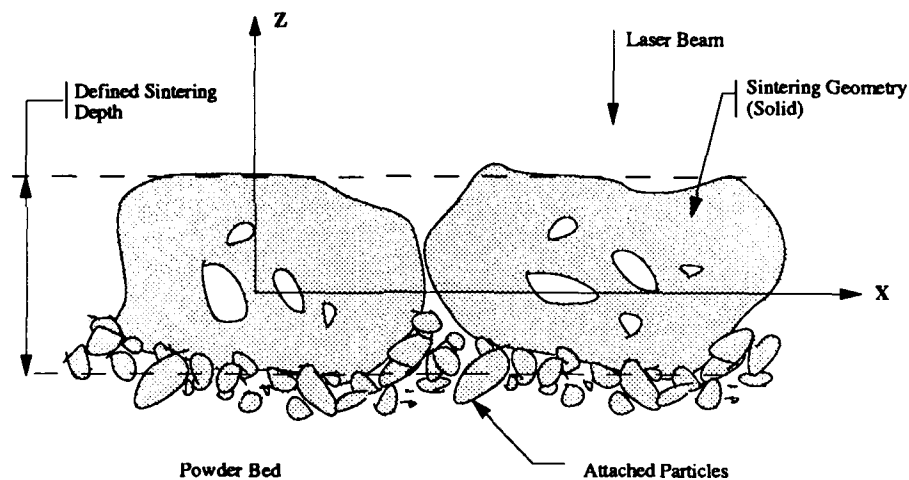
Fig.2 Determination of the sintering depth

Fig. 3 shows the relation of the sintering depth with scanning speed at different laser power 14, 16, and 20 W for single scans. The results can be explained using the SEM micrographs of the sintered lines. For example, for the laser power of 20 W, laser ablation occurred in the low scanning speed range up to 4 in/sec (Fig. 4a), resulting in a material removal during sintering and thus a thinner sintering depth. As the scanning speed increases, more and more sintering is involved in the process (Fig. 4b), the sintering depth first increases to a point where 100% sintering (no material removed) occurred and then decreases due to the shorter interaction time. Similar results were observed in the SLS of single layers [3].
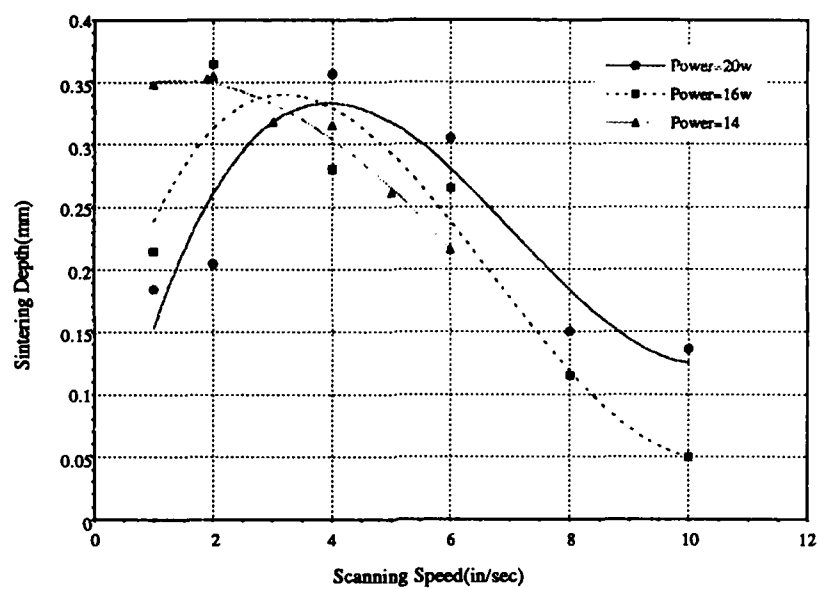
Fig. 3 Sintering depth as the function of scanning speed and laser power
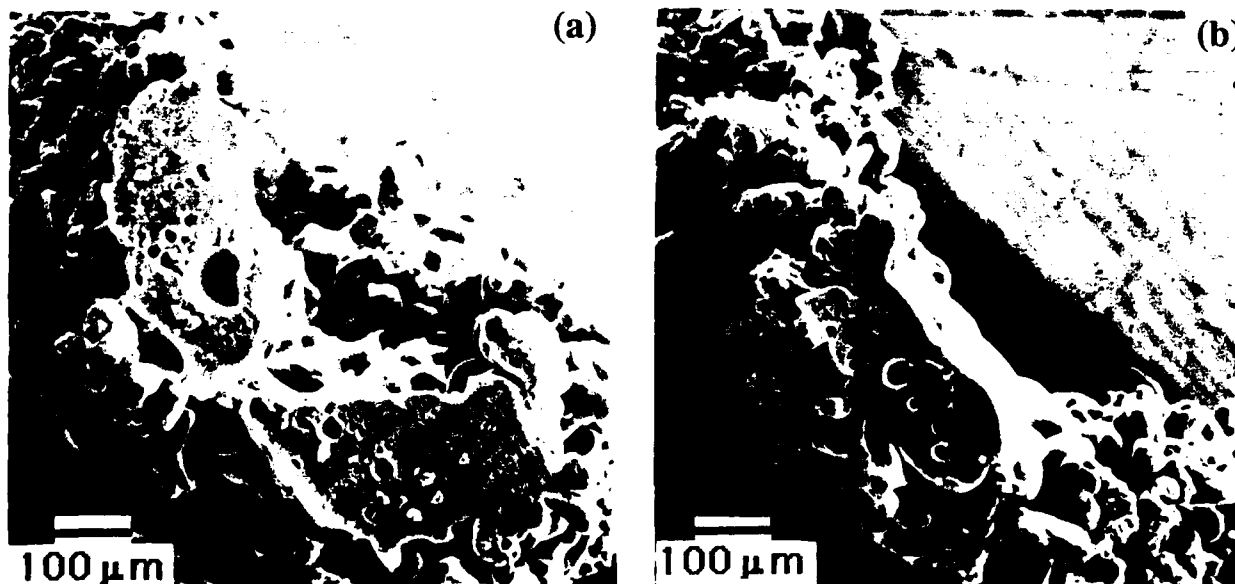
Fig. 4 A section view of sintered part at (a) P=20w, v=2in/sec, (b) P=20w, v=8in/sec.

3.2 Sectional sintering geometry versus powder packing density

Fig. 5 and Fig. 6 show the relations of the sintering depth and width with the powder packing density respectively. Two different packing densities (36.4% and 80%) result in totally different sintering geometry. High powder packing density results in a larger sintering width and a
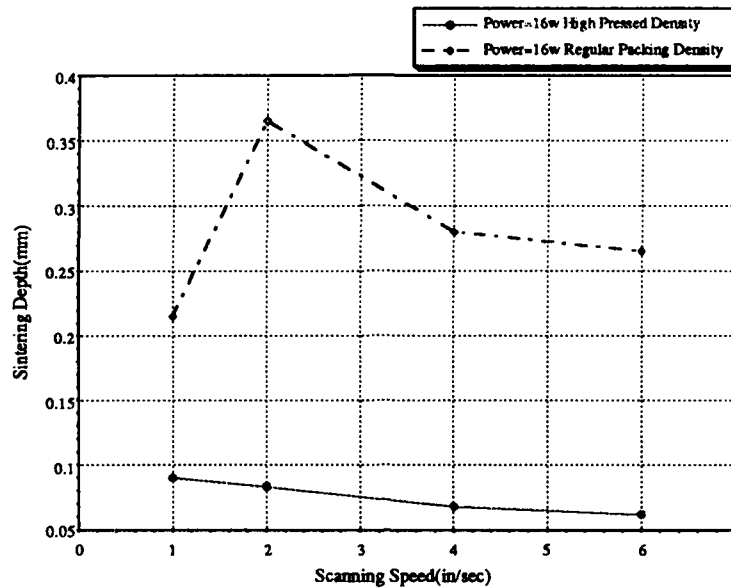
Fig. 5 The effect of packing densities on the sintering depth
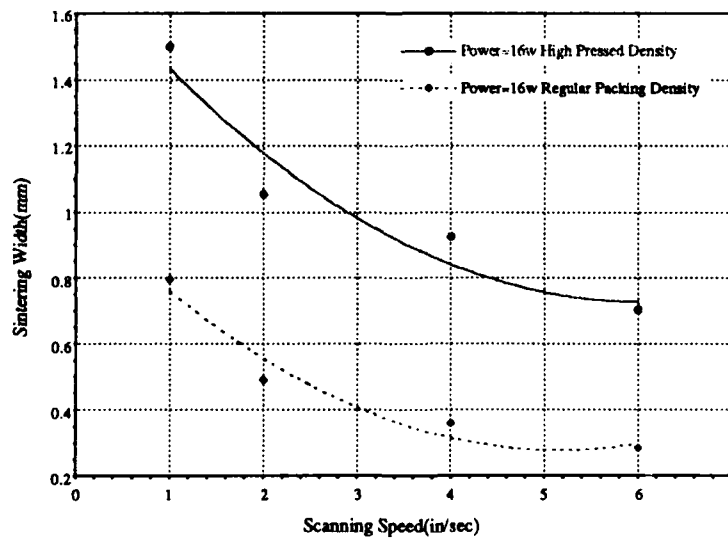
Fig. 6 The effect of the packing density on the sintering width in a single scan

106

smaller sintering depth. The higher of the powder packing density, the higher thermal conductivity that makes heat flux conduct fast, and therefore the wider sectional sintering geometry. Meanwhile, it reduces the laser lights passing through the powder bed so that the sintering depth is greatly decreased. It is notable that ablation was mild in the high range of powder packing densities due to the combination effect of relatively high thermal conductivity and high reflectivity of the pressed surface. Local curling and shrinking can be also reduced by increasing packing density of powder.

The significant effect of the packing density on the SLS product quality is shown in Fig. 7. In this figure, two samples were sintered under same sintering conditions other than the packing densities which were 0.43 g/cm^3(left) and 0.82 g/cm^3(right). It is obvious that the sample with higher packing density has a very smooth surface finish, clean edge definition, higher sintered density, precise geometric shape and less shrinkage than the lower one.
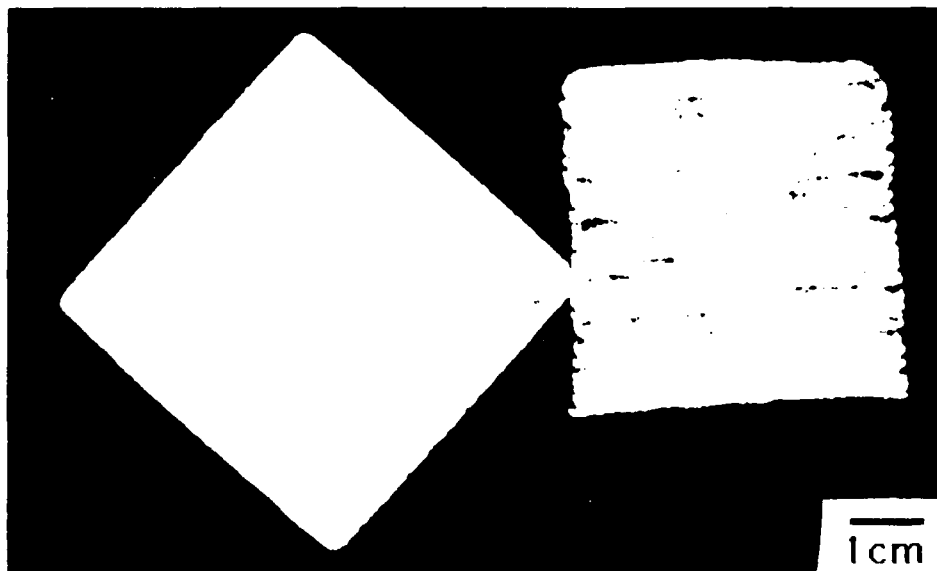
Fig. 7 A photograph showing the surface finish and shape generation of the different packing densities

3.3 Sectional sintering geometry versus beam profile and beam overlapping

Sectional sintering geometry can be changed when the scanning spacing or the amount of overlapping changes. The effects of the beam scanning path overlapping with the sintering depth are plotted in Fig. 8 which indicates that the sintering depth can be increased up to 70%. The fractional density also has significant changes (Fig. 9). The fractional density can be enhanced to a full density in the single layer basis.
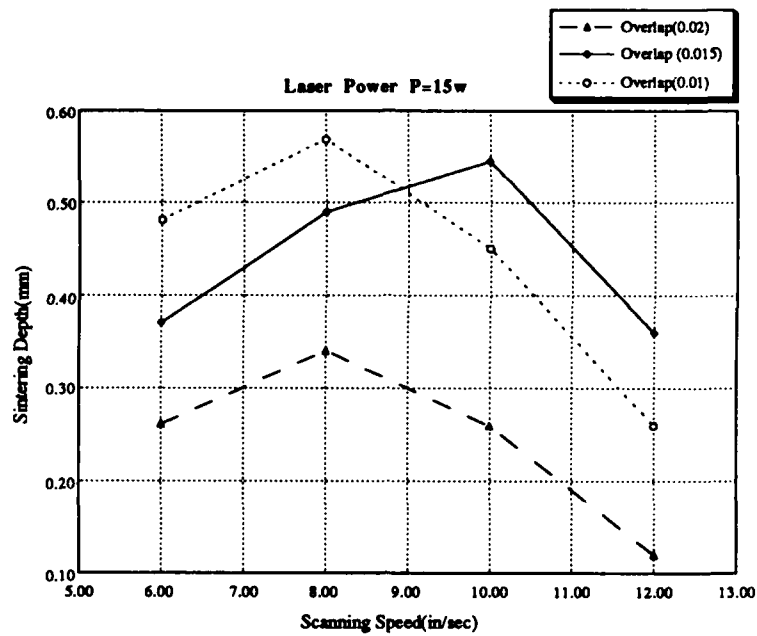
Fig. 8 Sintering depth corresponding to beam scanning path overlapping(in)
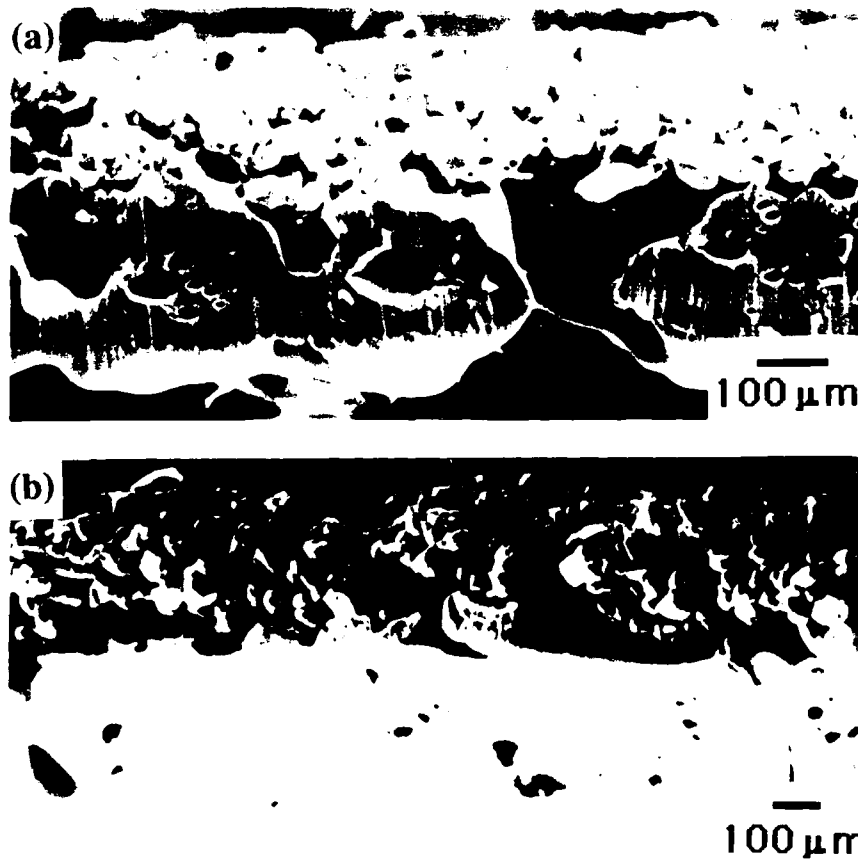
Fig. 9 Sintered samples with laser beam scanning path overlapping (a) 0.5mm, (b) 0.25mm.

5. Summary and Conclusions

Selective Laser Sintering involves many process parameters. It is not at all obvious how to set these parameters to obtain an acceptable part from a particular powder. Suitable parameters are material-dependent and part shape-dependent. A 'smart process' is a long term objective of SLS research. The focus of this research is on how the dominant parameters or factors affect the SLS process on the single scan and single layer basis. These parameters include laser power, laser beam scanning speed, scanning overlapping, and powder powder packing density.

This fundamental research has provided a qualitative parametric analysis for the SLS process. It was found that higher beam scanning speed produces a flat sectional sintering geometry. In other words, increasing laser duration time contributes to a larger value of sintering depth and vice versa. The higher laser powers and lower scanning speeds, the larger values of the sintering depth and sintering width. This is not always favorable, because ablation occurs once the input laser energy exceed certain levels. There is a limitation to the maximum sintering depth attainable. Increasing the powder packing powder density results in very significant sintering geometry changes. The main effects include increasing sintering density, preventing the local curling and balling, dramatically improving the sintering surface finish and edge definition, and reducing sintering shrinkage. Laser beam scanning path overlapping can increase the sintering depth and the sintering density.

References

1. J. J. Beaman, "Laser Sintering for Desktop Manufacturing," Design News 46(3), 1990, 65-6.
2. C. R. Deckard, "Selective Laser Sintering," Ph.D. Dissertation, Department of Mechanical Engineering, The University of Texas at Austin, 1988.
3. Deng, X., M.S. Thesis, Department of Mechanical Engineering, The University of Texas at Austin, 1992.
4. P. F. Forderhase, "Design of a Selective Laser Sintering machine Intended for Academic Research," M.S. Thesis, Department of Mechanical Engineering, The University of Texas at Austin, 1989.

DESIGN OF A HIGH TEMPERATURE PROCESS CHAMBER
for the
SELECTIVE LASER SINTERING PROCESS

John McWilliams, Christopher Hysinger, J.J. Beaman

Department of Mechanical Engineering
The University of Texas at Austin
Austin, TX 78712

ABSTRACT

The quality of parts made by the Selective Laser Sintering (SLS) process depends directly on controlling heat transfer to the part-bed. In this paper, we detail the thermal design of a HIGH TEMPERATURE PROCESS CHAMBER to be used for building parts from metals and ceramics. Modeling and experimental techniques are used to design radiant and convective heat transfer schemes to apply uniform heat flux to the part-bed. At the completion of the project, we expect to have a test-bed to study the effects of radiant and convective heat transfer on part quality in a high temperature environment.

BACKGROUND

Background of the HTW Project

In 1989, work began on a new SLS machine to directly sinter parts from metals and ceramics. This High Temperature Workstation (HTW) would require the powdered material to be heated to sintering temperatures in excess of 1500°C. One way to obtain these temperatures is to use a high-power laser. The decision was made to obtain a 1.1kW CO_2 laser and to design a workstation around this high-power laser. [Das]

In polymer systems, experience has shown that applying laser energy to a cold powder-bed often causes the newly formed layer to deform so that it curls up out of the plane of the part-bed. This phenomenon is known as "curling". The use of a heater to pre-heat the part-bed has been found to control the curling problem in polymer systems.

The first High Temperature Workstation was brought on line in October of 1991. This workstation utilized the 1.1 kW CO_2 laser, but had no heating system to pre-heat the powder. Single layer experiments were done using stainless steel and copper powders. Multiple layer experiments were then conducted using two alloy systems. [Wu]

As suspected, curling was a problem. Since this chamber had no built in heating, there was no way to control thermal stresses. A hot-plate heater was used at the base of the powder, which produced some improvement in part quality under certain conditions. This heating method, however, is impractical for multiple layer parts.

The Next Stage: High Temperature Selective Laser Sintering

This paper details the design, development, and testing of a HIGH TEMPERATURE PROCESS CHAMBER, the key component of the new HTW presently under construction. This phase of the HTW project required an evaluation of process requirements, the selection of a Heating Method and Temperature Control System, and the design, construction, and testing of a HIGH TEMPERATURE PROCESS CHAMBER. First, Design Specifications for the HIGH TEMPERATURE PROCESS CHAMBER were developed. Then, conceptual designs for a Heating Method were developed. The final conceptual design was evaluated and optimized using heat transfer models. The PROCESS CHAMBER was designed and built to accommodate the heating method. Finally, the completed chamber was performance-tested to identify any potential problems, and to compare real performance to model predictions.

DESIGN SPECIFICATIONS

A Design Group was formed to develop Design Specifications for the HIGH TEMPERATURE PROCESS CHAMBER. Researchers in the Material Science area formed an important part of the design group, since they would be the end users of the HTW. The group developed three important Design Specifications.

Maximum Temperature Specification

After examining some of the properties of the materials to be used in the HTW, the Design Group set a goal for a Maximum Operating Temperature of 1300°C. This value represents the final steady-state temperature that the powder-bed should reach with the heating system operating at full capacity. The group then set a Normal Operating Temperature range of 100°C to 1000°C. We define Normal Operating Temperatures as those temperatures which fall within the controllable range of the heating system.

Temperature Uniformity Specification

A high degree of Temperature Uniformity is required to eliminate curling. The Temperature Uniformity Specification was therefore one of the most important design considerations, but also one of the most difficult to quantify. Since surface temperature uniformity depends on many factors and is material dependent, the group decided to evaluate the potential uniformity of each heating method based on its heat flux uniformity. Since there is no direct relationship between heat flux and temperature distribution, no value was set for this requirement. Rather, the Design Group made the decision to simulate the heat flux distribution for different heater designs, and to use the results as an important selection criterion when choosing between different heating methods.

Controllability Specification

The controllability of the heating system depends on the dynamic properties of both the heating system and the control system. At this point in the design process, the design group could not quantify the Controllability Specification, but decided that it should be an important criteria in selecting a heating method.

Heaters vary greatly in thermal mass. In low thermal mass systems, the power output can be changed rapidly. In high thermal mass systems, power output changes very slowly in response to power input. A heating system with a low thermal mass is most desirable for flexibility in process control.

HEATING METHOD SELECTION AND ANALYSIS

In addition to the Design Specifictions given above, several other design constraints made selection of a heating method quite difficult. For example, the heating method had to allow the laser to scan the entire area of the part-bed. Simple models had shown that a very high heat flux is required to meet the Maximum Temperature Specification. In the selection process, the design group examined many high-power heating methods, including quartz infrared heaters, graphite ring heaters, direct resistance heating and induction heating.

Selection and Application of Dual Infrared Panel Heaters

The design group selected a dual infrared panel heater arrangement as the heating method for the HTW (Fig. 1). A similar system was developed by Brubaker for an infrared drying oven. High-density quartz panel heaters were selected. The system has a total power output of around 20 kW.

The design group chose the dual panel heater arrangement as the most promising design for several reasons. Most importantly, quartz heaters can deliver a higher surface heat flux than any other of the heating methods investigated (up to 780 Watts per square centimeter at the heater surface). Also, Brubaker's work suggested that the orientation of the heaters could be optimized to obtain a uniform heat flux. Finally, these heaters have a very low thermal mass which gives them excellent controllability. Their low thermal mass allows them to reach full power output in about one second.

Thermal Modeling and Analysis

Now that commercially available heaters had been found, the feasibility of the heating method could be evaluated. After we determined that the heaters could provide enough heat flux, two issues remained to be investigated. First, the heaters needed to be oriented to produce a relatively even heat flux across the part-bed. If it was possible to obtain an even flux, then an orientation had to be chosen to obtain the best combination of heat flux uniformity and heater efficiency. The following model was used to help achieve both of these goals.

For radiant heat transfer between two surfaces A and B in space, the heat flux from surface A to surface B is directly proportional to F_{a-b}, the view factor from A to B. This implies that if the view factors could be calculated, then the heat flux uniformity between the two surfaces could be evaluated. In our case, surface A is the heater and surface B is the powder-bed.

A simulation program was developed that calculates the view factors from two planes, representing the radiant heaters, to an array of differential planar elements, representing the powder-bed (Fig. 1). The two heaters are angled into the plane of the powder-bed at an angle ϑ. The outside edge of the two heater planes is at a height **h** above the powder-bed. The heaters are separated by a distance **d**. The program plots the view factor distribution across the plane of differential elements representing the powder-bed. The plane is the same size as the projected area of heaters. An efficiency is calculated as the percentage of infrared radiation that strikes this plane.

After evaluating several different heater orientations, the model predicted that a very uniform heat flux could be obtained for certain orientations. Figure 2 shows the view-factor profile for the final chamber design. At the center of the bed, the view factor is approximately 0.40. For this configuration, the model predicts that approximately 17% of the energy from the heaters should directly reach the powder-bed.
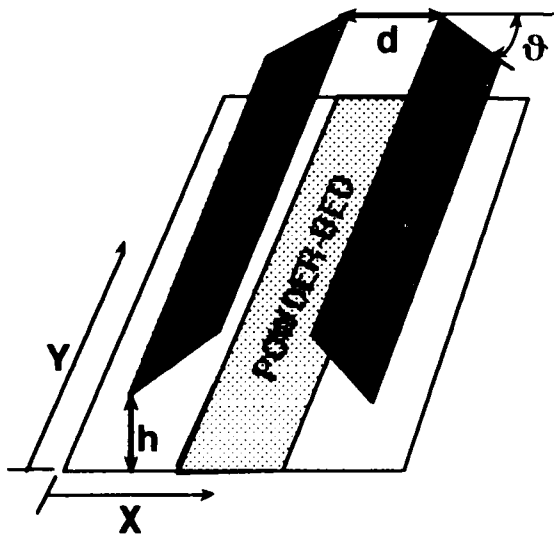
Figure 1: Heater Configuration
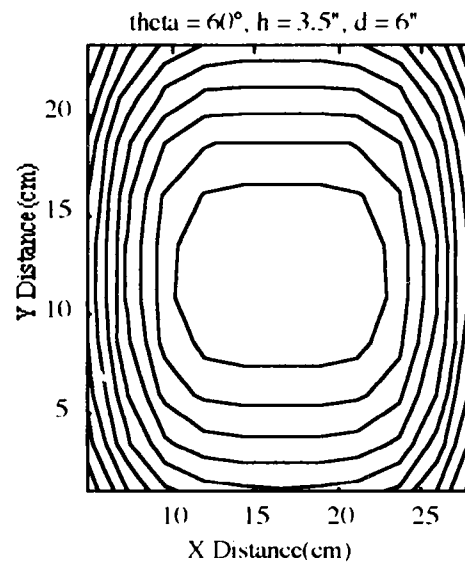
Figure 2: View Factor Contour Plot

112

SYSTEM DESIGN

Three principle systems make up the overall design of the HIGH TEMPERATURE PROCESS CHAMBER. The Chamber itself provides a sealed sintering environment. The Laser Window Cylinder isolates the laser window from the chamber environment. A Gas Handling System provides process gas to the Chamber without disturbing the temperature distribution on the part-bed. Finally, the Temperature Measurement and Control System measures the surface temperature of the part-bed and adjusts heater power to maintain a user-set temperature.

Chamber Construction

Design Considerations

The chamber must provide a controlled sintering environment. It must be gas tight, yet allow energy form the laser and from the heaters to reach the powder bed. It must contain and provide access to the powder-bed and accommodate leveling and powder-feed systems.

Design Solution

The chamber, shown in Figure 3, is constructed of 3/4" thick carbon steel plate. The heaters are mounted outside of the chamber. Quartz windows mounted in the chamber walls allow the infrared energy from the heaters to reach the powder-bed. To access the interior of the chamber, the chamber bottom plate detaches, eliminating the need for an access door. Viton™ O-rings seal all non-permanent joints. The entire interior of the chamber is lined with ceramic-fiber insulation to minimize heat absorption by the chamber walls.
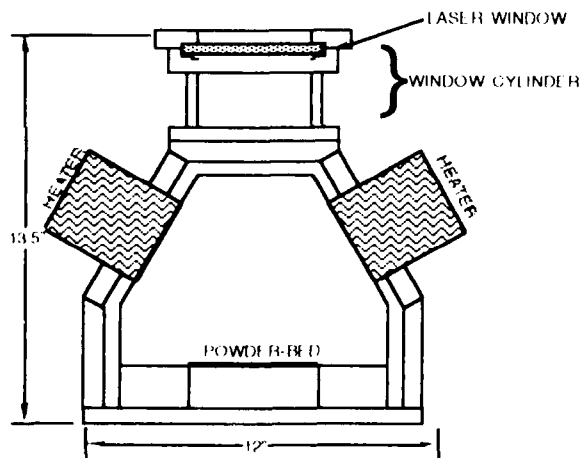
Figure 3: Chamber Configuration
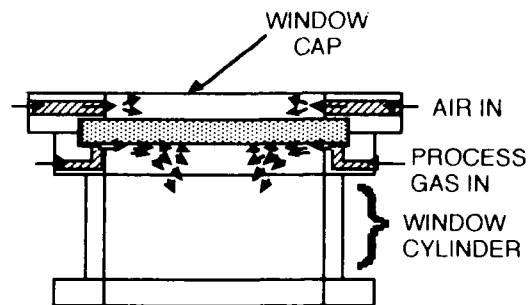
Figure 4: Window Flow Scheme

Laser Window Cylinder

Design considerations

The most important function of the Laser Window Cylinder is to keep the laser window below its high-temperature limit. Heat transfer analysis has shown that the window would experience a high heat flux from the chamber, and needs to be cooled.

In the previous HTW, the laser window tended to accumulate deposits from inside the chamber. Gas-born powder particles and vapors were carried up to the window by free convection from the hot powder-bed. In the past, a gas jet located in the wall of the Window Cylinder was used to purge the window. This method had some success, but produced turbulence that allowed deposits to accumulate on the edges of the window. In the new Window Cylinder, we hoped to achieve a significant improvement in this area.

113

Design Solution

An aluminum cylinder and cap were constructed to hold the laser window (Fig. 4). The window holder has provisions for gas flow across both sides of the window. The inside surface of the window cylinder has a gap that allows process gas to flow across the entire exposed surface of the window.

The cap also has provisions for gas flow, in this case across the outer surface of the window. Clean air is directed at the window through two jets, located at opposite ends of the cap.

Gas Handling System

Gas flow through the chamber and across the part bed will affect temperature distribution and part quality. An experimental approach was used to help design the Gas Flow System for the HIGH TEMPERATURE PROCESS CHAMBER.

Design considerations

We performed experiments with a thermal imager to determine the effect of convective flow on temperature uniformity across the powder-bed. The imaging experiments showed that free convection provided the most uniform temperature distribution across the powder-bed. The procedure and more complete results are given in the System Performance section.

Keeping in mind that gas flow must be introduced into the window cylinder to keep the window cool and clean, we used the experimental methods detailed below to help develop a gas flow system. The primary design consideration was to ensure that any gas flow scheme left the gas above the part-bed undisturbed so that it experienced only free convection. In the design of the Gas Flow System, another important consideration was to obtain efficient purging of oxygen and sintering by-products from the chamber.

Experimental Flow Analysis

In order to visualize the flow patterns established inside the HIGH TEMPERATURE PROCESS CHAMBER, a mock-up of the chamber was constructed. This test chamber was a 1:1 scale model of the actual chamber, but was constructed of clear polycarbonate sheet. The mock-up consisted of a window cylinder and the main chamber. In the actual chamber, the part bed would lie directly below the laser window cylinder in the plane of the plenum, which is an inch and a half above the base of the chamber. For a tracer, dry ice and water were placed in a cylinder located where the part bed would be. The boiling of the dry ice created CO_2 vapor. This vapor allowed us to observe the flow patterns over the part bed.

At this point, the greatest concern was to determine how flow from the window cylinder would effect the bed. We developed and tested a simple flow scheme (Fig. 5). In this scheme, all of the gas flow into the chamber entered through the window cylinder. The gas was drawn around the part-bed through holes in each plenum, which were located in a symmetrical pattern to either side of the part cylinder. The gas then exited the chamber through an exhaust port in the feed-side end of the chamber.

Design Solution

We found that for gas flow rates of less than 40 liters per minute, a stable flow pattern could be achieved around the part bed with the simple flow scheme described above. At these flow rates, we observed that the flow patterns of the CO_2 vapor over the part-bed remained undisturbed. From this observation, we concluded that the gas around the part bed also remained undisturbed, which was the primary design goal for the Flow System.

In the HIGH TEMPERATURE PROCESS CHAMBER, we plan to install two cross flow heat exchangers, one on each side of the part-bed. In the final system, gas will enter the chamber through the Window Cylinder, pass through the fins of the heat exchangers, and travel beneath the plenum to the feed-side of the chamber, where it will exit through an exhaust port. The purpose of the heat exchangers is to absorb the excess heat from the chamber and to cool the gas before it is released to the building exhaust system.

114
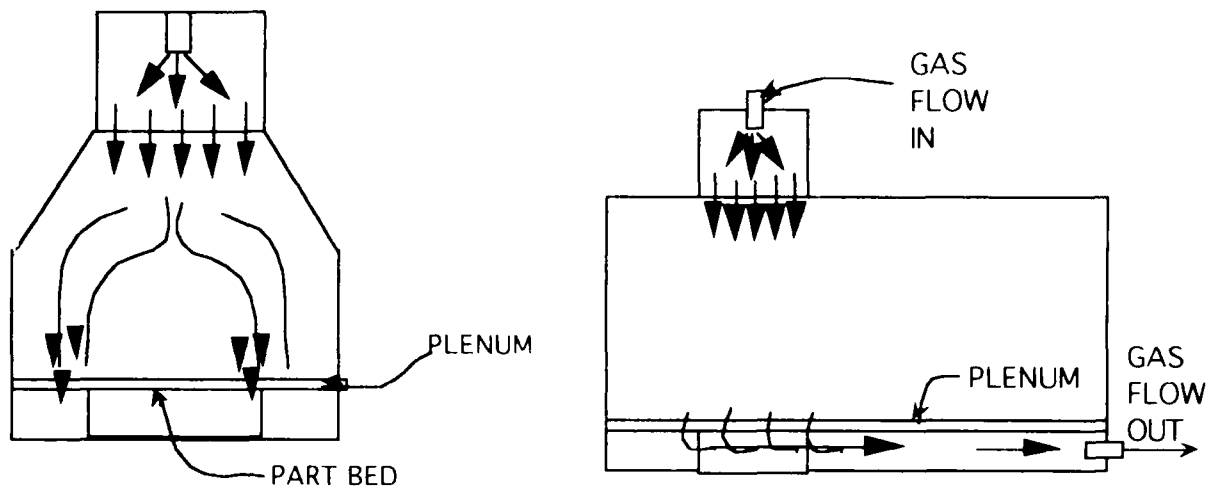
Figure 5: Chamber Flow Scheme

Temperature Measurement and Control System

The function of the temperature measurement and control system is to maintain the surface temperature of the powder-bed at a user specified set-point. In order to provide this function, three major sub-systems are required to: measure the surface temperature of the powder-bed; monitor the surface temperature and produce an output control signal; and supply power to the heaters in response to the control signal.

Design considerations

Measuring the surface temperature of the powder-bed presents some unique challenges. Measurements must be unaffected by radiant flux from the heaters. Measuring instruments must not interfere with the powder leveling roller, which passes over the entire surface of the powder-bed during each leveling operation. For these reasons, a non-contact method of temperature measurement was chosen.

Non-contact temperature measurement is generally done with an infrared (IR) thermometer. In selecting an IR thermometer, temperature range is an important consideration. For our process, we desired an instrument that could measure temperatures from room temperature to about 1500°C. Other important parameters include spectral response and field-of-view.

To automatically maintain the set point bed temperature, a Process Controller is required to read and display the input signal from the temperature sensor and output a control signal to the heater Power Control system. In selecting a Process Controller, several design parameters must be considered. These include the desired control scheme, input signal compatibility, and output signal compatibility.

Design Solution

A Raytek IR thermometer was chosen to measure the surface temperature of the powder-bed. The instrument has a measurement range of 260°C to 1700°C. Its spectral response is 3-5μm, which makes it insensitive to reflected energy from the heaters. The IR thermometer has a field of view that produces a spot size of approximately one inch on the powder-bed. It was mounted outside of the chamber, and sees its target through a sapphire window mounted on top of the chamber.

An Omega PID process controller was chosen to control powder bed temperature. The controller accepts a 4-20 mA input signal from the IR thermometer and sends a 4-20 mA control signal to the Power Controller.

A phase-angle fired SCR power controller was selected as the power supply for the heaters. This 208V single phase power supply supplies power to the heaters in response to the control signal from the Process Controller. A manual control mode is also available.

115

SYSTEM PERFORMANCE

When the chamber was completed, we developed a test plan to evaluate the performance of the chamber before it was installed in the workstation. Performance objectives were first developed, and then a series of tests were designed to evaluate the performance of the HIGH TEMPERATURE PROCESS CHAMBER.

Extended Burn-in Test

The main purpose of the Extended Burn-in Test was to determine if the heater windows and seals could withstand the temperatures to which they would be subjected. Another purpose of the test was to examine the affect of insulation on chamber and seal temperatures.

In this simple test, both ends of the chamber were removed, and a table-fan was used to blow air through the chamber for convective cooling. The heaters were run for 30 minutes, and then the condition of the window seals was inspected.

The first time this test was run, the Viton™ o-ring seals started to burn after about 10 minutes of heater operation at full power. The second time the test was run, the ceramic fiber insulation was installed inside the chamber. This time, the seals remained intact, and the chamber walls remained much cooler. This indicates that the seals absorbed most of the heat from the chamber walls, not directly from the heaters.

Water Bath Tests

The main purpose of the Water-bath Tests was to determine the efficiency of the heating system. In this case, we have defined efficiency as the proportion of the energy supplied to the heaters that reaches the heated surfaces.

Two tests were performed. The objective of the first test was to determine the heat flux across the entire area of the part-side of the chamber module base. In the second test, the objective was to determine the heat flux across the part-side of the powder-bed only. For each test, a tray containing a known weight of water was placed in the chamber, the heaters were turned on for 30 seconds, and the change in temperature was measured.

In the first water-bath test, the chamber base received an average of 134 kJ of energy. When averaged over the 30 seconds of the test, this works out to an average power 4.47 kW. The heat flux per unit area was 41 W/in^2 or 6.4 W/cm^2. The electric power input to the heater was maintained at 16.6kW. This yields an efficiency of 27%, which means that 27% of the electrical energy input to the heaters was converted into heat on the part-side of the chamber base.

The results of the second test indicate that the powder-bed will receive an average heat flux of 8.58 W/cm^2, yielding an efficiency of 18% on the powder-bed.

IR Scanner Tests

One of the most important design criteria for the heating system was to produce very uniform bed temperatures. In measuring the temperature distribution, we hoped to accomplish two goals. First, we wanted to see if the measured distribution coincided with what we expected from the View Factor Optimization. The second goal was to see how different parameters affected temperature uniformity. Tests were performed to determine how temperature distribution was affected by gas flow across the powder-bed and by chamber wall reflectivity.

To perform the IR scanner tests, the IR scanner was placed on top of the chamber, where it looked down the hole where the window cylinder would normally be installed. During each test, the heater power was kept constant by maintaining heater power at 30 A. A 3-5 μm filter was used to minimize the effect of reflected IR energy on the temperature reading. In each test, the specimen and chamber were set up and the heater power was turned on. After the temperature profile reached steady-state, the output from the IR scanner was recorded on video tape.

In one of the most important tests, the effect of convection across the powder-bed was investigated. In this test, the flow velocity across the powder-bed was varied using a

table fan. The results showed that natural convection produced the most uniform temperature distribution. These results helped motivate the gas flow scheme described previously. The other significant result of the IR Scanner tests showed that applying a reflective foil to the inside surfaces of the chamber increased the bed temperature significantly.

PROJECT STATUS AND FUTURE DEVELOPMENT

At this time, the performance of the HIGH TEMPERATURE PROCESS CHAMBER has been tested, and the results have been quite encouraging. Temperature distributions have been quite good, and bed temperatures in excess of 600°C have been obtained in brief tests. The only problem has been with cooling the laser window. This problem is detailed below. All systems are operational as described except for the Gas Flow System and the Temperature Control System. Other significant long and short term goals are given below.

Laser Window

In preliminary testing, the anti-reflective coating on the zinc-selenide laser window was damaged from excessive temperatures. The problem appears to be that the coating absorbed more energy than we predicted. Further heat transfer analysis is being conducted, and trials are being conducted with a sodium-chloride window, which can tolerate much higher heat fluxes.

Radiation Absorbers

The HIGH TEMPERATURE PROCESS CHAMBER has been shown to effectively heat the powder-bed, although only 18% of the radiant energy directly strikes the bed. The rest of this energy heats the process gas and the chamber itself. This excess heat must be removed if the HTW is to operate for long periods of time. A method to remove this extra heat has been studied and is being implemented on the HTW. Two water-cooled radiative absorbers are to be mounted on either side of the part-bed. Analysis predicts that the absorbers will remove about two thirds of the excess heat.

Feed-Side Heating

The present heating system heats only the part-side of the powder-bed. Past experience has shown that leveling "cold" powder from the feed side on a hot part-bed caused curling problems. To combat these problems, a small (~2000W) feed side heater will be installed in the chamber.

Phase III: The Next High Temperature Workstation

The next long-term goal for the High Temperature Workstation project is to make a process chamber that has high vacuum capability, in addition to high-temperature capability. This next phase in the HTW project will not be initiated until significant test data from this system is collected and evaluated.

REFERENCES

Brubaker, Stephen Randall. *Design and Testing of a 25kW Infrared Drying System.* Thesis. The University of Texas at Austin, 1990.

Das, Suman, and J. McWilliams, B. Wu, and J. J. Beaman. "Design of a High Temperature Workstation for the Selective Laser Sintering Process." *Proceedings of the Solid Freeform Fabrication Symposium.* August, 1991: 164-170.

Wu, Yong-Qiu. *Design And Experiments On High Temperature Workstation Intended For Academic Research Of The Selective Laser Sintering.* Thesis. The University of Texas at Austin, 1992.

The Application of an Artificial Body Force to the Selective Laser Sintering Process

by
Lawrence S. Melvin III
and Dr. J. J. Beaman
University of Texas at Austin
Department of Mechanical Engineering

Abstract

An artificial body force generated by a magnetic field is applied to the green powder bed of a ferromagnetic powder during the Selective Laser Sintering process. Preliminary experiments and theory are formed to determine whether the artificial body force is beneficial to the Selective Laser Sintering process and if it is usable within that process. Several applications are discussed including microgravity situations and two phase sintering processes. It is determined that the magnetic body force is beneficial to the Selective Laser Sintering process.

Introduction

The purpose of this experiment is to determine if an artificially generated body force applied to the powder bed during application and sintering will enhance the Selective Laser Sintering process. The force which is currently under consideration is a magnetostatic force applied to ferromagnetic materials. The addition of the artificial body force is expected to increase the green bed and part densities and therefore increase the part strength of the sintered work piece. In addition, the magnetic force is expected to induce a packing structure into the green powder bed. This packing structure generation was exhibited in an electrostatic powder application system, and therefore is expected in a magneto static system. Also, the magnetostatic system has the ability to generate a constant and controllable force during the sintering process.

The magnetostatic system is intended to be used to enhance part quality, replace gravity in a microgravity situation, and aid the powder application and leveling processes. The most important disadvantage of the magnetostatic force generation system is its nonlinearity with respect to radial position from the solenoid. This nonlinearity will eventually have to be designed out of the system in order to produce high quality parts. If a satisfactory field cannot be generated, the use of a magnetic body force in the Selective Laser Sintering process will not be feasible.

Theory

The magnetostatic system is currently being modeled in simple terms. This model will illustrate qualitatively how the particles are expected to behave in the magnetic force field. This information can then be used to design an appropriate core for magnetostatic force field generation.

The first step in generating a workable magnetic force field is to select the core parameters which are desired. The manipulation of the core parameters N, i, a, and d allow for the generation of a useful magnetic force field. A standard model of the magnetic field intensity H for a single solenoid on the vertical axis is presented below:

$$H_z = \frac{Ni}{2d}\left[\frac{\frac{d}{2a}-\frac{z}{a}}{\sqrt{1+\left(\frac{d}{2a}-\frac{z}{a}\right)^2}} + \frac{\frac{d}{2a}+\frac{z}{a}}{\sqrt{1+\left(\frac{d}{2a}+\frac{z}{a}\right)^2}}\right]$$

(1)

The magnetic core and sintering platform parameters are illustrated in Figure 1 below.
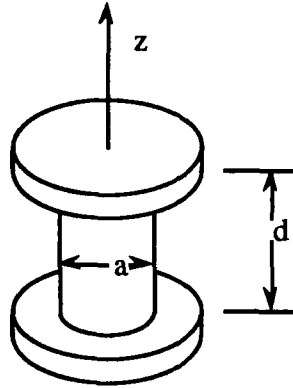
Figure 1
Solenoid calculation parameters
N is the number of turns on the solenoid
and i is the desired current

As the value of $\frac{d}{2a} \ll 1$ the model can be reduced to a more simple form,

$$H_z = \frac{Ni}{2a}$$

(2).

Equation (1) has been simulated to aid in the design of a suitable solenoid for the magnetic process. The parameters of N, a, d, and i were varied, and H_z as a function of z was generated and graphed. Many of the possible combinations of these parameters were simulated, but four general trends are illustrated here. A graph is presented below in Figure 2.

Several important facts can be learned from this simulation. The first fact is simply that the parameters N and i only affect the magnitude of the field. However, this simulation also illustrates that a and d can be manipulated to effect where and how the field breaks from its initial linear behavior to fall to small values of field intensity. This phenomena allows a design to be implemented which will produce a constant linear force by operating in the region before the field breaks.

Magnetic B Field vs. Vertical Distance From Core
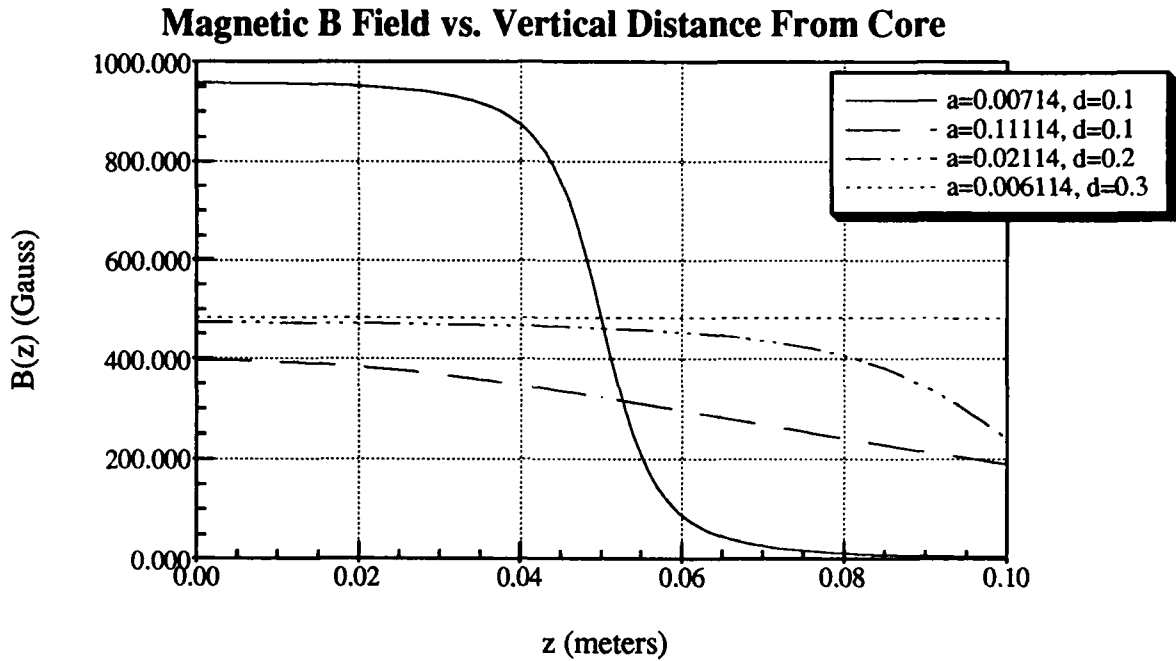
Figure 2
The magnetic field intensity as a function
of vertical displacement along the z axis

The force exerted on a ferromagnetic particle in this magnetic field can also be expressed mathematically. A simple model of the magnetic force is used to understand theses interactions.

$$F_z = \frac{ci^2}{z}$$ (3)

The constant, c, is a function of the windings and geometry of the solenoid. This model can be coupled with the magnetic field intensity relationship to produce a force model involving the magnetic field intensity.

$$F_z = \frac{4acH_z^2}{N^2z}$$ (4)

This relationship provides an insight to how the particles are affected along the vertical axis. As the particles are distributed radially further from the axis, the force influencing them will lessen. This fact leads to a potential problem during the application of the particles. It is possible and probable that this effect will lead to nonuniform powder layer distribution and possibly undesirable particle migration during the sintering process. This can be counteracted by designing an axially symmetric field and possibly by designing the Selective Laser Sintering process control software to account for this distortion. However, this problem is beyond the initial investigation which this experiment encompasses, and therefore it will be addressed in later work.

Experimentation

The Initial experiments have been performed on a one kilowatt laser in the High Temperature Work Station at the University of Texas at Austin. A solenoid consisting of 430 coils on a 5 cm long 2 cm diameter iron core was built and put into the part cylinder with a sintering platform of 304 stainless steel affixed to the top and bottom of the solenoid. Nickel powder was applied and leveled by hand to a thickness of 0.020 inches. The parts were then sintered with the laser using no outside heat source. One layer was sintered using either 1.5 A or 0 A current flowing through the solenoid.

Results

The initial results are very positive. Both the magnetized powder and the nonmagnetized powder failed to sinter to the top of the sintering platform on the solenoid. However, the magnetized sinter was 0.0165 in. thick while the non magnetic sinter was 0.011 in. thick. Also, both specimens exhibited ridges along the line of sinter, but the ridges in the magnetized sinter had sharp tops like triangles, while the nonmagnetized sinter has rounded tops. Both specimens were fragile and full of holes which let light shine through the work piece.

Once the sinters were viewed under the Scanning Electron Microscope, more differences appeared. Figure 3 and 4 are SEM photographs of the two sinters. The nonmagnetized specimen had powder grains sintered to one or two other grains while the magnetized specimen routinely had grains sintered to three, four, or five different grains. Also, the bonds on the magnetized sinter were routinely larger than those of the

Figure 3
Nickel powder sintered with no magnetic field.
Magnified 2000x

Figure 4
Nickel powder sintered with 1.5 A of
current producing a magnetic field.
Magnified 2000x

nonmagnetized sinter. In addition, there were many nickel particles in the magnetized
sinter which had numerous groves in them. However, most of the particles of the
nonmagnetized sinter had smooth surfaces, and those which did not had only a small
number of groves on them The magnetized sinter also exhibited some ridge like patterns
in the sintered work piece.

Experimental Variances

Three different experimental variances may have contributed to the observed
experimental results. First, the nonreflective coating was missing from the inside of the
zinc solenide window during these experiments. Secondly, the powder was jostled about
between the leveling and sintering processes when it was installed into the sintering
machine. Finally, the solenoid generates heat which transfers to the sintering area
through the sintering platform.

The missing window coating has made the effective sintering power lower than it
was set on the machine. For this reason, the balling effect which is exhibited when
sintering single layers of nickel was not exhibited and it may be deduced that the entire
region being sintered did not change to liquid phase during the heating process. Also, the
exact power which reached the sintered surface cannot be determined in a reliable
fashion. Because of these problems, these experiments are only comparable to

122

themselves. The other two variances cannot be linked to any effects on the sintered materials without drawing unsubstantiated conclusions.

Conclusions

These initial experiments support the conclusion that a magnetic field produces a beneficial and useful effect upon the Selective Laser Sintering process. The SEM analysis of the different sinters shows that the magnetized sinter is more dense than the nonmagnetized sinter because the particle to particle bonds are bigger, and there are more bonds present in the magnetized specimen. Also, the ridge effect and greater thickness of the magnetized sinter implies that the laser is able to penetrate further into the magnetized layer. This could be because there are less air gaps due to better packing under the influence of the magnetic field. The elimination of these air gaps would allow heat to conduct better between the powder particles.

Applications of a Magnetic Field

The magnetic field has many useful applications to the Selective Laser Sintering process. The immediate applications include densifying parts, replacing gravity in a microgravity situation, two phase sintering, and enhancement of the powder application process. The magnetic field also appears to be imparting a packing structure to the powder. This phenomena allows for specific placement of different material types in the green powder bed during the sintering process.

The applications to two phase sintering and particle placement will lead to advances in the material science of the Selective Laser Sintering process. These two applications could allow for repeatable alloying structures of pure elements during the sintering process. Using this structuring technique, it may be possible to produce exact homogeneous parts which can be designed to meet specific material property requirements.

The magnetic field's effect on part density and its potential in the powder application process are also very promising. The use of the magnetic body force to replace or counteract the gravitational body force during powder application and sintering will allow sintering in many different environments including low gravity and upside down. In addition, the densifying effect of the magnetic field will lead to greater part strength in the sintered materials as well as enabling the production of parts which are closer to traditionally machined parts.

References

Hammond, P., Electromagnetism for Engineers, The Macmillan Company, New York, NY, 1964.

Haus, Herman A., and James R. Melcher, Electromagnetic Fields and Energy, Prentice-Hall Inc., Englewoodcliffs, NJ, 1989, pp. 318-9.

Kuo, Benjamin C., Automatic Control Systems, Prentice Hall, Engelwoodcliffs, NJ, 1991, pp. 180-1.

Melvin, Lawrence S., III, "The Electrostatic Application of Powder for Selective Laser Sintering," Masters Thesis, The University of Texas at Austin, 1991.

Ceramic Structures by Selective Laser Sintering of Microencapsulated, Finely Divided Ceramic Materials

N. K. Vail and J. W. Barlow
Department of Chemical Engineering
The University of Texas at Austin

Abstract

The feasibility of producing ceramic green parts by Selective Laser Sintering from microencapsulated, finely divide ceramic powders has been reported in an earlier paper. Post-processing of a silica/zirconium orthosilicate system and an alumina system, both utilizing a polymer binder in the form of a coating, are discussed in this paper. Ceramic green parts require post-processing to remove the intermediate polymer binder and to impart strength properties to the ceramic bodies. In this paper, the use of ceramic cements and high temperature firing to realize strengths will be discussed. The effects of cement concentration and controlled drying rates on the strengths and dimensional accuracy of the ceramic bodies are also discussed.

Introduction

In recent years, in order for manufacturers to remain competitive, the need for the capability to rapidly prototype and develop objects has greatly increased. Concurrently, several novel approaches have emerged to realize rapid prototyping and development [1]. Most are processes which work by the layerwise addition of material. Polymers, with various properties, are the most predominant materials used by these processes although some are attempting to use high temperature materials such as ceramics and metals. While processes using the later materials are a few years away from fully realizing their goals, those processes which use polymers are making rapid progress in areas of application and resulting part quality.

Selective Laser Sintering (SLS) is one of these processes which has gained prominence in the area of rapid prototyping within the past few years. This process has proven itself extremely suitable to the handling of polymer materials. However, its usefulness is not limited to these materials. SLS has been successfully applied to other materials systems which either use an intermediate low-temperature binder or use direct sintering of high-temperature materials [2,3].

The use of low-temperature binders, namely, polymer binders in ceramic systems, has been described and proven effective as a means of producing shapes with good green strength, improved surface finish, and fine feature definition [4]. These "green" parts, however, require post-processing to remove the polymer binder and to impart greater strength. Greater strengths can be achieved by high-temperature firing to sinter the ceramic material. This method involves a certain amount of densification which results in shrinkage of the piece. Since most of the ceramic green pieces produced by SLS currently exhibit low relative densities, on the order of 40-50%, shrinkages involved to achieve desired strengths are large.

An alternative to high-temperature sintering is the use of ceramic cements to achieve strength. Infiltrating a green structure with a ceramic cement then processing it to remove

the polymer binder and cure the cement, is the proposed method of producing ceramic parts with good strengths and little dimensional change.

Materials and Methods

A sample of UCAR 430 Acrylic Polymer Latex was obtained from Union Carbide Corporation. UCAR 430 Latex is a styrene-methylmethacryate copolymer paint base. A sample of a polymethylmethacrylate (PMMA) latex exhibiting specific melt flow characteristics was provided by Rhome-Haas. The properties of these polymers are listed in Table 1. Silica and zircon were obtained from Ransom and Randolf, Inc. as Rancosil #4 and Zircon Flour 325, respectively. A sample of alumina was provided by Lanxide Corporation. The ceramic characteristics are listed in Table 2.

Three grades of inorganic ceramic cements were obtained from Aremco Products, Inc. These were Cerama-Bind™ products grades 542, 643, and 644. These binders are primarily silicate colloids which, upon curing, provide temperature resistances to 1750°C. In addition to these binders, three samples of *Ludox* Colloidal Silica were provided by E.I. duPont de Nemours & Co., Inc. These colloids and their properties are listed in Table 3.

Table 1. Polymer properties.

Polymer Latex	Particle Size, (nm)	Solids, (wt. %)	T_g, (°C)	M_w	Melt Index, (g/10min)
UCAR 430	320	45	45	200000	N.A.
PMMA	290	50	93	2000	20.0

Table 2. Ceramic powder characteristics.

Material	Purity, (%)	Particle Size, (μm)	Density, (g/cc)
Rancosil #4	99.8	63.0	2.25
Zircon Flour	99.8	17.0	4.56
Alumina	99.0	15.0	3.98

Table 3. *Ludox* Colloidal Silica properties

Grade	Type	Particle Size, (nm)	Solids, (wt. %)
SM	Silica	7	30
TM	Silica	22	50
AM	Silica/Alumina	12	30

Three samples of polymer coated ceramic materials were prepared using the method reported previously [4]. These samples included silica/zircon coated with UCAR 430, silica/zircon coated with PMMA, and alumina coated with PMMA. The material make-up and coating conditions for these samples are listed in Table 4. Samples #34 and #35 were admixed with pure ceramic materials to reduce their respective polymer contents to 15% vol (7.5 wt. % and 5.0 wt. %, respectively). This was done to further reduce the polymer content of the material, to enhance powder packing, and to introduce uncoated particle surfaces for interaction with ceramic cements during penetration. Admixing of polymer coated and uncoated particles was shown to improve observed bed densities without

significantly affecting the strength of the resultant SLS green part as long as the pure particle content was kept low [4].

Table 4. Coated ceramic powder make-up and coating conditions.

Sample #	Material	Content, wt. (vol.)	Feed Solids (wt. %)	Temp. (°C) Inlet	Temp. (°C) Outlet	Atomizer Speed, rpm
28	Silica	60.0 (62.8)	50	150	60	37500
	Zircon	30.0 (14.7)				
	UCAR 430	10.0 (22.5)				
34	Silica	60.0 (65.0)	50	175	82	37500
	Zircon	30.0 (15.2)				
	PMMA	10.0 (19.8)				
35	Alumina	90.0 (80.0)	50	175	88	37500
	PMMA	10.0 (20.0)				

Selective Laser Sintering

All materials were SLS processed using an SLS™ Model 125 equipped with a 25 watt CO_2 laser. SLS processing occurred in a nitrogen environment and with elevated bed temperatures. SLS processing conditions for the three powder samples are listed in Table 5. Several parts were made from each powder sample. Specifically, test bars with dimensions 1"x5" and 1"x3" with total thicknesses ranging from 20-80 layers were produced as were square parts with dimensions ranging from ¼" to 2" with thicknesses of ¼".

Table 5. Selective Laser Sintering operating conditions

Sample	Power, (W)	Layer Thickness, (mil)	Beam Spacing, (mil)	Scan Speed, (ips)	Temp., (°C) Bed	Temp., (°C) Air
28	12	5, 6	2, 5, 8	150	40, 50, 60	90
34	10	5	2	100	70	70
35	10	3, 4	2	20-100	80	35

Post-Processing of SLS Parts

SLS processed parts were brushed to remove loose powder and their densities were determined. Test samples were subsequently infiltrated with a ceramic cement material. Infiltration was performed simultaneously by capillary action and by dripping the infiltrating material onto part edges. Once a part had been infiltrated it was allowed to dry for an extended period at ambient conditions. When drying was complete residual moisture was removed by firing for one hour at 200°C. Polymer binder was then removed by firing for an additional one hour at 400°C. Following removal of polymer binder, parts were re-infiltrated with cement material, dried, and residual moisture removed by firing for an additional one hour at 200°C. The mass of each part was measured at the end of each step during the post-processing. Following the second curing, the strengths of several parts were determined by four-point bend analysis. Other samples were fired at high temperature using the firing cycle shown in Figure 1. Strengths of these fired parts were also determined by a four-point bend analysis.

126
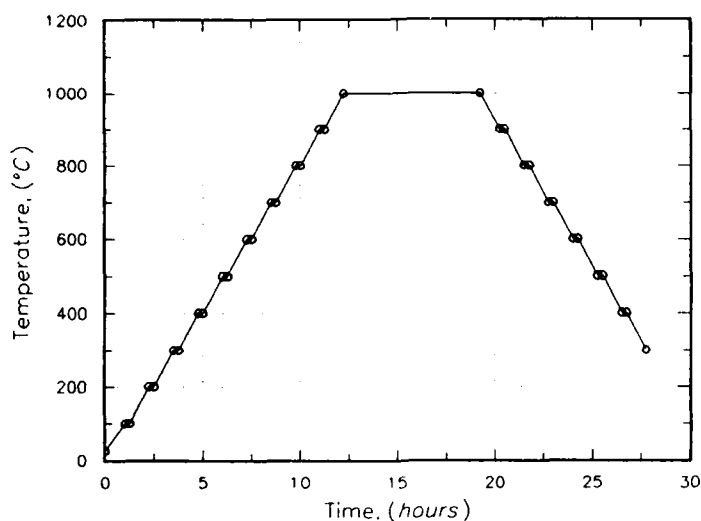
Figure 1. High temperature firing cycle.

Results and Discussion

All test parts made from the three powder samples had sufficient green strengths to permit handling and exhibited good surface finishes as well as good edge definition. Not surprisingly, test parts made from the alumina powder sample exhibited finer features due to its smaller particle size. Test bars made from each of the three powder samples, #28, #34, and #35, were determined to have relative densities of 39.5±1.4, 41.3±1.4, and 45.1±1.2, respectively. Densities increased slightly with increased part thicknesses.

Penetration experiments were conducted on parts made from all three powder samples. Initially, test pieces made from powder sample #28 (UCAR coated silica/zircon) were penetrated with the Cerama-Bind™ materials. However, during the first penetration tests of these pieces, it became apparent that the viscosities and surface tensions of these cements were too great to permit effective penetration. In a 1"x3" bar, infiltrated by capillary action, the penetration front would scarcely advance ¼" before no further movement of the front could be observed.

The viscosities and surface tensions were altered by diluting the cement materials with water. None of the three grades, however, was stable to the addition of water although the 643 grade took at least 24 hours to gel. Even when diluted to 50% by volume with water the 643 still did not penetrate test samples effectively. Subsequently, the binders were diluted with methanol to further reduce their surface tension. Only the 644 grade proved stable to the addition of methanol and penetration tests using this solution proved excellent. Test bars penetrated with a 50% by volume solution of 644 and methanol were wetted easily and completely within a few minutes.

Eight test bars were processed as described earlier using the binder-methanol solution. Three test bars failed after the polymer burnout stage of the post-processing, essentially turning to dust when moved. This weakness at the polymer burnout phase was attributed to the polymer coating which apparently leaves too few exposed ceramic surfaces to which the cement can bind. Extreme care was taken to not damage the

127

remaining test bars during post-processing. Also, the initial binder penetration step was altered to try to increase the uptake of cement. Further penetrant was drawn though the bar by placing it on dry towel and dripping more solution onto the surface. The dry towel would draw moisture from the bar thus pulling more material from the surface. This was done on all edges of the bar until no further moisture could be drawn from the bar by dry paper.

The results of mass changes of these test bars were all very consistent. A typical sample gained approximately 0.22 g/g of green material after the drying period. This amount dropped to 0.21 g/g of green material after firing at 200°C, indicating the low moisture content of the dried sample. Following polymer burnout the mass loss was 0.11 g/g of green material, corresponding to a polymer content of 9.6 wt. %. This is in agreement with the expected value of 10 wt. %. When infiltrated a second time a bar typically gained an additional 0.15 g/g of material after drying and firing at 200°C. This results in a typical mass gain of 41% or 0.29 g/g of polymer free material. Initial and final axial measurements are summarized in Table 6.

Table6. Summary of test bar dimensions

Part #	x, (%)	y, (%)	z, (%)	mass, (%)	Final Density, (%)
14	-2.34	-2.33	-1.32	39.3	45.7
15	-2.40	-2.27	-1.29	41.6	47.2
16	-2.37	-2.46	-1.30	42.2	46.4
20	-4.27	-4.35	-2.00	40.4	47.6
21	-3.41	-3.36	-1.66	41.2	46.5
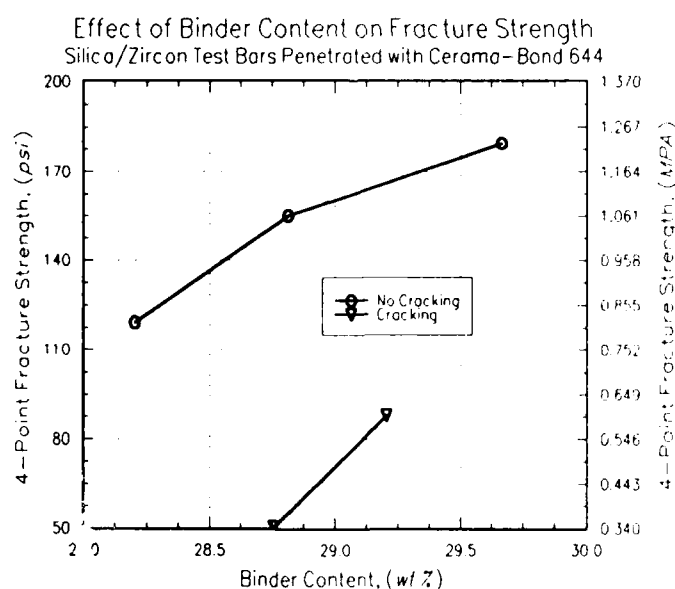
Figure 2. Effects of binder content.

Figure 2 shows the results of fracture strengths on the parts listed in Table 6. These data clearly show an increase in the resultant strength with increased cement content. The difference between the two sets of data shown in Figure 2 are attributed to the drying

128

conditions for the test bars. Those bars showing a higher fracture strength were dried on an open counter top while the remaining bars were dried in a vent hood with the vent operating. While all parts showed some warpage after drying, only those dried in the vent hood exhibited pronounced cracking of the exposed surfaces. It is presumed these cracks resulted from non-uniform shrinkage of the exposed surfaces due to an increased drying rate caused by the induced air flow of the vent. According to Mujumdar [5], in the drying of clay materials fast drying rates result in a case-hardening. Exposed surfaces shrink about the incompressible core and, as the inner material shrinks, the case will be unable to conform resulting in cracks at weak points. Cracking in these parts occurred primarily along layer boundaries. These large cracks apparently significantly reduced the strength of the bars.

In this series of experiments, both part failure following polymer binder removal and surface cracking during the drying phase severely affected the resultant part properties. In an attempt to eliminate these features of the post-processing modifications were made to the powder material and to the drying step. The powder material was altered, as described previously, by the addition of uncoated ceramic powder to the coated powder stock. This introduced exposed particle surfaces for interaction with the penetrating ceramic cement. The drying step was altered by drying infiltrated parts in a humidity controlled environment. With this modification the effective drying rate could be changed with the intent to try to reduce or eliminate cracking.

Several square pieces made from the two additional powder samples were infiltrated with a *Ludox* TM 50% by volume solution of 0.3% wt. Dupanol-ME surfactant in water. These cubes were dried in an 80% relative humidity environment at a temperature of 72°F for two days. No cracking was observed in these pieces. Following polymer binder removal all parts were significantly more rigid than samples previously observed.

Test bars, 1"x3"x¼", made from the alumina powder, were infiltrated with the Ludox TM colloid and fully processed as in previous experiments. A portion of the bars were tested for strength. The remaining portion of bars were fired at high-temperature prior to strength testing. A typical bar had a fracture strength of 1.86 MPa (270 psi) before firing and had a fracture strength of 14.55 MPa (2110 psi) after firing for 17 hours at 1000°C. X-ray analysis of the fracture surface fired bars indicated the composition of silica to be homogenous throughout the sample. From mass changes the silica contents of these bars were determined to be about 22% wt. Dimensional shrinkages were approximately 1.0% in all directions. The increase in silica and the small amount of shrinkage resulted in a typical relative density of 61.1%.

A number of turbine core samples were made from the alumina powder and post-processed in the manner just described. A representative core is shown if Figure 3. This part is approximately two inches square and, as can be seen in the figure, the definition of the part is excellent.

Conclusions

The use of ceramic cements has been shown to be an effective path to the production of full strength ceramic pieces from green objects produced by Selective Laser Sintering. While the results are very encouraging there are some issues which must be resolved. Some of these issues which are currently under investigation are the effects of drying conditions, firing cycles, the improvement of penetration, and the type of ceramic cement best suited to the process.
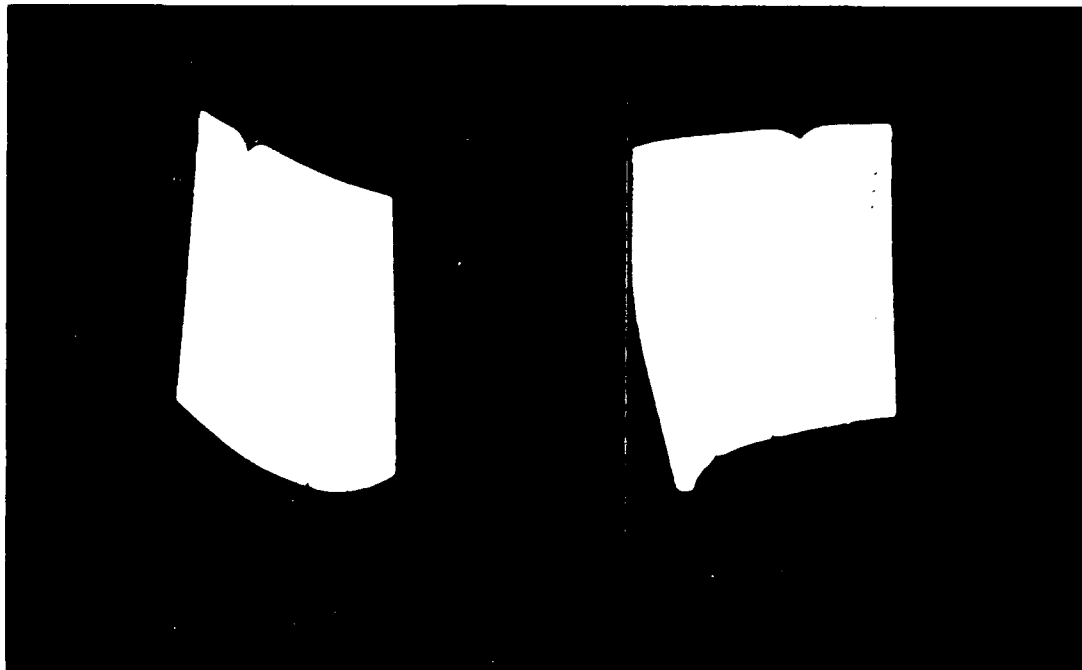
Figure 3. Turbine blade core.

References

1.   D.L. Bourell, et.al., "Solid Freeform Fabrication: An Advanced Approach", *Solid Freeform Fabrication Symposium Proceedings*, 1, 1-7 (1990).
2.   U. Lakshminarayan, "Selective Laser Sintering of Ceramic Materials", Ph.D. Dissertation, The University of Texas at Austin, 1992.
3.   W. Weiss and D.L. Bourell, "Selective Laser Sintering to Produce Ni-Sn Intermetalics", *Solid Freeform Fabrication Symposium Proceedings*, 2, 251-258 (1991).
4.   N.K. Vail and J.W. Barlow, "Effect of Polymer Coatings as Intermediate Binders on Sintering of Ceramic Particles", *Solid Freeform Fabrication Symposium Proceedings*, 2, 195-205 (1991).
5.   A.S. Mujumdar, Ed., 1987, <u>Handbook of Industrial Drying</u>, (New York: Marcel Dekkar).

THE MEASUREMENT OF THE THERMAL PROPERTIES AND ABSORPTANCES OF POWDERS NEAR THEIR MELTING TEMPERATURES

Samuel S. Sih and Joel W. Barlow
Chemical Engineering Department
University of Texas at Austin
July 15, 1992

Abstract

A new technique, using a laser as the heating source, has been adopted to measure the heat capacities, thermal diffusivities, thermal conductivities, and absorptances of powders (especially polymer powders) near their melting temperatures. This makes use of an unsteady state process. The data of the thermal conductivities obtained through this technique below 100°C are in concord with the values obtained through the other techniques, which predicts well for the use of this technique for still higher temperatures, up to the melting temperatures of the powders to be investigated.

Introduction

In the SLS process, a thin layer of powder is spread over a base and a computer-program-controlled laser scans and selectively sinters the layer. This process is continued until the part is generated. The unsintered powder part is brushed off after the entire job. Knowledge of the thermal properties, especially heat capacities, thermal diffusivities, thermal conductivities, and absorptances of powders, is essential to the study of many technical processes, including Selective Laser Sintering (SLS). This paper reviews the ways for measuring the thermal conductivities and thermal diffusivities of powders found in the literature and shows the data of the thermal diffusivities and thermal conductivities of some powders at temperatures below 100°C obtained through a method adopted agreed well with the values obtained through other methods. And this predicts well for the effective use of this technique for still higher temperatures, up to the melting temperatures of the powders.

Literature Review

The heat capacities and the thermal conductivities of the material powders at various temperatures during the sintering process have a strong influence to the process of fabrication and the quality of the product, and should certainly be precisely investigated.

1. The Measurement of the Heat Capacities of Powders.

The specific heats of all the powders found are quite the same as those of the corresponding solids. This is because of the mass of the gas phase in the powder relative to that of the solid phase. A Differential scanning calorimeter (DSC), DSC-7 made by the Perkin-Elmer Company, has been used [1] to measure the heat capacities at various temperatures between 0°C and 100°C for all of the powders used. The heat capacities of the powders were found to be function of temperature. The specific heats of all the powders investigated increase as the testing temperature is raised. This method has been used to measure the heat capacities of four kinds of PVC powders, ABS, two kinds of nylons, a glass supplied by the Potters Industries, two waxes supplied by the BFGoddrich Company and tin [2].

2. The Measurement of Thermal Conductivities of Powders.

For the investigation of the thermal conductivities of solids, especially those of the powders, the following methods are possible to be used, and have been used by some investigators.

(1) Steady-State Methods

(a) Plate (or Disk) Method. C.H. Lees first reported a method in 1908 for measuring the thermal conductivity of a solid by supplying heat at the top of the sample rod at a constant rate Q by an electric heater, and extracting heat at the bottom by the heat sink. The two thermocouples

measure the steady-state temperatures T_1 and T_2. In this arrangement, the thermal conductivity, k, at an average temperature of $\frac{1}{2}(T_1 + T_2)$ is computed from

$$k = \frac{QL}{A(T_1 - T_2)} \qquad (1)$$

For the measurement of the thermal conductivities of poor conductors such as semiconductors, and of powders, the sample is put in the form of a plate or a disk, with the specimen length to width ratio being greatly reduced to a small fraction, because the smaller the length to width ratio, the smaller is the ratio of lateral heat losses to the heat flow through the specimen, and the shorter is the equilibrium time. And the k is also given by the above equation. The rate of heat flow into the specimen may be determined by measuring the power input to a guarded electrical heater [3-5], by measuring the heat flow out of the specimen with a guarded water-flow calorimeter [6] at the low temperature end, by a boil-off calorimeter [7-10] , or by a heat flow meter[11]. (The heater or the calorimeter is guarded by a guard cylinder or ring for the prevention of heat losses.) A double plate apparatus was also used by C.H. Lees in which the heat was generated in a thin plate heater sandwiched between two identical plates of the sample material. Half of the heat then flows out through each plate. Such an apparatus is used for the measurement of the thermal conductivities from 300°K up to 1800°K of poorly conducting solids or powders. For the application of this method, a definite temperature difference must be obtained, which sometimes reaches to 90 Centigrade degrees, and the surface of the higher temperature one is deformed, and the thermal conductivity measured will have less accuracy.

(b) Cylindrical Method. Callendar and Nicolson first reported this cylindrical heat flow method under steady-state conditions [12]. A heater placed along the axis of the cylinder produces a radial flow of heat Q and the temperatures T_1 at a radius r_1 and T_2. at r_2 are measured. The thermal conductivity is given by

$$k = \frac{Q \ln(r_2/r_1)}{2\pi L(T_1 - T_2)} \qquad (2)$$

where L is the length of the cylinder. The guard rings at the extremities of the cylinder prevent heat loss out of the ends.

(c) Spherical and Ellipsoidal Methods. The heater is a small sphere embedded in the center of the sample [13] and the thermocouples are at temperatures T_1 at a radius r_1 and T_2. at r_2. The thermal conductivity is determined from the following equation.

$$k = \frac{Q (r_2 - r_1)}{4\pi r_1 r_2(T_1 - T_2)} \qquad (3)$$

Sometimes a prolate ellipsoid method is used instead of the spherical form [14]. The cylinder, sphere, and ellipsoid methods are generally used for determining k of poorly   conducting solids at temperatures from 300°K up to 2500°K. The advantage of these methods is supposed to be that heat losses by radiation transfer are small, but this is often offset by difficulty in fabricating the sample forms. The temperature differences used in these methods are all comparatively large, which influence the measurements in their accuracy.

(2) Time-Dependent (Non-steady-State) Methods

(a) Transient Hot Wire Method. The line heat source method was originally developed by Stalhane and Pyk [15]. This method is also now used for the measurements on loose-filled materials such as powders [16]. In this method, a long thin heater wire which serves as a line heat source was embedded in a large specimen initially at uniform temperature. The heater is then turned on, which produces constant heat, q_l. q_l is the power per unit length. The temperature at a point in the specimen is recorded as a function of time. The thermal conductivity is given by the expression

$$k = \frac{q_l}{4\pi(T_2 - T_1)} \ln\frac{t_2}{t_1} \qquad (4)$$

where $(T_2 - T_1)$ is the temperature difference at two times t_1 and t_2.

(b) Thermal Probe Method [17]. This method uses the same principle as the transient hot line method, but is more practical, in which the heat source is enclosed inside a probe for protection and easy insertion into a specimen. The use of this method for testing the thermal conductivities of dry brick powder, dry dune sand, dry cement, mica powder [18], and other powders [19] has been reported.

(c) Transient Hot Strip Method [20]. In this method, a metal foil works both as a continuous plane heat source and a sensor of the temperature changes in the foil itself. The platinum strip is embedded inside the sample material [21]. A constant current is passed through the strip and the voltage increase at the end of the strip is recorded by a digital microvoltmeter. In order to obtain a constant current throughout the experiment, a stabilizing circuit is used. As the constant current passes through the strip, heat is generated and the temperature of the strip is raised. There is a transfer of heat from the strip to the sample material surrounding it. As the strip is thin and it might be assumed that the strip is surrounded by an infinite solid, a solution of the heat transfer equation may be found in the book by Carslaw and Jaeger [22]. The change in the temperature of the strip is dependent on the heat flow between the strip and the surroundings, the thermal conductivity of the sample material, and the time of the passing of the constant current. As the resistivity of the metal strip increases when the temperature of the strip is raised, the electrical resistance of the strip and the voltage difference across the two ends of the strip all increase. So the voltage difference change may be used to show the temperature of the strip at various times from the start of the experiment. From the voltage vs. time curve of the circuit, one may calculate the thermal conductivity of the sample powder surrounding the strip, with known values of temperature coefficient of resistivity (TCR), the geometrical dimensions of the strip, the starting electrical resistance of the strip, the constant electrical current, the bulk density of the sample bed, and the heat capacity of the sample powder.

(d) The Water Baths Method [23, 24]. The thermal conductivities of powders are measured by an unsteady state method with two water baths of small temperature differences. The kinds of powders that have been investigated by this method include polycarbonate powder, four kinds of PVC powders, ABS powder, two kinds of Nylon powders, a purple wax, two kinds of glass powders, tin powder, and nickel powder. The range of the temperatures investigated, limited by the boiling point of water, was mainly from 30-90°C, i.e. below the sintering temperatures of the powders. As the temperatures used during the SLS process are not limited to the ambient temperatures, a new technique must be adopted in the pursuance of the further study for the higher temperatures.

Experimental Technique

For the measurement of the thermal diffusivities, thermal conductivities, and optical absorptances of the powder materials to be used for the fabrication up to their sintering temperatures, the following setup is used.

The method used here is a transient state one. This is owing to the fact that the steady-state experiments ordinarily use high temperature differences with long time of baking to reach the steady state, which will cause deformation of the powder surface and inaccuracy in the data obtained.

The technique developed by Ikeda et al. using laser as the heat source for the measurement of the thermal properties of the powders to be used is adopted [25]. As laser irradiation is the process used in the SLS fabrication, the use of laser as the heating source for the measurement of the thermal variables is certainly the best one to be chosen.

The experimental setup according to the Japanese workers is shown in Figure 1(a).

The Japanese workers used the finite slab configuration of the sample of theirs. For the convenience of doing experiments with powder samples, we used the semi-infinite bed configuration as shown in Figure 1(b). The principle of the experiment is to consider the heat transfer in the sample a one-dimensional conduction problem as in Figure 2.

133

(a)   (b)
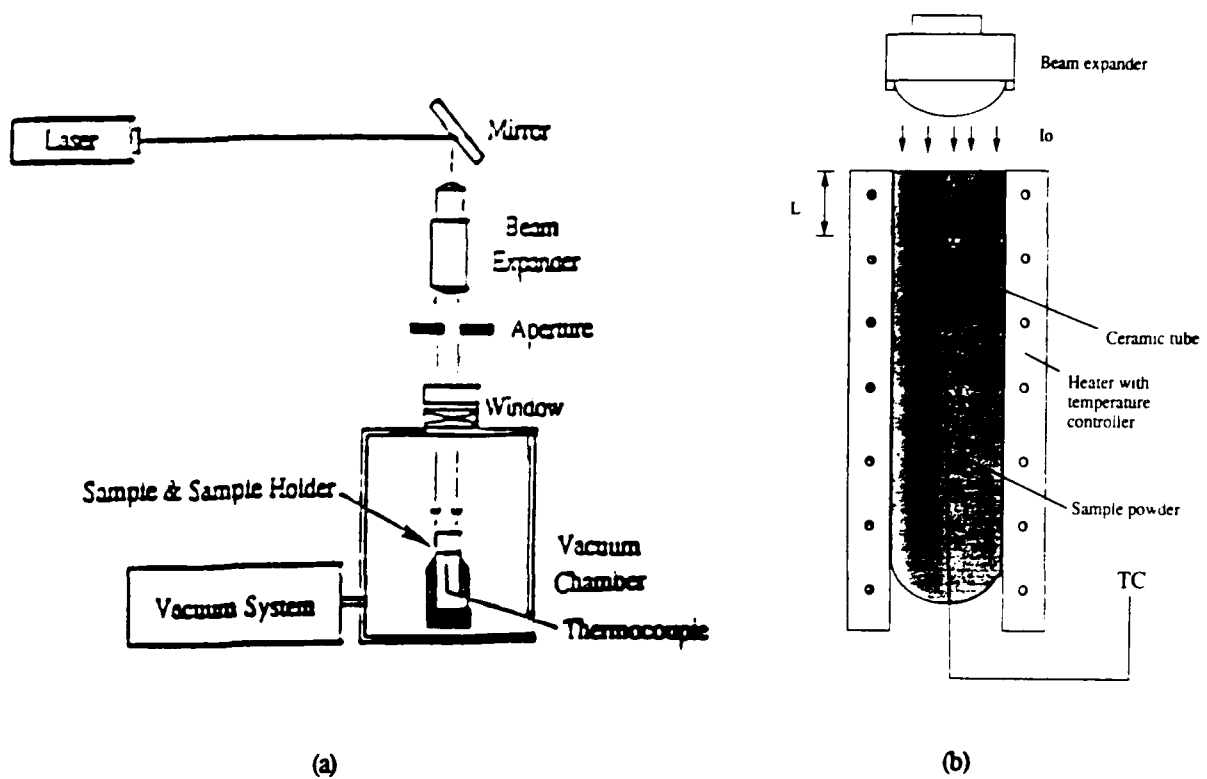
Figure 1. (a) The laser optical/thermal property measurement system; (b) the laser and the powder sample.
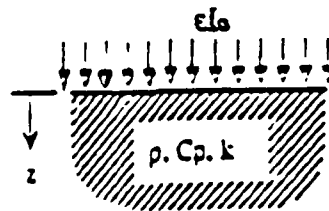
Figure 2. The 1-D conduction in a semi-infinite bed

The solution for this heat transfer problem is given as follows:

$$\Delta T(z,t) = \frac{2\epsilon I_o}{k} \sqrt{\alpha t} \, ierfc\left[\frac{z}{2\sqrt{\alpha t}}\right] \quad (5)$$

An example of the temperature rise curve (an explanatory one) is shown in Figure 3 to illustrate the principle for this method of measurement.

By defining the temperature rise ratio R as:

$$R = \frac{\Delta T(L, 2t_1)}{\Delta T(L, t_1)} \quad (6)$$

and with the Fourier number $Fo = \alpha t_1/L^2$, we may see from Equation (6) and Equation (5) that the relation between R and the Fourier number is independent of the material properties.

134
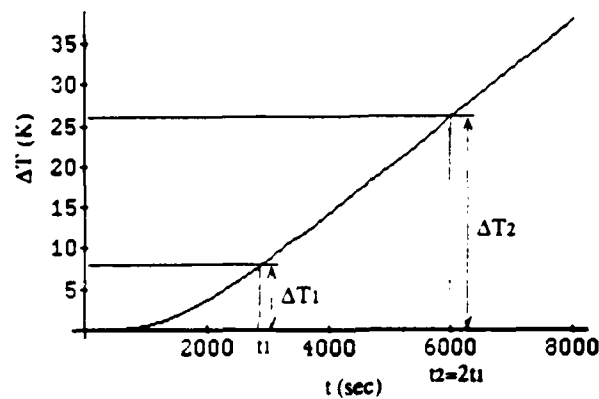
Figure 3. The temperature rise at z = L

The R vs. Fo relation for this case is shown in Figure 4. The curve is just a little lower than that for the finite-slab case.
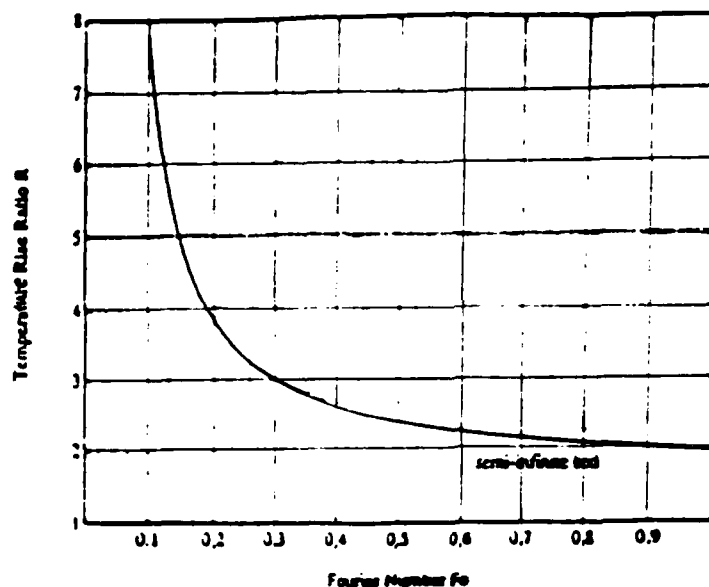
Figure 4. The R vs. Fo relations for semi-infinite bed configurations

When the heat loss to the environment is considered, one is to use the heat loss parameter a. When there is no heat loss, a =0, that will be the case of an experiment done in vacuum and at room temperature. For higher values of a, the R vs. Fo curves are a little lower than the no heat loss one. Their relationship for the finite-slab case is illustrated in Figure 5.

To determine the heat loss parameter a, as a is specific for the equipment, environment and the surface condition of the sample, etc., it is essential to do this by using a sample of which the thermal diffusivity is known beforehand, and if possible, just use a =0 for the case of doing the experiment in vacuum and at room temperature.

The thermal diffusivity of the sample may be found by measuring R from the temperature rise curve of the sample and finding the corresponding Fo value from Figure 4 and the following relationship:

$$\alpha = \frac{Fo L^2}{t_1} \qquad (7)$$

The thermal conductivity of the sample may be obtained by the multiplication of the thermal diffusivity α by the bulk density and the heat capacity of the sample powder.
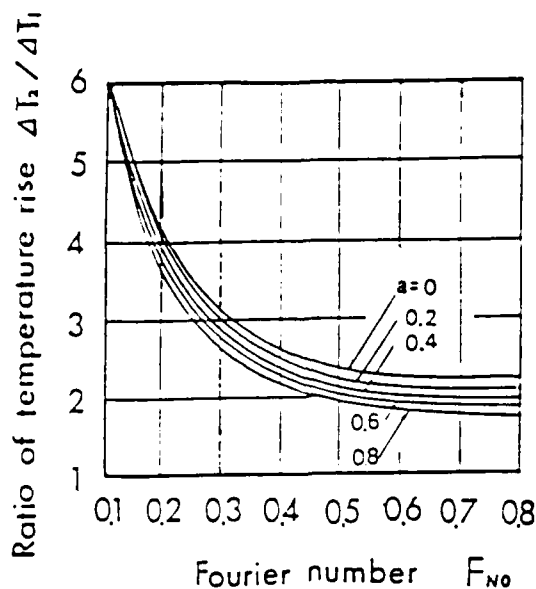
Figure 5. Relationships between the ratio of temperature rise and the Fourier number for various heat loss parameters in the finite-slab case.

For the surface absorptance, ε, one may use the following procedure:

(1) Measure the temperature rise of the sample powder vs. time. (2) Next, use the laser of the same power to irradiate the same sample covered by a thin layer of a material of which the surface absorptance is know beforehand, and measure the temperature rise vs. time curve once again. Owing to the following relationship,

$$Cp = \frac{\varepsilon I_0 A(t_2 - t_1)}{m(\Delta T_2 - \Delta T_1)} = \frac{\varepsilon_k I_0 A(t_2 - t_1)'}{m(\Delta T_2 - \Delta T_1)'} , \qquad (8)$$

one may calculate the surface absorptance of the sample, without knowing the quantity $I_0 A$.

Experimental Results and Analysis

Experiments are carried out using long tubes of powder samples (as shown in Figure 1) and the semi-infinite solution Eqn. (5). Nickel and Tin powders have been tested. A graph of a run of this experiment on nickel powder (porosity: 0.641) is shown in Figure 6.

In this run, the thermocouple was placed 1 cm below the surface of the powder bed. The starting bed temperature (room temperature) was 22°C. Take t_1 to be 120 sec; $2t_1 = 240$ sec. It may be found that $R = \frac{(\Delta T)_2}{(\Delta T)_1} = \frac{18}{5} = 3.6$. Fo is found from the graph of the relationship between R and Fo to be 0.23, assuming a = 0.2.

$$\alpha = \frac{Fo\ L^2}{t_1} = \frac{0.23 \times 1^2}{120} = 0.00192\ \frac{cm^2}{sec} = 1.92 \times 10^{-7} \frac{m^2}{sec} .$$

136
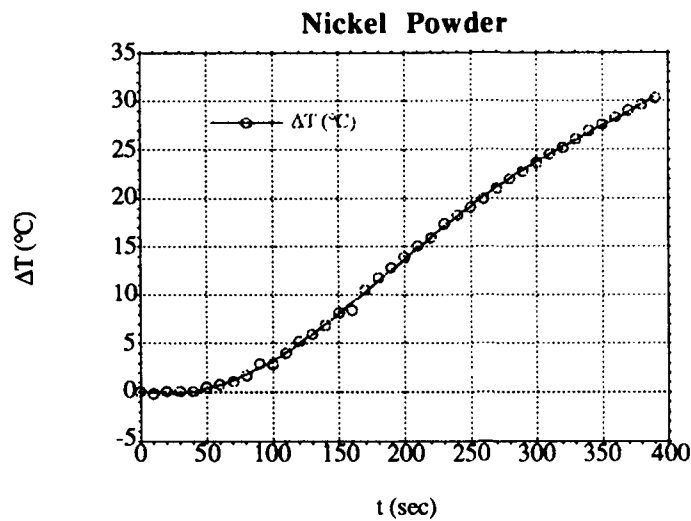
Nickel Powder

Figure 6. The temperature rise curve of nickel powder

Ni powder, k vs.T
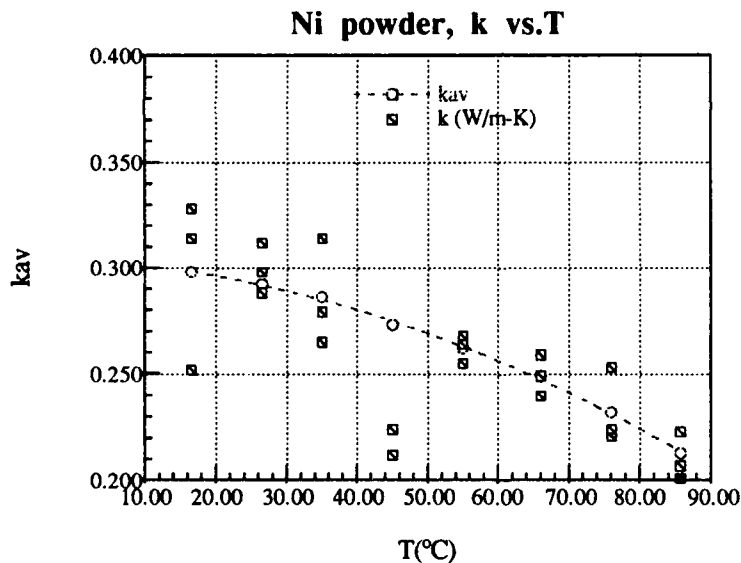
Figure 7. k of nickel powder (porosity:0.612) vs. temperatures graph. (Water baths method)

As $\rho = 3191.5 \frac{kg}{m^3}$ which is the bulk density of the powder used, and Cp of nickel is 443.5 $\frac{Joules}{kg\text{-}K}$, the thermal conductivity of the nickel powder is 0.272 W/m-K.

The k of nickel powder (porosity: 0.612) tested by the water baths method at various temperatures below 100°C are shown in Figure 7.

So the thermal conductivity of nickel powder found by the laser beam irradiation method is consistent with the values obtained by the water-baths method.

A graph of a run of this experiment on tin powder (porosity: 0.355) is shown below in Figure 8.

137

Tin Powder, 6

t (sec)
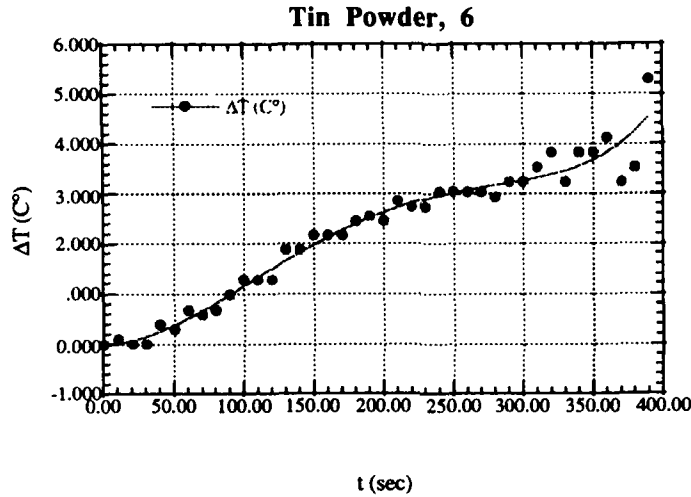
Figure 8. A temperature rise curve of tin powder

In this run, the thermocouple was placed 1 cm below the surface of the powder bed. The starting bed temperature (room temperature) was 25°C. Take t_1 to be 100 sec; $2t_1 = 200$ sec. It may be found that $R = \dfrac{(\Delta T)_2}{(\Delta T)_1} = \dfrac{2.7}{1.2} = 2.25$. Fo is found from the graph of the relationship between R and Fo to be 0.72, assuming a = 0.2.

$$\alpha = \frac{Fo\ L^2}{t_1} = \frac{0.72 \times 1^2}{100} = 0.0072 \ \frac{cm^2}{sec} = 7.2 \ \times 10^{-7} \frac{m^2}{sec}$$

k of Tin Powder vs. T(°C)

T(°C)
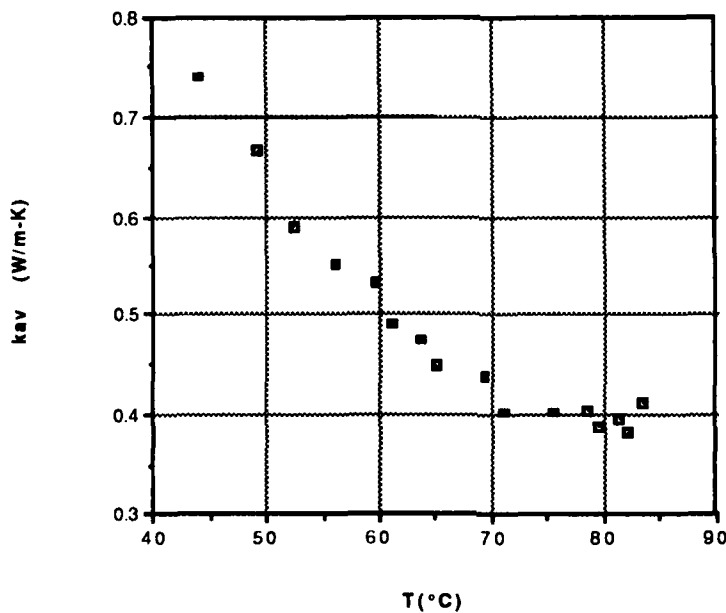
Figure 9. k of tin powder (porosity:0.417) vs. temperatures graph. (Water baths method)

As $\rho = 4704.5 \ \dfrac{kg}{m^3}$ which is the bulk density of the powder used, and Cp of tin is 230 $\dfrac{Joules}{kg\text{-}K}$, the thermal conductivity of the tin powder is 0.780 W/m-K.

138

The k of tin powder (porosity: 0.417) tested by the water baths method at various temperatures below 100°C are shown in the following graph.

So the thermal conductivity of tin powder found by the laser beam irradiation method is again consistent with the values obtained by the water-baths method.

Conclusion

As the water-baths method used by the authors for the investigation of the thermal properties of powders below 100°C must be changed for the investigation at higher temperatures, the new method adopted by the authors shows near results for thermal conductivity tests of the nickel and tin powder samples below 100°C to those obtained by the water-baths method. And this predicts well for the validity of this method for the investigation of the properties of powders near the sintering temperatures of the powders.

References

1. Xue, Samuel S. and Barlow, J.W., 'Thermal Properties of Powders', in the Solid Freeform Fabrication Symposium Proceedings, the University of Texas at Austin, Austin, Texas (1990), pp. 179-185.

2. Xue, S.S., Master's thesis, The Thermal Properties of Polymer Powders, the University of Texas at Austin, December, 1991, pp. 69-71, 76.

3. ASTM, 'Standard Method of Test for Thermal Conductivity of Materials by Means of the Guarded Hot Plate,' ASTM Designation : C177-63, in 1967 Book of ASTM Standards, Part 14, 17-28, 1967.

4. Poensgen, R., 'A Technical Method for Investigation the Thermal Conductivity of Slabs of Material,' VDI Zeitschrift, 56(41), 1653-8, 1912.

5. Jakob, M., 'Measurement of the Thermal Conductivity of Liquids, Insulating Materials, and Metals,' VDI Zeitschrift, vol. 66, 688-93, 1922.

6. ASTM, 'Standard Method of Test for Thermal Conductivity of Refractories,' ASTM Designation : C201-47 (1958), in 1967 Book of ASTM Standards, Part 13, 170-7, 1967.

7. Wilkes, G.B., 'Thermal Conductivity, Expansion, and Specific Heat of Insulators at Extremely Low Temperatures,' Refrig. Eng., Vol. 52 (1), 37-42, 1946.

8. Schröder, J.,'A Simple Method of Determining the Thermal Conductivity of Solids,' Philips Tech. Rev., vol.21(12), 357-61, 1959-60.

9. Schröder, J.,'Apparatus for Determining the Thermal Conductivity of Solids in the Temperature Range from 20-100 C,' Rev. Sci. Instr., vol. 34(6), 615-21, 1963.

10. ASTM, 'Tentative Method of Test for Thermal Conductivity of Insulating Materials at Low Temperatures by Means of the Wilkes Calorimeter,' ASTM Designation : C420-62T, in 1967 Book of ASTM Standards, Part 14, 172-9, 1967.

11. ASTM, 'Standard Method of Test for Thermal Conductivity of Materials by Means of the Heat Flow Meter,' ASTM Designation : C518-67, in 1967 Book of ASTM Standards, Part 14, 230-8, 1967.

12. Callendar, H. L. and Nicolson, J. T., 'Experiments on the Condensation Steam, Part I. A New Apparatus for Studying the Rate of Condensation of Steam on a Metal Surface at Different Temperatures and Pressures,' Brit. Assoc. Adv. Sci., Rept. Ann. Meeting, 418-22, 1897.

13. Laws, F. A., Bishop, F. L., and McJunkin, P.,'A Method of Determining Thermal Conductivity,' Proc. Am. Acad. Arts Sci., Vol.41 (22), 455-64, 1906.

14. Adams, M. and Loeb, A. L., ' Thermal Conductivity: II. Development of a Thermal Conductivity Expression for the Special Case of Prolate Spheroids,' J. Am. Ceram. Soc., Vol. 37(2), 73-4, 1954.

15. Stalhane, B. and Pyk, S., 'New Method for Measuring the Thermal Conductivity Coefficient,' Tekn. Tidskr., Vol. 61 (28), 389-93, 1931.

16. Touloukiau, Y.S., Powell, R.W., Ho, C.Y., and Klemens, P. G., edit., Thermophysical Properties of Matter, the TPRC Data Series, Vol. 1, Thermal Conductivity, Metallic Elements and Alloys, p. 24a.

17. Hooper, F.C. and Lepper, F. R., 'Transient Heat Flow Apparatus for the Determination of Thermal Conductivities,' Heating , Piping and Air Conditioning. ASHVE J. Sect. 22(8), 129-34, 1950.

18. Pande, R.N., Saxena, N.S., and Chaudhary, D.R., 'Measurement of Effective Thermal Conductivity of Building-Construction Materials at Different Interstitial Air Pressures,' Indian Journal Of Technology, Vol. 22 February, pp. 66-69, 1984.

19. Saxena, N.S., Chohan, M. Aslam and Gustafsson, S.E.,'Effective Thermal Conductivity of Loose Granular Materials,' J. Phys. D: Appl. Phys. vol. 19 (1986) 1625-1630.

20. Gustafsson,S.E., Karawacki, E. and Khan,M.N., J. Phys. D: Appl. Phys. vol.12, 1411.

21. Singh, R., Saxena, N.S. and Chaudhary, D. R., 'Simultaneous Measurement of Thermal Conductivity and Thermal Diffusivity of Some Building Materials Using the Transient Hot Strip Method,' J. Phys. D: Appl. Phys., vol. 18 (1985) 1-8.

22. Carslaw, H.S., and J. C. Jaeger, Conduction of Heat in Solids, Oxford University Press, Oxford, 1959, p.112; 256-263.

23. Dieter Naumann and Klaus-Jürgen Seydel, "Messung der Wärmeleitfähigkeit von Pulvern," Plaste und Kautschuk, vol. 30, no.4 (1983), p. 233-234.

24. Xue, Samuel S. and Barlow, Joel W., 'Thermal Properties of Powders', in the Solid Freeform Fabrication Symposium Proceedings, the University of Texas at Austin, Austin, Texas (1990), pp. 179-185.

25. Taniguchi, N., Ikeda, M., Miyamoto, I., and Miyazaki, T., Energy-Beam Processing of Materials, Clarendon Press, Oxford, 1989.

26. Ikeda, M. et al., 'Basic Techniques of Laser Processing,' Precision Machinery,(in Japanese) vol.51 (1985), no. 12, pp. 2253-2258.

Metal Parts From Selective Laser Sintering of Metal-Polymer Powders

B.Badrinarayan, and J.W.Barlow
Dept. of Chemical Engineering,
The University of Texas at Austin,
Austin,Texas- 78712,U.S.A.

Abstract

This paper deals with the manufacture of metal parts using polymer as an intermediate binder. Copper electrodes for Electric Discharge Machining were made by Selective Laser Sintering of copper - polymethylmethacrylate powder mixtures followed by gradual binder burnout and subsequent metal sintering. The low density of the fired parts obtained from the present process method results in low strength and mechanical properties. Polymer coating of the metal powder as well as use of optimal particle size distributions can result in higher densities and strengths.

Introduction

Selective Laser Sintering for manufacture of metal parts by using a polymer binder is being developed at University of Texas at Austin. In this process a polymer is used as a binder for the metal powder in SLS processing to form a green metal part. The green part is subsequently fired under reducing conditions to obtain the pure metal part. The SLS process has been described in detail in literature[1, 2]. We are currently using Polymethylmethacrylate (PMMA) as the polymer binder for copper powder in SLS. PMMA has good flow, is stable under the laser beam, and readily decomposes cleanly to gas in a reducing atmosphere.

Results and Discussion

Copper Electrodes for Electric Discharge Machining(EDM) were manufactured using PMMA as binder in SLS followed by a gradual postprocessing step in a hydrogen furnace. Fig 1 shows the firing cycle used for the manufacture of the copper electrodes. Fig 2 shows the green and fired electrodes. The fired electrode was tried out for EDM to make a mold in a steel block and this was compared with an electrode made by investment casting. The electrodes made by SLS showed a high rate of erosion. This is due to the fact that the fired density of the copper parts was 48% of the theoretical density. We feel that increasing the final density of the parts would go a long way in making the parts competitive to those made by casting. Strength of a part is proportional to its porosity. Knudsen[3] reports that the equation by Bal'shin could satisfactorily represent the relation of some data on the porosity and tensile strength of porous sintered copper powder compacts. Equation (1) shows the relation between strength and porosity.

$$S = S_0 D^m \qquad (1)$$

where   S   = Strength of porous part

141

S_0 = Strength of the fully dense part

D = Relative density (1- porosity)

The value of m varies between 3 and 6 for metal-ceramics. The copper parts made by SLS showed a strength of 1164 psi which is about 4% of the tensile strength for copper.
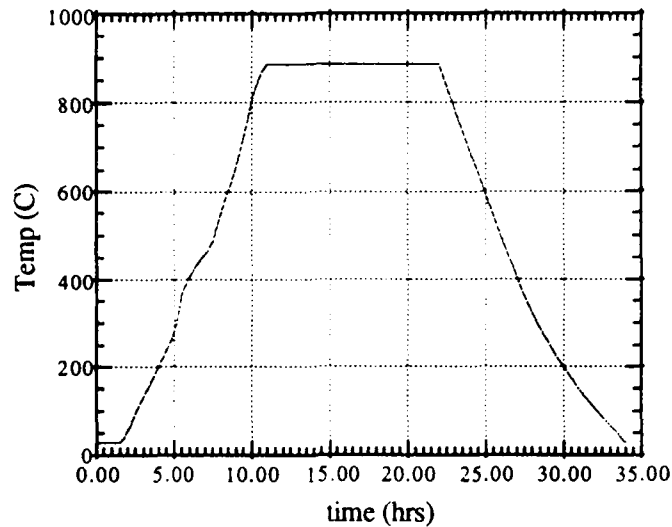
Fig 1. Firing Cycle for Copper-PMMA Parts
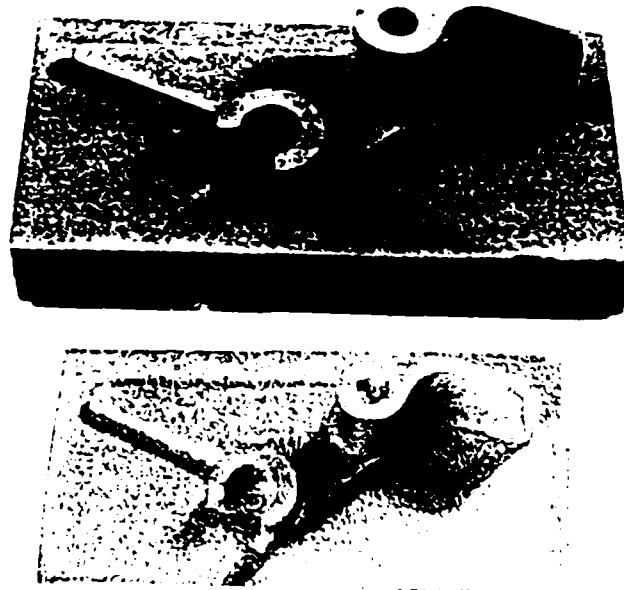
Fig 2. Green and Fired Copper Parts from SLS

High fired densities result from having a high green density and optimal firing conditions. Green density of parts can be enhanced by increasing the bed density in SLS. Reed [4] has reviewed the particle packing characteristics of powder systems. Use of mixtures of particle sizes increases the bulk density of powder compacts because the smaller particles can fit into the interstices between larger particles. Fig 3 shows the effect of bimodal distribution on packing density for a copper powder system. An increase of 12% in bed density is seen when we have 60% powder as large particles.
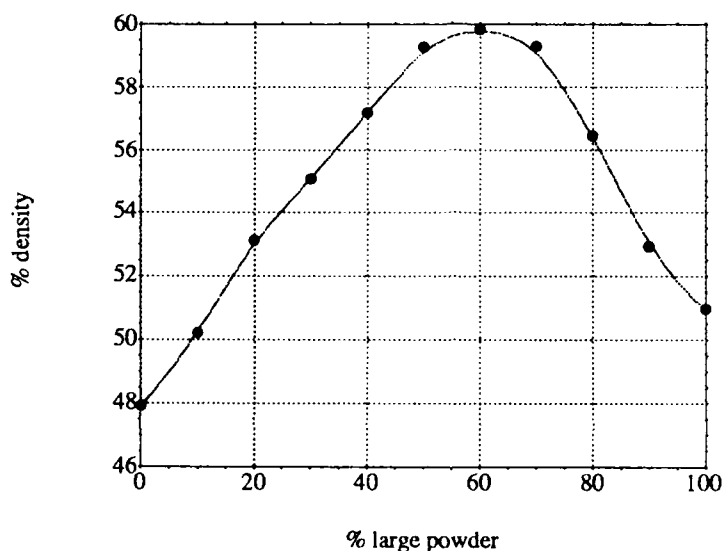
Fig 3. Effect of bimodal size distribution on bed density

Processing of polymer coated powders in SLS has shown that polymer coated powders on SLS processing yield parts that have greater green strength and density than mixed powders. This has been studied for the ceramic system[5]. The data for the polymer coated ceramic powder shows a twofold increase in strength for the same polymer composition. Moreover coated powders are homogenous in composition at all points. This provides the rationale for using coated metal powders for making metal parts. Coating of metal powders was carried out by suspending the metal powder in a polymer emulsion and spray drying the same. The result is a polymer coated metal powder which can be directly used for SLS processing. The main issue in the spray coating of the metal powder is that the metal powder settles down and clogs the feed tube and atomizer wheel in the spray dryer assembly. This problem was overcome by using a viscosity enhancing gum to prevent the settling. Figure 4 shows the atomizer used for spray coating metal. Fig 5 shows the solution viscosity data for different viscosity enhancers. A vaned atomizer was designed to prevent clogging in the wheel. The spray dryer operating conditions for coating copper (5-10 µm) with a UCAR 430 latex (styrene - methyl methacrylate - acrylic acid copolymer) and polyox 6000 as viscosity enhancer are given below :

143

Inlet temperature   =   125 ° C
Outlet temperature   =   150 ° F
Atomizer Speed   =   32000 rpm

Figure 6 shows the Scanning Electron Micrograph of a polymer coated copper agglomerate.

Top View

0.4655"

1/8"

0.236"
0.4375"

2.481"

1.0218"

Number of slots = 12

Cross Section

0.44"

0.16"
0.345"

0.32"

0.9375"

0.2065"
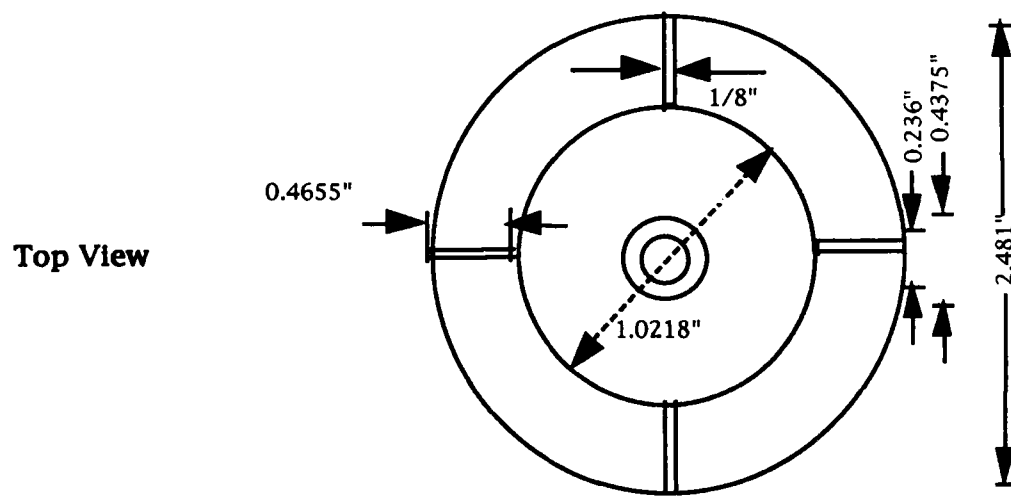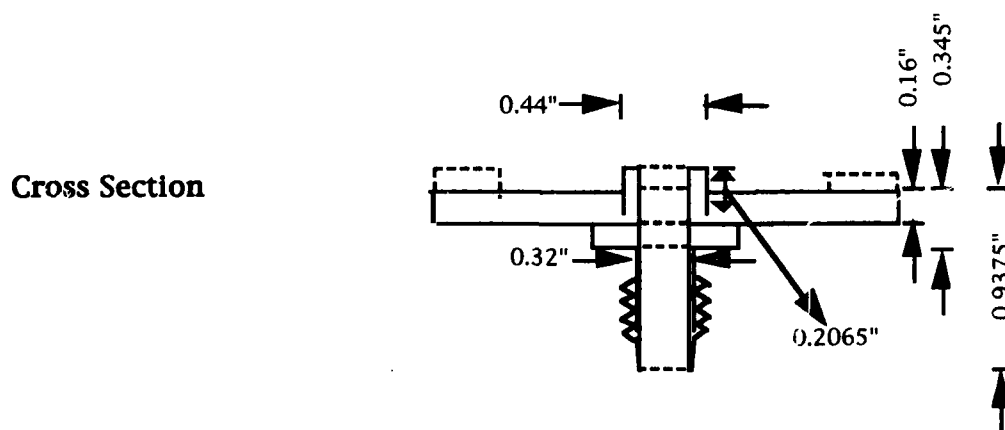
Fig 4. Vaned Atomizer Wheel for Spray Coating of Metal Powders.

144
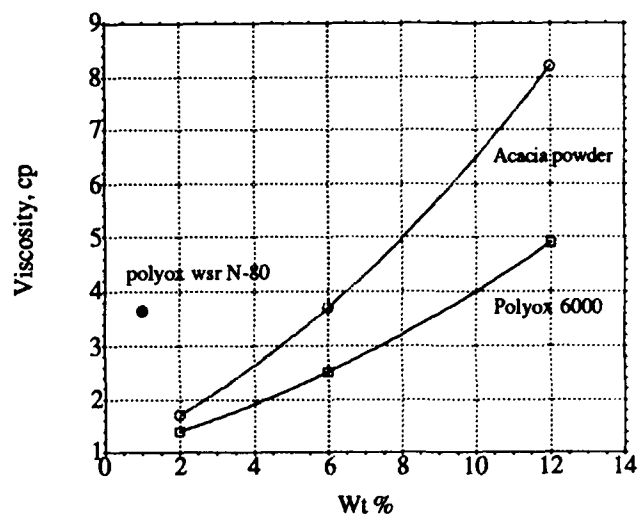
Fig 5. Viscosity vs concentration for different viscosity enhancers

Fig 6. SEM picture of Copper coated with UCAR430 polymer

Summary

The SLS process has been used to manufacture metal parts using polymer as an intermediate binder. This process would be profitable if we could manufacture high density metal parts. High fired density of parts depends on the green density of parts from SLS and the firing cycle. Future work will focus on use of polymer coated metal powders and optimzation of firing cycle.

References

1. Carl Deckard and Joseph Beaman, *15th Conference on Production Research and Technology*, University of California at Berkeley, p 623 - 630, (1989).
2. Harris L. Marcus, Joseph Beaman, Joel W. Barlow and David L. Bourell, *JOM*, **42**(2), p 8-10, (1990).
3. F. P. Knudsen, *J. of Am. Ceram.Soc.*, **42**[8], 376 - 387, (1959).
4. James S. Reed, " Introduction to the Principles of Ceramic Processing ", 185, (1988).
5. N. K. Vail and J. W. Barlow, *Proc. of the Solid Freeform Fabrication Symp.*, 195 - 204, (1991).

Development of a Selective Laser Reaction Sintering Workstation

B.R. Birmingham, J.V. Tompkins, G. Zong, and H.L. Marcus

Center for Materials Science and Engineering
The University of Texas at Austin
Austin, Texas 78712

Abstract

The purpose of this paper is to describe the design and operation of a Selective Laser Reaction Sintering workstation developed at The University of Texas. The workstation allows the study of solid freeform fabrication of reaction sintered materials on a research scale. The mechanical and control systems of the workstation are detailed, and Selective Laser Reaction Sintering as a technique is discussed including example material systems that are currently under study.

Introduction

Solid freeform fabrication (SFF) is any manufacturing process that produces a three dimensional part without the use of standard or part specific tooling. One form of SFF, Selective Laser Sintering (SLS), uses a laser to sinter selected areas of a powder bed. Additional layers of powder are spread on top of the first, and specific areas of each layer are scanned and sintered by the laser before the next layer is spread. In this way, a three dimensional sintered part is built up layer by layer. At the end of the process, the manufactured shape may be removed from the surrounding loose powder. Parts have been made from various polymers, metals and ceramics using this technique [1,2]. Selective Laser Reaction Sintering (SLRS) combines SLS with a simultaneous gas/powder reaction process known as reaction sintering or reaction bonding [3]. This simultaneous reaction typically involves the decomposition of a gas to solid or a gas interacting with a liquid or solid to produce another solid. The SLRS process has the potential of producing parts made of monolithic materials and composites that are difficult or impossible to sinter using SLS as well as producing microstructures that are unobtainable using standard sintering techniques.

Equipment

To be successful a SLRS system must accomplish three basic functions. These functions are 1) supply controlled laser power to a selected area, 2) provide multiple layers of a powder bed having proper thickness and density and 3) provide the

147

appropriate gas environments including vacuum. An overall schematic of the SLRS system is seen in figure 1.
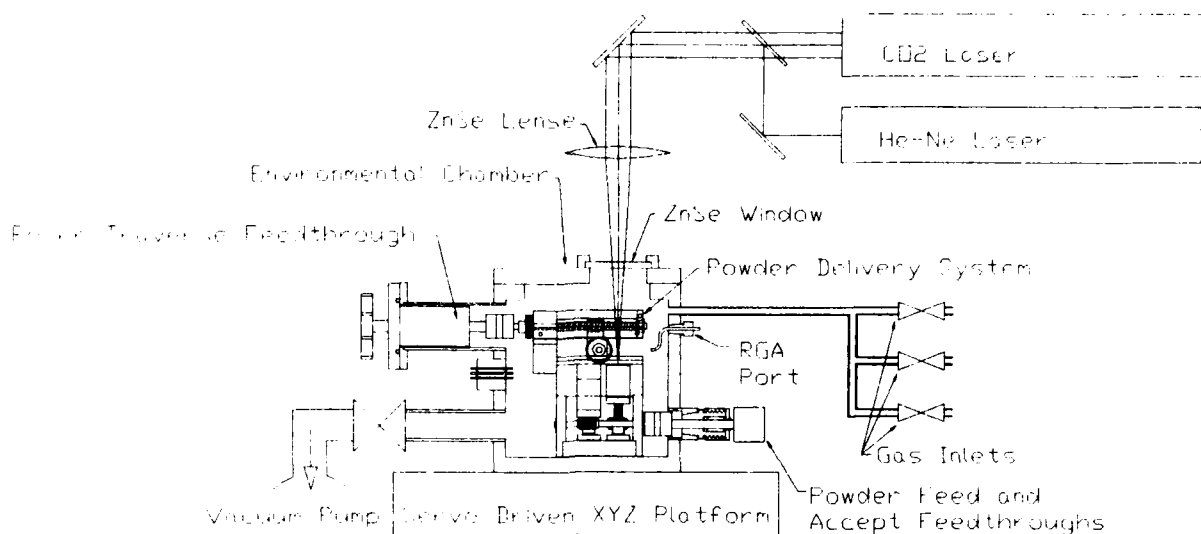
Figure 1.

With the exception of the powder delivery mechanism, the basic arrangement of this system has been previously described in the literature [4]. The laser beam from a 25 watt CO_2 laser is directed onto a substrate that is located in an environmentally controlled chamber. A motor driven X-Y table moves the chamber/substrate under the stationary beam effectively "scanning" the beam. Both laser power and X-Y table controls have been upgraded for this workstation. Laser power fluctuations have been reduced to less than 5% of setting by using a pulse width modulation controller developed at the University [5]. Power level can be adjusted manually or by computer. Positional accuracy of the table/beam is now better than $20\mu m$ and repeatability better than $5\mu m$ at scan speeds to 3mm/sec using a computer controlled dc servo system.

Environmental control is achieved by locating the powder delivery mechanism/substrate inside a vacuum chamber. The chamber has three independent gas inputs with the emphasis on flexibility due to the research nature of the system. The gas inputs have allowed for the introduction of a variety of gases including N_2, N_2/H_2, NH_3, Ar, H_2, O_2, CH_4, and C_2H_2. The chamber is currently set up for static gas environments, but minor modifications could easily make it a flowing gas system if desirable. Mechanical pumping initially provides 10^{-3} Torr vacuum to minimize gas impurity content. Mechanical and resistance vacuum gauges monitor system pressure. Power and thermocouple feedthroughs provide the ability to heat substrates and monitor and control temperature using a PC based data acquisition system. A gas sampling port has also been included to enable connection to a gas analyzer system(RGA). This will be used to gather information about reactants and by-products during the reaction sintering process. Mechanical feedthroughs currently enable manual operation of the powder delivery mechanism. The mechanism will be automated in the future.

148

The powder delivery system is similar in concept to one previously reported [6], but considerable miniaturization was required to fit the entire mechanism inside the available five inch diameter by 5 inch in height vacuum chamber . A schematic and photograph can be seen in figures 2 and 3. Two rotation feedthroughs marked Powder Feed and Powder Accept are coupled to worm/gear/leadscrew arrangements that ultimately drive the powder feed and powder accept pistons up and down in their respective cylinders. The rotation feedthrough marked Roller Traverse drives a spur gear/leadscrew arrangement that causes the roller to traverse across the top of the stage.
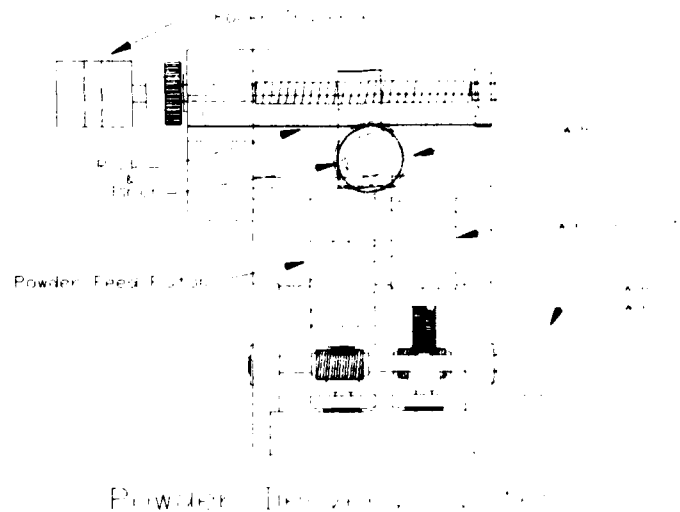
Figure 2.
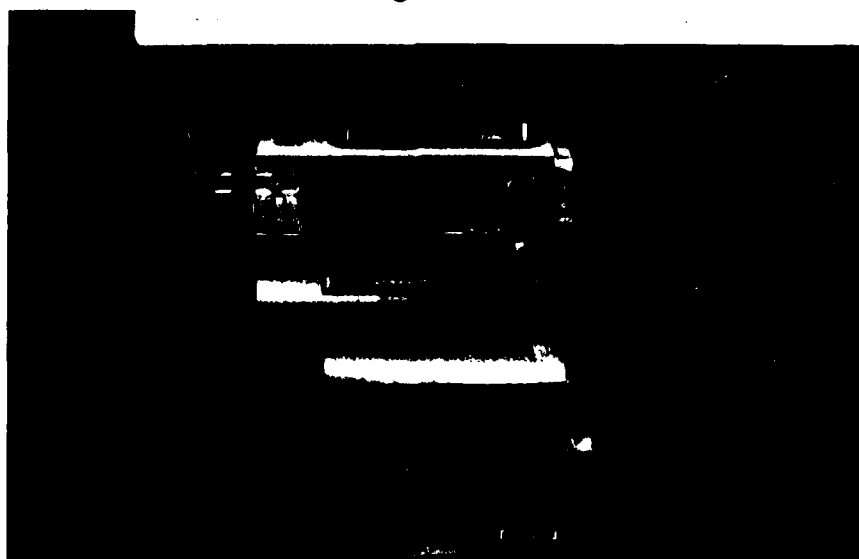
Figure 3.

During a standard production cycle the system starts with the traversing roller to the far left, the powder feed piston would be down and its cylinder full of powder, and the powder accept piston would be up. Powder is made available to the roller by raising the powder feed piston an incremental amount. The roller is then traversed across the

149

stage and then back, spreading the powder into a thin layer. As the roller traverses, a rack and pinion causes the roller to spin so that the roller surface in contact with the powder is actually moving in a direction opposite to traverse direction. This is done for improved powder spreading. After the new powder layer is spread, a laser scan is performed, sintering specific areas of the powder layer above the powder accept piston. When the scan is complete, the powder accept piston is lowered some specified layer thickness. The powder feed piston is again raised, providing another incremental amount of powder. The roller is brought across the stage, spreading a fresh layer of powder over the powder accept piston and the previously sintered layer. The laser is scanned again resulting in a second sintered layer. The powder accept piston is lowered and the process is repeated until the part has been built up layer by layer. Maximum part size from this mechanism is roughly a 1.5cm by 1.5cm by 1.5cm cube. The gearing of the mechanism enables layer thickness control to within a few microns. Working on this scale is advantageous when using difficult to make, hazardous or expensive materials because of the small amounts of precursor required to load the system. When the materials systems have been proven on this scale they can easily be adapted to a larger system.

Applications

Laser reaction sintering can be used in a variety of ways to produce a variety of results. The following discussion is by no means all inclusive, but is meant to give examples demonstrating some of the interesting aspects of this technique.

Standard pressureless sintering of oxides, nitrides, and carbides is difficult. However, formation of an oxide, nitride or carbide may be achievable by reaction sintering in the corresponding oxygen, nitrogen, or carbon rich atmosphere. One example is the reported success of sintering an aluminum/alumina mixture in the presence of oxygen to form an alumina pre-form [7]. These pre-forms will be infiltrated to create a metal-ceramic or ceramic-ceramic composite part.

Composite structures can be produced directly by partial conversion of powder by reaction. A multi-layer Cu-TiN part was produced by this SLRS system using a Cu-10Ti alloy as base material. Reaction sintering in a nitrogen atmosphere caused the Ti to migrate to the surface of the alloy particles where it reacted with nitrogen to convert to TiN. The result was a copper matrix with a sub micron TiN layer on each of the original powder particles. TiN presence was confirmed by x-ray diffraction and the dispersion of Ti rich areas(TiN) was mapped using EDS. Figure 4 shows a side view of a 6mm by 6mm by 3mm thick Cu-TiN rectangular solid made using SLRS. Note that the part is composed of 15 layers. The delamination observed can be eliminated with proper substrate pre-heating. The microstructure of the part can be seen in Figure 5, which contains a backscattering electron micrograph and a Ti element map of the same region. The element map clearly shows the Ti migration to the surface of the alloy particle where it formed a nitride coating on the particle. It is believed that proper control of powder size and operating parameters can result in very fine microstructures unobtainable by standard sintering techniques.

0043 10KV   X14   1mm WD39

Figure 4.

25KU X30   1 18 8U UTHSE
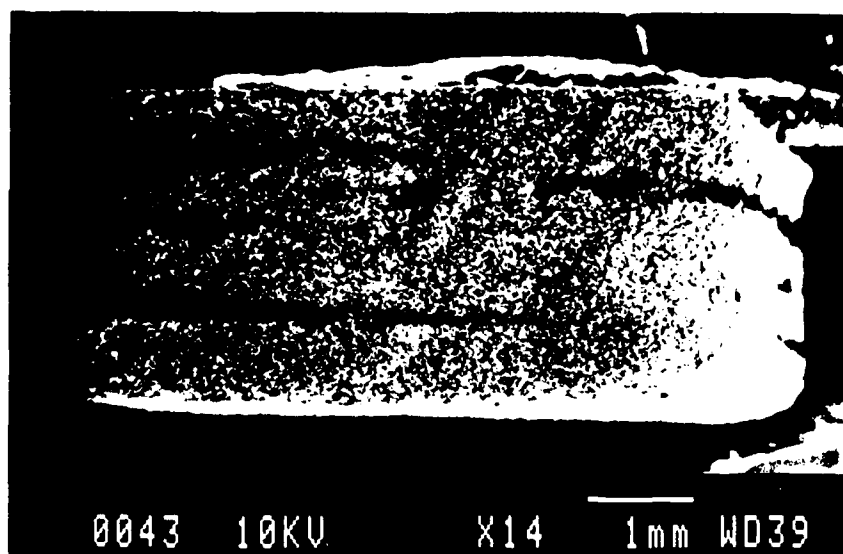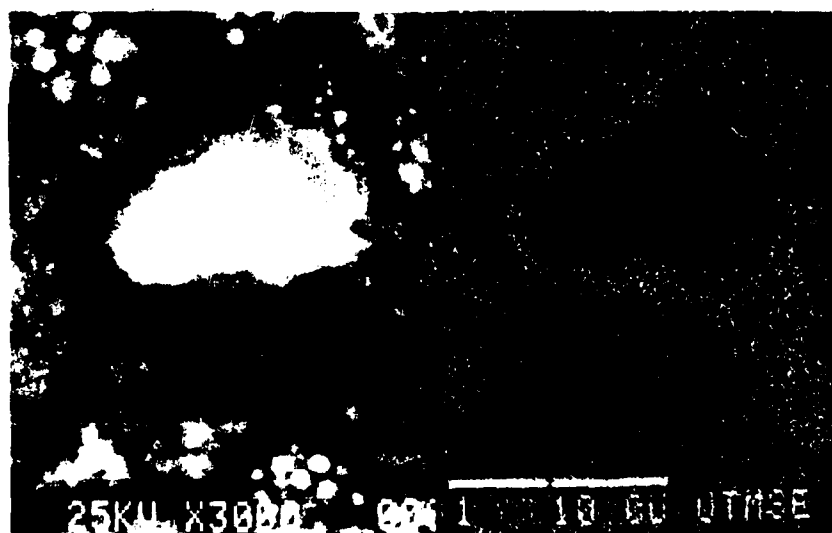
Figure 5.

A third technique involves laser sintering and simultaneous vapor deposition and infiltration. One system currently under study combines the pyrolitic formation of SiC from an organometallic gas precursor with the sintering of a SiC base powder. The pyrolitically produced SiC infiltrates the SiC base powder and binds it together. Single and multi-layer parts have been formed in this fashion. Figure 6 shows the side view of a single layer of SLRS SiC. Starting powder was 16μm SiC. Note the density variation through the layer. Figure 7 is the top view of a 6mm square by 1mm thick SiC rectangular solid. The six layer part was also made using 16μm SiC. Bonding between the layers is limited, but it is believed this can be improved by optimization of process parameters including laser power, gas pressure, powder size and layer thickness.

151
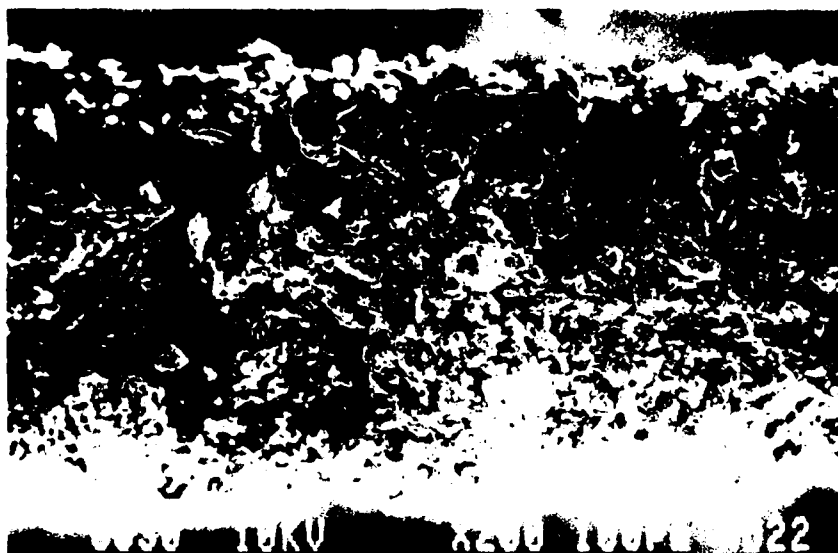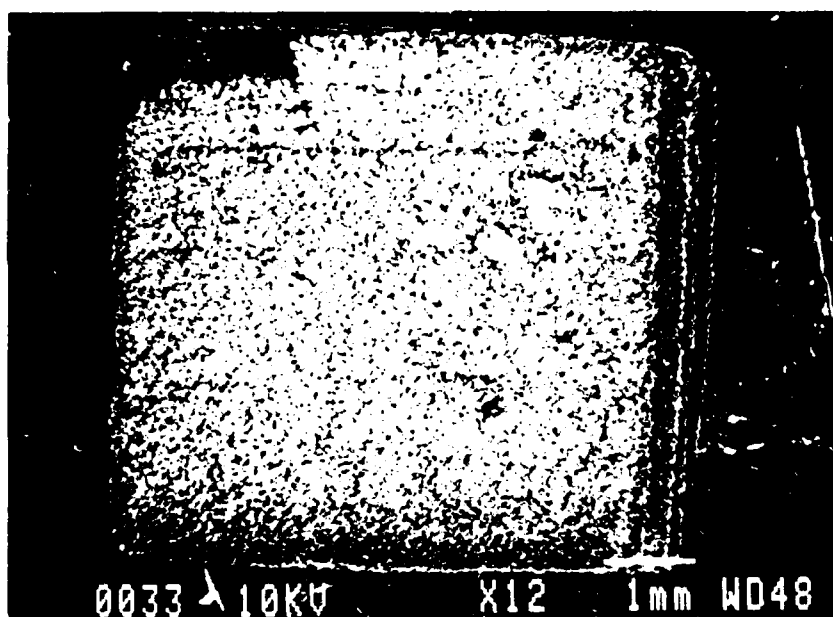
Figure 6.

Figure 7.

Conclusions

A Selective Laser Reaction Sintering workstation is in place and operational. It is capable of producing multi-layer solid freeform parts in an environmentally controlled chamber. This will enable the study of laser sintering combined with gas phase/powder reactions. It is believed that this combination is capable of producing materials and structures unobtainable by standard sintering techniques. Preliminary studies are positive.

Acknowledgments

References

1   Harris L. Marcus, Joseph J. Beaman, Joel W. Barlow, and David L. Bourell, "From Computer to Component in 15 Minutes: The Integrated Manufacture of Three-Dimensional Objects," JOM,42[4], 1990,pp. 8-10.

2   "Rapid Prototyping Systems," Mechanical Engineering, edited by Steven Ashley, April 1991, pg 41.

3   M.E. Washburn, W.S. Coblenz,"Reaction-Formed Ceramics," Ceramic Bulletin, Vol 67, 2, 1988, pp. 356-363.

4   Guisheng Zong, R. Carnes, H.G. Wheat, and H.L. Marcus, "Solid Freeform Fabrication by Selective Area Laser Deposition," Proceedings of the Solid Freeform Fabrication Symposium, Austin, Texas, August 6-8, 1990, pp. 83-90.

5   J.V. Tompkins, "Computer Control of Laser Intensity for Selected Area Laser Deposition," Masters Thesis, University of Texas at Austin, Austin, Texas, 1992

6   C. Deckard and J.J. Beaman; pp. 623-629 in Advances in Manufacture, Integration and Processes, Proceedings of the 15th Conference on Production Research and Technology, Berkeley, California, January 9-13, 1989. NSF Design, Manufacturing and Computer Integrated Engineering Division, Washington D.C., 1989.

7   P.K. Subramanian, G. Zong, and H.L. Marcus, "Selective Laser Sintering and Reaction Sintering for the Fabrication of Ceramic Composites," Proceedings of The Solid Freeform Fabrication Symposium, Austin, Texas, August, 1992.

Application of Factorial Design in Selective Laser Sintering

Xiaoming (Michael) Deng and Joseph J. Beaman
Department of Mechanical Engineering
The University of Texas at Austin, Austin, TX 78712

Abstract

Selective Laser Sintering (SLS) is a complex process involving many process parameters. These parameters are not all independent. A factorial design technique is utilized to study the effects of three main process parameters, laser power, laser beam scanning speed, and powder packing density as well as their interactions on the sintering depth and fractional density. The results of this investigation provide useful information for the further experimental analysis of the process parameters and for selecting suitable parameters for SLS process.

1. Introduction

The SLS processing parameters and their interactions have strong effects on the quality of SLS products. These parameters are summarized in Figure 1. An experimental cross parametric evaluation and a parametric analysis effort has been conducted to assess the effects of the major process parameters on the quality of the SLS products [1]. It was focused on the investigation of geometric phenomenon, sectional sintering geometry, and density in a single layer basis. For simplification, the effects of environmental influences and material were fixed. In other words these factors were treated as constants. Machinery influences were neglected other than the powder packing density. Many interesting results of the effect of the individual processing parameter on the quality of the SLS products have been achieved in that experimental research. However, the effects of the interaction of these parameters on the quality of the SLS products are still unclear. In this paper a fractional design technique was utilized to to determine the most effective factors for SLS part production and to study the interactions of the parameters. Sintering quality is described using sintering depth and fractional density and is examined in terms of major input parameters including laser power, laser beam scan speed, and powder packing density .

2. Experimental Data

The experimental approaches used in this study are described in Reference [1] in this proceedings. The sintering depth and fractional density data for different laser powers, scan speeds, and powder packing densities are listed in Table 1 and Table 2, respectively. Sintering

depth can be identified from a so-called sectional sintering geometry. Sectional sintering geometry is a section view of the sintered part (path). It is defined from sintered surface, along

Fixed for this research
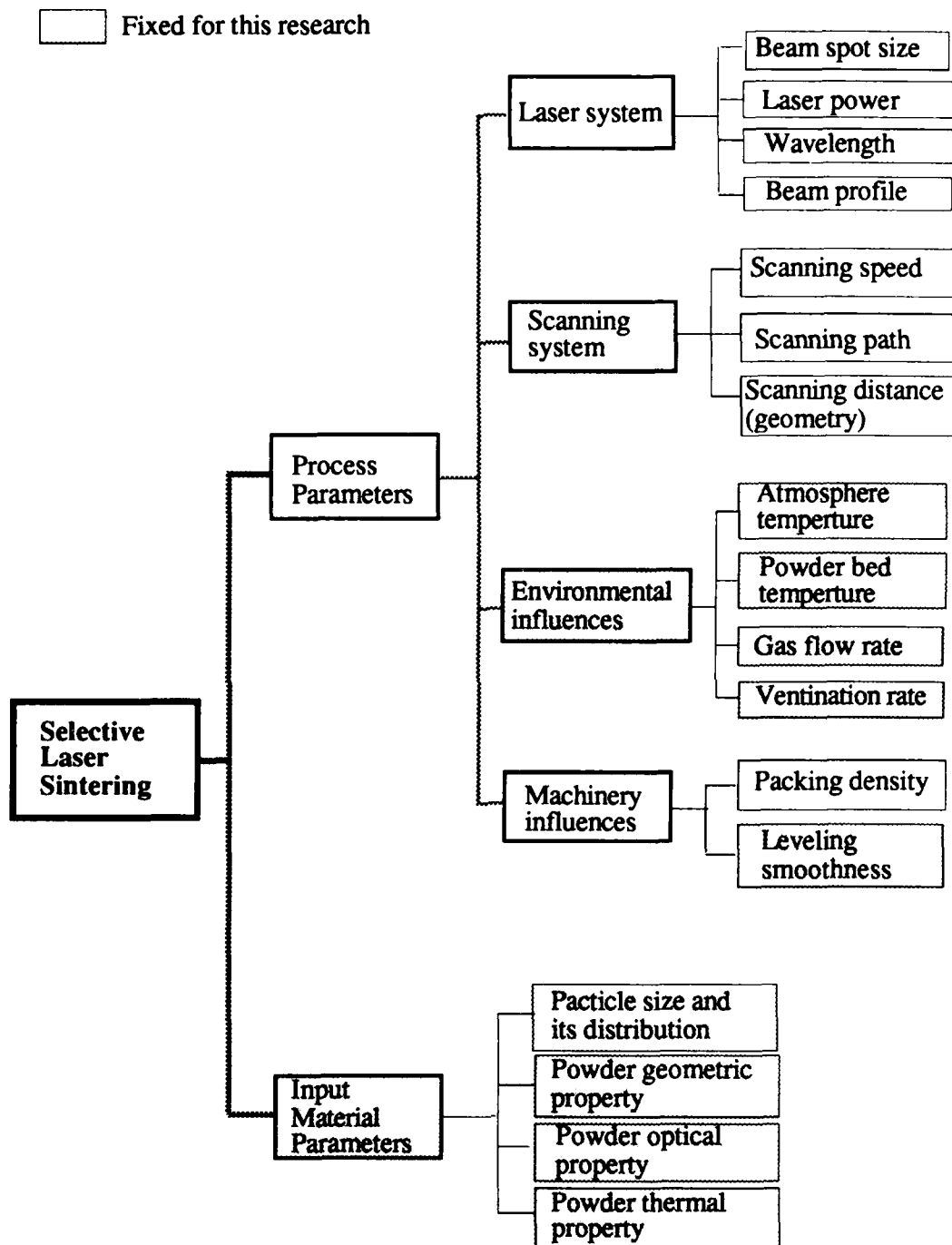
Figure 1 Parameters in SLS process

the direction of laser beam (Z-axis), to a region that sintering density appears obviously reduced (Figure 2). The sintering depth is defined within a solid sintering region. It is

evaluated by means of the mean heights of the solid sectional sintered portions. The sectional sintering geometry can be clearly observed and measured using SEM. The fractional density is defined as the area ratio of the solid sintered region to the void region within the average height of the sintering geometry.
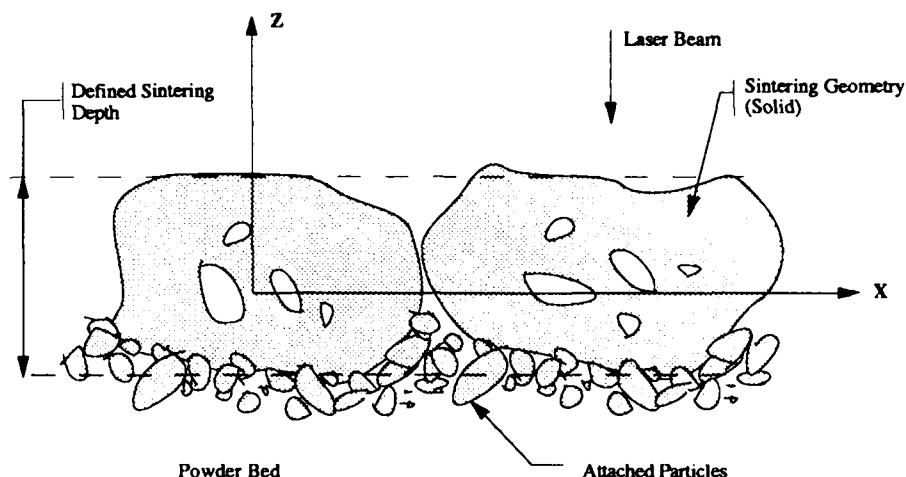
Figure 2 Determination of the sintering depth

Table 1 Experimental sintering depth (mm) data

Scanning Speed (A)	Packing Density(C)			
	0.43 g/cm3		0.68 g/cm3	
	Laser Power (B)		Laser Power (B)	
	8 W	20 W	8 W	20 W
6	0.3290	0.3152	0.0882	0.1284
	0.3206	0.2902	0.1225	0.1353
	0.3424	0.2957	0.1098	0.1294
	0.3750	0.3424	0.1000	0.1392
8	0.2663	0.2913	0.0814	0.1745
	0.2880	0.3228	0.0863	0.1853
	0.2826	0.2772	0.0530	0.1686
	0.2880	0.2956	0.0593	0.1794
10	0.1880	0.2772	0.0392	0.1696
	0.1847	0.2641	0.0451	0.1529
	0.2830	0.2445	0.0588	0.1588
	0.2207	0.2391	0.0450	0.1696
12	0.1630	0 3098	0.0294	0.1225
	0.1696	0.2435	0.0290	0.1289
	0.1739	0.2865	0.0210	0.1333
	0.1800	0.2921	0.0230	0.1112

Table 2 Experimental fractional density data

	Packing Density(C)			
	0.43 g/cm3		0.68 g/cm3	
	Laser Power (B)		Laser Power (B)	
Scanning Speed (A)	8 W	20 W	8 W	20 W
	Fractional density			
6	0.440	0.644	0.625	0.958
	0.393	0.548	0.500	0.978
8	0.600	0.694	0.290	0.940
	0.600	0.667	0.220	0.950
10	0.222	0.556	0.080	0.900
	0.208	0.640	0.075	0.916
12	0.250	0.360	0.000	0.720
	0.208	0.375	0.000	0.750

3. Fractional Design Analysis

3.1 Model

The model of the analysis of variance [2] for this experiment can be written as

$$Y_{ijk}=\mu+S_i+P_j+D_k+SP_{ij}+SD_{ik}+PD_{jk}+SPD_{ijk}+\mathcal{E}_{(ijk)l},$$

$$i=1,2,3,4$$
$$j=1,2$$
$$k=1,2$$
$$l=1,2$$

where

Y_{ijk}:   sintering depth or fractional density of the ith scanning speed, jth laser power and kth pressed density

μ: overall mean

S_i: effect of the ith scanning speed

P_j: effect of the jth laser power

D_k: effect of the pressed density

SP_{ij}:   the effect of the interaction of the ith scanning speed with the jth laser power

SD_{ik}:   the effect of the interaction of the ith scanning speed with the kth pressed

157

density

PDjk: the effect of the interaction of the jth laser power with the kth pressed density

SPDijk: the effect of the interaction of the ith scanning speed with the jth laser power and kth pressed density

ε(ijk)l: the experimental error

3.2 Analysis of variance

The analysis of variance for sintering depth is summarized in Table 3. It is obvious that the pressed density, laser power and scanning speed effect sintering depth. The effective degree of these three factors to the sintering depth is ordered from high to low: pressed density, laser power and scanning speed. The scanning speed-laser power, laser power-pressed density and laser power-pressed density interaction also affect the sintering depth. The scanning speed-laser power-pressed density interaction is significant at 5 percent, indicating a relative mild interaction among these factors.

Table 3 Analysis of Variance for sintering depth

Source of Variation	Sum of Squares	Degrees of Freedom	Mean Square	Fo
Scanning speed (A)	0.052206	3	0.017402	67.32 [a]
Laser power (B)	0.062082	1	0.062082	240.15 [a]
Pressed density (C)	0.422256	1	0.422256	1633.41 [a]
AB	0.025730	3	0.008577	33.18 [a]
AC	0.013883	3	0.004628	17.90 [a]
BC	0.010447	1	0.010447	40.41 [a]
ABC	0.005679	3	0.001893	7.32 [b]
Error	0.012409	48	0.000259	
Total	0.604693	63		

[a] Significant at 1 percent.
[b] Significant at 5 percent

The analysis of variance for fractional density is summarized in Table 4. In this calculation, the results show that fractional densities are dominant by laser power. All of the factors and their interactions are significant at 1 percent. The interaction of the laser power with the packing density are the second largest effective factors to fractional densities.

3.3 Experimental errors

The major experimental errors come from the stability of the laser power and the environmental temperature. But the error can be minimized if the laser is at steady state before every experiment start. The calibration of the laser power for each setting is necessary. In

general, the experimental errors can be greatly reduced if the experiment is properly conducted and the initial conditions are properly controlled. A better laser power controller can be very helpful for improving the power setting accuracy.

Table 4 Analysis of Variance for fractional density

Source of Variation	Sum of Squares	Degrees of Freedom	Mean Square	Fo
Scanning speed (A)	0.503667	3	0.167889	123.22 [a]
Laser power (B)	1.481351	1	1.481351	1087.21[a]
Pressed density (C)	0.070032	1	0.070032	51.40 [a]
AB	0.104389	3	0.034796	25.54 [a]
AC	0.091840	3	0.030613	22.47 [a]
BC	0.441565	1	0.441565	324.08 [a]
ABC	0.047752	3	0.0159 17	11.68 [a]
Error	0.021800	16	0.001363	
Total	2.762396	31		

[a] Significant at 1 percent.

Measurement errors are dependent on the accuracy of the SEM. In general, the measurement error of the SEM is less than 10%, and this error can be controlled if the SEM is calibrated before each measurement.

Sample preparation can also cause a measurement error if the viewing section is not paralleled to the surface of the SEM sample base. However, this error can be reduced by sample preparation since the titled angle is generally smaller than 2 to 3 degrees, and the projection effect of this angle is too small to affect the measurement in normal circumstance.

3.4 Discussions

As the results of the factorial design, the three selected factors: laser power, scanning speed and packing density are significant to sintering depth and fractional densities. The results show that

1) the sintering depth is dominant by the powder pressed density,

2) the sintering fractional density is dominant by the laser power,

3) laser power effects the sintering depth more than scanning speed does,

4) scanning speed affects fractional density more than laser power,

159

5) the interaction of the laser power and packing density is significant to the fractional density,

6) the interaction of three factors is significant to the sintering depth only at 5%.

The experimental and measurement errors are small. In this investigation, the research interest is focused on a parametric qualitative analysis that are most important SLS processing.

4. Summary and Conclusions

The results from factorial design indicate that these three factors are all significant at 1% to the sintering depth and sintering fractional density. Their interactions are significant to sectional sintering geometry as well. Sintering depth is affected most by the powder pressed density. Sintering fractional density is affected most by the laser power. Further investigation should be conducted more thoroughly to study the effects of all the factors significant to the SLS process on the SLS part quality.

Acknowledgements

References

1. X. Deng, G. Zong, and J. J. Beaman, "Parametric Analysis for Selective Laser Sintering of a Sample Polymer System," Proceedings of Solid Freeform Fabrication Symposium, edited by H. L. Marcus, J. J. Beaman, J. W.. Barlow, D. L. Bourell, and R. Crawford, Austin, TX, August 3-5, 1992.
2. D. C. Montgomery, Design and Analysis of Experiments, John Wiley & Sons, 1991.

Preliminary Experience with Selective Laser Sintigraphic (SLS) Models of the Human Temporal Bone

Richard A. Levy, M.D.
Department of Radiology, The University of Michigan Medical Center
1500 E. Medical Center Drive, Ann Arbor, MI 48109-0030
and
Sashidhar Guduri and Richard H. Crawford
Department of Mechanical Engineering
The University of Texas at Austin

Purpose

To assess the accuracy of three-dimensional models of the human temporal bone generated from computed tomographic (CT) data.

Materials and Methods

Thin section CT of a left human cadaveric temporal bone was performed using multiple scan planes (axial, coronal, sagittal) at 1.5 mm slice thickness, 0.25 mm pixel size with an edge enhancement 2D algorithm. CT data was converted to toggle point format based upon a threshold value of 200 obtained from prior experimentation with a CT phantom (unpublished data). Selective Laser Sintering of polycarbonate powder was performed at a beam thickness of 0.060 inches, 100 scan lines/inch, layer thickness of 0.010 inches, and layer repeat factor of 4. The polycarbonate models were then scanned in the axial, coronal and sagittal planes and compared with the original CT data. Anatomic dissection of the models was performed for further verification of the imaging findings.

Results

Models of high anatomic accuracy were generated. Shortening along the Z axis secondary to the layer repeat factor of 4 resulted in distortion of the models. No distortion in the XY plane was observed. Differences in model accuracy based upon initial CT scan plane were observed. A significant amount of non- or partially-sintered polycarbonate resulted in intermediate density on the CT images.

Conclusions

Selective Laser Sintering can result in accurate modeling of detailed anatomic structures in the human temporal bone. Further investigation of factors contributing to the accuracy of SLS in the manufacturing of high-resolution anatomic models is warranted.

References

Levy, R.A. Three-dimensional Model Generation Using Multiple Angle Tomographic Scan Planes. Patent Pending.

Levy, R.A., Edwards, W.T., Mayer, J.R. and Rosenbaum, A.E. Facial Trauma and 3-D Reconstructive Imaging: Insufficiencies and Correctives. AJNR 13:885-892, May/June 1992.

Acknowledgment

Figure 1a: Sagittal two-dimensional (2D), computerized tomographic (CT) section, through the middle ear cavity of a left human temporal bone. White arrowhead points to the manubrium of the malleus. White arrow points to the long crus of the incus.

Figure 1b: Sagittal 2D CT section lateral to that in Figure 1a. White arrow points to incudomalleolar articulation. Black arrow points to head of malleus.
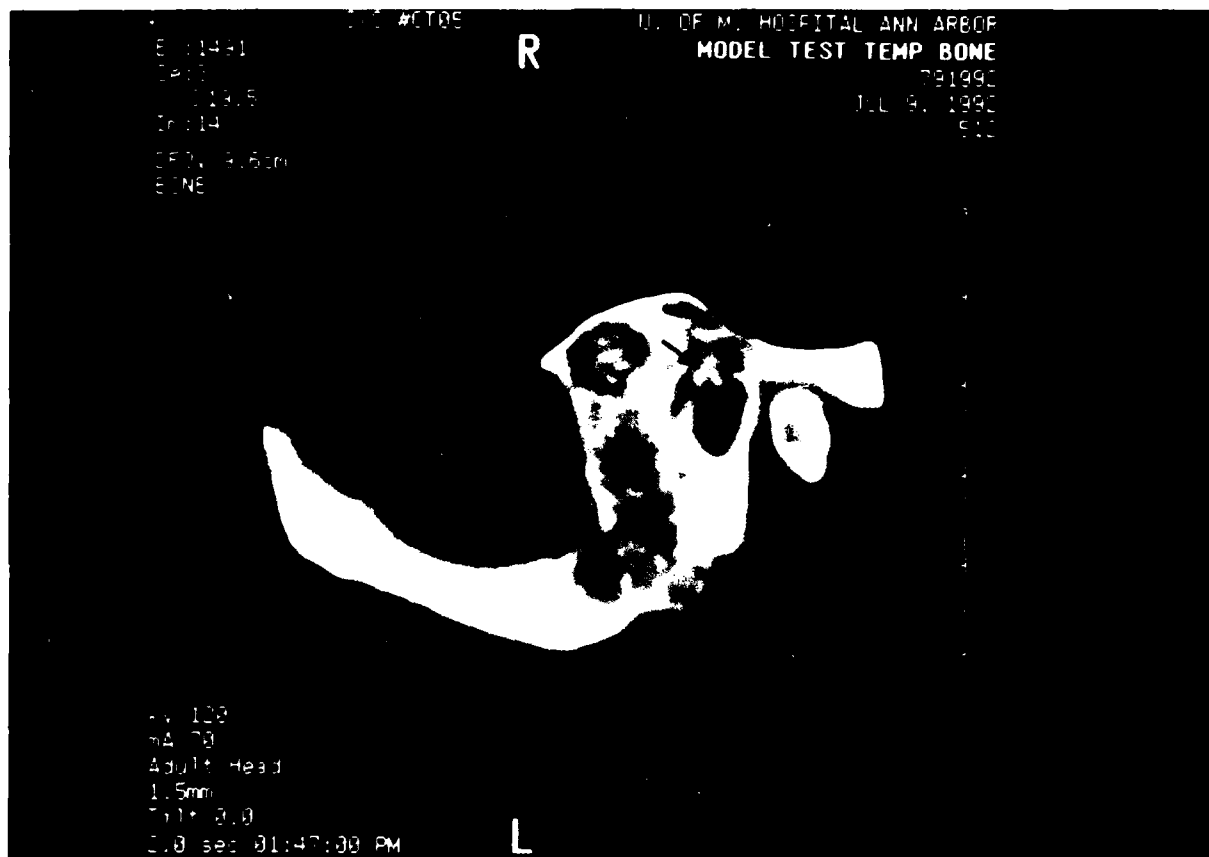
Figure 1c: Sagittal CT section of SLS polycarbonate model generated from sagittal data corresponding to CT image in Figure 1a. Black arrowhead points to manubrium of the malleus. Black arrow points to long crus of the incus.
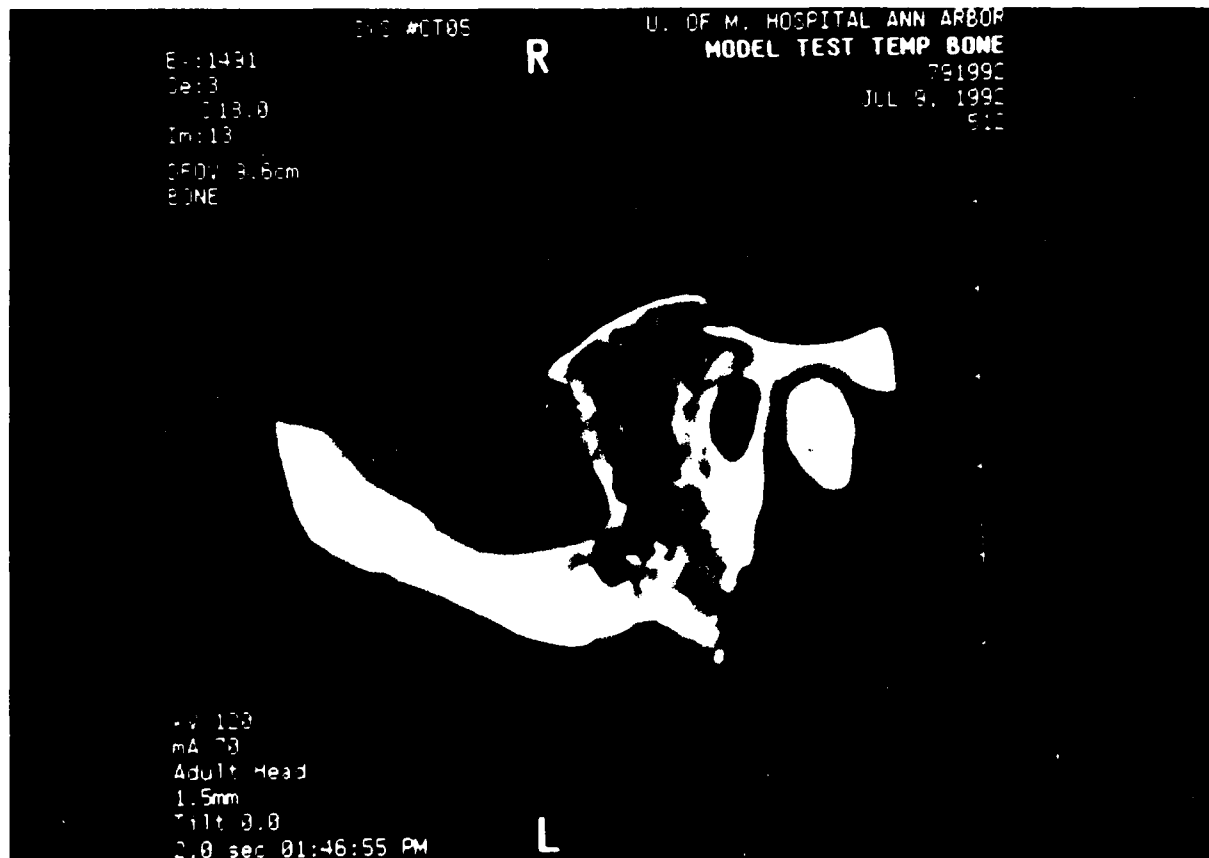
Figure 1d: Sagittal CT image of model generated from sagittal CT data corresponding to image in Figure 1b. Region of incudomalleolar articulation is identified, less distinct than on the corresponding CT image in Figure 1b (black arrowhead).

Figure 1e: Post-dissection sagittal CT scan of polycarbonate model generated from sagittal CT data corresponding to imaging plane in Figure 1c. White arrow indicates "resected" area of loose polycarbonate powder in the middle ear cavity, now showing normal air density. Black arrow points to head of malleus, better appreciated than in Figures 1a and 1c, and similarly to Figure 1b.
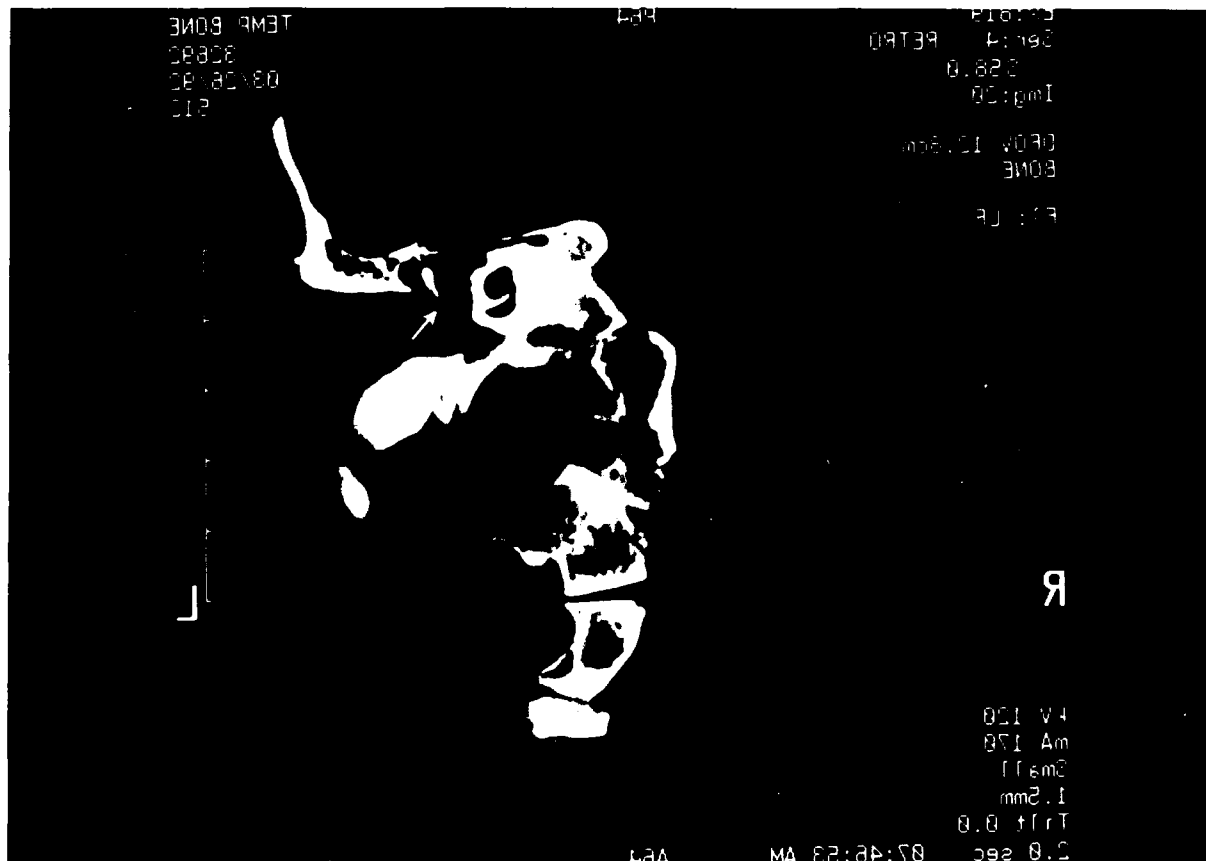
Figure 2a: Coronal 2D CT section through the same specimen as in Figure 1. Note mirror-image reversal from the polycarbonate model in Figure 2c. White arrowhead points to head of malleus. White arrow points to the manubrium of the malleus.

Figure 2b: Coronal 2D CT section posterior to that in Figure 2a. Black arrow points to long crus of incus. Black arrowhead points to region of oval window and stapes footplate.
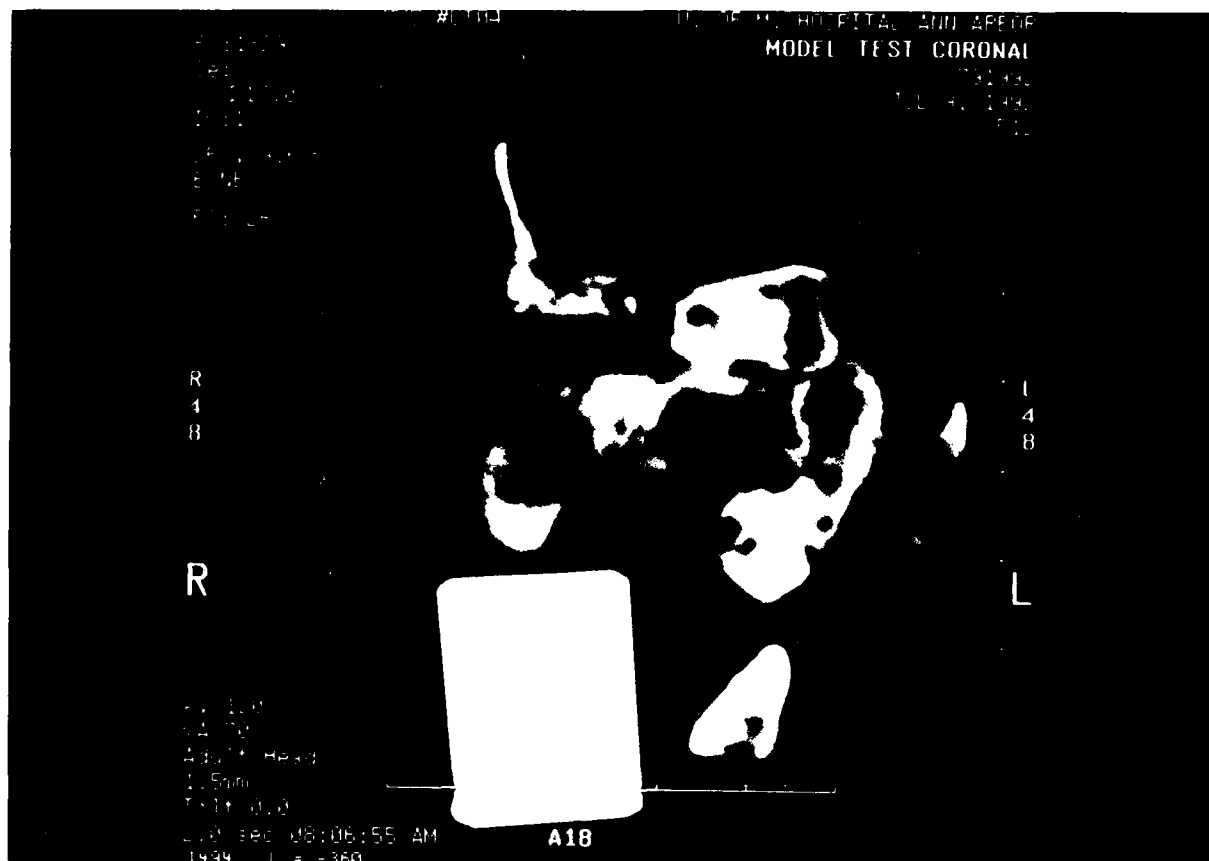
Figure 2c: Coronal CT scan of polycarbonate model generated from coronal 2D CT data. Only the head of the malleus is reproduced. The model generated from the sagittal plane (Figure 1) more accurately reproduces ossicular anatomy than does that generated from the coronal plane. This was verified at dissection.
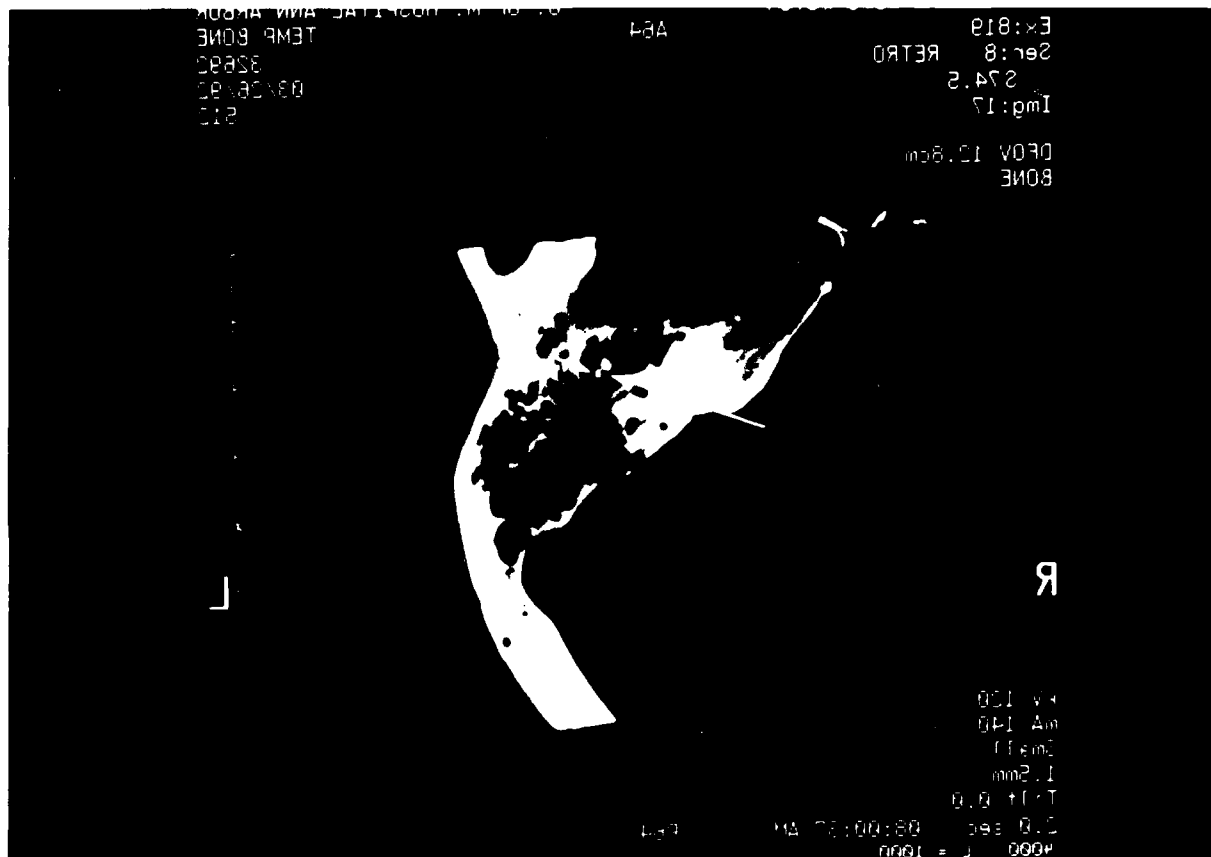
(Figure 3a)

Figures 3a&b: Axial CT sections through the same specimen as in Figures 1 and 2. Black arrowhead points to head of malleus. Short white arrows point to body and short crus of incus. Long white arrow points to the incudomalleolar articulation. Note mirror image reversal from model in Figures 3c and d.
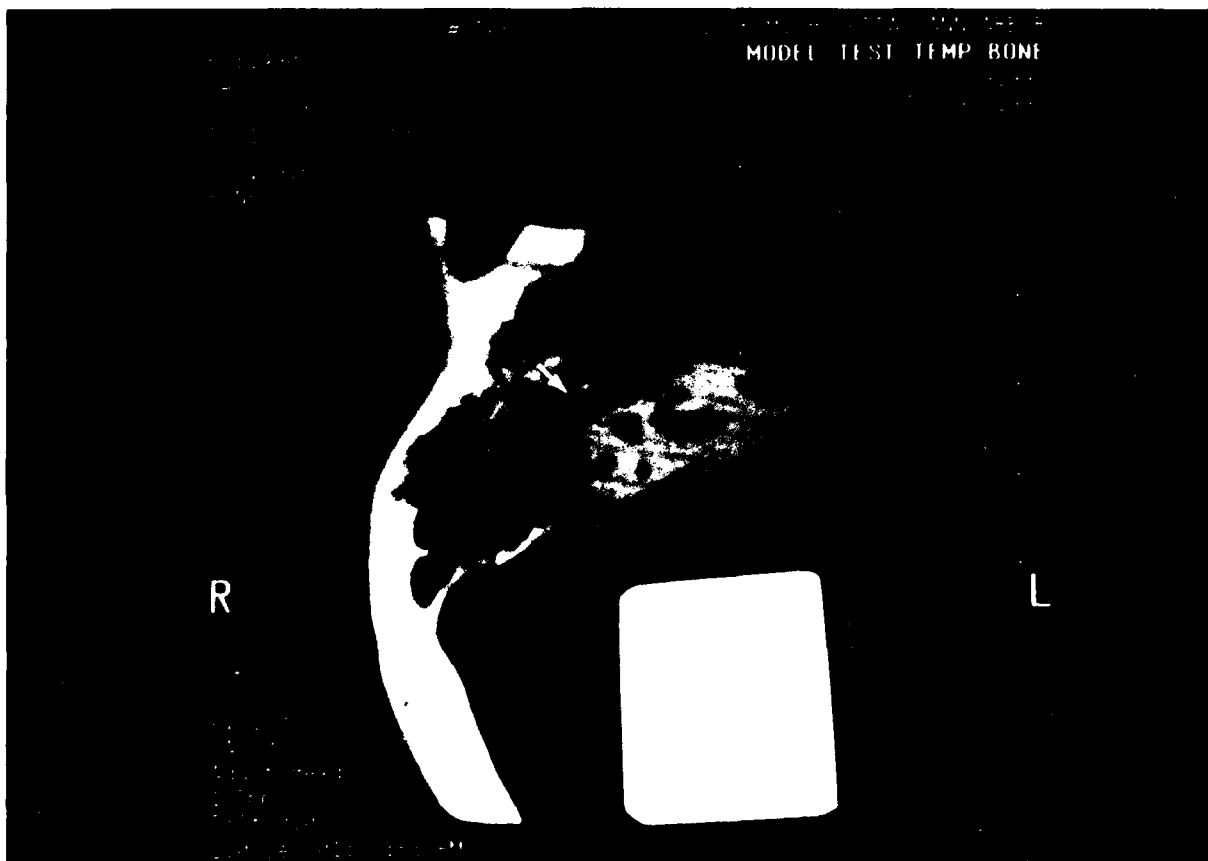
(Figure 3b)

(Figure 3c)

Figures 3c and d: Axial CT sections through polycarbonate models generated from axial CT data corresponding to the images in Figures 3a and b. Black arrowheads point to head of malleus. Short white arrows point to incus, as in Figures 3a and b. The manubrium of the malleus or long crus of the incus were not reproduced by SLS, although present on the initial axial CT sections (not shown).

(Figure 3d)

Richard F. Aubin
United Technologies/Pratt & Whitney
400 Main Street MS 118-38
East Hartford, CT 06108
Phone 203-565-9073

A CASE STUDY IN RAPID PROTOTYPING

INTRODUCTION:

Since the first quarter of 1988, Pratt & Whitney (P&W), a Division of United Technologies Corporation (UTC), has been involved in the development for the use of rapid prototyping technologies that use a "layer-by-layer" building approach. Based on over 4 1/2 years experience with Stereolithography, this paper will address three aspects of our experience including: Implementation, Current Operations, and Future Plans.

BACKGROUND:

Component parts for gas turbine engines are required to function in environments that are unlike any other industry, with combustor temperatures reaching 2,500 degrees F., and pull loads on our 1st blades reaching 50,000 g's. However, manufacturing these parts is accomplished using conventional methods that are similar to other industries.

Conventional methods for prototype fabrication, small batch production and manufacturing process development have relied on drawings, hard tooling, numerical control programming, complex machining and/or extensive hand work. These approaches are typically characterized by long lead-time, high cost and multiple iterations to achieve desired results.

There are many organizations today, that continue to employ these methods, but before they can make the transition into the new era of rapid prototyping, they must recognize that they are out of step with the current environment. Without feeling the need to change, the "*Boiled Frog Phenomenon*" is likely to occur.

The Boiled Frog:

This phenomenon is based on a classical experiment in biology. A frog which is placed in a pan of cold water but which still has the freedom to jump out can be boiled if the temperature change is gradual, for it is not aware of the barely detectable changing heat threshold. In contrast, a frog dropped in a pot of boiling water will immediately jump out: it has felt the need to survive. In a similar vein, organizations and managers that are insensitive to gradually changing environments, are likely to become "boiled frogs"; they act in ignorant bliss of environmental triggers and eventually are doomed to failure.

Richard F. Aubin
United Technologies/Pratt & Whitney

IMPLEMENTATION:

Up until 1988, P&W was deeply involved in conventional prototyping methods. We had an extensive investment in CAD/CAM equipment and trained personnel, but still had to "iterate" at the expense of extended lead times and increased costs. However, unlike the frog, we felt the water getting warm before it was too late.

Along came an opportunity to "beta test" a new technology called Stereolithography (SLA) from 3D Systems Inc., of Valencia, California. Although faced with many unknowns and associated risks, we decided to get involved, and acquired 2 "beta machines" in January - February 1988. One SLA machine with a 9-inch part building capacity was located at our facility in West Palm Beach, Florida, while the second one was located at our manufacturing facility in East Hartford, Connecticut.

We were fortunate to have extensive resources in computer modeling hardware and software, and experienced people proficient in its use. Initially, we used floppy disks to transport the computer models from the CAD systems to SLA, but learned quickly that complex computer models were very large in size. By using our shop computer network system (ethernet), we are now able to download computer models directly to the SLA machine.

To increase the exposure of this new technology and to demystify its operation, we gave walking tours and presentations to:

- Managers - So they understood its potential "fit" for their requirements,
- Engineers - So they understood the computer modeling requirements, e.g., bases & supports,
- Mfg. Shop - So they could understand its capabilities and how to get access.

We soon felt that we were a "tours-r-us" operation, but it paid off. Shortly, we were building a large variety of prototype objects and identified many tangible and intangible benefits.

One of the most significant tangible benefits was the identification of design errors early in the design process. Because SLA was so fast and relatively inexpensive to produce a prototype as compared to traditional methods, engineers were given more latitude to improve their designs, so design quality was enhanced prior to reaching manufacturing. In the past, too many design flaws were uncovered after the manufacturing departments made the tooling and the parts, investing time and resources only to find out they did the "wrong part right." By working out these errors before involving manufacturing, we can better align our shop resources to doing the "right part right."

Joel Mokyr, Professor of Economics and History at Northwestern University and author of

his recently published book titled, The Lever Of Riches, states: "*Technological progress has been one of the most potent forces in history in that it has provided society with what*

Richard F. Aubin
United Technologies/Pratt & Whitney

economists call a 'free lunch,' that is, an increase in output that is not commensurate with the increase in effort and cost necessary to bring it about." There have been several occasions where, as a result of rapid prototyping, we have had a taste of this "*free lunch.*"

Another tangible benefit was the improvement in communications among design engineers, and between engineering and manufacturing personnel because they now had a physical object to use instead of a sketch or drawing that was subject to interpretation.

On the intangible benefits side, the SLA process provided an incentive and reward mechanism to our engineers to learn and use computer solid modeling that for more than just "pretty pictures". By generating computer models of their design ideas, they would be rewarded with the satisfaction of possessing a physical prototype in return.

Although considered intangible, our engineers were thus enabled to "think-out-loud", meaning that they were now able to generate physical objects directly from their computer models quickly and inexpensively. A new degree of enthusiasm resulted in the engineering community as a result of this new capability that essentially kept them "fresh" instead of growing "stale" while waiting for the hardware to arrive.

Further, engineers were now receptive to change by incorporating suggested improvements from peers and from manufacturing personnel.

Needless to say, these benefits provided significant time and cost savings.

By the end of the first year of using SLA, we recognized the value of working together with other "beta test companies". Collectively, we worked and shared ideas to improve accuracy and surface finish. We also identified errors in the SLA process, and provided suggestions for improvement by submitting enhancement proposals to 3D Systems. Eventually, these enhancements were manifested in later revisions of the software, so mutual benefit was realized as a result of team-playing.

With a few "free lunches" under our belt, we finished the first year with some valuable lessons learned, and unlike the "boiled frog," we found ourselves rewarded by being sensitive to our changing environment.

After beta testing the early version of the SLA device, we were given another opportunity. This time, 3D Systems was offering their larger SLA machine for beta test, that had a 20-inch part building capacity. This gave P&W the capability to build larger prototype objects; we proceeded without hesitation.

Having recognized the benefits of working with other companies throughout the beta testing programs, P&W and the other beta test companies took the initiative to establish the SLA users group. This group was comprised of all users of SLA for the purpose of providing a forum for technical information exchange among the SLA users community. Through this forum,

companies share lessons learned, and identify strategies to improve their output. P&W provided leadership to this group by chairing this organization from its inception through its first year.

Internally, P&W decided to expand its rapid prototyping capabilities, and share its lessons learned with our sister divisions of UTC by establishing what we called an "Express Prototype Consortium." This consortium served as a vehicle for technology transfer with: Carrier, Hamilton Standard, Otis Elevator, Pratt & Whitney Canada, Sikorsky Aircraft, and United Technologies Automotive.

CURRENT OPERATIONS:

Currently, our operation in East Hartford has grown to include a total of 4 SLA machines and through the benefits of economies of scale, we are able to be responsive to the prototyping demands of our entire corporation. Last year, 1990, over 1,600 prototypes were processed at our East Hartford facility.

We see this activity in several basic areas:

- Design Verification

    As previously mentioned, there is great value in identifying design errors prior to manufacturing involvement. Improving designs by "iterating in plastic" is much more effective in time and cost than by conventional manufacturing techniques which iterate in "hard tooling."

- Manufacturing Producibility Studies

    Rapid prototyping is one of the key facilitators of integrated product development or concurrent engineering. Our manufacturing shops can get an earlier startup on process development by having a replica of a part to use to prove out tooling and fixturing while the actual real parts are being produced. For example, while investment castings are being processed, plastic replicas can be used in the manufacturing environment to ensure proper fixturing and tooling for final machining. When the actual parts arrive, the machining process is already up and ready.

- Prototype Parts For Test And Conversion To Other Materials

    Occasionally, the plastic object can serve directly as a prototype in a test where the physical properties of the plastic can suffice. Techniques to convert the plastic object to other plastic materials having improved physical properties are also commonly available in industry through injection molding processes. And lastly, investment castings can be generated in a fraction of the time through the use of temporary tooling.

Richard F. Aubin
United Technologies/Pratt & Whitney

- Research and Development Efforts

    To date our biggest limitation with the photo-curable resins has been accuracy and surface finish. Our focus therefore has been to improve the process steps which affect them. We have learned that all variables in the total process must be considered, including: computer modeling preparation, hardware and software development, materials, and post-processing.

Additional activities we have pursued include development relationships with resin suppliers to improve the basic resins themselves for less shrinkage, distortion, and better surface finish.

Because of the benefits we realized from beta testing Stereolithography, we are currently involved in the beta testing of new emerging technologies:

- Selective Laser Sintering (SLS), from DTM Corporation of Austin, Texas. This is a process that uses the heat of a CO_2 laser to sinter powdered materials in a layer-by-layer technique. The materials offered include wax and poly carbonate plastic.

- Fused Deposition Modeling (FDM) from Stratasys Inc., of Minneapolis, Minnesota. This is a process that uses a heated extruder mechanism to deposit thin layers of wax or nylon-like plastic materials.

Both technologies build prototype objects directly from computer models, and each has its advantages; however, because of beta testing and non disclosure agreements, further information is prohibited at this time and is best derived directly from the companies developing the technologies.

Finally, we are actively involved in several rapid prototyping consortia with academia including MIT, and the University of Texas.

FUTURE PLANS:

As you have seen, we have been very active players in the Stereolithography field. We look forward to improvements in that field as it improves and in other technologies that we are hearing about in this conference. We feel strongly that continued development is essential to improve the accuracy and surface finish for prototype objects and to come closer to the "real" physical properties of "production-like parts."

As leaders in the application of rapid prototyping, we can't wait for these developments to mature. Although much can be done unilaterally and internally, more can be accomplished by pro-actively working with the manufacturers of rapid prototyping technologies, other users, and academia to drive development in the direction for maximum benefit to industry.

The next "free lunch" just may evolve through dedicated continuous improvement.

Laser Tracking Control Implementation for SFF Applications

Ying-Jeng Engin Wu
Department of Mechanical Engineering
The National Yunlin Institute of Technology
Touliu, Yunlin, Taiwan, R.O.C.

and

Joseph J. Beaman
Department of Mechanical Engineering
The University of Texas at Austin

Abstract

From a three-dimensional computer graphic model, Solid Freeform Fabrication produces solid objects directly without special tooling and human handling. In order to increas process productivity and accuracy, a time-efficient laser tracking control technique is needed. Based on the minimum time optimal control solution, the desired laser scanning control system is designed and implemented. To obtain uniform solidification during time-efficient tracking which has variable speed, laser power intensity is also controlled in real time by an acousto-optic modulator.

Introduction

A time-efficient tracking control for a laser scanner with on-line laser power adjustment is designed and implemented in order to increase productivity and to improve the geometric accuracy or the isotropic property of parts when one needs to trace the boundary of a part in SFF. It is not appropriate to use conventional raster scanning. Due to repetitive starts and stops, straight-line vector scanning mode can be slow when curves exist in the contour path. Several articles have presented various schemes for this problem. The preview scheme (Tomizuka, Dornfeld, Bian, and Cal, 1984) and the adaptive algorithm (Tsao, and Tomizuka, 1987) need on-line computation effort which is too large for SFF application. The cross coupled compensator (Kulkarni and Srinivasan, 1985) is designed to reduce the tracking error (minimizing the contour error) at a sharp corner, however contouring analysis and optimal speed trajectories are not developed for more general paths. The control trajectory scheme (Doraiswami, and Gulliver, 1984) is directly obtained from a specified path with three simple functions regardless of the capability of the actuator. The trajectory generation scheme (Butler, Haack and Tomizuka, 1988) focuses on constant tracking speed which does not give a minimum time solution. The control technology used in this paper is based upon the results (Wu and Beaman, 1990) of Pontryagin's minimum principle and phase plane techniques (Bobrow, Dubowsky and Gibson, 1985)[6], (Shin and McKay, 1985). The control system implemented in this paper uses the feedback control design model identified by Wu and Beaman, 1991.

The objective is to control a pair of galvanometers to direct the laser beam on the working surface to track a specified path as fast as possible with limited available driving torque and to obtain uniform laser energy exposure by on-line laser power adjustment. As shown in Figure 1, designed trajectories are stored in a computer as driving and reference signals. Through an interfacing board, on-line feedback control for a galvanometer-mirror system is implemented. The laser beam is modulated by an acousto-optic intensity modulator, focused by optics, deflected by a pair of galvanometer-mirror scanners, and directed onto the working surface, to track a prescribed path as shown in figure 2. The following sections include minimum time optimal control, feedback control and simulation, implementation and results, conclusions and references.
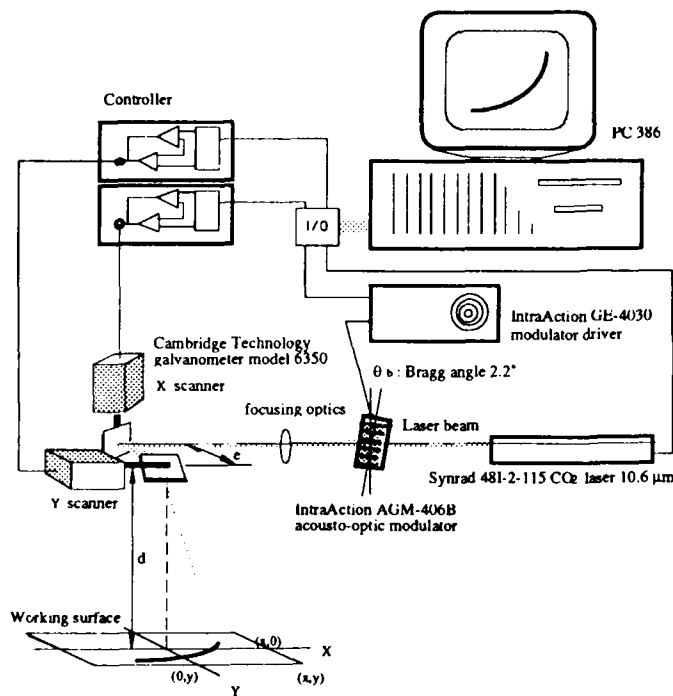
fig.1 The scanner control system
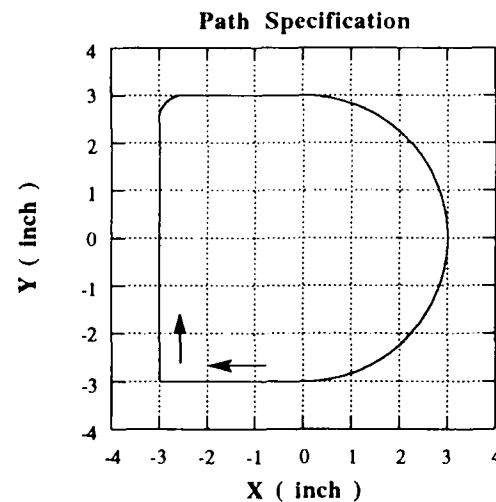
fig.2 The specified path

Minimum time optimal control

According to a trade-off between rapid scanning speed, available scanning torque or force and maximum tracking speed due to available laser power, a minimum time optimal control problem is defined and solved, (Wu and Beaman, 1990 and 1991) From the physical system described in Figure 3, a minimum time optimal control problem formulated in the θx-θy domain is conceptually straightforward. The state variables are chosen as θx, ω_x, θy, ω_y.
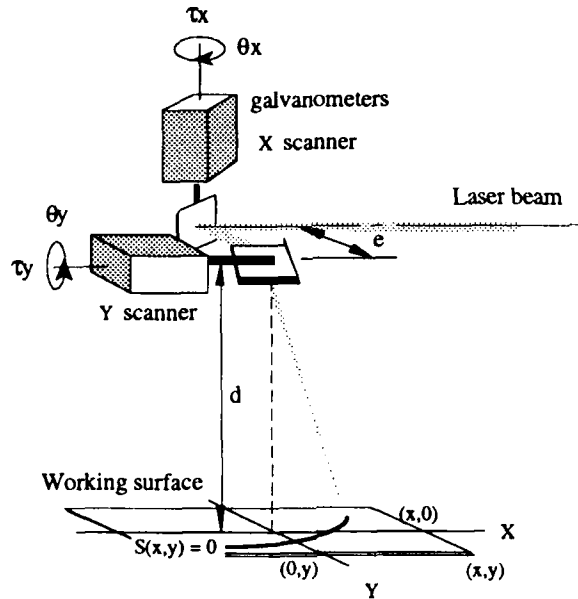
fig.3 The optimal control system

min $\mathbf{J}$ = min t_f where t_f is final time

subject to : $d\theta_x/dt = \omega_x$,

           $d\omega_x/dt = -\ 4.9717e{+}03\ \theta_x - 1.4102e{+}01\ \omega_x + 576762\ I_x$,

           $d\theta_y/dt = \omega_y$,

           $d\omega_y/dt = -\ 2.5878e{+}03\ \theta_y - 1.5261e{+}01\ \omega_y + 359706\ I_y$,

and $-1.1 \le I_x \le 1.1,$ $-1.1 \le I_y \le 1.1,$

           ($I_x = -e_{xin}/3$ and $I_y = -e_{yin}/3$ in the simplified model)

           Tracking speed $v \le V_p$ (320 inch/sec.),

           where V_p is the allowable speed under the available laser power

           S(x,y) = 0, shown in Figure 2.

           $x(0) = -3,\ x(t_f) = -3,\ v_x(0) = 0,\ v_x(t_f) = 0,$

           $y(0) = -3,\ y(t_f) = -3,\ v_y(0) = 0,\ v_y(t_f) = 0,$ are given.

with the nonlinear geometric relation between θ_x-θ_y space and X-Y space as :

$$\theta_x = G_1(\ x,\ y\ ) = 0.5 * atan[\ \frac{x}{\sqrt{12^2+y^2} + 0.75}\ ]$$

and $\theta_y = G_2(\ x,\ y\ ) = 0.5 * atan[\ \frac{y}{12}\ ]$

     The solution is shown in figure 4. Note that tracking speed is accelerated from 0 to 320 inch/sec in 31 microseconds.
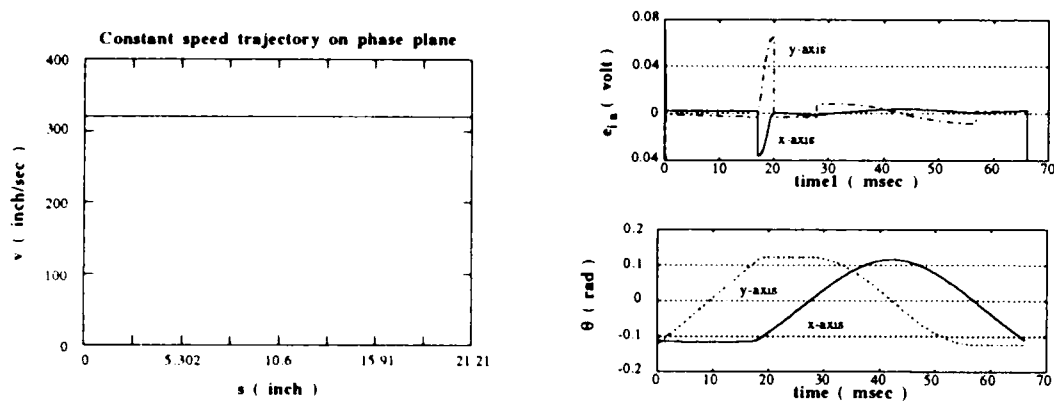
fig.4 The trajectory with 320 inch/sec tracking speed limit

Feedback Control and Simulations

A two-channel PID feedback control design supplies the best advantage in this application and achieves the specifications as simple, low computational load for computer control, fast response, small overshoot in time response and good stability robustness. Performance robustness is an important issue for scanning accuracy also. There is no good technique which may assure it. This will be tested by numerical simulation.

Before implementing a control system with the designed control trajectories and feedback scheme, numerical simulation is necessary. There are two ways to implement the control system with our results of open loop optimal control trajectory planning and the feedback compensator design. One uses a position reference trajectory $\theta_{ref}(t)$ only, and the other uses both position reference trajectory $\theta_{ref}(t)$ and the designed control trajectory $e_{ref}(t)$. Both implementations will be simulated and compared. With the trajectories designed for 320 inch per second of tracking speed, the best performance with 4.7 thousandth inch of maxError could be achieved under various physical limitations. If a better tracking accuracy is required, it is necessary to reduce the tracking speed. The following results are simulations with various desired tracking speeds.

tracking speed v_d (inch/second)	320	200	100	50
maxError (inch)	0.00470	0.00421	0.00275	0.00060

The simulation results also give guide lines on how parameter variations affect tracking performance shown in Figure 5. The worst performance resulted from the inertia variation. However, compared with estimates for the damping factor and the spring constant, it is not difficult to obtain a more accurate estimation of the inertia such that one may expect a little inertia uncertainty exists only with no significant effect on tracking performance. Thus, it is obvious that tracking performance of the implementation with $e_{ref}(t)$ is better under the conditions with both nominal and perturbed system parameters.
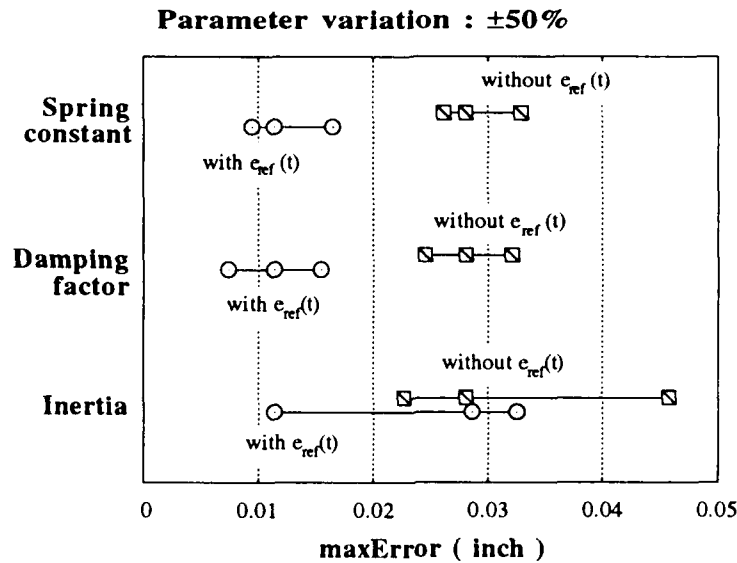
Figure 5   Performance variation due to parameter variation

Implementation and results

For digital control, the feedback control law is implemented by computer software. Besides noise rejection, flexibility is one of the important advantages of digital control. Another advantage is that software can handle a very complicated control algorithm. However, all computations must be finished within the desired sampling interval. Because of the available facilities in the laboratory and an extremely short sampling interval is desired in this application, the digital control scheme does not work and the final results are performed by the analog controller.

A dual channel analog PID controller is designed.(shown in Figure 6) For each channel, a summing amplifier, a gain amplifier, a gain attenuator, a differentiator and an integrator are designed with care for circuit stability, noise attenuation, bias reduction. (Stout, 1976) The signal conditioning unit for the acousto-optic modulator is a unit gain buffering amplifier used for matching impedance.
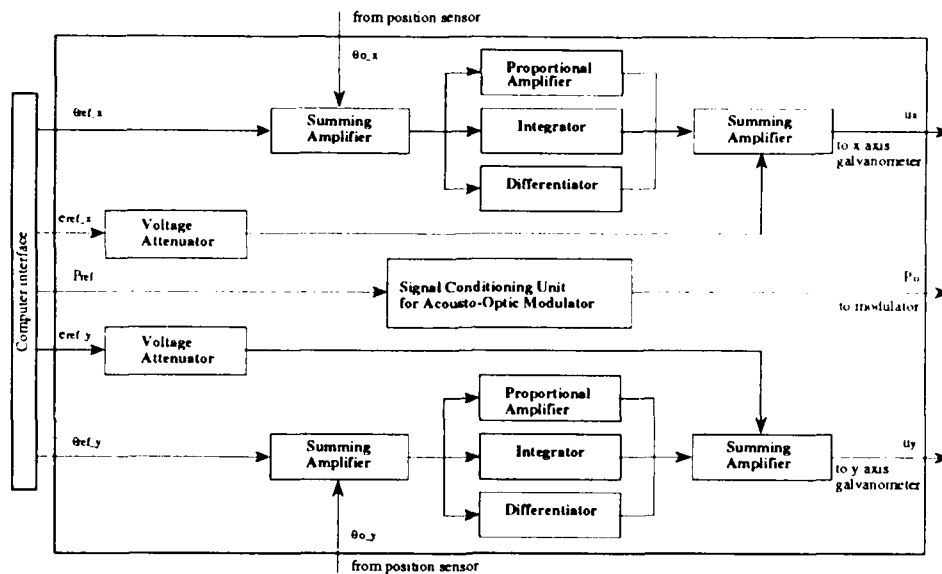
Figure 6   **Block diagram of dual channel analog controller**

A traveling laser spot (red HeNe laser) is shown in Picture 1 with 320 inches per second tracking speed. The control design in this paper shows fast and smooth performance when high speed tracking is desired.

Picture 1   **Traveling of Red HeNe Laser Spot**

184

Uniform laser exposure is achieved by smooth tracking speed trajectory design and the acousto-optic power modulator, where the laser power level is determined by the designed tracking speed trajectory. Compared with the vector scanning shown in Picture 2, the control design in this paper has no repetitive starts and stops such that fas' and smooth tracking results (shown in Picture 3) when curves exist in the contour path. Notice that there exists an overheated spot at every end-point of the scanning vector in Picture 2.
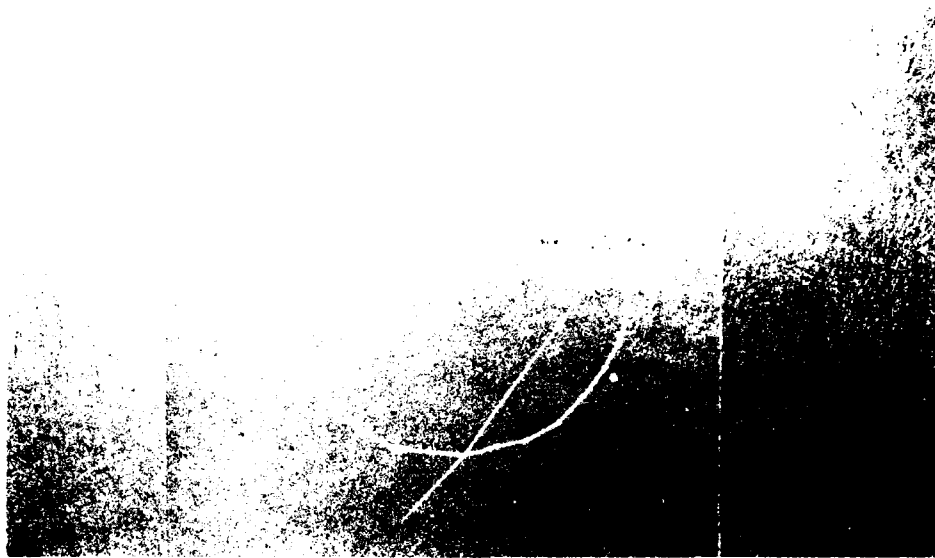
Picture 2   The Result of Vector Scanning
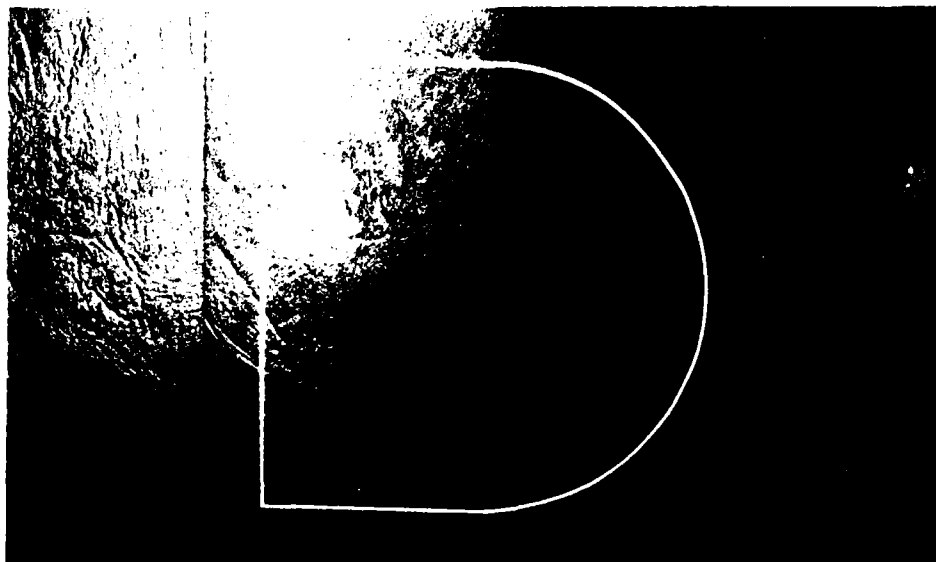
Picture 3   The Result of Control Design in This Paper

Conclusions

While part boundaries need continuous scanning, conventional raster scanning does not work. Compared with a straight-line vector scanning mode, the advantages in this study are fast, smooth curve tracking without repetitive starts and stops. It is a minimum time optimal solution with constraints of available driving torque, specified tracking path and available laser power. Since the feedback measurement for the closed loop control system is from the galvanometer shaft position instead of the location of the laser spot on the working surface, accurate calibration for the nonlinear geometry between the galvanometer axis and the working surface is necessary to obtain a better geometric tracking accuracy. Sophisticated optical accessories are also needed to obtain better alignment for the optical path.

For industrial applications, two main issues must be researched in the future. One is a convenient algorithm to convert CAD geometric data into parametric curve representation with uniform point distribution. The other is a convenient software to automatically generate optimal trajectories in the phase plane. The initial idea is to setup a computer library with some common paths, for example, circle path, line segment, splines etc.

Reference

Bobrow, J.E., Dubowsky, S. and Gibson, J. S., " Time-Optimal Control of Robotic Manipulators along Specified Paths ", The international Journal of Robotics Research, Vol.4, No.3, Fall 1985, p.3-17.

Butler, J., Haack, B. and Tomizuka, M., " Reference Generation for High Speed Coordinated Motion of a Two Axis System ", Symposium on Robotics, The Winter Annual Meeting of the ASME, Chicago, Illinois, November 27 - December 2, 1988, p.457-470.

Doraiswami, R. and Gulliver, A., " A Control Strategy for Computer Numerical Control Machine Exhibiting Precision and Rapidity ", Journal of Dynamic Systems, Measurement, and Control, Transactions of the ASME, Vol. 106, March 1984, p.56-62.

Kulkarni, P. K. and Srinivasan, K., " Cross Coupled Compensators for Contouring Control on Multi-axial Machine Tools ", 13th. North American Manufacturing Research Conference Proceedings, University Of California at Berkeley, Berkeley, California, May 19-22 1985, p.558-566.

Shin, Kang G. and McKay, Neil D., " Minimum-Time Control of Robotic Manipulators with Geometric Path Constraints ", IEEE Transaction on Automatic Control, Vol.AC-30, No.6, June 1985, p.531-541.

Stout, D. F., " Handbook of Operational Amplifier Circuit Design ", McGraw-Hill Book Company, New York, 1976.

Tomizuka, M., Dornfeld, D., Bian, X.-Q., and Cal, H.-G., " Experimental Evaluation of the Preview Servo Scheme for a Two-Axis Positioning System ", Journal of Dynamic Systems, Measurement, and Control, Transactions of the ASME, Vol. 106, March 1984, p.1-5.

Tsao, Tsu-Chin , and Tomizuka, M., " Adaptive Zero Phase Error Tracking Algorithm for Digital Control ", Journal of Dynamic Systems, Measurement, and Control, Transactions of the ASME, Vol. 109, December 1987, p.349-354.

Wu, Y.-J. Engin and Beaman, J. J., " Contour Following for Scanning Control in SFF Application : Control Trajectory Planning ", presented at the Solid Freeform Fabrication Symposium, Austin, Texas, August 6-8, 1990.

Wu, Y.-J. Engin and Beaman, J. J., " Solid Freeform Fabrication Laser tracking Control ", presented at the Solid Freeform Fabrication Symposium, Austin, Texas, August 12-14, 1991.

Numerical Simulation of Viscous Sintering under Mechanical Loads

Michael B. Hsu
MARC Analysis Research Corporation
Palo Alto, California

Abstract

This paper describes the use of swelling and creep models in a general purpose finite element program for the simulation of Scherer's constitutive relation for a viscous sintering under uniaxial load. Numerical results of the finite element analysis are presented for validating the models. In the finite element model both the apparent modulus (F) and the apparent Poisson's ratio (N) are used for the stress-strain relation and the stress state considered in the model is multi-dimensional.

Introduction

The growing interest in numerical simulation of sintering processes leads to the recent study of the application of finite element methods to the process [1]. It has been observed that a non-linear general purpose finite element program can be adequately used for modeling the heat conduction in a sintering process. The generality in the finite element approach allows for the study of multi-dimensional problems as well as non-linear material behavior in the process. Based on the assumption that a satisfactory sintering model (e.g. Scherer [2]) is available, the finite element simulations of the sintering process can be expected to include the following areas:

(1) Transient heat conduction problem
(2) Rate dependent elastic stress problem
(3) Rate dependent elastic-plastic stress problem
(4) Coupled thermo-stress problem.

As described in Ref.[1], the study of temperature distributions in laser sintered parts using finite element model has been successful. The sintering models in the study are based on the analyses of Scherer and Mackenzie-Shuttleworth and both the density and conductivity of the particle bed are treated as functions of the void fraction of the bed in the transient finite element heat conduction analyses.

The rate dependent elastic-plastic analysis of a sintering process using finite element simulation has rarely been reported. However, investigation of the hot isostatic pressing (HIP) in powder metallurgy has recently been carried out [3]. The current HIP model assumes visco-plastic representation for the time dependent behavior. It follows classical von Mises yield condition as well as associated flow rule. The yield condition can also be a function of relative density of the powder material. In addition, both the elastic and the thermal constants of the material can be dependent on relative density of the powder material and/or temperatures.

Although finite element coupled thermo-stress analyses have been available for a long time, the author is not aware of any applications of the finite element method to thermo-stress coupling problems in sintering processes. In the conventional coupled thermo-stress analysis, both non-linear material behavior and non-linear boundary conditions can be included in the analysis. Either transient or steady state solution of the problem can be obtainable. With more understanding of the sintering process in terms of thermal and mechanical modeling, it is very possible to perform fully coupled thermo-stress simulation of sintering process sometime in the future.

The attempt in this paper is to carry the finite element modeling one step further into the area of stress analysis of a sintering problem. After reviewing the results of Scherer's [2], it seems to be possible to simulate the rate dependent constitutive equation in the sintering process by swelling and creep models in a general purpose finite element program. In addition, an equation of state approach can be used for the transient solution. It is expected that Scherer's results can be reproduced by the finite element model, and the finite element model can easily be extended to two- or three-dimensional geometries. However, it is not the intent of this paper to discuss the coupling between thermal and mechanical behaviors, as well as inelastic responses such as plasticity, in sintering process.

In the remaining of the paper the sintering model and the constitutive relation described in [2] will be summarized first. Next the swelling and creep models in the finite element analysis will be discussed. Numerical results are included in the subsequent section while an attempt to arrive at some conclusions concludes the paper.

189

Scherer's Models

In ref.[2] both the free strain rate and the constitutive equations for a porous viscous material are discussed in detail. A summary of the discussions is as follows:

(1) Free Strain Rate

Using Scherer's notations, the appropriate free strain rate can expressed as

$$\dot{\varepsilon}_f = -\frac{K}{\eta}\frac{(3\pi)^{1/3}}{6}\frac{2-3cx}{x^{1/3}(1-cx)^{2/3}} \tag{1}$$

for $\rho/\rho_s < 0.94$, and

$$\dot{\varepsilon}_f = -(\frac{K}{\eta})\frac{1}{2}(\frac{4\pi}{3})^{1/3}(\frac{\rho_s}{\rho}-1)^{2/3} \tag{2}$$

for $\rho/\rho_s \geq 0.94$.

Eq.(1) is due to Scherer, using a micro-structural model consisting of cylinders, and Eq.(2) is given by Mackenzie-Shuttleworth.

(2) Constitutive Equations

For a porous viscous material the following constitutive equations have been proposed by Scherer.

$$\dot{\varepsilon}_r = \dot{\varepsilon}_f + \frac{1}{F}[\sigma_r - N(\sigma_\theta + \sigma_z)] \tag{3a}$$

$$\dot{\varepsilon}_z = \dot{\varepsilon}_f + \frac{1}{F}[\sigma_z - N(\sigma_r + \sigma_\theta)] \tag{3b}$$

$$\dot{\varepsilon}_\theta = \dot{\varepsilon}_f + \frac{1}{F}[\sigma_\theta - N(\sigma_z + \sigma_r)] \tag{3c}$$

Note that Eq.(3c) is not given in [2].
In Eq.(3) σ_r, σ_z, σ_θ are the radial, axial and hoop stresses, respectively. The apparent

modulus (F) and the apparent Poisson's ratio (N) can be approximated by

$$F = \frac{3\eta\rho}{(3\rho_s - 2\rho)}$$

(4)

$$N = \left(\frac{1}{2}\right)\left[\frac{\rho}{(3\rho_s - 2\rho)}\right]^{1/2}$$

In these equations, η is the shear viscosity, $\rho(t)$ is the bulk density, ρ_s is the theoretical density of the pore-free sample. As ρ approaches ρ_s, we have $F \rightarrow 3\eta$ and $N \rightarrow 0.5$, and Eq.(3) reduces to the usual constitutive equations for an incompressible viscous liquid.

Finite Element Models (Swelling and Creep)

In the finite element modeling of stress problems, the total strain vector in the structure is assumed to be a linear combination of various strains

$$\varepsilon = \varepsilon_e + \varepsilon_{sw} + \varepsilon_{cr}$$

(5)

Rewriting Eq.(5) in the rate form we have

$$\dot{\varepsilon} = \dot{\varepsilon}_e + \dot{\varepsilon}_{sw} + \dot{\varepsilon}_{cr}$$

(6)

where $\dot{\varepsilon}$ is the total strain rate, $\dot{\varepsilon}_e$, $\dot{\varepsilon}_{sw}$ and $\dot{\varepsilon}_{cr}$ are total elastic, swelling and creep strain rates, respectively. For a given time step Δt, the assumption of a linear variation of strain in time, yields the following relation of incremental strains

$$\Delta\varepsilon = \dot{\varepsilon}\Delta t = \Delta\varepsilon_e + \Delta\varepsilon_{sw} + \Delta\varepsilon_{cr}$$

(7)

Rewriting Eq.(7), we obtain the expression of incremental elastic strain as

$$\Delta\varepsilon_e = \Delta\varepsilon - \Delta\varepsilon_{sw} - \Delta\varepsilon_{cr} \tag{8}$$

The expression of incremental stress vector is

$$\Delta\sigma = D\Delta\varepsilon_e \tag{9}$$

where D is the constitutive matrix.

Following the principle of virture work, the following expression of incremental equilibrium equation can be obtained.

$$[K]\,\Delta u = \Delta p + \int_v B^T D\,(\Delta\varepsilon_{sw} + \Delta\varepsilon_{cr})\,dv \tag{10}$$

In Eq.(10), K is the stiffness matrix, and Δu and Δp are incremental displacement and incremental nodal force vectors, respectively. The integral

$$\int_v B^T D\,(\Delta\varepsilon_{sw} + \Delta\varepsilon_{cr})\,dv \tag{11}$$

is a pseudo load vector due to the swelling and creep strain increments, in which B is the strain displacement relation and D is the stress-strain relation.

Comparing Eq.(3) with Eq.(6) one observes that the free strain rate $\dot{\varepsilon}_f$ in Eq.(3) can be treated as the swelling strain rate in Eq.(6), while the remaining term in Eq.(3) can be represented as the creep strain rate in Eq.(6). Consequently, it can be seen from Eq.(10) that the incremental swelling and creep strains can be estimated from the strain rate expressions with a given time step. The pseudo force vector can then be evaluated from the volume integral shown in Eq.(11) and added to the load-side of the incremental equilibrium equation (Eq.(10)). Accumulations of the incremental displacements obtained from solution of Eq.(10) represent a deformation history of the structural system. It is noted that the stiffness matrix K in Eq.(10) can be elastic or, inelastic depending on the material behavior of the structure. The finite element swelling and creep models can easily accept material non- linearities providing non-linear material data are available in sintering processes.

Case Study

In order to validate the swelling and creep models in the finite element analysis, for the simulation of a sintering process, two problems were investigated in this study. The first analysis demonstrates that Scherer's results can be reproduced, and the second problem shows an application of the models to a sintering problem of a simple three-dimensional geometry. Finite element results of Analysis one compares well with Ref.[2].

(1) Deformation of a Solid Cylinder

The geometry of a solid cylinder, as discussed in [2], is shown in Fig.1a. In the finite element analysis, both the 4-node two-dimensional axisymmetric element and the 8-node three-dimensional brick element were used. The total creep time was chosen to be 0.8, and a total of 11 time increments were needed for the completion of the creep analysis. The free strain rate equations, Eq.(1) and Eq.(2), were selected for the swelling strain rate in the finite element analysis.
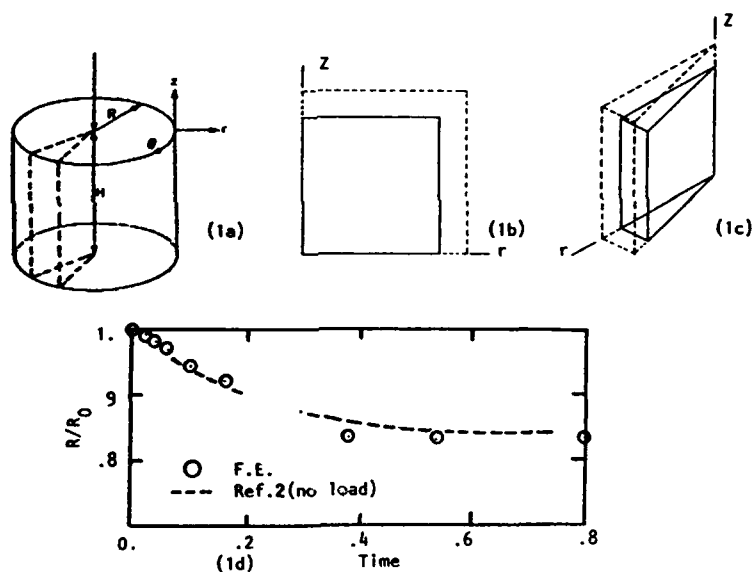
Fig. (1a) Solid Cylinder (Ref.[2]), (1b) Deformed Cylinder (4-node model), (1c) Deformed Cylinder (8-node model), (1d) Radial Reduction vs. Time

Fig.1b shows deformation of the cylinder at the end (t=0.8) of the creep, in the two-dimensional analysis. Final deformation of the three-dimensional analysis is also given in Fig.1c. Favorable comparison of the time variation of radial reduction with Scherer's results (see Fig.1d) is quite evident.

193

(2) Fixed End Column

Fig.2a shows the geometry of a square column with both ends fixed in space. Due to symmetry, only one eighth of the column was modeled in the finite element analysis. Four 8-node three-dimensional brick elements were used for the finite element model. In this analysis, both the swelling strain rate and the creep time were assumed to be the same as in Analysis one.
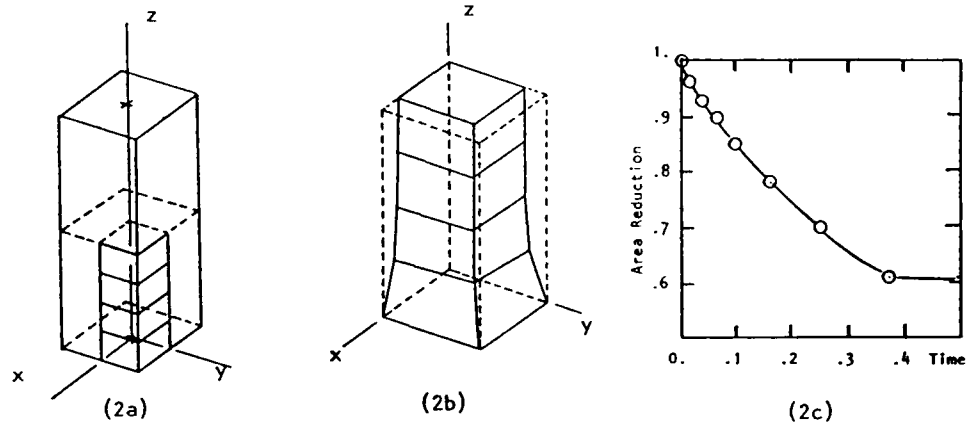
Fig (2a) Square Column, (2b) Deformed Column,
(2c) Area Reduction vs. Time

The deformation of the column at end of creep (t=0.8) is shown in Fig.2b. The time variation of the area reduction due to sintering, shown in Fig.2c appears to be satisfactory.

Conclusions

Numerical results presented in the paper clearly demonstrated the validity of using swelling and creep models in the finite element analysis, for the prediction of deformations of sintered structures. In the current study, both the two- and the three-dimensional geometries have been analyzed and the results have been found to be satisfactory. The finite element models have long been recognized to be able to deal with various non-linearities in the problems. The obvious difficulty in a successful simulation of a sintering process remains to be the lack of good understanding of the constitutive relation of the sintered material.

References

[1] Weissman,E.M. and Hsu, M.B., "A Finite Element Model of Multi-Lauered Laser Sintered Parts," SFF, Austin, Texas, 1991

[2] Scherer, G.W., "Viscous Sintering Under a Uniaxial Load," J.Am. Ceram. Soc.69 [9], 1986

[3] Zhao, K., "Finite Element Analysis in Hot Isostatic Pressing Applications," (to be published), MARC analysis research corp., 1992

FUNDAMENTALS OF STEREOLITHOGRAPHY

July 1992

Dr. Paul F. Jacobs

Director of Research & Development

3D Systems, Inc.
Valencia, California

1. INTRODUCTION

It has only been a little over four years since the introduction of the first StereoLithography system, the SLA-1. From early 1988 until June 1992 over 300 SLA-1, SLA-250, SLA-190 and SLA-500 units have been sold by 3D Systems. These machines, currently operating in 20 countries on five continents, amount to about 90 percent of all the rapid prototyping systems now in use.

Notwithstanding these figures, the field of rapid prototyping is still quite young. The author has been surprised to note that even among existing users, knowledge of the most basic relationships of this new technology is at best uncertain. For newcomers, even less is known.

It is therefore appropriate, on the occasion of the 1992 Solid Free-Form Fabrication Conference in Austin, for us to develop those fundamental relationships which form the foundation of this technology. In the transition of StereoLithography from an art to a science, it is natural that we should attempt to develop a model of the process. Although the mathematics may seem formidable to some readers, the physical model is actually quite simple. While requiring only <u>three</u> key assumptions, we shall derive <u>seven</u> fundamental relationships, leading to <u>nineteen</u> important conclusions.

The interaction of actinic photons with reactive photopolymer involves some very complex physics and chemistry. Nonetheless, the theoretical predictions of the model described herein are in good agreement with numerous experimental measurements, at least to first order. The primary benefit of this analysis is the development of a good physical understanding of the basic phenomena. This description avoids the extreme complexity and inevitable loss of generality that would likely result from either analytical or numerical attempts at an even more accurate model. While advanced studies continue, it was felt that the material presented is certainly appropriate at the operational level.

2. GAUSSIAN LASER SCANNING

Consider an actinic laser beam being scanned in a straight line, at constant velocity, over the free surface of a vat of liquid photopolymer. We shall make three key assumptions:

1. The photopolymer resin obeys the Beer-Lambert law of exponential absorption.

2. The laser irradiance distribution is Gaussian.

3. The resin transitions from the liquid phase to the solid phase at the so-called "gel point".

Let us now define a coordinate system as shown in Figure 1. Here the laser is scanned directly along the x axis, in the direction of increasing x. The y coordinate is laterally orthogonal to the laser scan axis, with positive y defined by the right hand rule. Thus, y = 0 directly under the centerline of the laser scan axis. Finally, the positive z coordinate extends downward into the resin, and is measured normal to the x-y plane of the free resin surface, where z = 0. To define the origin, consider some arbitrary point Q(x,y,z) within the resin. Let Q'(0,y,0) be the projection of Q onto the resin surface. We shall arbitrarily select the origin such that both the x and z coordinates of Q' are zero.

From the Beer-Lambert law (Reference 1),

$$H(x,y,z) = H(x,y,0) \exp[- z/Dp] \qquad (1)$$

where H(x,y,z) is the irradiance at any arbitrary point, H(x,y,0) is the surface irradiance at any point x,y,0, and Dp is the "Penetration Depth" of the resin at the laser wavelength. Dp is defined as that depth of resin which will reduce the irradiance to 1/e (about 37 %) of the surface irradiance.

Further, if we assume that the laser irradiance distribution is Gaussian (as seen in Figure 2, this is generally a reasonably good approximation), then from Reference 2,

$$H(x,y,0) = H(r,0) = Ho \exp[-2 r^2/ Wo^2] \qquad (2)$$

where Wo is the <u>radius</u> of the Gaussian beam, defined per Reference 2 at the $1/e^2$ point (i.e. at that location where the local irradiance equals about 13.5 percent of the peak irradiance, Ho). Note that since the Gaussian function is circularly symmetric, it is also convenient to perform some of the calculations in cylindrical coordinates.

3. <u>TOTAL LASER POWER</u>

To determine Ho, we recognize that the total laser power incident on the resin surface, P_L , must equal the integral of the laser irradiance distribution over the entire resin surface (i.e. from r = 0 to r = ∞). Thus,

$$P = \int_0^\infty H(r,0) \, 2\pi \, rdr \qquad (3)$$

$$= 2\pi Ho \int_0^\infty \exp[-2r^2/ Wo^2] \, rdr$$

LASER

V_s

x

$Q'(0, y, 0)$

y

$Q(x, y, z)$

z

FIGURE 1

GAUSSIAN LEAST SQUARES FIT   Photon Inc.
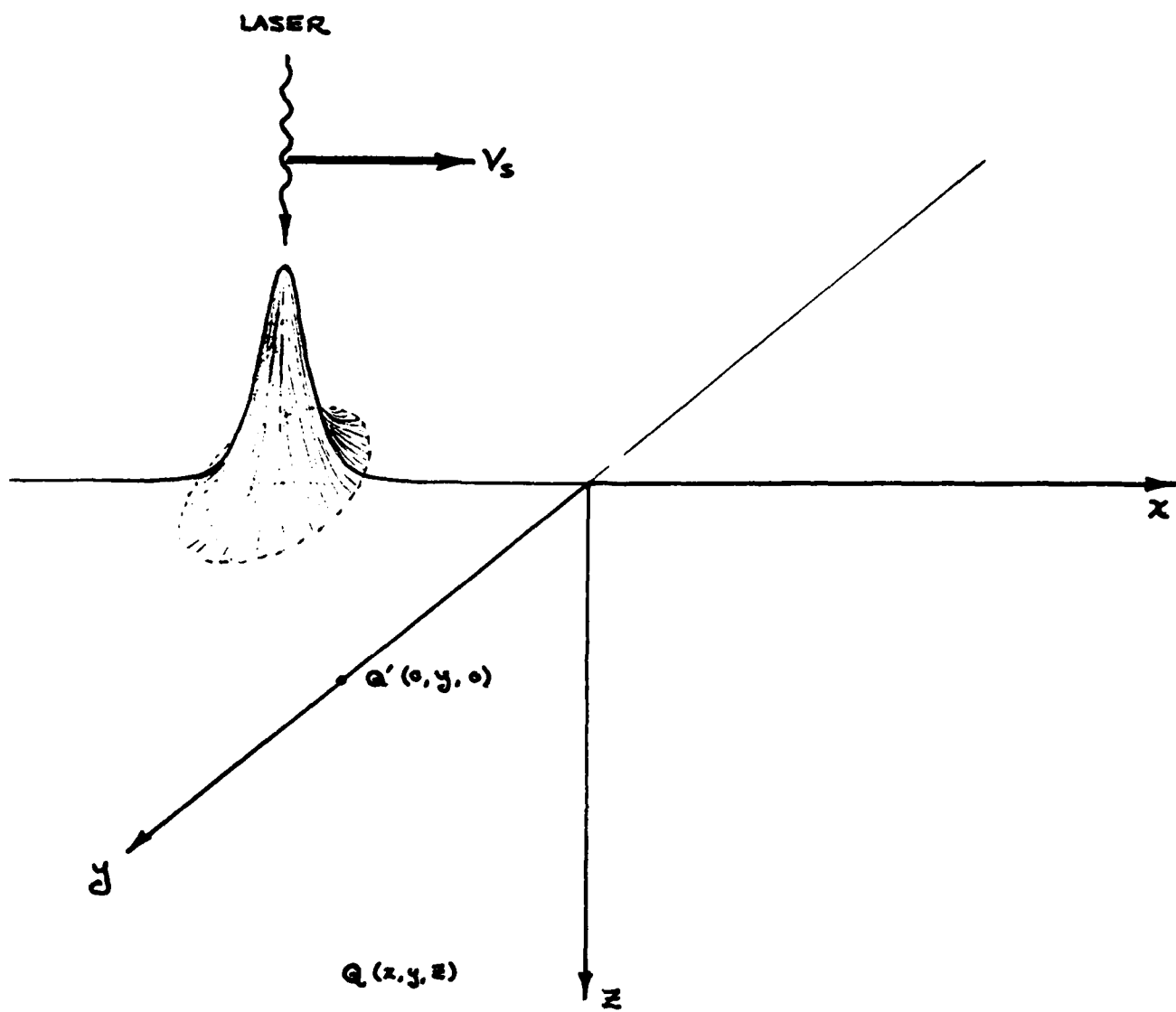
ID: BETA4 slitN2 140 mw @ head
Date: 2/12/92
Position (data)   : 2704.3
Position (gauss) : 2703.7
Goodness Of Fit   : 0.012

Clip Level	Beam Dia.	Gauss Dia.
5.0%	322.9	282.8
13.5%	239.8	231.2
36.8%	167.8	163.4
50.0%	140.7	136.8
60.7%	119.7	115.5

POSITION (microns)

INTENSITY

FIGURE   2
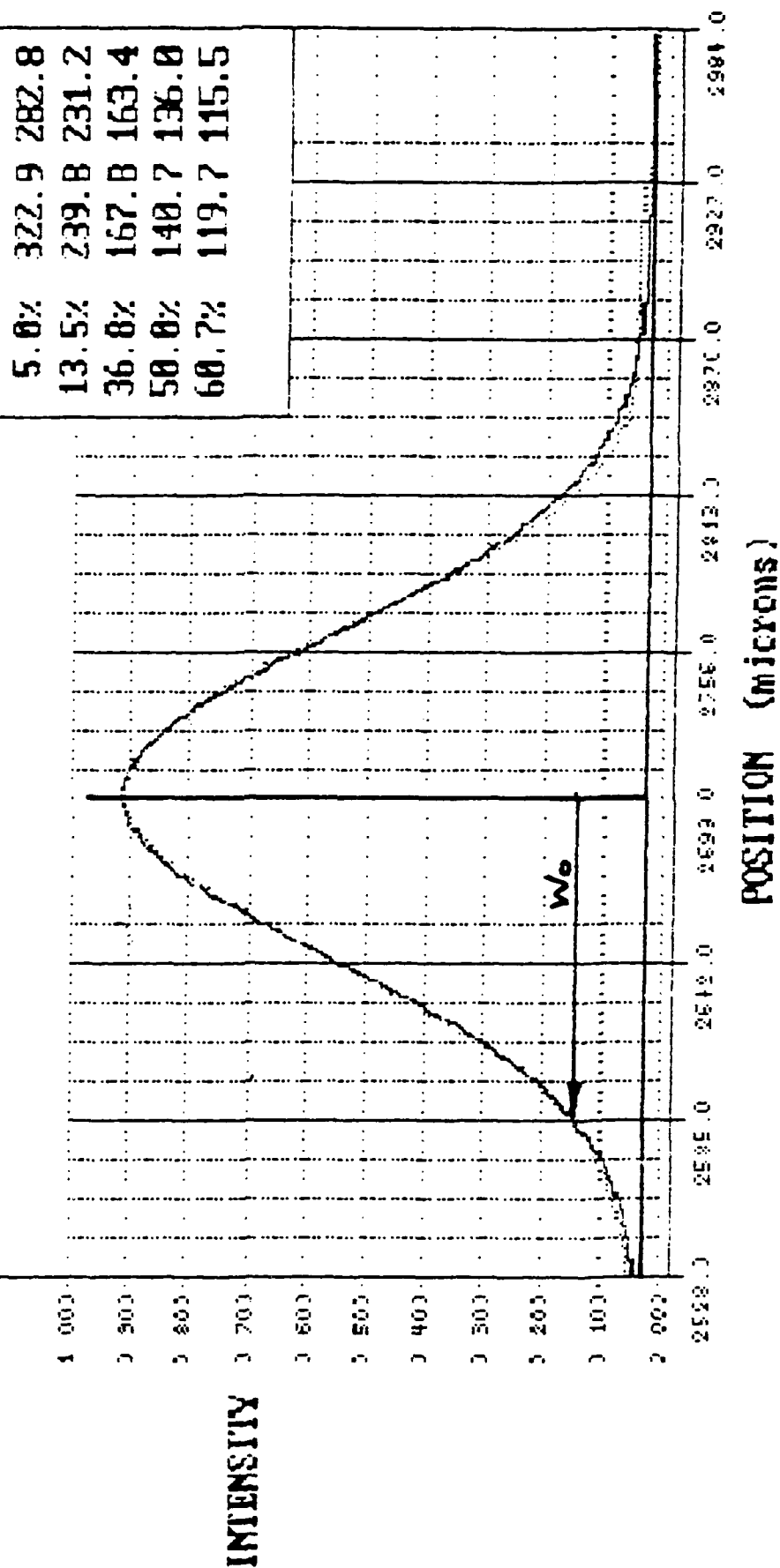
Define $\quad u \equiv 2r^2/Wo^2 \quad$ or $\quad rdr = (Wo^2/4) \, du \quad\quad$ (4)

Substituting equation (4) into equation (3),

$$P_L = \frac{\pi}{2} Wo^2 Ho \int_0^\infty \exp[-u] \, du = \frac{\pi}{2} Wo^2 Ho \quad\quad (5)$$

Solving for the peak irradiance at the free resin surface, Ho , we obtain the result,

$$Ho = 2 P_L / \pi Wo^2 \quad\quad (6)$$

Substituting this result into equation (2), and then into equation (1), we obtain the Gaussian laser irradiance distribution function in cylindrical coordinates,

$$H(r,z) = (2 P_L / \pi Wo^2) \exp[-z/Dp - 2r^2/Wo^2] \quad\quad (7)$$

4. THE EXPOSURE FUNCTION

For StereoLithography photopolymers, the extent of reaction depends upon the number of actinic photons absorbed per unit volume. This quantity can be shown to be directly proportional to the actinic exposure, E , which has the units of energy per unit area (e.g. millijoules per square centimeter). By definition, the actinic exposure is the time integral of the actinic irradiance. Hence,

$$E = \int H \, dt \quad\quad (8)$$

Since the laser is being scanned at constant velocity, Vs , along the x axis, with x increasing, then

$$Vs = dx/dt \quad\quad \text{or} \quad\quad dt = dx / Vs \quad\quad (9)$$

Substituting equations (7) and (9) into equation (8) ,

$$E(r,z) = (2 P_L / \pi Wo^2 Vs) \exp[-z/Dp] \int_{-\infty}^{\infty} \exp[-2r^2/Wo^2] \, dx \quad\quad (10)$$

where the factor $\exp[-z/Dp]$ can be moved outside the integral sign since z is not a function of x. From the Pythagorean theorem,

$$r^2 = x^2 + y^2 \tag{11}$$

thus,

$$\exp[-2r^2/W_0^2] = \exp[-2x^2/W_0^2] * \exp[-2y^2/W_0^2] \tag{12}$$

Substituting equation (12) into equation (10), moving the factor $\exp[-2y^2/W_0^2]$ outside the integral, as it is also not a function of x, and further recognizing that since the integral of equation (10) is symmetric about $x = 0$ (viz. the contribution from $-\infty$ to 0 is exactly equal to that from 0 to ∞) then the total integral must be twice the value from 0 to infinity. Therefore,

$$E(y,z) = (4P_L/\pi W_0^2 V_s)\exp[-z/D_p - 2y^2/W_0^2]\int_0^\infty \exp[-2x^2/W_0^2]dx \tag{13}$$

Define

$$v \equiv \sqrt{2}\, x / W_0 \tag{14}$$

Taking differentials of equation (14),

$$dv = (\sqrt{2}/W_0)\, dx \qquad \text{or} \qquad dx = (W_0/\sqrt{2})\, dv \tag{15}$$

Thus, evaluating the integral in equation (13), by substituting from equations (14) and (15), we obtain,

$$\int_0^\infty \exp[-2x^2/W_0^2]\, dx = (W_0/\sqrt{2})\int_0^\infty \exp[-v^2]\, dv \tag{16}$$

This integral is related to the error function. From Reference 3 we find that

$$\int_0^\infty \exp[-v^2]\, dv = \sqrt{\pi}/2 \tag{17}$$

Substituting equations (16) and (17) into equation (13), we obtain after some algebra,

$$E(y,z) = (2/\pi)^{1/2}\{P_L/W_0 V_s\}\exp - [z/D_p + 2y^2/W_0^2] \tag{18}$$

From equation (18) it is evident that the exposure reaches its maximum value $E = E_{max}$ when $y = 0$ (i.e. on the laser scan axis) and $z = 0$ (i.e. on the free resin surface). This <u>maximum laser exposure</u> value is given by the wonderfully simple expression;

$$\boxed{Emax \quad = \quad (\, 2 \, / \, \pi \,)^{1/2} \; P_L \; / \; Wo \; Vs} \qquad\qquad (19)$$

Equation (19) is our <u>first</u> important result. It shows that the maximum actinic laser exposure is:

*   <u>Directly proportional to the laser power</u>.
*   <u>Inversely proportional to the product of the beam radius and the scan velocity</u>.
*   The proportionality constant is simply $(\underline{\; 2 \; / \, \pi \,)^{1/2} = \; 0.7979}..,$ a pure number involving no empirical quantities whatever.

5. <u>THE PARABOLIC CYLINDER</u>

For photopolymer resins, when the exposure is less than a critical value, Ec , the resin remains liquid. When E > Ec , the resin undergoes at least partial polymerization. However, if E = Ec, the resin is at the so-called "gel point", corresponding to the transition from the liquid phase to the solid phase. Hence, we may solve for the locus of points y = y* , and z = z* , which are just at the gel point. All points <u>inside</u> this locus will be at least partially solidified while all points <u>outside</u> this boundary will still be liquid. Clearly, the resulting boundary will then define the cross-sectional shape of a single laser cured photopolymer "string".

Thus, setting y = y* and z = z* when E = Ec in equation (18), after some algebra we find,

$$exp \, [\; 2y^{*2} / \, Wo^2 \; + \; z^* \, / \, Dp \;] \quad = \quad (\, 2 \, / \, \pi \,)^{1/2} \{ \; P_L \, / \, Wo \; Vs \; Ec \; \} \qquad (20)$$

Taking natural logarithms of equation (20), and substituting from equation (19), we obtain the result,

$$\boxed{2 \, y^{*2} / \, Wo^2 \quad + \quad z^* \, / \, Dp \quad = \quad \ln \, [\; Emax \, / \, Ec \;]} \qquad\qquad (21)$$

This is our <u>second</u> important result. We may write equation (21) in the form

$$A \, y^{*2} \; + \; B \, z^* \; = \; C$$

where A, B, and C are all positive constants. From Reference 4, this is the equation, in three dimensions, of a <u>parabolic cylinder</u> whose axis is the x axis, which, by definition of our coordinate system is precisely the laser scan axis.

Figure 3 shows a parabolic cylinder which results from simply scanning an actinic laser in a straight line at constant velocity over the surface of a vat of liquid photopolymer, provided that Emax > Ec. Thus, the <u>fundamental building elements of StereoLithography are actually parabolic cylinders</u>, often referred to as "strings".

6. <u>THE WORKING CURVE</u>

We may now define the <u>maximum cure depth</u> of a single laser cured string by the symbol Cd . From either Figure 3, or equation (21), it is evident that z* = z(max) = Cd when y* = 0. Or, simply stated, the maximum cure depth will occur directly under the laser scan axis. Thus, setting z* = Cd when y* = 0 in equation (21), we finally obtain the fundamental "Working Curve" equation of StereoLithography,as discussed in Reference 5;

$$Cd = Dp \ln [Emax / Ec] \tag{22}$$

This is our <u>third</u> important result, and is <u>absolutely fundamental</u> to an understanding of this technology. Equation (22) shows that:

* <u>The cure depth should scale as the natural logarithm of the maximum actinic laser exposure</u>.

* <u>A semi-logarithmic plot of Cd vs ln Emax should result in a straight line relationship,</u> known as the Working Curve.

* The <u>slope</u> of the Working Curve is exactly the <u>penetration depth</u> , Dp , of the resin, at the laser wavelength.

* Since ln(1) = 0, the <u>intercept</u> of the Working Curve (i.e. the value of Emax where Cd = 0) is precisely the <u>critical exposure</u>, Ec , of the resin, at the laser wavelength.

* Since Dp and Ec are purely resin parameters, then within the limits of this model, both the slope and the intercept of the Working Curve should be <u>independent</u> of either the laser power, P_L , the laser spot size, Wo , or the laser scan velocity, Vs.

Figure 4 shows an actual Working Curve for Ciba-Geigy resin XB 5149. Note the excellent linearity of this semi-logarithmic plot. The resulting values of Dp and Ec are indicated.

204

L_w

$Z_{max} \equiv C_d$
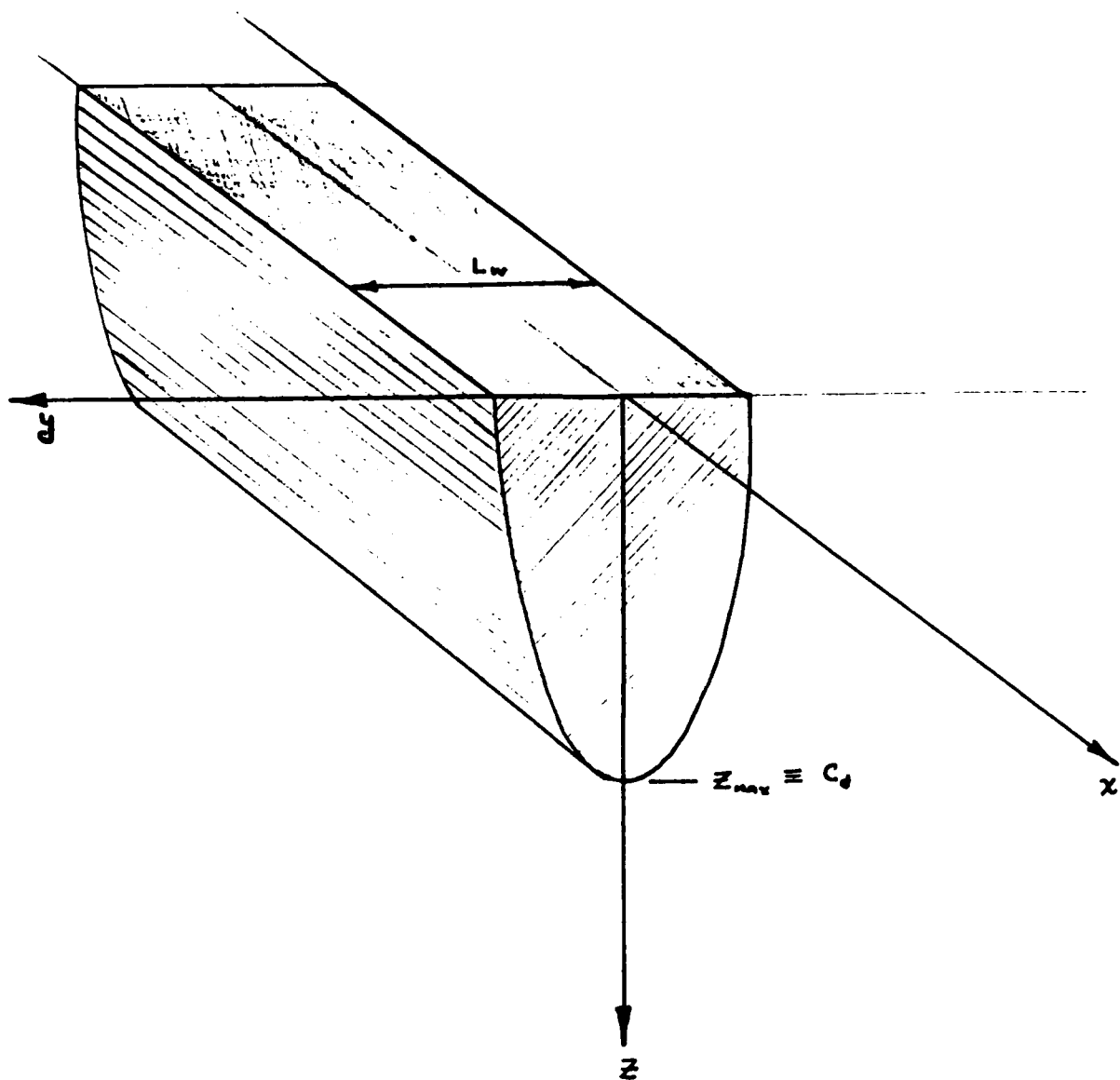
FIGURE 3

WORKING -- CURVE

Resin : XB 5149

Dp = 5.8 mils   Ec = 6.8 mJ/cm^2

Cure Depth (mills)

EXPOSURE (mJ/cm^2)
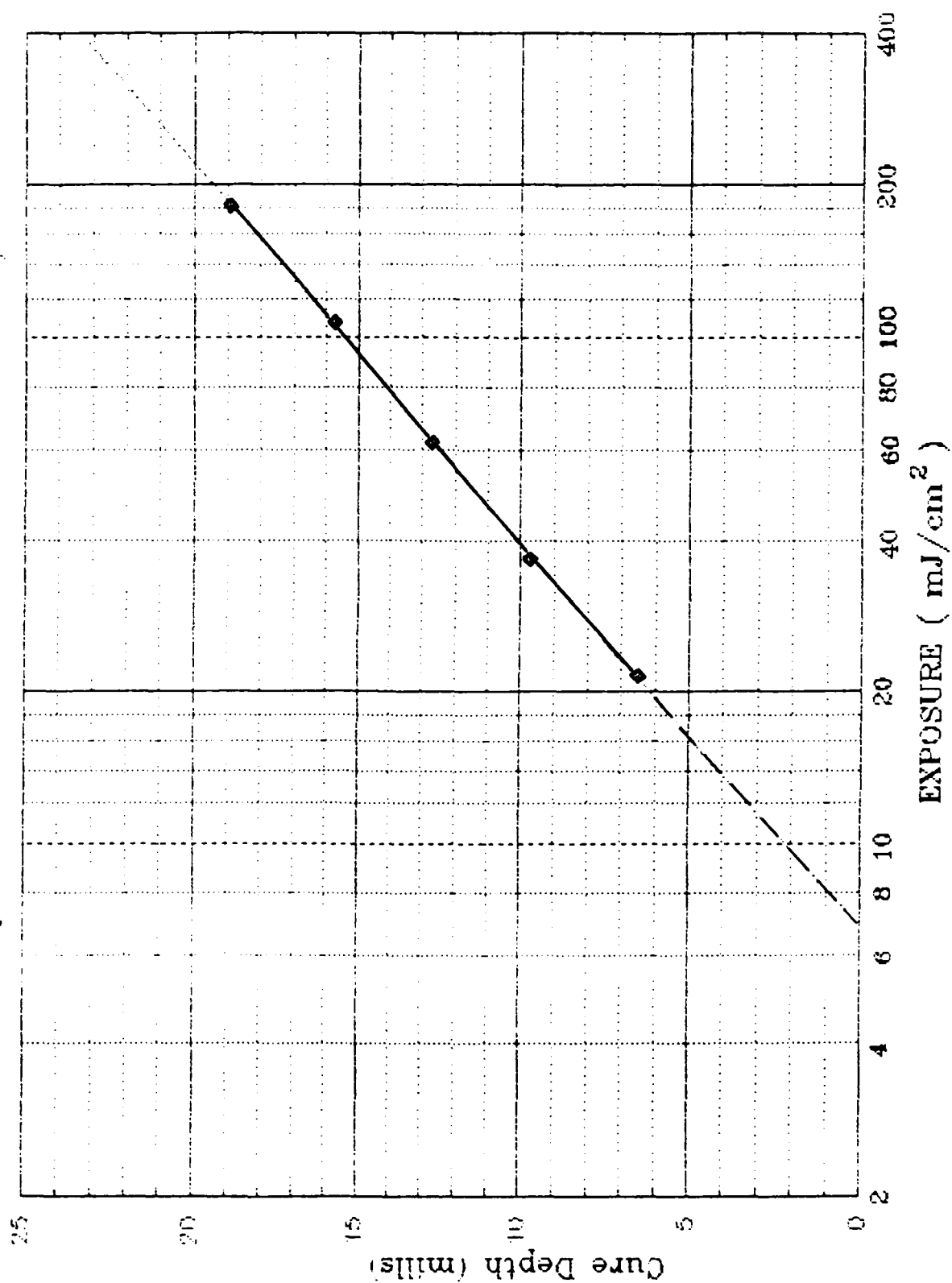
FIGURE 4

7. THE CURED LINEWIDTH

Returning to equation (21) and Figure 3, it is also clear that the maximum cured linewidth, Lw , will occur at the resin surface, where the parabolic cylinder has its greatest width. Therefore, setting y* = y(max) = Lw /2 , when z* = 0, we obtain after some algebra,

$$Lw = \sqrt{2} \; Wo \; \{ \; \ln \; [\; Emax \; / \; Ec \;] \; \}^{1/2} \tag{23}$$

Substituting for ln [Emax / Ec] from equation (22), we obtain the basic "Cured Linewidth" equation,

$$Lw = Wo \sqrt{2 \; Cd \; / \; Dp} \tag{24}$$

This is our fourth important result. It shows that:

* The cured linewidth of a string is directly proportional to the laser spot size at the plane of the resin surface. In calculating numerical values, remember that Wo is the radius of the laser spot, not the diameter.

* The cured linewidth is also proportional to the square root of the ratio of the cure depth to the resin penetration depth. Thus strings of greater cure depth will also be wider, but their width will not increase linearly with Cd.

* Even if Wo and Cd are held constant, the cured linewidth will depend upon the resin penetration depth. This is important to remember whenever one changes resins.

8. LASER SCAN VELOCITY

A modified form of equation (22) may be written as follows:

$$Emax = Ec \; \exp \; [\; Cd \; / \; Dp \;] \tag{25}$$

Substituting for Emax from equation (19) we find,

$$Emax = (\; 2 \; / \; \pi \;)^{1/2} \{ \; P_L \; / \; Wo \; Vs \; \} = Ec \; \exp \; [\; Cd \; / \; Dp \;] \tag{26}$$

Solving for the laser scan velocity, Vs , we obtain the result

$$Vs = (2 / \pi)^{1/2} \{ P_L / Wo\ Ec \} \exp [-Cd / Dp] \qquad (27)$$

This is our <u>fifth</u> important result. It illustrates the following:

* <u>The laser scan velocity is directly proportional to the laser power</u>. Thus, subject to system servo limits, the higher the laser power the faster the scan speed for a given resin, laser spot size, and cure depth.

* The laser scan velocity is <u>inversely proportional to the laser spot size</u>. Thus, increasing the spot size decreases the laser scan velocity for a given laser power, resin and cure depth.

* The laser scan velocity decreases in an <u>exponential</u> manner with an increase in the ratio Cd / Dp. For a given resin, this is the reason why increased cure depths draw much more slowly than shallow cure depths.

* Again, the <u>constant of proportionality</u> predicted by this model is the same pure number, $(2 / \pi)^{1/2} = 0.7979\ldots$.

Equation (27) is currently incorporated into 3D Systems software. It is the basis for all automatic laser scan velocity calculations on the SLA-190, the SLA-250, and the SLA-500. Experimentally measured cure depths, generated using the automatic laser scan velocity algorithm, are typically within a few percent of the desired values. Further, the residual errors are approaching the limits of the experimental technique (viz. standard deviations of +/- 0.15 mil or about +/- 4 microns).

9. DRAWING TIME PER UNIT AREA

In StereoLithography, the great majority of the laser drawing time is spent "hatching" to solidify the regions of parts interior to their borders. Except for very tiny parts, the time required to draw the borders is generally a small fraction of the time required to complete the hatching process. For complete generality we could analyze any arbitrary cross section. However, to simplify the calculations, let us consider a rectangle of length L , in the scan direction, and width w, perpendicular to the scan direction. Figure 5 shows this rectangle, whose area is simply A = Lw .

Now, let us perform the hatching operation by drawing straight parallel vectors with a hatch spacing, hs , as occurs with the advanced building techniques WEAVE™ and STAR-WEAVE™ . Neglecting finite acceleration and deceleration effects at the ends of each hatch vector, the time required to draw a single string of length L is simply:

208
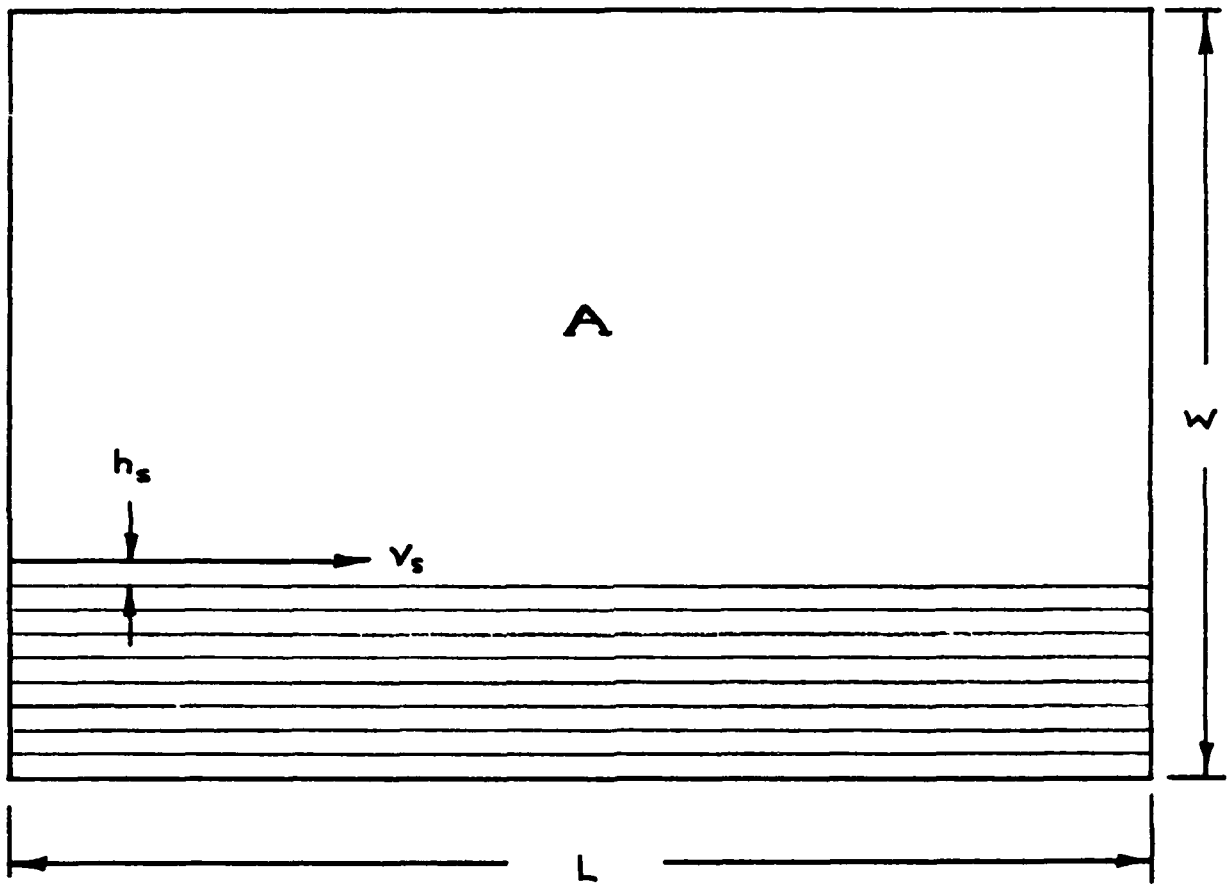
FIGURE 5

$$t = L / Vs \qquad (28)$$

Within integer round-off, the number of such vectors, N, is given by

$$N = w / hs \qquad (29)$$

Thus, to close approximation the laser drawing time, t_d, is given by the following:

$$t_d = N t = (w / hs)(L / Vs) = A / hs Vs \qquad (30)$$

Finally, in the advanced build methods WEAVE™ and STAR-WEAVE™, the hatch spacing is taken proportional to the laser spot size Wo. Thus,

$$hs = k Wo \qquad (31)$$

where k is a constant, generally near 2, so that the optimum hatch spacing is of the order of the beam diameter. Substituting equations (27) and (31) into equation (30) we obtain after some algebra:

$$t_d / A = (1/k)(\pi / 2)^{1/2} \{ Ec / P_L \} \exp [Cd / Dp] \qquad (32)$$

This is our <u>sixth</u> important result. Equation (32) indicates that within the accuracy of the approximations we have made;

* The drawing time per unit cross-sectional area is <u>directly proportional to the resin critical exposure</u>, Ec. Resins with higher values of Ec will draw more slowly.

* The drawing time per unit area is <u>inversely proportional to the laser power</u>, P_L. As one might expect, higher power lasers will reduce draw time, provided one has not reached the system servo limit.

* The drawing time per unit area <u>increases exponentially with increased cure depth to penetration depth ratio</u>. For a given resin with a specific value of Dp, increased cure depths draw <u>much more slowly</u>. Thus, in addition to improved part accuracy, because the advanced techniques WEAVE™ and STAR-WEAVE™ utilize reduced cure depths relative to the former Tri-Hatch method, they actually draw faster even though many more individual vectors are required.

* Finally, and especially significant, is the observation that at least to first order, the laser drawing time per unit area is independent of the laser spot size. This result, which is probably not intuitively obvious, has been substantiated experimentally for all the approved StereoLithography resins.

The latter point leads to the seventh important result. Since laser drawing time is independent of laser spot size to first order, then dynamic optical zoom is of limited utility in such a system, unless one is always operating at the servo limit. Dynamic zoom (viz. the ability to vary the laser spot size over a wide dynamic range) would increase system cost, increase system complexity, reduce reliability, and, as the above analysis shows, provide productivity gain only for those laser power levels which exceed the system servo limit.

10. SUMMARY

We have derived some of the most fundamental relationships of StereoLithography. Each of these results has been experimentally confirmed to varying levels of accuracy. Higher order effects such as optical self-focusing, resin "bleaching", radiation scattering, non-Gaussian laser modes, finite acceleration and deceleration intervals, and system servo limitations will alter the trends somewhat. Nonetheless, the mathematical results discussed in this paper are predominantly valid, and should be considered fundamental to a solid understanding of this technology.

REFERENCES

1. Kauzmann, W., " An Introduction to Quantum Chemistry ", Academic Press, New York, 1957, pp. 578-579.

2. Siegman, A.E., "An Introduction to Lasers and Masers", McGraw-Hill, New York, 1971, Chapter 8, pp. 312-314.

3. Sneddon, I.N., "Special Functions of Mathematical Physics and Chemistry", Oliver and Boyd, London, 1961, pp. 13-14.

4. Sherwood, G.E.F. and Taylor, A.E., "Calculus", Prentice-Hall, Inc., Englewood Cliffs, New Jersey, Third Edition, 1958, pp. 310.

5. Richter, J., and Jacobs, P.F., "The Present State of Accuracy in StereoLithography", Conference Proceedings, Second International Conference on Rapid Prototyping, University of Dayton, Dayton, Ohio, June 23-26, 1991, pp. 269-294.

THE MATERIALS ADVANTAGE OF THE SLS™ SELECTIVE LASER SINTERING PROCESS

DTM Corporation
Luke L. Kimble
Market Development Manager
July 29, 1992

Introduction

The rapid prototyping market continues to progress in terms of processes and materials used for the creation of conceptual and functional parts and prototype tooling. As this market continues to mature, the market leaders will be able to offer rapid prototyping processes and materials that provide parts which are accurate, have good surface finish, and provide properties which support functional applications. The materials used for these parts will be polymers, metals, and ceramics. The strength of the SLS™ Selective Laser Sintering Process is the potential to use a wide variety of powdered materials for the creation of models, patterns, and some forms of prototype tooling. This paper will cover the types of materials currently used in the SLS process and their inherent advantages and discuss current research into the development of new materials.

Powdered Materials

The use of powdered materials in the SLS process has several inherent features that address the basic requirements for fast modeling, prototyping, and pattern-making within almost all industries. These include:

1) Speed;
2) The additive-layer nature of the part building process; and
3) The ability to employ a variety of heat-fusible powdered materials.

Speed

The main factor affecting the speed at which a part can be built is the thickness of the layers being sintered. A part which is being sintered with a layer thickness of 0.005 inch (0.125mm) will take approximately twice as long as a part being sintered with a layer thickness of 0.010 inch (0.25mm). This is due to the total number of layers needed to manufacture the part. At 0.005 inch (0.125mm)it will take 200 layers to build 1 inch of part height. Using a 0.010 inch (0.25mm) layer thickness, the 1 inch part will require 100 layers to build the part.

The time needed to scan a layer of a part is determined by the area of the layer, the complexity of the layer, and the number of parts being built simultaneously. As the size, complexity, and number of parts increase, the time needed to complete a layer in the process increases.

The type of material will also greatly affect the time needed to complete a part. The wax requires more time to process since a cool down time is added to each layer at the end of the scanning process. This cooling period may be from 1 to 30 seconds depending on the geometry and size of the parts. Typical build times for materials used in the SLS process are:

Wax build rate of 0.125 to 0.5 inch (3.125 to 12.5 mm) of vertical height per hour
Thermoplastic build rate of 0.2 to 1.0 inch (5.0 to 25.4 mm) of vertical height per hour.

To further increase the overall speed, the SLS process software performs concurrent slicing of the part geometry files while processing of the object is taking place. Moreover, no post-production curing is necessary with the SLS process when using wax or thermoplastic.

An Additive Layer Process

The additive-layer nature or layered manufacturing technique of the SLS process also allows for the creation of very complex parts without the need for external support structures or fixtures, clamping, or repositioning of specific portions of the design geometry. This is possible because the unsintered powder that surrounds the fabricated part during the SLS process provides a customized support structure that is easily removed upon part completion. Designs with internal cavities, overhangs, undercuts, and other intricate geometries, which are difficult to achieve through other processes, are easily produced using the SLS process. In short, the SLS process allows a degree of total design freedom never before realized because of the constraints tooling placed on designs.

Multiple Materials

The SLS process can use a variety of materials. In fact, virtually any material that softens and has decreased viscosity upon heating or that can sinter with the application of heat can potentially be used. Materials currently available include: investment casting wax, polycarbonate, and nylon. Other thermoplastics that have shown potential as powdered materials in the SLS process include polyester, polyurethane, and a glass filled nylon.

The natural evolution of the SLS technology is also heading toward the use of powdered metals and ceramics. Current market research indicates that this capability will have widespread application throughout manufacturing industries, primarily because more than 80 percent of all design prototypes are currently made from various metals using conventional processes.

Metals and Ceramics

In response to these market requirements for metals and ceramics, DTM is currently funding research using powdered metals and ceramics with the SLS process. This research is focused in the areas of direct and indirect sintering using the SLS process. The indirect method involves combining a low temperature binder with a powdered metal or ceramic to form a powdered material which can be fused into a "green shape" using a low temperature SLS process. The green part is then removed from the SLS process and placed in a high temperature furnace. Temperatures in the furnace are sufficient to burn off the binder and sinter the metal or ceramic particles together. This process is analogous to metal or ceramic injection molding. Early tests have focused on polymer coated copper, alumina, glass, and zircon and inorganic binders such as ammonium phosphate and boron oxide have been used with alumina. Already verified in practice on the existing Sinterstation™ 2000 System product platform, materials such as copper mixed with binders have been fabricated to produce EDM electrodes. Alumina ceramic molds for investment casting have also been produced in the same low temperature process. The process of indirect sintering is shown schematically on the following page.

Indirect Sintering

```
┌─────────────────────────┐
│ POWDERED MATERIAL       │
│ METAL OR CERAMIC        │
└─────────────────────────┘
                  ┌──────────────────────┐      ┌────────────────────┐
                  │ LOW TEMPERATURE      │ ───► │ SLS PROCESSING     │
                  │ FUSABLE MATERIAL     │      └────────────────────┘
┌──────────┐ ───► └──────────────────────┘
│ BINDER   │
└──────────┘

┌──────────────┐     ┌──────────────────────┐      ┌──────────────────────┐
│ GREEN PART   │ ──► │ POST PROCESSING      │ ───► │ METAL OR CERAMIC     │
└──────────────┘     │ BINDER BURNOUT       │      │ PART                 │
                     └──────────────────────┘      └──────────────────────┘
```
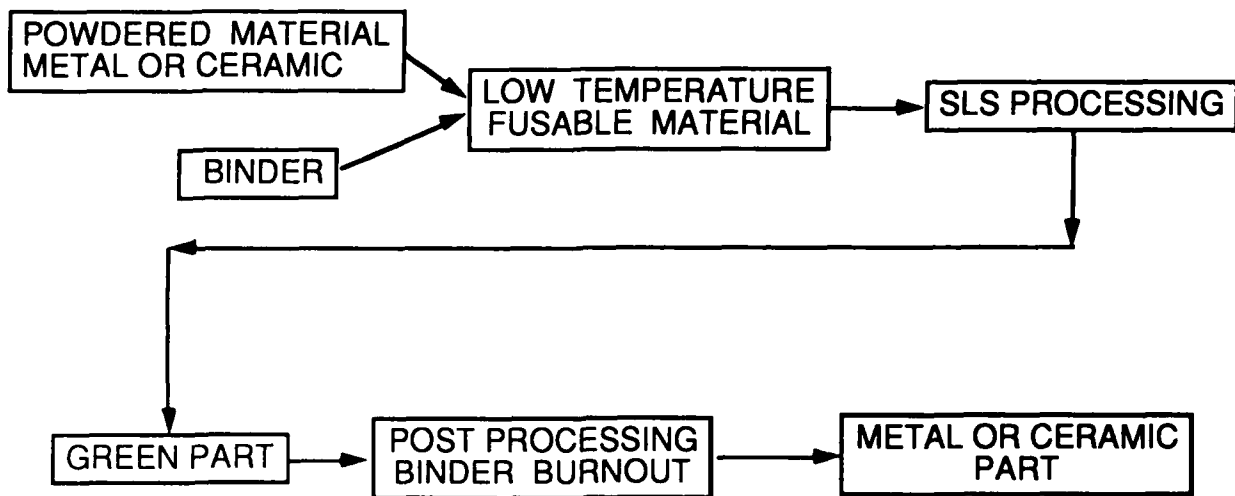
Direct Sintering

The direct method of Selective Laser Sintering involves using a higher temperature process chamber and a higher wattage laser to fuse metal and ceramic particles. This process is being used on an experimental basis at The University of Texas in Austin. The University, through DTM funding, has constructed an High Temperature Workstation (HTW) which employs a 1000 watt laser and a process chamber capable of reaching 1832 $^\circ$F (1000 $^\circ$C). Using the direct method of sintering, no post-sintering is required to complete the parts. The goals of this research program are the determination of the optimum process parameters for materials used in the next generation of SLS systems that will sinter metals and ceramics for future applications that include the direct manufacture of prototype tooling and complex parts.

```
┌─────────────────────────┐
│ POWDERED MATERIAL       │
│ METAL OR CERAMIC        │
└─────────────────────────┘
                      ┌──────────────────────────────────┐
                      │ HIGH TEMPERATURE                 │
                      │ WORKSTATION (HTW)                │
                      │ • 1000 WATT CO₂ LASER            │
                      │ • 1000C PART BED                 │
                      │ • DIRECT SINTERING/MELTING       │
                      └──────────────────────────────────┘
                                         ┌──────────────────────┐
                                         │ METAL OR CERAMIC     │
                                         │ PART                 │
                                         └──────────────────────┘
```
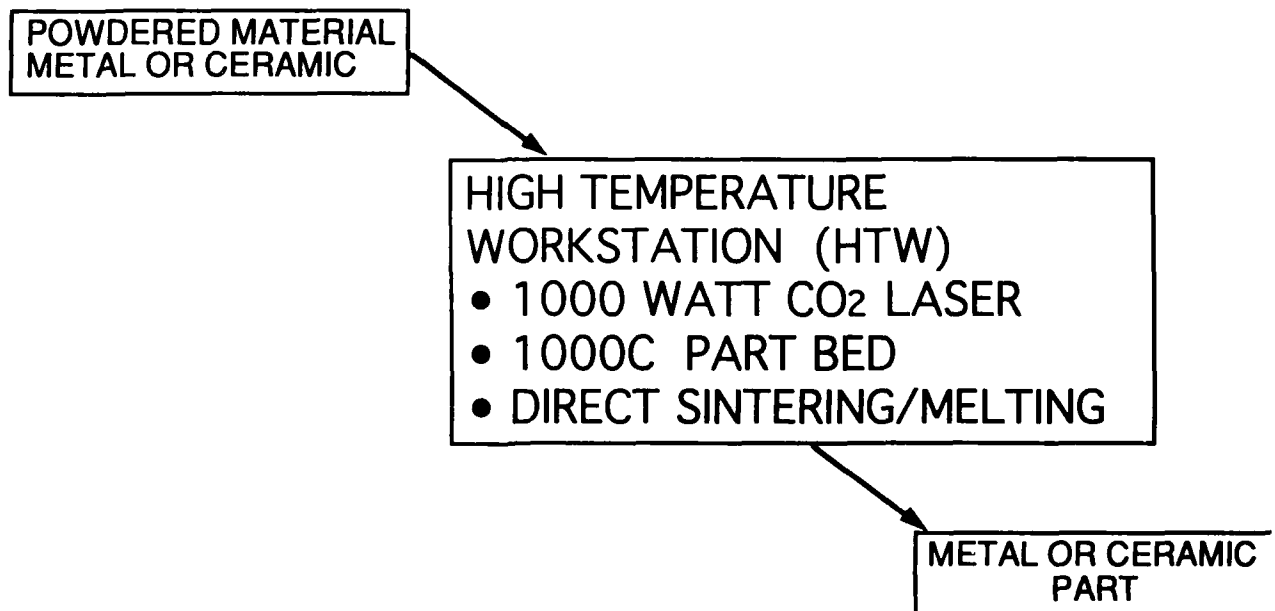
The areas of current research with metal and ceramics are summarized in the following table:

	Sintering Method	
Material	Indirect	Direct
Metal	Polymer Coated Copper	Cobalt-Tungsten Carbide Copper-Nickel Aluminum-Silicon Carbide
Ceramic	Polymer Coated: Alumina Glass Zircon Alumina/Ammonium Phosphate Alumina/Boron Oxide	Aluminum-Aluminum Oxide

The addition of metals and ceramics to the SLS process will greatly enhance the possible applications of the process. It may be feasible in the future to directly sinter a number of metals into 3-D solid shapes. Using a pure copper or copper-tungsten powder in the process may allow EDM electrodes to be made directly in the SLS process. This will significantly reduce the time required to generate EDM electrodes which have complex shapes for mold building.

Using select metals, it may be possible to generate core and cavity inserts for injection molds. Because of the unlimited design potential of the process, these molds may have water-cooling channels and bubblers that are curved to accommodate the core and cavity surfaces. This would allow for a uniform temperature distribution across all mold surfaces, which is not easily obtainable with conventional mold-building techniques.

Investment Casting Wax

The investment casting wax used in the process is an investment casting wax that The BFGoodrich Company purchases then powders in a patented process. This material has been in use for over 18 months and has gone through several improvements. The patterns made from this investment casting wax go directly into the investment casting process and can follow the procedures normally used for patterns generated via molding wax. Thus the problems of long burnout cycles associated with photopolymer resins are eliminated. Other benefits of the SLS process with investment casting wax include:

- Accuracy within the specifications of most investment casting applications. The average tolerances range of wax patterns made in the SLS process range from ±0.002 to ±0.010 inches (±0.04 to ±0.25 mm). This meets the accuracy requirements for most investment casting applications.

- A surface finish that is suitable for most investment casting applications, typically 100 to 120 average micro inches RMS. When smoother finishes are required, secondary polishing and finishing may be employed.

215

- Eliminating the tooling stage translates into numerous benefits for investment casters, including minimized up front tooling costs and significant time savings for prototypes and the ability to produce complex shapes that were previously too difficult to produce via simple tooling.

Most parts made of wax in the SLS process have very complex geometries and are typically produced in very small quantities, typically less than 10 pieces. Some sample applications include:

- Aerospace parts produced in titanium or other exotic alloys which are difficult to machine. The use of the investment casting process with the SLS process to quickly produce wax patterns allows for the rapid prototyping of parts which would normally take months to manufacture.

- In the transportation industry, wax patterns are used to quickly produce functional metal prototypes for use on the engine or drive train. These pieces would be time consuming to prototype via traditional methods.

- In medical prosthetics industry, custom made prosthetic implants can be quickly made in investment casting wax from CAT scan data then cast in the alloy of choice.

Polycarbonate

Polycarbonate has been used in the SLS process for a variety of purposes, ranging from functional models to patterns for tooling to an actual tooling material. Currently, the most common use of the material has been for the development of functional models. The advantages of the SLS process are significantly impacting product design capabilities in the plastics industry, resulting in shorter design cycles and superior design. The process allows the designer to make a part directly from a 3-D CAD design for visual inspection of form and fit and also allows the designer to perform some limited functional testing. Applications for these functional models span almost every industry. In effect, the use of the SLS process serves as a time-saving, communications-enhancing bridge between design and manufacturing. Thus, it is an excellent tool to aid in concurrent or simultaneous engineering efforts. Every market segment that produces parts via injection molding has used the SLS process. Some of the more common uses are listed here:

- Computer housings and printers have been prototyped using the SLS process. The parts for these housing have been assembled and tested for form, fit, and some functional testing. The SLS generated parts may be painted to give the appearance of an injection-molded part.

- Toys have been made for test marketing purposes. If there is large market acceptance, then a mold is made and the item is produced in large quantity.

- Automotive electrical components are built to assess fit and function and to verify the design. In some cases, these parts are finished to give the appearance of an injection-molded part.

- Electrical enclosures are made to give the designer and manufacturer information on how efficient the design will be and how easily it may be manufactured.

- Power tools are prototyped to provide an operating model and to allow manufacturing, tooling, and assembly operations to review the parts and make recommendations on improving or adjusting the design before hard tooling is built.

216

All of these markets have one thing in common: There is a requirement to evaluate the plastic part before making large commitments in terms of time and money for production tooling.

The functional models may also be used as patterns to generate prototype tooling in a variety of ways. There are three categories of molds that can be made when using the SLS process. They include mold patterns which are used for the direct manufacture of prototype parts and part patterns which are used as a master for both rigid and soft tooling.

Selective Laser Sintering

SLS Pattern	Plastic Mold	Plastic Part/Pattern	
Intermediate Process	Molding of Wax, Thermoformed Plastic, and Cast Urethane Patterns	**Soft Tooling** RTV Silicon Urethane	**Ridged Tooling** Spray Metal Kirksite Epoxy
Final Parts	10-500 Wax Patterns, Thermoformed Plastic, Cast Urethane	1 - 100 Wax Patterns Cast Urethane	50 - 10,000 Wax Patterns Plastic parts

Prototype molds made of polycarbonate in the SLS process may be used in a variety of processes. These include molds for wax injection which will produce patterns for investment casting, thermoforming tools, and patterns for sand casting. The thermoforming or vacuum-forming molds are used for materials with a forming temperature of less than 170°C (338°F). Materials that are formed below this temperature include polypropylene, polyethylene, polystyrene, and ABS.

Rigid tooling is used where a small number of injection molded samples are required. The most popular method of making these molds currently is the TAFA spray metal process. It consists of defining a parting line on the pattern then spraying a low temperature molten metal over the pattern to build-up a core or cavity detail which may be approximately 6.3mm (0.25 inch). These shells are then backed with a low-melting-temperature metal or a metal-filled epoxy. Ejector pin holes are added and the mold is assembled.

Other methods for building ridged tooling include nickel vapor deposition, metal plasma deposition, Kirksite casting, and epoxy casting. The number of parts obtainable from any of these ridged tooling techniques depends on the type of material being injected into the mold. As a general rule, materials which process at higher temperatures, require greater pressures, and are filled, will shorten the life expectancy of the mold.

For a very limited number of parts, soft tooling may be used. These are molds generated in RTV silicone or a flexible urethane. These molds may be used to generate parts from cast urethane materials or from wax to be used in the investment casting process.

Nylon

The latest material being added to the line of SLS materials is a Nylon. This material was selected based on its performance in early testing. It offers improved toughness and strength over polycarbonate and will expand the number of functional applications for SLS-generated parts.

Since the material is a crystalline polymer, it offers improved chemical resistance over the polycarbonate and has successfully been used in high temperature caustic plating baths.

New applications include:

- Functional automotive components with the thermal properties to withstand the on-engine temperatures and the chemical resistance for use as a functioning prototype.

- Connectors with the detail and functionality to be used as prototypes.

- Prosthetic devices that can be custom made and used directly from the SLS process.

New Material Development and Characterization

When a material is selected for use in the SLS process, safety is a primary concern. The first step in the safety process is to review the MSDS sheets to ensure that the material is safe for the operator to handle. If the material is non toxic and safe, then it is reviewed to ensure that it will not cause a safety hazard in the machine. Once safety criterion are met, then the material will be tested via a single layer test to begin to understand how it sinters on a layer basis before multi-layer tests begin.

Further testing will include a 10 hour normal run test that will be used to collect gas data and determine if any gasses are being generated in a normal running mode.

Another test performed on a new material is called an upset test which is designed to determine what happens to a material exposed to high temperatures in the SLS process. This 90 minute test is performed by running the heaters at a high temperature with no nitrogen flowing through the system. The laser power is set at 100% to further degrade the material. Again, gas samples are collected and analyzed to determine if any harmful materials are begin emitted from the system.

Process Developments and Improvements

With the development of new materials, the sintering process is continually enhanced and refined to produce quality parts specific to each new materials. Since this is a thermal process, the distribution of heat across the machine is critical and the design improvements in the Sinterstation 2000 have been to provide a uniform thermal distribution across the part bed. Currently, DTM is using thermal imaging to study temperature distribution in the SLS process chamber. Again, these improvements in the process will lead to improvements in the strength, surface finish, and accuracy of the parts.

Other improvements to the process over the last year include:

- The addition of a beam off setting software to improve the accuracy.

- A redesign of the SLS model 125 into the Sinterstation 2000 System that offers improvements in powder handling, laser delivery, and a graphical user interface.

218

Summary

The SLS process is a viable time and money saving method for generating complex prototype parts in the plastics and metals industries based on the materials employed in the system. The benefits of using the system include:

The ability to use a variety of materials and the future ability to expand the variety of materials which will work in the process. Current materials include investment casting wax, polycarbonate, and nylon. Future materials will include additional thermoplastics and the addition of metal and ceramic parts made with binders in an indirect sintering process and the direct sintering of metals and ceramics in a high temperature SLS process.

The ability to generate very complex parts using powdered materials. This can be accomplished since the powder acts as a natural support structure during the build process. With some materials and some designs, the fabricated parts may require the use of a base grid to minimize distortion of the part.

A process which is very fast. The powder is fused together in a thermal process and there is no need for secondary curing.

The wax patterns made in the SLS process can be used directly in the investment casting process. This eliminates the need for excessive burnout cycles normally associated with photopolymer based systems. The process can be used to effectively generate small quantities of parts (1 to 20 pieces) without the need for expensive and long lead time tooling.

In the plastics industry, the process can be used to generate functional models from three-dimensional CAD models to visualize part form, verify fit, and test some aspects of the function. These functional models are and excellent aid for concurrent engineering because they clarify the communication between the designer, manufacturing, and marketing departments.

Prototype tooling may be generated by a variety of techniques using SLS generated part patterns and mold patterns. These prototyping techniques include generating the mold pattern using a powdered polycarbonate material. These mold patterns may be used for wax injection applications. From this SLS-generated part pattern, prototype soft or rigid molds may be produced using secondary processes such as RTV molds and spray metal tooling.

MICROSTRUCTURAL ELEMENTS OF COMPONENTS DERIVED FROM 3D PRINTING

M.J. Cima, A. Lauder, S. Khanuja, and E. Sachs
Departments of Materials Science and Engineering and Mechanical Engineering,
Massachusetts Institute of Technology, Cambridge, MA 02139

ABSTRACT

Three Dimensional Printing is a rapid prototyping technique to manufacture functional components directly from computer models. The process involves spreading the powder in thin layers and then selective binding of the powder using a technology similar to ink-jet printing. Layers are added sequentially until a part is completed. The simplest microstructural feature of a 3DP part results from the interaction of a binder droplet with the powder bed; termed as "primitive." These primitives have denser powder packing than is found in the loose powder bed. Formation of the primitives is found to be dependent on the physical and chemical characteristics of the powder and binder. The present study discusses the effect of size, morphology and packing density of different alumina powder on the microstructural features and densification of the primitives.

INTRODUCTION

Solid Freeform Fabrication (SFF) techniques are largely viewed as methods for replicating macroscopic structures derived from computer descriptions of solid models. One can envision, however, components where both the *macrostructure* and *microstructure* are designed by computer. Never before have materials engineers had complete freedom to design microstructures. Microstructure is usually developed within the confines of the manufacturing process. Thus, designers must compromise component performance with manufacturability. SFF processes build components on a point-by-point basis and may make it possible to vary the composition and structure of a component from position to position with complete freedom. Potential applications of such a technology are numerous, such as components with anisotropic thermal, electrical, or mechanical properties or microengineered porosity. This paper is one of a series in which the basic microstructural features of 3D Printed components are discussed [1,2]. Knowledge of the physical processes which control the microstructure of 3D Printed parts will aid in its use as a tool for the production of microengineered materials.

3D Printing is among those rapid prototyping technologies that deposit matter during the building process. Thus, it can selectively control composition within the build plane by varying the composition of printed material. Significant amounts of matter can be deposited in selective regions of a component on a 100 μm scale by printing solid dispersions or solid precursors through the ink-jet. Multiple jets of different composition

or concentration could be employed to prepare components with composition and density variation on a fine scale. A recent study has shown that several factors contribute to the formation of 3DP microstructure [1]. Experiments were carried out to trace the development of the microstructure from its smallest units to a complete part by examining single-droplet primitives, lines formed by printing binder in a continuous bead across the powder bed, and walls prepared by printing lines close enough together that they binder to form macroscopic structures. Single-droplet primitives are the structures created when a single binder droplet impacts the powder bed. The ballistic impact of the binder droplets causes cratering and ejection of powder over a large distance [2]. Capillary action draws liquid into the powder in cases where the liquid wets the powder surface. If, however, the capillary stress exceeds the cohesive strength of the powder bed then significant particle rearrangement will occur as the particles are drawn into the liquid [1]. Thus, the microstructure is largely the result of the relative influence of capillary and cohesive forces.

This study reveals the relationship between the structure of single droplet primitives and the nature of the powder used in the piston. The primitive size, morphology, and packing density were characterized for several powders that could be useful for making investment casting molds and cores by 3D Printing [3,4].

EXPERIMENTAL PROCEDURE

The powders used in this study are described in Table 1. Colloidal silica (Nyacol 830, Nyacol Products Inc., Ashland, Massachusetts) was used as the binder for all experiments.

Primitives were prepared by using a 3D printing machine which is described elsewhere [5]. The printhead used for this study was the continuous-jet type. Thus, droplets are produced continuously at 50 to 60 kHz. These droplets are selectively charged by applying a voltage between the binder and the charging plates that are placed near the jet orifice. Charged droplets are deflected when passed between high voltage deflection plates. Uncharged droplets proceed unimpeded until they impact the powder bed. A special circuit was designed to drive the charging cell. This circuit allowed only one droplet out of every 32 to remain uncharged and strike the powder bed. The printhead was driven over the powder bed at a velocity of 2.5 m/s in a raster fashion with trajectories separated by 780 μm. Thus, neighboring droplets along a line were separated by almost 0.8 mm and were too far apart to stitch together. Powder was spread over the piston in layers, 380 μm thick. Complete coverage of 90 x 90 mm powder bed produced more than 10,000 primitives per layer. The powder was carefully scooped out of the piston after printing and fired at 900° C for 2 hours. The fired powder was then passed through several sieves of different mesh sizes to separate the primitives from the unbound powder.

Three sets of experiments were used to characterize primitives. Skeletal density measurements were conducted by a helium pychnometer (Quantachrome, Syosset, NewYork). The sample size varied between 2 and 4 g. Pychnometer measurements were

taken using pressures of approximately 140 kPa. Repeated measurements were taken until three values for sample volume agreed within 1%.

Microscopic analysis of the primitives was performed by scanning electron microscopy (SEM). These samples were prepared by affixing a few milligrams of primitives on aluminum stubs using adhesive press tabs followed by gold coating in a sputter coater.

Mercury porosimetry was used to determine the bulk density and pore-size distribution of the primitives. Measurements were made using an automated porosimeter (Micromeritics, Norcross, Georgia). The penetrometer was loaded with primitives and evacuated to a pressure of 50 μm-Hg. The chamber was then filled with mercury at a pressure of 21.6 kPa. High pressure infiltration of mercury was then used to determine the total infiltration volume. Accurate calculation of the average primitive density required that a correction be applied to the infiltration volume since, in some cases, the low pressure infiltration was not sufficient to completely infiltrate the inter-primitive pores. The details of the data correction are described elsewhere [6]. Briefly, the infiltration volume of the intraprimitive pore space was taken as the difference between the total infiltration volume and the infiltration volume at the pressure required to begin infiltration of the loose alumina powder from which the primitives were made. The operative assumption is that the primitives contain no pores that are larger than the largest pores found in the loose powder

Table1: Powders used for construction of single drop primitives		
Powder	Average size (microns)	Shape
Norton 325 mesh alumina*	45	Faceted gravel-like
Norton 30 micron alumina*	30	Hexagonal plates
Spray dried alumina	15	Porous spheres
ICD alumina #	10	Solid spheres

* Norton Company, Waltham, Massachusetts.

ICD Group, Lyndhurst, New Jersey

RESULTS AND DISCUSSION

Single drop primitives, regardless of the powder used, were found to be roughly spherical in shape. Primitives prepared from spherical powders are noticeably larger than those from irregular shaped or plate-like powders. Those primitives prepared from the spherical ICD alumina had diameters between 200 and 300 μm. The spray-dried and angular shaped powders, however, gave primitive diameters between 100 and 200 μm. Figures 1 and 2 are primitives made from 325 mesh alumina and ICD alumina, respectively. High magnification observation of primitives, Figure 3 and 4, reveal how the particles are bound by the silica. Irregular powders generally bond across large flat faces with silica wetting across the entire bond. Spherical powder, however, is bonded by small amounts of silica at the necks between the particle spheres.
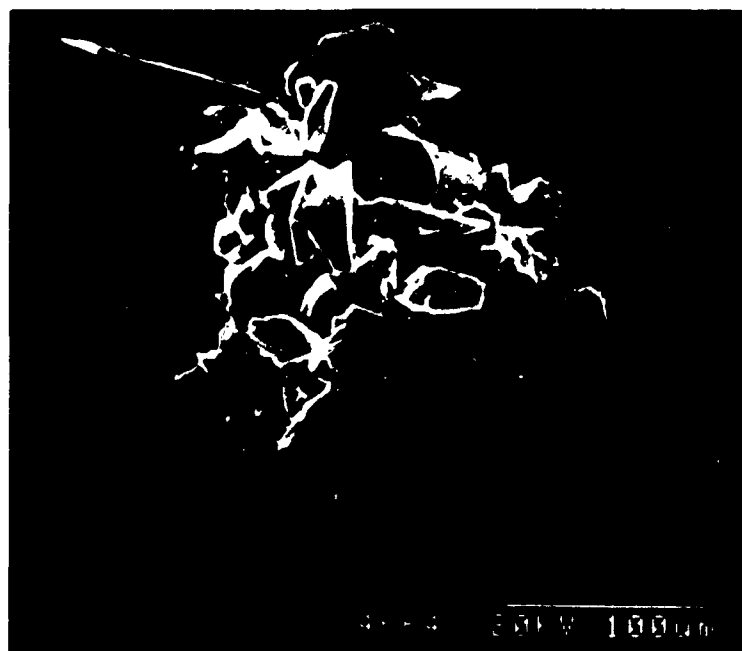
Figure 1. Micrograph of a single drop primitive made from 325 mesh alumina.
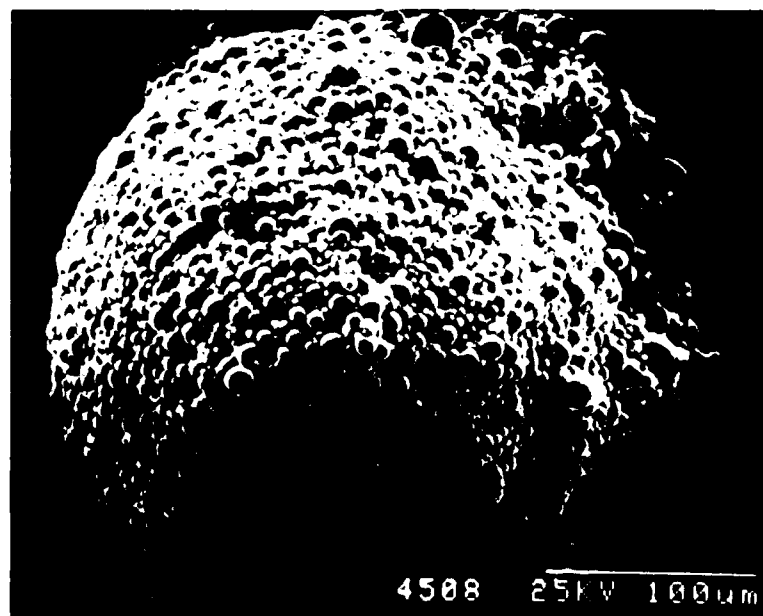

Figure 2. Micrograph of a single drop primitive made from ICD alumina.

Figure 3. High magnification of the surface of a primitive made out of faceted 325 mesh alumina.

Figure 4. High magnification of the surface of a primitive made from spherical spray dried powder

Skeletal density data for individual primitives can be used to determine the relative amounts of alumina and silica contained in the primitive. The skeletal densities were used to calculate the volume fractions of silica and alumina for each type of primitive, using the known densities of alumina powder and silica glass. This calculation is subject to some error arising from inaccurate skeletal density measurements due to closed porosity. The error tends to over estimate the amount of silica in each primitive and reduce the estimate of the alumina powder packing density within the primitive. The error is thought to be minor but the calculated alumina packing density reported here should be interpreted as a lower limit. Figure 5 shows the results of these calculations compared with the measured density of the powder bed for each powder. The alumina packing density in the primitives is substantially higher than the bed powder packing density in every case.
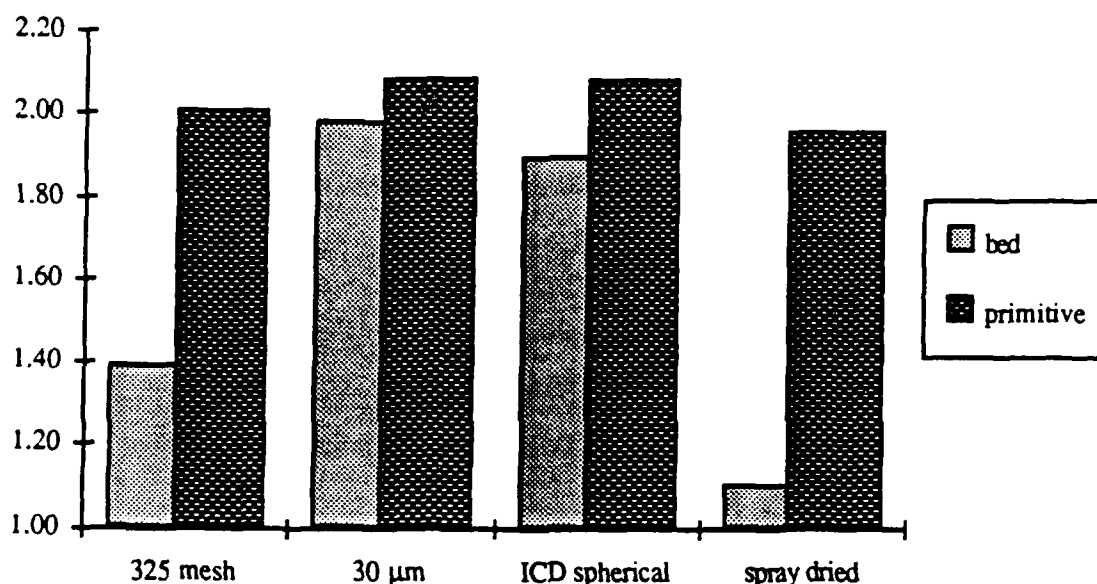
Table 5. Alumina packing (ml/g) in primitives vs. in the powder bed.

The generally spherical shape of the single droplet primitives is likely to be the result of liquid surface tension forces. Liquid coats the particles as the binder droplet penetrates the powder bed. Capillary pressure draws binder selectively into the necks between the particles. The liquid attempts to minimize its surface energy by reducing its surface to volume ratio and minimizing the area of liquid/vapor interface. The result is densification of the powder particles as the particles slide over one another in response to the surface tension of the liquid. Particles may be pulled together more tightly as the liquid dries causing further densification. The influence of surface tension forces will be greater in powder beds more susceptible to rearrangement, such as those with low initial packing densities or spherical particles which can rearrange much easier.

Figure 6 summarizes the measured bulk and skeletal densities for each kind of primitive. The bulk density increases in the order, spray-dried, solid spherical, 325 mesh, 30 micron. The skeletal density follows in exactly the reverse order, although it is much

less sensitive to powder type. Low skeletal density corresponds to high silica content, as discussed above. Thus, the alumina content of the primitives increases in order, spray-dried, solid spherical, 325 mesh, 30 micron.
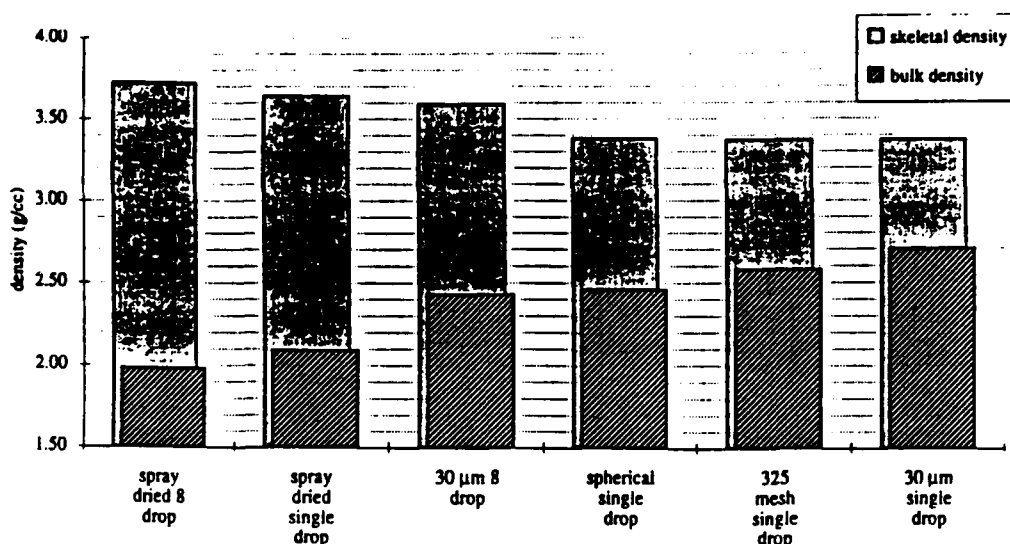
Figure 6. Summary of measured bulk and skeletal densities for primitive.

This observation is interesting given that each primitives is made from the same size binder droplet and must, therefore, contain the same total silica content. The data indicate that powder morphology controls the amount of alumina bound by a single binder droplet. A single binder droplet binds significantly more powder in the case of the spherical powders. The reason for this can be established by reference to Figures 3 and 4. Only small amounts of binder are required to bond the spherical particles since it readily segregates to the idealized two particle necks. Faceted particles, however, rearrange so that large flat surfaces face one another. Much more binder segregates to this type of neck because of its large surface area. Thus, for a given amount of binder, primitives from spherical powder should contain more alumina and should, therefore, be larger. Indeed, the primitives from the ICD spherical alumina were the largest of all the powders. The primitives from spray-dried alumina were not noticeably larger, but they undoubtedly were much less efficient in spreading binders because of their large amount of internal porosity.

The relationship between primitive structure and powder morphology is very important for the development of the 3D Printing process. We have established that spherical powders require much less binder than highly faceted powders. Thus, larger primitives are produced from spherical powders than from highly faceted particles for a given binder droplet size. This information has immediate impact on the development of materials for 3D Printing since it suggests that the minimum feature size that can be produced from spherical powders may be larger than that produced from highly faceted powders. This conclusion does not account for other effects such as the shrinkage which occurs due to capillary forces shown in Figure 5. The low packing density of the highly

226

faceted powders in the bed causes large amounts of linear shrinkage upon impact of the binder droplet. This effect will undoubtedly cause dimensional difficulties when fine structures are printed into faceted powders.

CONCLUSIONS

This study establishes the relationship between powder morphology and primitive structure. Significant increases in powder packing density can occur when binder droplets impact the powder bed. The particle rearrangement is caused by capillary forces created by liquid surface tension. The largest linear shrinkage will occur for powders with low packing density in the bed. Spherical powder efficiently uses binder since the necks between particles have small area and only small amounts of binder are required per neck to effectively bond the particles. High faceted powders have large area necks between particles which require much more binder per neck. The result of more efficient use of binder for the spherical powders is larger primitives for a given binder droplet size. Thus, each type of powder has advantages and disadvantages.

REFERENCES

1. Lauder A., M.J. Cima, E. Sachs, and T. Fan,"Three Dimensional Printing: Surface Finish and Microstructure of Rapid Prototyped Components"; in Proceedings, Synthesis and Processing of Ceramics: Scientific Issues, Boston, MA, 1991.

2. Fan T.,A. Lauder, E. Sachs, and M.J. Cima, "The Surface Finish in Three Dimensional Printing," presented at the Third International Conference on Rapid Prototyping, University of Dayton, Dayton, OH 1992.

3. Cima M.J., and E. Sachs,"Three Dimensional Printing: Form, Materials, and Performance "; in Proceedings of the Solid Freeform Fabrication Symposium, Austin, TX, 1991.

4. Sachs E., M. Cima, J. Bredt, and Alain Cordeu, "CAD-Casting: The Direct Fabrication Ceramic Shells and Cores by Three Dimensional Printing," Manufacturing Review,.vol. 5, no. 2, pp 117-126, June 1992

5. Sachs E., M. Cima, P. Williams, and D. Brancazio,"Rapid Tooling and Prototyping by Three Dimensional Printing,"pp 41-45 in Transactions NAMRI/SME, 1990

6. Lauder A.,"Microstructure and Particle Arrangement in Three Dimensional Printing," S.M. Thesis, Dept. of Materials Science and Engineering, Massachusetts Institute of Technology, September 1992

Relating Operating Parameters between SLS Machines which have Different Scanner Geometries and Laser Spot Sizes

J. C. Nelson and J. W. Barlow
Department of Chemical Engineering
University of Texas at Austin

Abstract

As the number of SLS machines in operation increases, the opportunities to share operating parameters with other SLS operators also increases. However, if the machines are not identical down to the spot size of the laser beam, the quality of parts made on each machine can be different. The most likely differences between two SLS machines are the laser spot size and the scanning radius of the optics. The total energy flux to the powder surface is a function of the spot size and the scan speed. The algorithms defined to correct for machine differences are verified both experimentally and numerically using a one-dimensional empirical SLS model.

Introduction

The art of Selective Laser Sintering (SLS) has developed significantly over the past several years, but there are still gray areas that are not fully understood. Computer control is one such gray area. Ideally, the SLS machine should automatically set parameters and produce a sintered part once the material system has been specified. However, operation of an SLS machine will remain as an interactive process between the operator and the machine until an optimal set of operating parameters is found. These operating parameters are both powder specific and sometimes machine specific. This paper deals with the machine specific aspects of the operating parameters.

Understanding the machine specific parameters, which include the laser scanning radius and the laser spot size, is important in the development of algorithms that will correct for differences between SLS machines. Machine differences can be compensated for by modifying the controllable operating parameters like beam speed and laser power. As new materials are developed for use in the SLS process, the importance of generalizing the operating parameters will become evident. The consumer should not have to spend his time to find a good operating range for new material when the material supplier could supply a set of SLS operating parameters along with the specifications of the SLS machine that was used to process the material.

There are numerous combinations of the SLS operating parameters that can be used to make good quality sintered parts. This paper does not provide a guide line for the operating parameters that should be used in the SLS machine, rather this paper is a tool that allows one to modify a set of operating parameters to work on any SLS machine. The operating parameters derived by the following methods have been used to make test parts in an SLS machine and have been simulated numerically using a multilayer sintering model.

Description of Parameters

The amount of energy that is applied to the powder surface during SLS is a function of several operating parameters which include laser spot size, scan radius, laser power, scan spacing and the laser scanner parameters (SS and SP). The size of the laser spot and the scan radius are both machine specific and may differ from one SLS machine to another.

The flow diagram in Figure 1 shows how the energy to the surface is a function of the operating parameters. The energy input at the surface is a function of the flux of the pulse, the duration of the pulse, and the delay between successive pulses. These three parameters are calculated as a function of the independent operating parameters. The calculation of the energy input is based on the assumption that the laser output has a Gaussian intensity distribution. This assumption is valid for the CO_2 laser that is most commonly used in the SLS process.
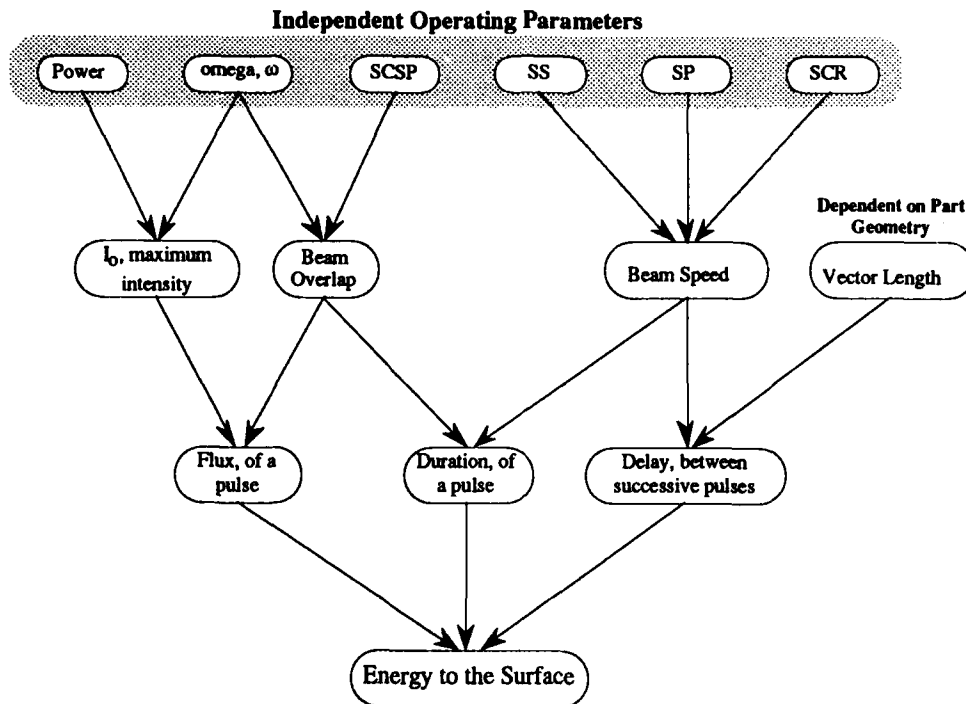
Figure 1 A flow diagram showing how the energy input at the surface is a function of the operating parameters.

Independent Operating Parameters

The **laser spot size** can be represented by a characteristic radius, ω, that can be measured using a beam profilometer. The beam profilometer measures the intensity profile across the laser spot at the surface of the powder bed using a knife edge method [1]. The maximum intensity is in the beam center and decreases radially as shown in equation (1).

$$I = I_o \exp\left(\frac{-2\ r^2}{\omega^2}\right) \tag{1}$$

The **scan radius**, SCR, is the distance from the fast axis scanning mirror to the sintering plane. The maximum scan width is determined by the scan radius because the galvo mirrors only have a range of 40° over the surface of the powder bed. The scanning speed is a function of the scan radius and the laser operating parameters as shown in equation (2).

$$\text{beam speed} = 1.04378 \left(\frac{SS\ *\ SCR}{SP}\right) \tag{2}$$

The **laser power** is often the preferred parameter to adjust by the operator during processing because it is easy to adjust and results are intuitive. When the power is increased, the energy at the surface is increased. The power tuning knob can be calibrated prior to sintering which allows the operator to make small adjustments in the laser power.

The **laser scanner parameters**, *SS* (step size) and *SP* (step period), specify the speed at which the galvo mirrors turn and in conjunction with the scan radius define the beam speed. However, there is a range for *SS* and *SP* outside of which the scanners may reach a mechanical limitation. If the step size is too large or if the step period is too short, the actual beam speed will deviate from the beam speed calculated by equation (2).

The **scan spacing**, SCSP, is the distance between adjacent scan vectors. The scan spacing can be adjusted to change the amount of beam overlap during a scan prior to sintering when the layer is divided into a series of parallel scan vectors. Beam overlap occurs when the radius of the laser spot is greater than the spacing between scan vectors.

Definition of Dependent Variables

The **flux of a pulse** is a function of the maximum intensity of the laser output and the position of the beam relative to a reference point. When the radius of the laser spot is greater than the spacing between scan vectors, SCSP, the laser adds energy to points along adjacent scan lines causing beam overlap. The flux along an adjacent vector can be calculated by integrating the laser intensity along that scan vector, equation (3). The maximum intensity of the laser is a function of the characteristic radius and the power setting, equation (4).

$$\bar{q} = \frac{1}{S_x} \int_0^{S_x} I_o \exp\left(\frac{-2r^2}{\omega^2}\right) dx = \frac{I_o \sqrt{\pi}\, \omega\, \text{erf}\left(\frac{\sqrt{2}S_x}{\omega}\right)}{S_x\, 2\sqrt{2}\, \exp\left(\frac{2(y-y_o)^2}{\omega^2}\right)} \tag{3}$$

$$I_o = 0.239 * \frac{P}{\pi\omega^2} = \left[\frac{cal}{cm^2\text{-sec}}\right] \tag{4}$$

The nomenclature used to calculate the average flux is illustrated in Figure 2. In the figure, the laser spot overlaps a scan vector on each side of the current vector. During scanning, beam overlap preheats the powder along adjacent scan lines which increases the amount of heat that is absorbed by the powder bed.

The **duration of the pulse**, *dp*, refers to the time necessary for the beam to pass over a reference point on the scan vector and is therefore a function of beam speed and the position of the reference point relative to the beam center. The duration is equal to the length of the vector under the beam divided by the beam speed as shown in equation (5).

$$dp = 2\frac{S_x}{bs} \tag{5}$$

The **delay between pulses** is defined as the time necessary to scan one complete scan vector. The delay includes the scanner settling time between vector scans in addition to the time required to scan the entire scan vector. As the vector length increases, the time required to scan the vector increases. The delay is therefore a function of the part geometry and the laser operating parameters, (*SP*, *SD*, and *LF*) as shown in equation (6).

$$\begin{matrix} \text{delay between} \\ \text{successive pulses} \end{matrix} = \left[\frac{\text{vector length}}{\text{beam speed}} + (SD*SP*10\mu s + LF)*10^{-6}\frac{s}{\mu s}\right] \tag{6}$$
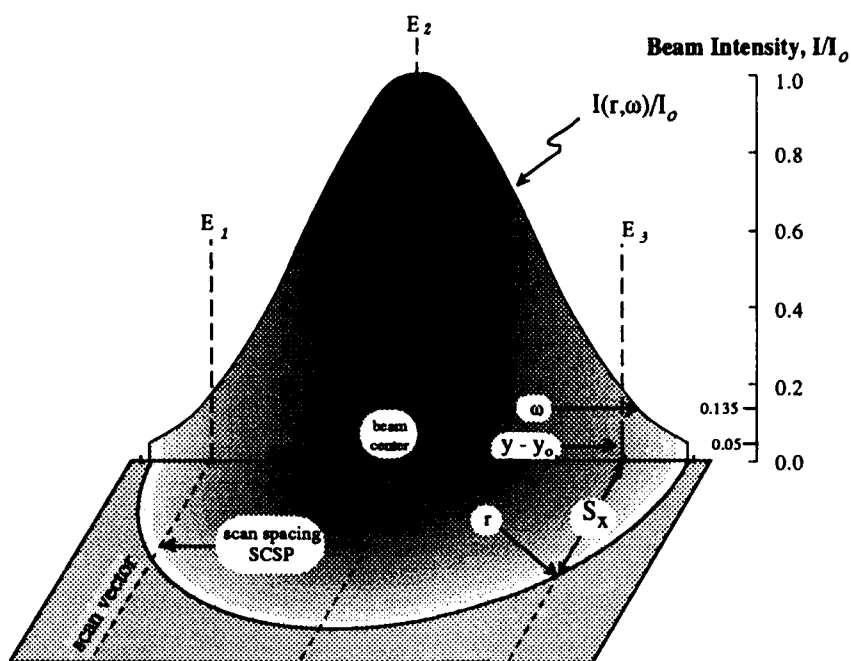
Figure 2 Nomenclature used in the calculation of flux to the surface.

Results and Discussion

The primary goal of this paper is to define a method to generalize the operating parameters used to produce a part by the Selective Laser Sintering method. This will enable the transfer of operating parameters known to work on one SLS machine to any SLS machine that may have different machine specific parameters. The ability to transfer parameters will reduce the startup time that often accompanies new materials, if the powder supplier provides a set of well documented operating parameters with the powder. Also, these equations can be used in the development of a real-time control algorithm that would maintain a constant energy input for scan vectors of various lengths by controlling the laser power and beam speed.

The generalization of the SLS operating parameters, to allow the transfer of parameters to other SLS machines, would prove useful to anyone unfamiliar with all the intricacies of selective laser sintering. Operating parameters that were known to produce good quality SLS parts with a specific powder could be made available along with some machine specific information such as the laser spot size and the scan radius. These parameters could then be translated, using the following method, to account for any variations in the laser spot size or scan radius. The new parameters should produce an SLS part which has density similar to the original part. The linear conversion of parameters does not account for variations in the scan vector length. To adjust for variations in vector length within a single layer one would need to control the laser power and the beam speed dynamically.

Development of Operating Parameter Transformations

The new operating parameters are calculated in four steps. To simplify the derivation, machine #1 refers to the SLS machine from which the operating parameters are taken and machine #2 refers to the recipient of the new operating parameters. In the following equations, a subscript *1* or *2* refers to machine #1 or machine #2, respectively.

231

First, the scanning speed, bs_2, is chosen. The scan speed can either remain constant or it can be changed to take advantage of a change in the scan radius.

The second step is the calculation of the laser power. The energy to the surface is a product of the average flux and the duration of the pulse as shown in equation (7). Therefore, by substituting equations (3) and (5) in equation (7), one can solve for the laser power as a function of the beam speed, bs_2, as shown in equation (8).

$$\frac{\text{energy to}}{\text{the surface}} = (\bar{q} * dp)_1 = (\bar{q} * dp)_2 \tag{7}$$

$$P_2 = \left(\frac{\omega_2}{\omega_1}\right)\left(\frac{bs_2}{bs_1}\right)P_1 \tag{8}$$

Next, the new scan spacing is calculated. A ratio of the characteristic radii is used in this step to maintain the same amount of beam overlap. The scan spacing is reduced if the size of the laser spot is reduced as shown in equation (9). Beam overlap improves sintering because it preheats the powder during a scan.

$$SCSP_2 = \left(\frac{\omega_2}{\omega_1}\right) SCSP_1 \tag{9}$$

Finally, new values of SS and SP are calculated to maintain the beam speed chosen in the first step. Because there are two unknowns, SP_2 and SS_2, in equation (2), an initial value of SP is chosen and SS is calculated using equation (10). SP represents the pause after each position change of the fast axis scanning mirror. In most cases, the default value of SP is used to calculate SS. However, if the calculated value of SS exceeds approximately 90 LSB's a new value of SP should be chosen. The limit on the value of SS is a mechanical limit that has been estimated from empirical data.

$$SS_2 = \left(\frac{bs_2}{bs_1}\right)\left(\frac{SCR_1}{SCR_2}\right)\left(\frac{SP_2}{SP_1}\right) SS_2 \tag{10}$$

Table 1 Comparison of operating parameters. Shaded areas indicated parameters calculated by the equation outlined in this paper.

location: machine:	UT at Austin Bambi	DTM Tool #4
machine specific: SCR, cm (inches) ω, cm (inches)	 30.5 (12) 0.0622 (0.0245)	 66.0 (26) 0.0279 (0.0110)
independent parameters:		
<u>case 1:</u> SCSP, cm (inches) Power, W SS, LSB's SP, 10μs bs, inches/sec	 0.033 (0.013) 16 26 15 21.7	 0.0148 (0.00583) 7.2 21.6 27 21.7
<u>case 2:</u> SCSP Power SS	 0.0284 (0.0112) 16 26	 0.013 (0.0050) 16 48

232

SP	15	27
bs	21.7	48.2
vector length, inches	1.0	2.0

Table 1 list typical operating parameters for both the University's SLS machine and DTM's Tool #4. The machine specific parameters, characteristic radius of the laser beam and the scan radius, are also listed for each machine. The shaded areas represent operating parameters calculated using the equations (8) through (10). The differences in the beam size and the scan radius between the two SLS machines are large compared to the differences that would be present between similar SLS machines manufactured by DTM.

Evaluation of Parameter Transformations

The evaluation of the parameter transformation equations can be done using an empirical sintering model which differs from previous theoretical sintering models [2,3] in the method used to calculate void fraction. The empirical sintering model is based on empirical sintering rates measured using an isothermal oven sintering technique [4]. The sintering data used in this example is for polycarbonate, which is an amorphous polymer. The model calculates the temperature and void fraction profiles within powder bed. The thermal properties of the polymer such as the thermal conductivity and the heat capacity are temperature dependent and void fraction dependent. Also, the flux input used in the empirical sintering model, $Q(x=0,t)$, includes a pulsed energy input related to beam overlap.

Figure 3 compares sintering depths measured from parts sintered in UT's SLS machine with sintering depths calculated numerically using a finite elements model. The sintering depths were measured optically with a microscope by viewing a thin cross-section removed from an SLS part. The sintered layer appears transparent in areas that are fully sintered and appears opaque in the areas where the powder is not sintered completely.
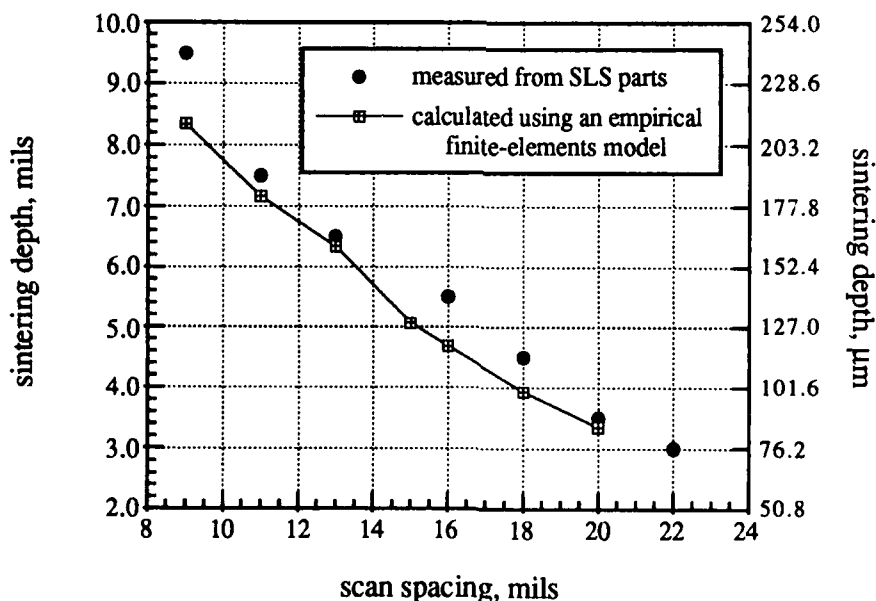

scan spacing, mils

Figure 3 Sintering depths of polycarbonate parts sintered in UT's SLS machine compared to depths calculated using an empirical finite elements model. (Independent parameters: Power = 16 Watts, ω = 0.0245 mils, *SS* = 26, *SP* = 15, SCR = 12 inches)

Table 2 Sintering depths calculated for the operating parameters listed in Table 1.

location: machine:	UT at Austin Bambi		DTM Tool #4	
	calculated (mils)	measured (mils)	calculated (mils)	measured (mils)
case 1:	6.52	6.5	6.46	??
case 2:	7.14	7.5	7.10	??

The sintering depths that result from the parameters specified in Table 1, are calculated using the sintering model and listed in Table 2. The measured values for the sintering depths are included when available. The calculated sintering depths show excellent agreement between layers sintered on the two SLS machines. The measured sintering depths support the SLS model results. We can see that the sintering depths are slightly smaller in the parts made on the DTM SLS machine. The energy input is identical during the processing on the two SLS machines However, the size of the laser spot differs which leads to a difference in the amounts of heat lost from the part surface during processing. For example, as the spot size decreases the following observations can be made:

- the intensity at the center of the beam increases, equation (4),
- the surface temperature increases as a result of the energy being more focused,
- less energy is absorbed into the powder because the radiant heat losses increase and,
- the number of scan vectors is increased to ensure beam overlap.

Real Time Control of the Operating Parameters

The implementation of a real time controller to control the laser power and beam speed may become necessary to provide a uniform energy density to sintered layers which contain both long and short scan vectors. With the current vector scanning technique, the laser power and the beam speed are specified before the first layer is scanned, and they remain constant throughout the SLS process. Therefore, a series of short scan vectors would receive more energy than a series of longer scan vectors because the delay between successive pulses is much smaller.

Feed back control of the laser power would be ideal for such an application if the temperature at the laser spot could be monitored accurately. The laser power could be adjusted dynamically to maintain a constant temperature during a scan which would lead to a uniform sintering depth in the layer. However, a temperature monitoring system with the accuracy necessary is not readily available. Therefore, a feed forward controller should be investigated to maintain a constant energy density across the powder surface.

Feed forward control anticipates the energy density using the current parameters and corrects for fluctuations in the energy to the surface by controlling the beam speed and the laser intensity. Controlling the beam speed during the scan of a layer would allow for adjustments to be made for scan vectors of varying length. However, adjustment of the beam speed alone would not maintain a constant energy input. The laser power would need to be adjusted simultaneously. For example, short scan vectors would be scanned with a slower beam speed and lower laser power than long scan vectors. Implementation of a real time controller using equations (8) through (10), is relatively easy if the laser power can be controlled during the scanning process.

Adjustment of Operating Parameters

Another application for equations described above is the adjustment of beam speed and laser power. Operating parameters would not necessarily have to be transferred between SLS machines to take advantage of the parameter transformation equations. Equations (8) and (10) can be used to calculate power settings for various beam speeds that would maintain a constant energy density. For example, if a set of operating parameters has produced good quality SLS parts, but the beam speed was too slow. A faster scanning speed could be chosen to reduce the total time required to scan a part, and equation (8) could be used to calculate a new laser power setting. Since the laser spot size remains constant, the scan spacing would remain constant and the power setting is simply a ratio of the beam speeds.

Conclusion

Equations can be derived to describe the effects of the independent operating parameters on the energy input to the powder surface. The energy can be approximated and modified as a function of laser power, scan speed and scan spacing.

These equations can be used in at least three applications. First, operating parameters used on one SLS machine can be transferred to other SLS machine that may have a different laser spot size and scan radius. Second, a feed forward control algorithm based on these equations could dynamically control laser power and beam speeds to maintain a constant energy input during the laser scan of an SLS layer. And third, the ratio of beam speed to laser power, in equation (8), can be used to calculate power settings for various beam speeds that would maintain a constant energy density.

Verification of the transformation equations has been made both experimentally and numerically using an empirical sintering model. The sintering depths calculated for parts made from the operating parameters that resulted for the parameter transformations were very similar to the sintering depths of the original parts, Table 1.

References

1. W. W. Duley, *Laser Processing and Analysis of Materials*, Plenum Press, New York, 1983, pp 19-23.
2. E. M. Weissman and M. B. Hsu, "A Finite Element Model of Multi-Layered Laser Sintered Parts," Solid Freeform Fabrication Symposium Proceedings, pp 86 - 94, August 1991.
3. M. M. Sun and J. J. Beaman, "A Three Dimensional Model for Selective Laser Sintering," Solid Freeform Fabrication Symposium Proceedings, pp 102 - 109, August 1991
4. J. C. Nelson and J. W. Barlow, "Sintering Rates in the Selective Laser Sintering Process," Solid Freeform Fabrication Symposium Proceedings, pp 146 - 154, August 1990.

Notation

ω = characteristic radius of the laser beam, cm

bs = beam speed of the laser scan, in/s

I_0 = the maximum intensity of the laser at the beam's center, cal/cm^2-s

LF = Laser Off, scanner operating parameter, μs

LSB = Least Significant Bits, 1 step size = 1/65536 of the full field dimension

P = laser power, Watts

p = emissivity of solid surface

$\bar{q}$ = average flux at a reference point along a scan line, cal/cm^2-s

$Q_{(x=0,t)}$ = laser heat source, cal/cm^2-s

SCR = scan radius, inches

SCSP = scan spacing, inches

SD = Scan Delay, scanner operating parameter, $SP*10\mu$s

SP = Step Size, scanner operating parameter, 10 μs

SS = Step Size, scanner operating parameter, LSB

S_x = the distance along the scan line from the axis of symmetry to the beam circumference

x = direction of the fast axis, parallel to the scan vector

y = direction of the slow axis, perpendicular to the scan vector

$y-y_0$ = the distance perpendicular to the scan vector from the beam center to the scan line

Rapid Prototyping at Zero Gravity for In-Flight Repairs and Fabrication on Space Station Freedom

Floyd Roberts, Marshall Space Flight Center; David Lomshek, Pittsburgh State University; and William E. Brower, Jr., Marquette University

ABSTRACT

The ability to perform in-flight rapid prototyping would be of great benefit to NASA in two ways. First, repair parts could be fabricated from CAD designs beamed up from earth based laboratories which might allow a failed experiment to proceed. The mission specialists themselves, under the creative influence of space flight, might design a new part or tool and fabricate it on board in a matter of hours. Second, with metal casting and ceramic sintering facilities on board, rapid prototyping would allow manufacturing in space. This paper presents some test criteria for evaluating two of the rapid prototyping techniques, stereolithography and fused deposition, in microgravity conditions. Effects of the variation of head speed and strip width for the fused deposition process on the resulting mechanical properties are presented. The mechanical strength of the polyamide test bars increased with both increasing head speed and strip width. Increasing head speed would be desirable in microgravity applications.

INTRODUCTION

Goals and ambitions of the National Aeronautics and Space Administration for the exploration and development of space go hand in hand with advances in remote processing. Remote processing allows materials processing and component production to be performed in environments which are untenantable, or cost prohibitive using human labor. The separation of physical processing and the designer allows exploration and development activities to be immediately and practically supported by earthside manufacturing experts. The interest in solid freeform fabrication via rapid prototyping arises from its preeminence in the arena of remote processing technology. Especially relevant is the ability of remote processing technologies to immediately supply astronauts on the space station with tools and components. This advantage can hardly be understated. Tools which were not anticipated, or which fill too selective a niche to be stocked on the station could be readily supplied by ground transmission or supplied by a CD ROM on board library. This advantage, of course, applies to failed components which could be replaced on a temporary (awaiting resupply) basis.

Additionally remote processing would provide investigators the luxury of changing their design of an experiment on the space station during the course of their residence. If an inventive alteration occurred to a scientist while an experiment was being conducted on the space station, remote processing would allow new experimental parts to be designed and built while the experimenter was on station running the experiment. This would also apply to innovations developed by the astronauts during space station operations. New ideas and inventions could be investigated on an immediate trial basis.

Referencing the Lunar and Mars missions, remote processing technologies, using lunar regolith or martian simulant may be the only feasible means of materials supply for these enterprises.

The planned activities of Space Station Freedom include Life Science, Materials Science, Earth Science, and Astronomical Science experiments, but no manufacturing experiments (1). Each module on Space Station Freedom (SFF) contains racks for experiments with a volume of 35 cubic feet; the 3D Systems Model 250 Stereolithography Unit and the Statasys 3D Modeler Fused Deposition Unit would both fit in an SFF rack. One of the modules is a centrifuge, so that one gravity operation might be possible.

Before utilization on the Space Station, each rapid prototyping technique would have to be evaluated in microgravity in a series of preliminary modes. These modes are summarized in Table 1 to show the time available at zero gravity and the rapid prototyping result during such weightless times. The drop tower approach would not be feasible for the two rapid prototyping techniques considered here. Not enough of a part could be produced to be dimensioned, as only a portion of a single layer could be built in the 1-10 seconds available. Thus, model systems to simulate the behavior of the full unit would have to be employed. Liquid model systems are being evaluated in drop towers to evaluate surface tension effects in microgravity. Concus and Finn (2) report liquid to be stable in a round container, but to climb the corners of a square container. This would suggest modification of the present Stereolithography cubic liquid photopolymer vat to a cylindrical shape. The KC-135 flights using multiple 25 second weightless dives would be able to produce a small test part for dimensioning with a Rapid Prototyping unit on board. If the KC-135 tests were successful, a modified rapid prototyping unit could be sent on a Shuttle flight, where a full sized part could be built in microgravity. If the Shuttle experiments were successful, the relevant time factor on the Space Station for Rapid Prototyping would be driven by the Mission needs, since the Rapid Prototyping capability would be permanent.

PROCEDURE

The current test series is designed to determine processing parameters which impact strength and reliability of fused deposition modeled components. The material chosen was the current high strength material supplied by Stratasys Corporation, "plastic 300", a polyamide. Any component produced using fused deposition modeling differs from a bulk extruded polymer in the interfacial region between deposition strips. The number of interfaces, the construction of the interface, and the macroscopic and microscopic morphology of these interfaces will play a role in the mechanical behavior of the final part. We chose to initially look at the "road width" of the deposition strip, and the linear speed of the polymer extrusion head.

Fused deposition modeling uses the extrusion of a .050" diameter feed material filament through a melting chamber and into an extruder. The extrudate is then passed through a heated tip and, after swelling has been accounted for, lays down a deposition strip with a characteristic "road width". The extrusion head encompasses two degrees of freedom (X & Y) and the deposition platform rises and falls to produce the third (Z) degree of freedom.

Tensile test samples were produced with road widths of .030", .040", and .050". The linear speeds for the polymer extrusion head used were .400" per second, and .500" per second. The layer thickness or "Z slice" thickness in all cases was .015". The samples were produced with the strip orientation within the gauge length parallel to the direction of tensile stress.

The samples were tested according to ASTM D638-84 in the Marshall Space Flight Center Materials and Process Lab. Type Three specimens were fabricated as mentioned above. The temperature was 74°F and the relative humidity was 57% during the tests. The surface finish of all specimens was left in their original as produced form. The strain rate for all tests was 2 inches/minute. During the test there was not uniformity of strain behavior within the gauge length. The material in all cases underwent necking prior to failure, and in one case failure did not occur due to complete and uniform necking within the gauge length.

RESULTS AND DISCUSSION

There was a significant increase in stress at peak and stress at break over the increase from .040" strip width to .050" strip width. This occurred over same interval as the speed increase from .400"/second to .500"/second. The data shown in Figure 1 gives a good linear fit to the plots of the speed of the extruder tip vs. peak stress, 2% yield stress, and fracture stress. The correlation coefficients are in all cases equal to or above .996. On the other hand attempting to fit plots of the road width vs. the stresses with a linear fit results in no correlation coefficient higher than .756. The road width vs. stress plots all, however, are well fit by a 3rd order polynomial, as shown in Figure 2.

The mechanism of strength increase may be associated with a better linking between adjacent layers during sequential deposition. For an improvement in linking of two deposition strips two factors present themselves. First, a change in the polymer morphology present at the fusing edges may occur as a result of the change in the shear level of the deposited polymer. The change in shear level is due to increased pressure at the extrusion head, resulting in increased shear and an increase in the strip width. The second factor postulated is an increase in the temperature at which the fusion between strips takes place. An increase in fuse temperature could occur due to either a decrease in the cooling rate due to the increase in thermal mass from the wider strip width, or, a decrease in cooldown time between successive deposited strips due to increase speed of deposition.

CONCLUSIONS

The improvement in the polyamide mechanical properties with fused deposition head speed is encouraging for microgravity applications. Faster head speeds may be required to minimize distortions during the liquid extrusion phase of the fused deposition process.

REFERENCES

1.   R. Moorehead, "Space Station Freedom Program and Operations," Meeting of the Wisconsin Space Business Round Table, Madison, Wisconsin, July 1992.

2.   USRA Quarterly, Winter-Spring, 1992.

Table 1. Microgravity Test Modes for Rapid Prototyping

Test Mode	Time at Zero Gravity	Rapid Prototyping[*] Result During Test
DROP TOWEP Small-Stairwell Large-Skyscraper	1-2 seconds 5-10 seconds	None-use model system None-use model system
KC-135 Flights	25 sec/dive, multiple dives	small part
Shuttle Flight	days	full sized part
Space Station Freedom	years	manufacturing

[*]Stereolithography = 10-20 sec/layer
Fused Deposition = 10 inches/sec

$$y = 5.687E\text{-}5x + .259, \quad r^2 = .999$$

.52

.5

.48

.46

.44

.42

.4

.38

Speed of extruder tip

2400 2600 2800 3000 3200 3400 3600 3800 4000 4200 4400

Stress at peak

O Speed of extruder tip

Fig. 1b

$$y = 8.985E\text{-}5x + .269, \quad r^2 = .997$$

.52

.5

.48

.46

.44

.42

.4

.38

Speed of extruder tip

1200 1400 1600 1800 2000 2200 2400 2600
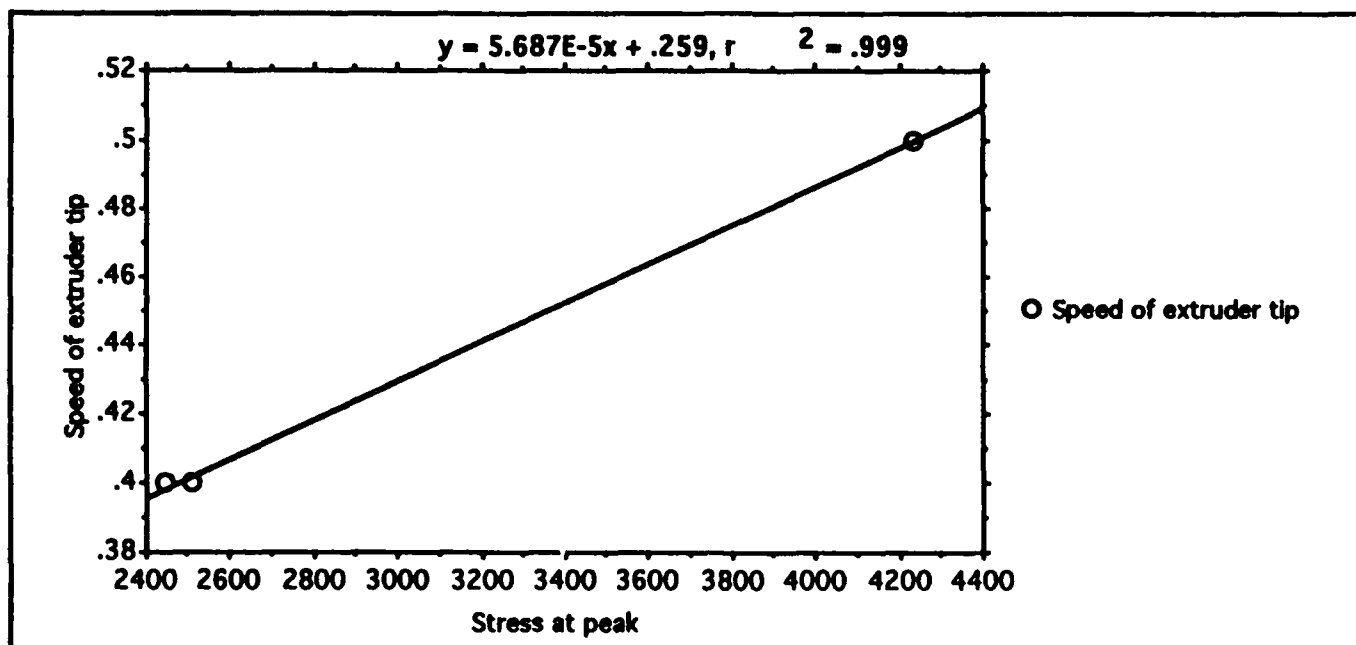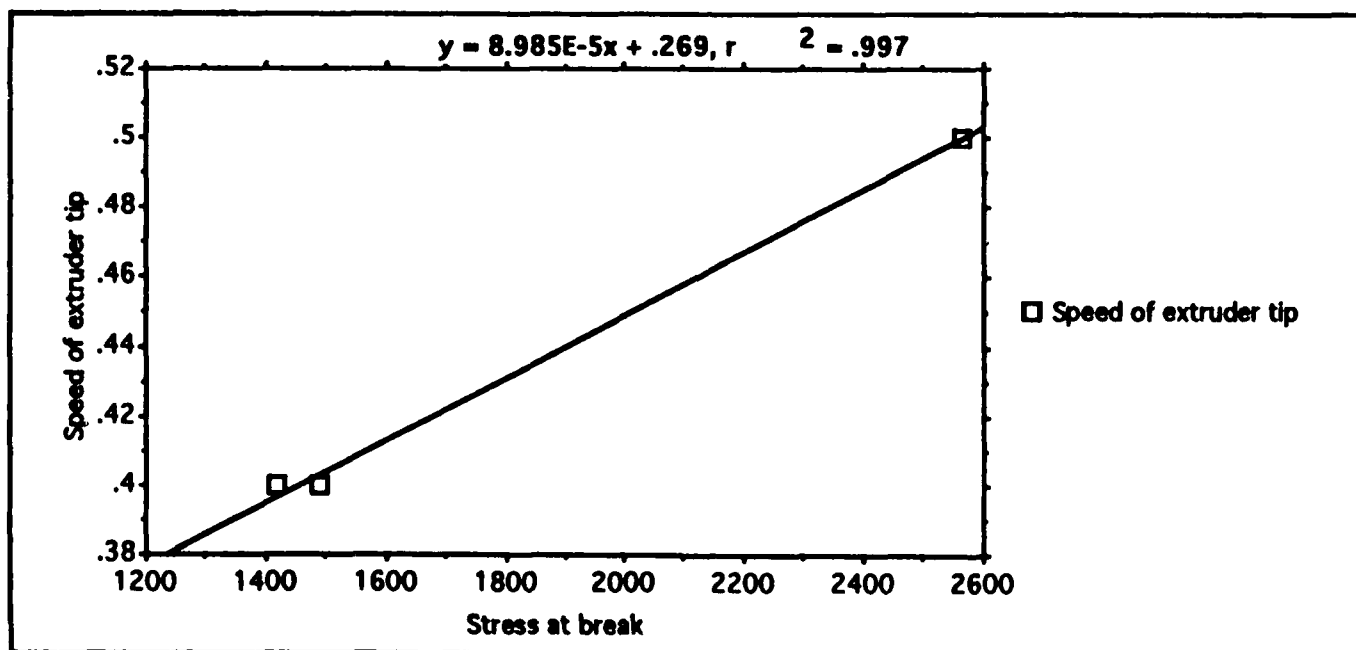
Stress at break

□ Speed of extruder tip

Figure 1. Variation of Polymer Strength with Fused Deposition Extruder Strip Speed

a. Peak Stress
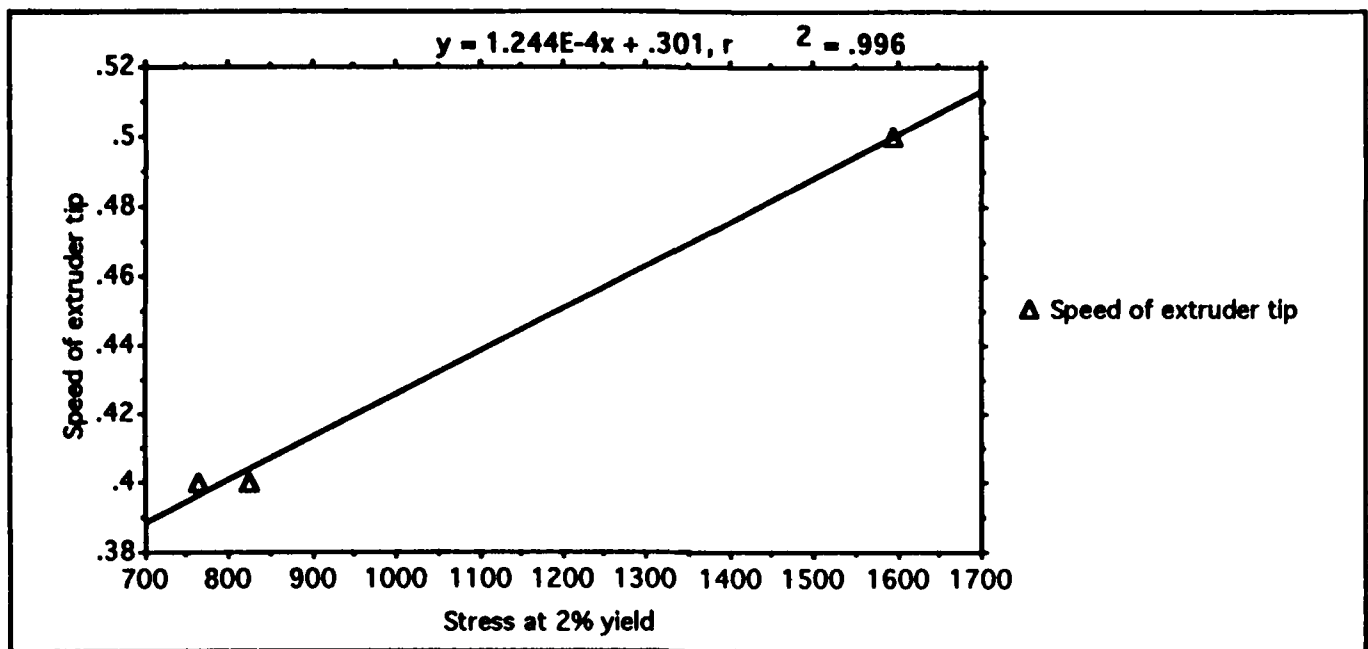
b. Fracture Stress

c. 2% Yield Stress
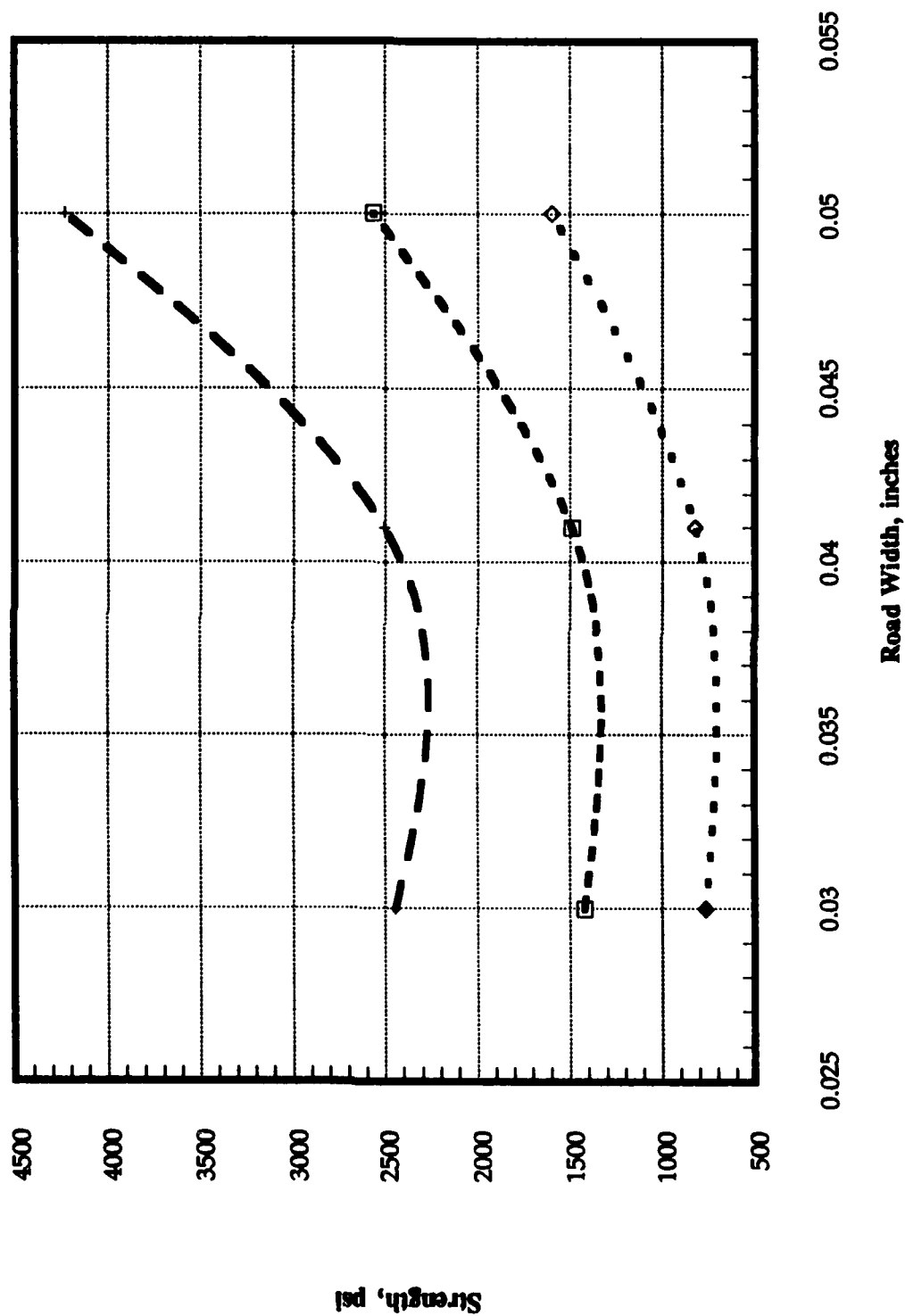
241

Fig. 1c

$y = 1.244E{-}4x + .301, r^2 = .996$

Figure 2. Variation of Polymer Strength with Fused Deposition Road Width

Summary NYL 01,02,03 Means

+ Stress at peak
□ Stress at break
◇ Stress at 2% yield

Road Width, inches

Strength, psi

METAL PARTS GENERATION
BY
THREE DIMENSIONAL PRINTING

Steven Michaels, Emanuel M. Sachs, Michael J. Cima
Massachusetts Institute of Technology

Abstract

Three Dimensional Printing is a rapid prototyping process in which powdered materials are deposited in layers and selectively joined with binder from an ink-jet style printhead. Unbound powder is removed upon process completion, leaving a three dimensional part. Stainless steel and tungsten parts have been created from metal powder with the 3DP process. The parts have green properties similar to those produced by metal injection molding. A tooling insert made from 316L stainless steel powder was used to injection mold a polypropylene part. The 3DP process is easily adaptable to a variety of materials systems, allowing the production of metallic/ceramic parts with novel compositions. This paper will discuss the use of the 3DP process to produce injection molding tooling and end-use parts.

Introduction

Metal parts to be used as end-use parts and injection molding tooling inserts have been made using the 3DP process. This paper describes a process where 316L stainless steel powder is selectively bound with a latex emulsion binder using the 3DP process, producing a green part with strength comparable to parts produced by metal injection molding (MIM). A series of post-processing steps similar to those found in powder metallurgy processing were used to obtain an all-metal part which was then used as a tooling insert to injection mold a polypropylene part.

The 3DP Process

Three Dimensional Printing (3DP) is a process for the rapid fabrication of three dimensional parts directly from computer models [1] . A solid object is created by printing a sequence of two-dimensional layers. The creation of each layer involves the spreading of a thin layer of powdered material followed by the selective joining of powder in the layer by ink-jet printing of a binder material. A continuous-jet printhead is raster scanned over each layer of powder using a computer controlled stepper motor driven x-y table. Individual lines are stitched together to form 2D layers, and the layers are stitched together to form a 3D part. The printing nozzle has a circular opening 46 μm in diameter. The nozzle is stimulated by a piezoelectric transducer vibrating at 60 kHz to break the stream into droplets 80 μm in diameter. Commands to modulate the binder stream are derived from CAD data. The powder bed is lowered at the completion of each layer by lowering the bottom of the rectangular cylinder which contains the bed. Figure 1 is a drawing of the 3DP system. Unbound powder temporarily supports unconnected portions of the component, allowing overhangs, undercuts and internal volumes to be created. The unbound powder is removed upon process completion, leaving the finished part.
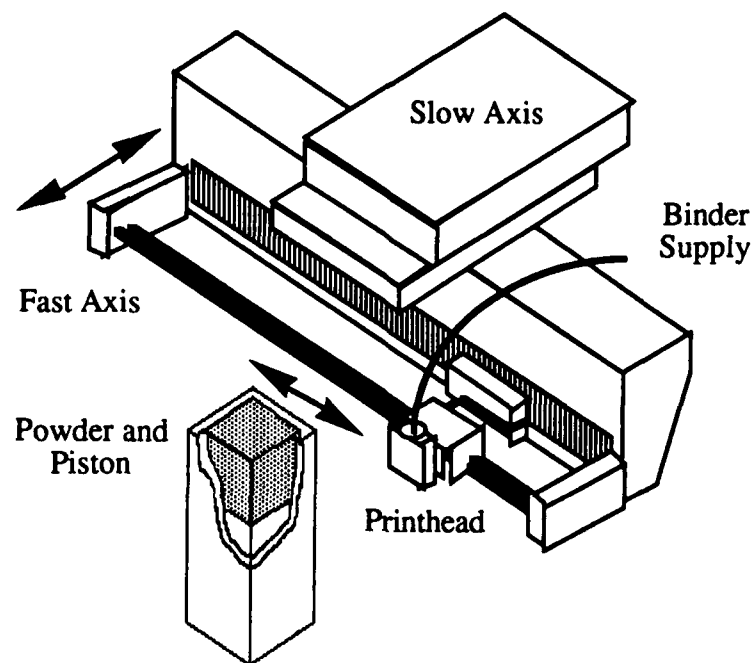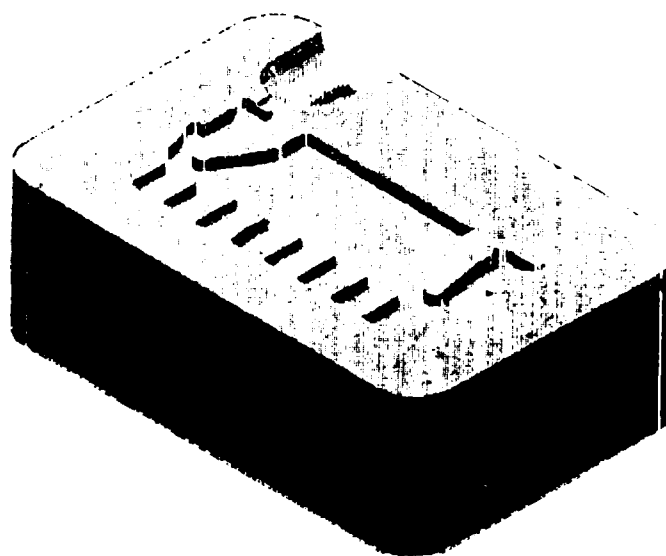
Figure 1. The 3DP System.

Figure 2. CAD Rendering of an Injection Molding Tooling Insert.

Printing a Stainless Steel Part

The overall process to create a metal part can be divided into several steps. First, the green part is printed using the 3DP system by using a temporary organic binder. The part is processed using techniques similar to those used in MIM . The organic binder thermally decomposes in an inert gas furnace. Subsequent firing at high temperature sinters the part and increases its strength. Firing schedules can be devised to densify the component or increase the particle-particle bonding without densification. Figure 2 is a CAD drawing of the part printed in these experiments. Only the top portion of this part was printed in order to reduce printing time.

3D Printing

The powder used in these experiments was a 316L spherical stainless steel powder with a size range of 15 - 30 μm [2] . This powder exhibited a typical packing density of 57% when spread into layers during the 3DP process. The thickness of each layer was 175 μm in all the experiments.

An aqueous acrylic copolymer emulsion was used as the binder [3] . This emulsion is self-crosslinking and cures by drying in air to form a high durometer solid. The binder was diluted with water to 25% acrylic solids by weight. The binder was filtered through 1.2 μm capsule filters under pressure before then passing through the printhead. Total flowrate was 1.2 cc/minute. The individual printed lines which are stitched together to form each layer were spaced 175 μm apart. Preliminary experiments showed that proper choice of flowrate and binder dilution yielded parts with high strength and stiffness while still being easy to print.

Initial attempts at printing with this combination of powder and binder were unsuccessful because of significant particle rearrangement. The binder stream cut a large trench into the powder surface upon impact and capillary action would then draw the powder up into large agglomerates. Figure 3 is a strobe photograph of this impact effect. The printhead, not visible in the photograph, is traveling right to left. Ejected powder can be observed on the powder surface over an area as wide as 5 mm.

Several methods were tried to give the powder surface enough cohesive strength to resist deformation during printing. First, the entire powder layer surface was sprayed with water from an ultrasonic sprayer prior to printing in order to bind the layer together via capillary tension. The desired cohesive strength was obtained, but the presence of moisture in the top layer of powder greatly enhanced transport of the binder material in the powder bed. The resulting binder "bleeding" caused a complete loss of edge definition in each printed layer and produced an unacceptable part.

The final solution was to pretreat the metal powder with a thin coating of metal salt. A slurry composed of metal powder and dilute aqueous salt solution was blended, dried and sieved to create the coated powder. During the printing process, a layer of treated powder was spread, misted with ultrasonic water mist and dried with forced hot air. The presence of the metal salt significantly increased the cohesive strength of the layer. Presumably, the metal salt on the powder surface recrystallized during wetting and drying, forming interparticle bonds which were strong enough to resist binder stream impact and the subsequent interparticle capillary forces. Less than 0.05 weight % salt (based on final part weight) was required to achieve this cohesive effect. Figure 4 shows the dramatic improvement which the powder surface locking process has on the printing process.

The entire powder bed was placed in an oven after completion of the printing process and fired at 100°C for one hour to completely cure the acrylic binder. The green part was then removed from the powder bed. Salt bonded material is extremely weak compared to the polymer bonds in the green part. Thus, the remaining attached powder was easily blown off with compressed air. Excess powder was sieved and reused.

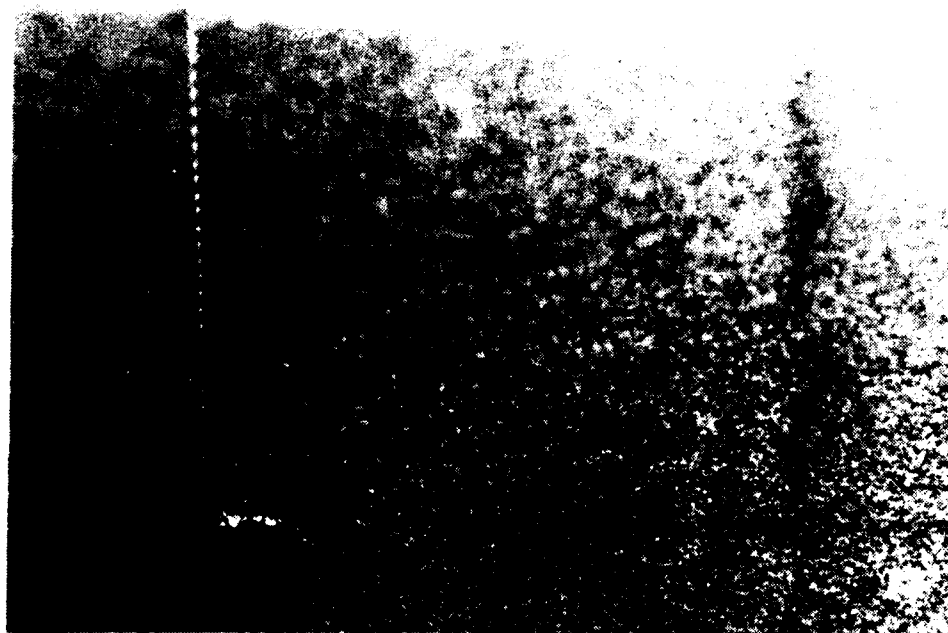Figure 3. Printing Into Untreated Stainless Steel Powder.

Figure 4. Printing Into Stainless Steel Powder Treated with Metal Salt.

Debinding

Binder was removed from the green part by thermal decomposition in an inert gas tube furnace [4]. The binder polymer chains are broken by heating during thermal decomposition and the binder is evolved as a gaseous product. Binder removal from 3DP parts is similar to debinding of MIM parts but is inherently faster because less binder is required in the 3DP process. A typical 3DP green part is 10% by volume binder, leaving approximately 30% open porosity. MIM parts, being solid metal/binder composites with little open porosity, must be debound very slowly to prevent the formation of internal gas pockets which can rupture the part. No such limitation exists for 3D Printed parts.

Debinding was done in an argon atmosphere tube furnace. Parts were heated to 400°C to burn out the acrylic binder, followed by firing at 1000°C to provide the skeleton with sufficient strength to be handled after debinding. A typical debinding process requires six hours. Upon completion of the debinding process, parts exhibited dimensional change of +/- 0.2% along the x and y axes and up to +2% in the z axis. (The x axis is along the printed line, the y axis is across the printed line, and the z axis is across the printed layers.)

Sintering

Metal skeletons have sufficient strength to be handled after the debinding step described above. Tooling inserts were, however, sintered to higher density. Various firing schedules were used to obtain parts with final densities between 65% and 92% of theoretical. Figure 5 is a photograph of a green and sintered part. In this case, the part had been sintered to 78% of theoretical density, resulting in obvious shrinkage.

Injection Molding

A 3DP part was used to demonstrate plastic injection molding from a SFF generated die. The 3DP part was machined to fit into an aluminum runner assembly block and installed into an Engel EC88, 25 ton injection molding machine located at MIT. The mating half of the mold was a simple cavity cut into an aluminum block which gave the injection molded part additional thickness and strength.

Approximately 40 polypropylene parts were injection molded. Melt temperature and pressure were 230°C and 1200 psi, respectively. Figure 6 is a photograph of the tooling insert and injection molded part. Part removal from the 3D printed mold was made difficult due to the absence of knockout pins in the mold, the lack of draft angle in the mold features, and the relatively rough finish of the infiltrated mold surface. These factors contributed to the rough finish on the plastic parts.

Economics

The green parts produced by the 3DP process can be compared directly to those produced by metal injection molding. In both cases, green parts are approximately 60 vol. % metal, held together with a polymeric binder. The most important cost associated with MIM is that of the hard tooling required for each part. The analogous cost in 3D printing is the 3D printing machine itself. The 3DP machine is, however, a universal tool capable of producing any shape. A calculation of the tooling cost associated with 3D printing reveals the economic feasibility of producing end-use 3D printed metal parts. A production capacity 3D printing machine has an estimated price of $200,000. Over a 20,000 hour service life, an additional $50,000 would be spent on maintenance and operating costs. The powder printing surface on such a machine might typically measure 30 cm x 30 cm. The vertical build rate for a 32 nozzle printhead would be 2.5 cm per hour. Many small parts distributed throughout the powder bed could be printed simultaneously. Over 140 green parts with overall dimensions of 2.5 cm x 2.5 cm x 2.5 cm could be
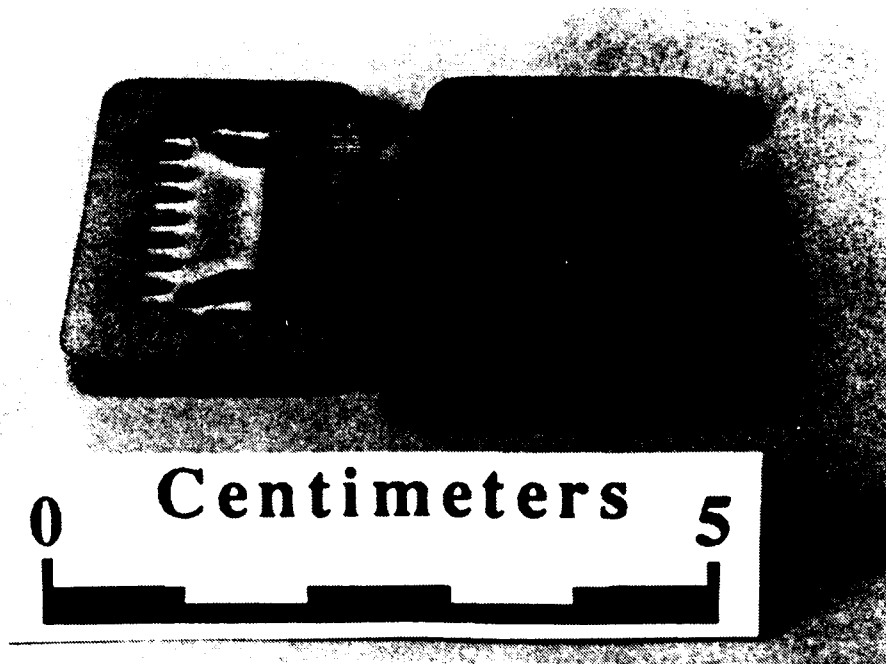
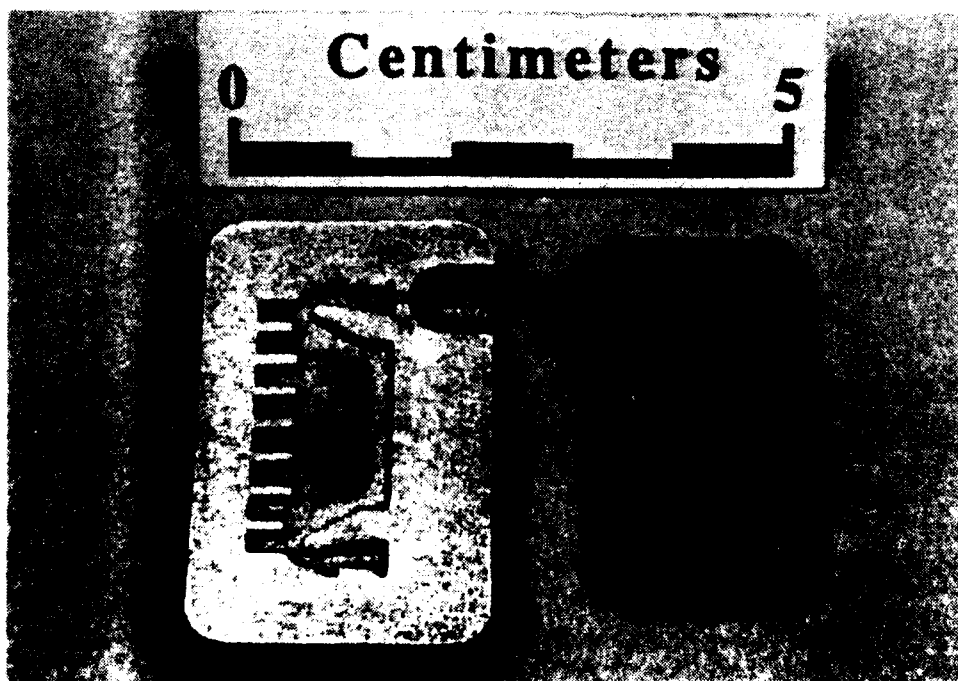Figure 5. A 3D Printed Part Sintered to 78% Density (left) and a Green Part (right).

Figure 6. A Tooling Insert and an Injection Molded Polypropylene Part.

printed together, requiring an hour to produce one "layer" of parts. The associated tooling cost per part would be $ 0.09. A MIM mold to produce the same part would cost approximately $50,000. In this case, 3D printing can economically compete with metal injection molding in batch sizes of up to 500,000 parts.

The rough estimate above demonstrates that the 3DP process is a viable method for metal part production. An important aspect of this analysis, however, is that there is no minimum batch size associated with the 3DP process. Batches of 10 or 10,000 all have the same tooling cost . Most importantly, the "tool" can be redesigned as quickly as new CAD information can be downloaded.

Conclusions

3D printing has the capability to produce a wide variety of complex metal parts to be used as tooling and end-use parts. In addition, nearly any material system whi h can be provided in powder form can be used in the 3DP process to produce parts with ovel material compositions. To date, green parts have been printed with iron, stainless steel, tungsten, tungsten/nickel alloy, tungsten carbide and tungsten carbide/cobalt alloy.

Areas of future work include an investigation of the parameters related to part dimensional accuracy, surface finish and material properties. Methods for increasing the green density of as-printed parts need to be in investigated. A better understanding of the ballistic interaction of the binder stream and the powder layer is needed, as well as new methods for preventing powder rearrangement during the printing process.

References

1.	Sachs, E., Cima, M., Williams, P., Brancazio, D., and Cornie, J., "Three Dimensional Printing: Rapid Tooling and Prototypes Directly From a CAD Model", Accepted for publication in the Journal of Engineering for Industry.

2.	Ultrafine Powder Technology, Woonsocket, RI 02895

3.	HA-16, Rohm and Haas, Philadelphia, PA 19105

4.	German, R.M., Powder Injection Molding, Metal Powder Industries Federation, Princeton, NJ, c. 1990.

Generating Topological Information
from a "Bucket of Facets"

Stephen J. Rock
Michael J. Wozny

Rensselaer Design Research Center
Rensselaer Polytechnic Institute
Troy, New York 12180

Abstract

The STL *de facto* data exchange standard for Solid Freeform Fabrication represents CAD models as a collection of unordered triangular planar facets. No topological connectivity information is provided; hence the term "bucket of facets." Such topological information can, however, be quite useful for performing model validity checking and speeding subsequent processing operations such as model slicing. This paper discusses model topology and how to derive it given a collection of unordered triangular facets which represent a valid model.

1 Introduction

Computer Aided Design (CAD) model data is frequently passed to various Solid Freeform Fabrication processes using the STL polygonal facet representation [1]. Facet models represent solid objects by spatial boundaries which are defined by a set of planar faces. This is a special case of the more general Boundary Representation which does not require object boundaries be planar [2]. In general, the term facet is used to denote any constrained polygonal planar region being used to define a model boundary; however, in the Solid Freeform Fabrication (SFF) community the term facet is typically understood to mean *triangular* facet. Representing models using triangular facets has both good and bad points [3]. Facets do provide a "greatest common denominator" geometrical form for data exchange between many CAD systems and SFF processes. Non-CAD scalar field data, such as that from CT imaging, can also be used to generate facet models [4]. However, facet models are generally only an approximation of mathematically precise CAD models.

Precise CAD models must be tessellated, where defining model surfaces are subdivided into planar facets, to create polygonal facet models [5]. As model precision demands become more stringent, the number of facets required to adequately approximate a model will increase. Model tessellation should yield a set of facets which define a closed region representing the material boundary of a part. Unfortunately, many commercial CAD system model tessellators are not robust, and sets of facets which do not define closed regions result. This missing facet problem is particularly prevalent where surfaces intersect in the original CAD models. A set of facets which, when assembled, forms a solid object with holes in its surface is incomplete and is termed an *invalid* model. In addition to missing facets, other causes of model invalidity exist. They include errors due to numerical round-off, missing data, altered data, and sometimes the presence of extraneous or redundant data.

The *de facto* industry standard STL model representation defines models as a set of triangular facets [1]. Unfortunately, these facets are stored independently, as if each facet were created and tossed into a bucket with no particular ordering and without information relating a given facet to any other facets in the bucket. Since many CAD systems fail to generate valid facet model tessellations, it is necessary to perform model validity checking before subsequent processing operations are undertaken. Given only the data in an STL file, performing model validity checking is computationally expensive. Attempting to

determine the relationships, or topology, between model facets from the "bucket of facets" is the first step in performing validity checking. The resulting topological information is important for use in subsequent processing operations such as model repair, model slicing, and finally during the scan conversion operation.

2 Topology

Topology describes the connectivity relationships between various geometric entities [2]. A facet can reference the three edges which bound it. Each edge can reference the two vertices which define it. Topological connectivity relationships are not limited to individual facets. For instance, a facet can reference the three facets which share edges with it. An edge can reference not only the two vertices which define it but also the two facets which share it. Vertex points can contain connectivity information to all edges or faces which share it. Such references are all examples of topological connectivity information.

It is important to consider two topological classes of boundary representation models: manifold (two-manifold) and non-manifold. A two-manifold is defined as a two-dimensional, connected surface where each point on the surface has a neighborhood topologically equivalent to an open disk [6]. In a two-manifold, every edge in the model is shared by two and only two facets. This is the case for most facet models where only the facets representing a part's spatial boundaries exist. One side of a facet is directed toward part material, and the other is directed away from it. The spatial boundaries of a facet model are expected to have a distinct "inside" and "outside" which is consistent across all facets defining the model boundary; such a model is termed *orientable* [2]. Non-manifold conditions occur where, for example, two distinct enclosing volumes share one facet or a set of facets as a common boundary [7]. In this case, the shared facet no longer has a clear "inside" or "outside". Both sides of the facet are surrounded by part material. This typically occurs when facets representing multiple solids which are tangent along some boundary are not properly delimited as belonging to individual solids in an STL file.

3 Benefits of Topological Information

The STL format represents facet models with nearly the minimal information necessary to define a solid object. Each facet, along with its normal, is specified explicitly and no topological connectivity information is provided. This "bucket of facets" approach to model representation has many limitations, both with respect to ensuring valid models and subsequent processing.

3.1 Validity Checking

When no topological information is provided, model validity checking involves computationally expensive searching operations. If model topology were available, validity checking would be a much simpler and efficient operation.

3.2 Model Repair

When invalid models are encountered, topological information is useful for attempting to repair the models. Such information makes it readily apparent when greater than two facets share a single model edge. In the case of model holes, it is important to know how the facets surrounding a hole are connected and this too can be easily determined given topological information.

3.3 Subsequent Processing

Facet model slicing performance can also benefit from topological information which makes it possible to march from facet to neighboring facet performing simple edge/plane intersection calculations [8]. This same topological information can be passed to subsequent processing phases, such as scan conversion, which occur after slicing.

3.4 Model Representation

Finally, model topology generation capability has facilitated the development of a richer facet model representation format [9]. Storing topological information with a facet model, although increasing the information content of the model, reduces the volume of data required when compared to an equivalent model represented in STL format. The net result is a more robust representation with less data.

4 Topology Reconstruction Concepts

Reconstructing model topology given a "bucket of facets" is basically a searching operation. Entity relationships must be found by searching the unordered model data. These relationships, or topology, must then be stored for later use. The conceptual steps for producing such topology will now be discussed; however, implementation details, such as the searching algorithms or structures used, will be dealt with separately after the topology reconstruction concepts are understood.

4.1 Vertex Merging

Each facet is defined by three vertices whose coordinates are explicitly specified. The first operation performed when reconstructing model topology is *vertex merging*. Here, equivalent, explicitly specified vertices are replaced by a single entry in a list of unique vertices. Each face then references three vertices in the list instead of being defined by actual vertex values. This removes significant redundancy present in the model representation. It also allows vertex comparisons to be made based on vertex references without comparing actual floating point coordinate values. Figure 4.1 illustrates the savings realized by using model topology and representing each vertex uniquely.

5 Vertices
(15 doubles, 12 pointers)
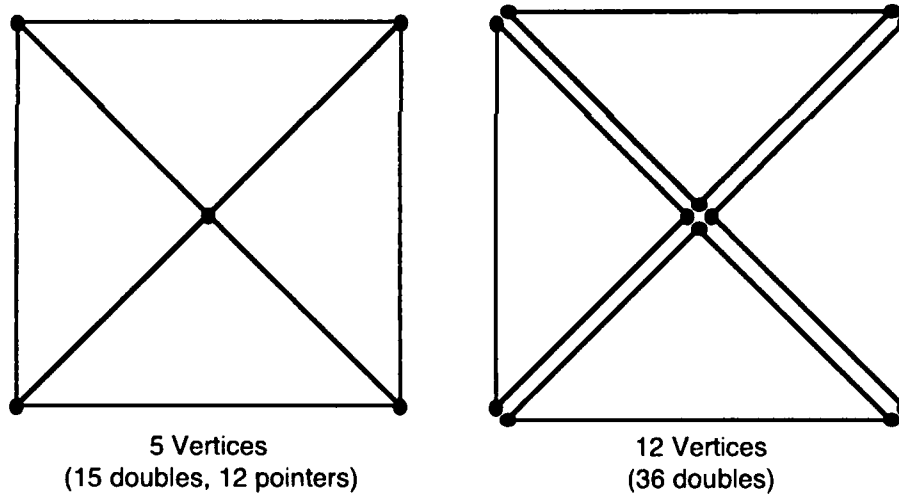
12 Vertices
(36 doubles)

Figure 4.1 - Storage Reduction with Topological Information

Without topological connectivity information, the vertex shared by the four facets shown would be represented four times. Assuming a vertex is specified by three double precision values, and a double precision value requires eight bytes, the four facets shown could be represented by 288 bytes (4 facets x 3 vertices/facet x 3 doubles/vertex x 8 bytes/double). By using topological information, a unique definition of each vertex can be referenced by the facets using pointers. If a pointer consumes four bytes, this will reduce the memory required to represent the four facets shown to 168 bytes (5 vertices x 3 doubles/vertex x 8 bytes/double + 4 facets x 3 pointers/facet x 4 bytes/pointer). This figure shows a significant storage savings where only four faces meet. However, in a real model which is closed and likely more complex, many facets will share each single vertex. This will result in even greater savings by using topology and representing each vertex uniquely.

The final benefit of vertex merging is that vertices within a predetermined numerical round-off tolerance of each other can be easily merged, and this can be used to overcome errors introduced by inconsistent numerical round-off. Such errors can occur when a slightly different sequence of mathematical operations is used to calculate the same vertex value. For example, given three finite precision binary numbers A, B, and C, the operation A + B + C may not produce the same result as the operation A + C + B due to rounding or chopping errors [10]. Figure 4.2 provides a two-dimensional example of how vertex merging can also remove facets smaller than the size of the numerical round-off tolerance.
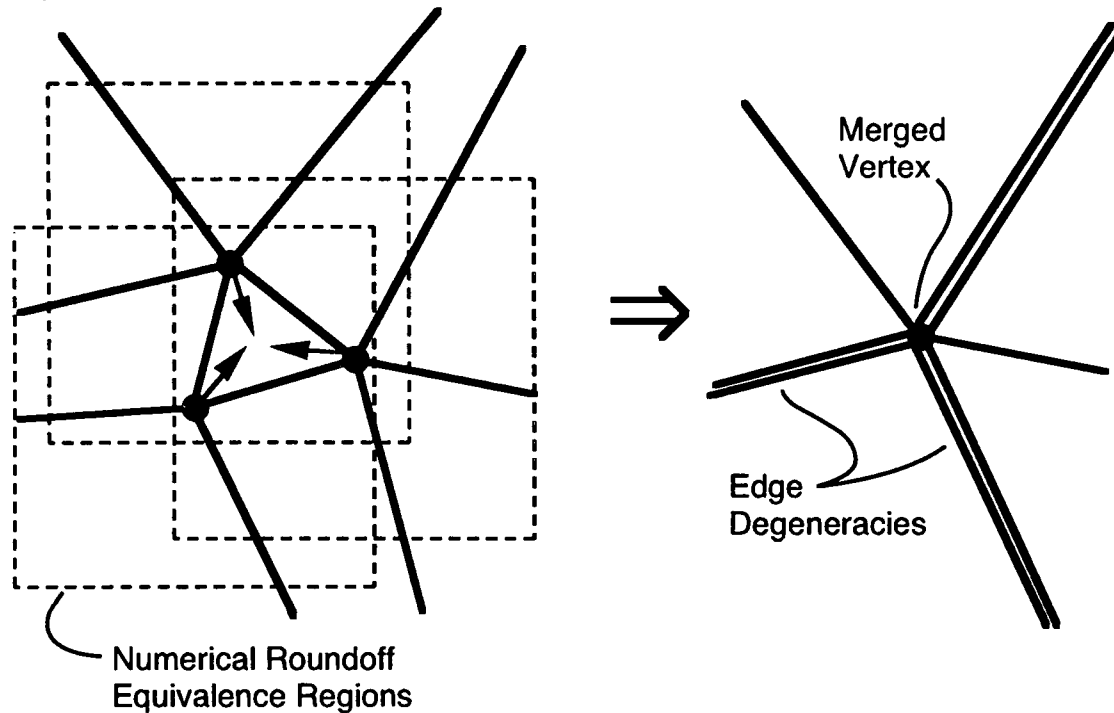

Figure 4.2 - Facet Removal by Vertex Merging

The facet defined by the three vertices shown is smaller than the specified numerical round-off tolerance. The squares drawn with dashed lines and centered on each of these vertices indicate the equivalence regions defined by the numerical round-off tolerance setting. Since the vertices are within the equivalence regions, they are considered equivalent and should be merged into one vertex. This is illustrated by the three arrows pointing toward the center of the left hand figure. Notice that as the three facet edges collapse, the remaining edges of the three adjacent facets will approach each other.

The figure on the right shows what happens to the model after the three equivalent vertices have been replaced, by merging, with one new vertex. The three facets which were adjacent to the facet removed by vertex merging now have two identical vertices (the vertex resulting from the merging operation). Note that this creates a degenerate condition where three of the facets surrounding the merged facet have effectively collapsed to an edge. The facet topology is still present; however, two facet vertices are the same in each of the degenerate facets.

4.2 Face & Edge Creation

A face entity must be created to represent each facet in the model. Since vertices are represented uniquely, each face maintains references to the three vertices which define it. Each face entity also carries with it a facet normal. This aids in determining which side of the face is inside the model; however, this information could also be computed if it were not given, provided the right-hand rule for vertex definition is adhered to [1].

Similarly, it is possible to create edge entities to represent model edges. Each edge can reference the two vertices which define it and the two faces which share it. Edge information is not provided by STL format files, but it can have utility when slicing facet models and can be represented using alternative file formats [3]. The following section will show that it is appropriate to wait until face relationships have been determined before creating model edges.

4.3 Determining Face & Edge Relationships

When face entities are created, they not only contain references to the defining vertices and normal, but they also contain unassigned references to the three adjacent faces and corresponding edges. Figure 4.3 provides a graphical depiction of adjacent face and edge references .
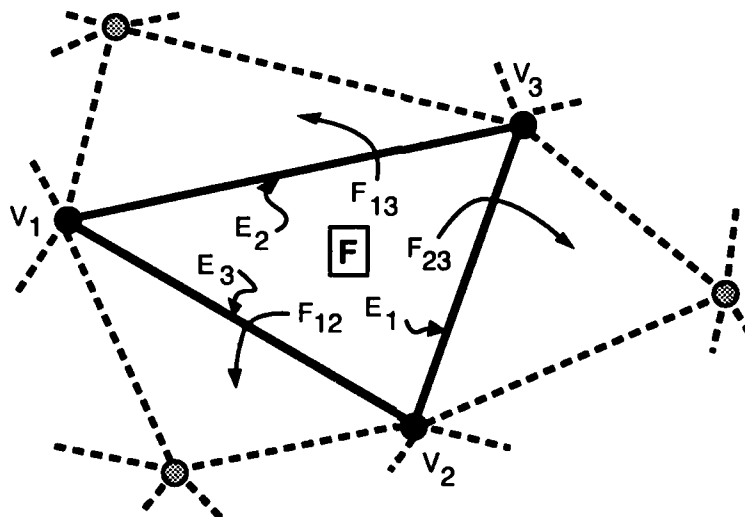

Figure 4.3 - Adjacent Face and Edge References

These references will be assigned as model topology is determined. After all face relationships are determined, the relationships between model edges can be determined using the face relationship information.

Face relationships are determined by searching. For each face in the model, searching is performed to determine what other faces share two common vertices. The existence of a pair of such faces defines an edge. When such a face is located, the adjacent face references of each face corresponding to the shared edge are cross-referenced. This establishes one topological relationship between two faces. This process is repeated until all adjacent face references are set. Notice that this assumes each model edge is shared by exactly two faces; invalid models exist where this is not the case.

After defining all face adjacency relationships, it is possible to define model edges. The three vertices which define each face and the three adjacent faces of each facet are known. Edge topology can be derived by using this information. The three edges of each face, defined by the face's vertex pairs, can be added to an edge list if they do not already exist. When an edge is added, the vertices which define it are known, so its vertex references can be set accordingly. One of the faces which shares the edge is immediately known, as this is the face being used to reference the edge's defining vertices. The other face which shares the edge is also known after the face adjacency relationships have been determined. By sequencing through all faces in the model after the face adjacency relationships are known, complete edge topology can be created without additional searching.

255

5 Data Structures & Algorithms

The fundamental operations used to reconstruct model topology have been discussed, but few operational details were provided. If brute force approaches to vertex merging and adjacent facet searching are used, computational cost will quickly become prohibitive as model complexity increases. Consequently, care must be taken to ensure the data structures and algorithms employed facilitate efficient searching.

Facets are read sequentially from a data file with no particular ordering. Each time data representing a facet is read, a face entity is created. Three vertex entities, each of which may already exist or need to be created, are referenced by each face entity. A linear list, although a poor structure for sorting and searching, can be used to store the face entities because they are not searched directly. Vertex entities must, before they are created, be tested to ensure an equivalent vertex does not already exist. If it does, this equivalent vertex should be referenced by the newly instantiated face entity instead of creating a new vertex entity and referencing it. A searching operation is required to perform this equivalence testing, and it is repeated for each model vertex. Repeatedly searching, and maintaining in sorted order, a linear list of vertex entities is a costly proposition. An alternative to the linear list data structure should be used.

5.1 The AVL Tree for Vertex Merging

With the goal of vertex merging in mind, a linear list is clearly an unacceptable solution for storing the unique vertices. Each time a vertex entity is added, the complete list would have to be sorted and/or searched. Recall that one requirement for vertex merging is that all *equivalent* vertices be merged. This suggests that for a vertex entity to be added, there must be no existing equivalent vertices. Consequently, a range of vertex values in the neighborhood of the search key must be tested. This makes a hash table an unattractive storage structure. A sorted array could be used, but because vertex data is continually being added as each model facet is read, repeated insertions into the array and the block moves which result make this an unattractive solution. A binary search tree could be used; however, the input data ordering is unknown. In the degenerate case, this could be equivalent in performance to searching a linear list of vertex values, and this is unacceptable.

A balanced binary search tree, termed an AVL search tree, overcomes these limitations [11]. It never degenerates to the equivalent performance of searching a linear list because its balance is maintained as each element is inserted in it. It also meets the requirements for being able to traverse through the data and efficiently allow range searching, which is used to determine equivalence within a set numerical round-off tolerance after an initial search value if located.

As each vertex defining a face is read, it is added to an AVL search tree if an equivalent vertex does not already exist in the tree. If the vertex is added, the corresponding vertex reference for the face being added is set to this vertex element in the AVL tree. If an equivalent face exists, the corresponding vertex reference for the face being added is set to the equivalent vertex already in the AVL tree and the vertex data read is discarded. The AVL search tree data structure works well to provide an efficient equivalence detection mechanism for vertices being added. After vertex merging is completed, face adjacency relationships must be determined.

5.2 Searching for Face Adjacencies

Face comparisons are performed in an attempt to locate face adjacencies. Recall that face adjacencies are determined for each face in the model by sequentially stepping through a list of model faces, searching for adjacent faces, and cross-connecting references when adjacencies are located. A linear list of faces provides the ability to sequentially process faces, but it is clearly not the solution for an efficient searching structure.

The structure imposed to effect efficient adjacency searching is simply a list of face pointers attached to each vertex in the model. As new vertices are created or existing vertices are referenced by a given face, the reference value of this face is added to a list of face references for each vertex which defines the face. Consequently, each vertex knows of every face which references it after all model faces have been read from the data file. Searching for adjacencies is greatly simplified using this structure. Instead of searching every face in the model for a face which shares two vertices with a test face, now only the faces contained in the face lists corresponding to the three vertices defining a test face need to be searched.

If for each edge of a test face, all other model faces in a list structure were searched to determine adjacency relationships, this would be of order $O(3n^2)$ where n denotes the number of facets in the model. However, by maintaining for each vertex a list of faces which share it, searching complexity is reduced to an order $O(3nk^2)$ problem where n is again the number of facets in the model and k is the average number of faces sharing each model vertex. Figure 5.1 depicts the data available for a given face and is useful in understanding how adjacencies are determined.
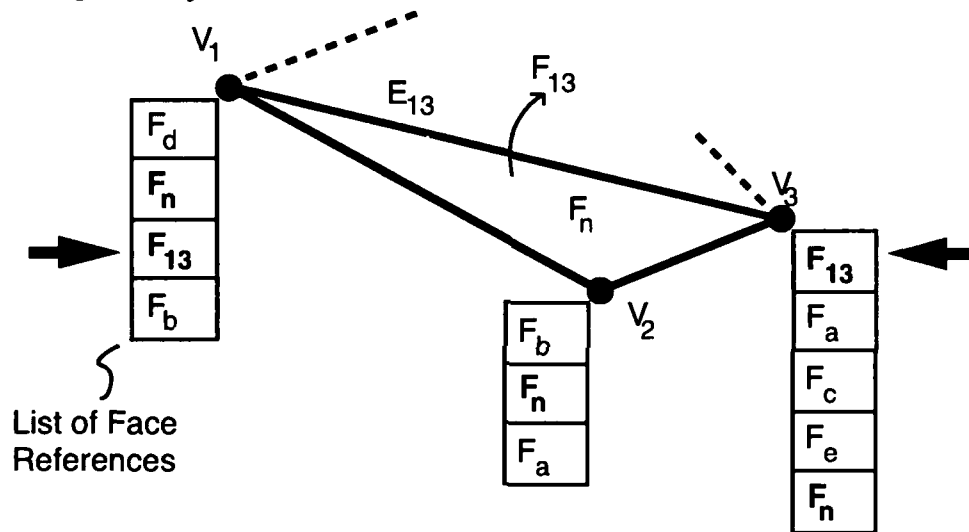

Figure 5.1 - Face Data Used for Adjacency Searching

Consider the searches necessary to locate the facet adjacent to face F_n which shares edge E_{13}. Instead of searching all facets in the model, the search is confined to the lists of face pointers maintained by vertices V_1 and V_3. The reference to face F_n should appear in the three vertex lists; however, there should be one and only one other identical face reference contained in both the face lists for V_1 and V_3. This should reference the face which shares edge E_{13} with the facet F_n under test and is labeled F_{13} in the figure. This provides a useful way to bound the search space which must be traversed each time an adjacency must be sought. Since in most cases, the number of facets in a model far exceeds the number of facets sharing a particular model vertex, this provides a significant reduction in the number of elements which must be searched throughout the adjacency determination process. It is also important to note that only face references, not actual vertex coordinate triples, must be tested during searching. This too contributes to the efficiency of this algorithm.

6 Results & Conclusions

There is a definite up-front cost associated with generating topological information from a "bucket of facets" model representation such as the STL *de facto* standard.

However, an investment in such pre-processing adds information which can be used to realize a healthy dividend in later model processing operations.

6.1 Results

Topology generation, given only a "bucket of facets", can be computationally prohibitive if a brute force approach is taken. Appropriate data structures and algorithms must be used to make topology generation an profitable exercise. An important lesson illustrated by this work is that a marginal increase in storage requirements can effect a significant increase in processing performance.

Storing additional face reference lists for each vertex increases memory requirements; however, it provides a very necessary performance increase. By using an $O(3nk^2)$ algorithm instead of an $O(3n^2)$ algorithm, processing time for model topology generation is significantly reduced. For a model with approximately 82,500 facets, 8.6 CPU hours on a Sun SPARCstation2 were required to generate its topology when the brute force $O(3n^2)$ algorithm was employed. However, the $O(3nk^2)$ algorithm performed the same task in only 9.1 CPU minutes on the same machine. It is important to note that these performance figures are for an ASCII format STL file. Preliminary evaluation of an optimized version of the parser for binary format STL files suggests that the contrast between the brute force and AVL tree approaches is even larger because parse time contributes significantly to the 9.1 CPU minute figure cited above[12].

6.2 Conclusion

Model topology is clearly important for successful model processing, and generating it can be a costly endeavor. Unfortunately, the SFF community's STL *de facto* standard for representing facet models does not support the definition of model topology. It must instead be reconstructed from an unordered "bucket of facets" provided by the STL representation. This requires significant searching through model facet data which is typically very voluminous for real part models. The approach presented in this paper realized better than an order of magnitude performance improvement when contrast to a brute force topology generation approach.

Ideally, topological information should be generated during model tessellation which is most likely performed by a CAD system. This would not only prevent the need to reconstruct it later, but it would also make data transfer more robust and concise. The RPI format demonstrated a significant redundancy reduction while increasing the information content in a file by utilizing topological information [9]. While facet models may fade as the primary representation for future SFF data exchange, topological information and some of the lessons learned from this work will remain important for higher-order geometrical entities such as parametric surface patch models.

Acknowledgments

References

1. "Stereolithography Interface Specification," 3D Systems, Inc., June 1988.

2. Michael E. Mortenson, Geometric Modeling, John Wiley & Sons, Inc., 1985.

3. Stephen J. Rock, "Solid Freeform Fabrication and CAD System Interfacing," M.S. Thesis, Rensselaer Polytechnic Institute, Troy, NY, Dec. 1991.

4. James V. Miller, "On GDM's: Geometrically Deformed Models for the Extraction of Closed Shapes from Volume Data," M.S. Thesis, Rensselaer Polytechnic Institute, Dec. 1990.

5. Donald Hearn and M. Pauline Baker, *Computer Graphics*, Prentice-Hall, Inc., 1986.

6. Kevin Weiler, "Edge-Based Data Structures for Solid Modeling in Curved-Surface Environments," *IEEE Computer Graphics and Applications*, Vol. 5, Num. 1, pp. 21-40, Jan. 1985.

7. Kevin Weiler, "The Radial Edge Structure: A Topological representation for Non-Manifold Geometric Boundary Modeling," in: *Geometric Modeling for CAD Applications*, M. J. Wozny, H. W. McLaughlin, J. L. Encarnacao (eds.), North-Holland, pp. 3-36, 1988.

8. Stephen J. Rock and Michael J. Wozny, "Utilizing Topological Information to Increase Scan Vector Generation Efficiency," in: *Solid Freeform Fabrication Symposium Proceedings*, H.L. Marcus, J. J. Beaman, J.W. Barlow, D.L. Bourell, and R.H. Crawford (eds.), The University of Texas at Austin, Aug. 1991.

9. Stephen J. Rock and Michael J. Wozny, "A Flexible File Format for Solid Freeform Fabrication," in: *Solid Freeform Fabrication Symposium Proceedings*, H.L. Marcus, J. J. Beaman, J.W. Barlow, D.L. Bourell, and R.H. Crawford (eds.), The University of Texas at Austin, Aug. 1991.

10. Kendall Atkinson, Elementary Numerical Analysis, *John Wiley and Sons, Inc.*, 1985.

11. Daniel F. Stubbs and Neil W. Webre, *Data Structures with Abstract Data Types and Pascal*, Brooks/Cole Publishing Company, 1989.

12. Jan Helge Bøhn, Personal Communication, June 30, 1992.

STEREOPHOTOLITHOGRAPHY: A BRAND NEW MACHINERY

A.L. ALLANIC, C. MEDARD and P. SCHAEFFER

I. ALTERNATIVE DEVELOPMENT STRATEGIES (1984-1991):

I.1 LASER 3D S.A. (1991-1992).

Stereolithography (SPL) is only one of the new technologies developed originally and simultaneously in FRANCE (CNRS- July 84. French Patent N° 84 11 241) and in the USA (U.V.P- C. HULL Aug. 84 . USA Patent N°45 75 330) to tackle "Rapid Prototyping" (RP) bottlenecks, as well as faster and better design needs (CAD induced).

SPL applications have developed at different speeds in the USA and in EUROPE, due partly to different patent positions, industrial motivations and market demands. Today in EUROPE (June 92), two companies are proposing very similar SPL machinery systems of what we call first generation SPL/L-S (L-S stands for Liquid- Solid), the 3D SLA 250/500 family (1988-92, USA) and EOS STEREOS 400/600 family (summer 1991-1992, GERMANY). A recent article ("Industries&Techniques"-May 92) underlines the obvious similarities between the two first generation systems.

A third company, LASER 3D S.A. entered the RP field in France in 1991, by acquiring all patents and know-how controlled by the original french team (1984-1991). After analysing with american (1990-1991) and european users (1991-92), the technical constraints imposed by the first generation SPL/L-S machines, LASER 3D has designed (March 92) and is putting on the european market in the fall 92 a totally new technical concept (second generation SPL/L-S Sept 92- Appendix 1) the SPL 1000/LSA using for the first time high power UV lasers (1 Watt). L3D marketing strategy is also entirely new and was requested by several "sophisticated" SPL users who are more interested in CAD Design optimization and product development than in expensive first generation SPL machinery operations. LASER 3D will provide experienced operating SPL personnel that the SPL user won't need to have or train. Users can concentrate on what they know best: their product development and CAD design optimization.

I.2 Alternative development strategies (1984-1991):

Two independent researchers started SPL technologies in 1984: Prof. J.C. ANDRE of CNRS-ENSIC in Nancy and Mr. C. HULL of UVP in California. They followed very different R&D development strategies; Mr. HULL put first a SLA 250 machinery in the field and sold it, making technical improvements along the way (1988-92); Pr. ANDRE did not put the machinery in the field: he built first several prototypes to study the most important physical laws controlling SPL applications (1986-91). Then the new SPL 1000/LSA was finally designed in 1992, taking advantage of both 1/ scientific knowledge accumulated from 1988 to 1992 and also, 2/ of a much broader user experience leading to the definition of a simpler more efficient SOFTWARE architecture.

From 1984 to 1992, continuous research was conducted in the CNRS-ENSIC laboratory in Nancy, not only in the SPL-L/S (photopolymerization of liquid resins), but also in SPL-S/S (solid-solid process using solid films) and in SPL-P/S (powder-solid process or sintering).

In SPL-L/S, photopolymerization was studied with UV, visible and IR light; the best results in terms of ACCURACY and SPEED were obtained with UV light.

SPL-S/S (solid-solid technology) is based on the phototransformation of thin films. FIRST FRENCH PATENT was filed in 1986; new work was conducted and new patents were filed later on, extending the process to cover the use of composite materials, including fillers and/or fibers.

In SPL-P/S (powder-solid technologies), research started in the mid 80's. Many different materials were studied. Today, research is concentrating on CERAMIC MATERIALS.

I.3 Prototypes and concrete results:

Several prototypes were built from 1984-1992, to follow technical advances and to exploit concrete experimental results. We shall only list the most important prototypes below:

<u>1988:</u> First fully automatic SPL-L/S machine using already a high power 500 mW Ar. Ion laser.

<u>1989:</u> More efficient machinery, using galvanometric mirrors and a high power 500 mW Ar.Ion laser. Faster scanning speeds were possible. Software architecture was very flexible, thus allowing to study efficiently a very wide range of working parameters. Many PHD students were trained on this machine between 1989 and 1992 (5 years experience with high power UV Ar.Ion laser).

<u>1990:</u> The feasibility of the SPL-S/S process was fully completed; the first SPL COMPOSITE PART was made. This original work was then developed in 1991, in cooperation with DASSAULT AVIATION, and new patents have been filed worldwide. An industrial machinery could be defined by L3D in 1993, allowing hopefully the construction of large SPL structural parts by 1994. One key process variable still needs to be properly managed to make the process very attractive.

<u>1991:</u> A third SPL-L/S prototype was built to prove the industrial potential of a new recoating process, defined earlier. The interesting characteristic of this apparatus is that the RECOATING TIME is totally masked- i.e the laser is creating a solid material WITHOUT INTERRUPTION. For the moment this prototype is still limited to particular part geometries, but it is possible to extend the principle to other geometries.

A new 1991 prototype machinery was designed , to consolidate earlier work done in powder sintering and to extend earlier research into ceramic sintering applications. Ceramic parts are <u>currently made in 1992</u>. Key process variables are still being assessed before defining a real efficient industrial process SPL/P-S.

261

II L/S TECHNOLOGY: KEY PARAMETERS:

II 1 ACCURACY: importance of resin material

For the Liquid-Solid technology (SPL-L/S) it is very important to work with the proper resin. The problem is to find materials combining several characteristics which are often in opposition (low viscosity and low shrinkage, high reactivity and high conversion degree, etc...). Recent major chemical companies entry in SPL-L/S should (Allied Signal, Grace, Loctite, etc...) make available several new attractive materials with better, more flexible SPL properties. We can hope that industrial materials improvements will accelerate. We will underline below two essential problems, related to resin behaviour, in the Stereolithography process, which are directly linked to the end-product qualities (surface finish, macroscopic accuracy).

II.1.1 Recoating system:

Different recoating systems are working today on several SPL-L/S machines. All of them are leading to liquid surface deformation, and a certain amount of time is needed to obtain complete relaxation of the surface. Experimental work pointed out that the liquid surface deformation is exponentially decreasing with time (see fig.1), relaxation time for a given resin is almost exponentially rising with decreasing layer thickness. Decreasing layer thickness is an objective which controls GOOD SURFACE FINISH.

It is clear that increasing viscosity leads to increasing relaxation times, but resins are not simple rheological materials, and one can sometimes obtain curious results. For example, comparing a 1.2 Pa s acrylate resin, and a 0.6 Pa s epoxy resin, we could observe an inversion point following the relaxation of these two products versus time. Figure 2 shows in fact that in the beginning of the experiment, the lowest viscosity resin (epoxy) is relaxing faster than the acrylate resin, but after this first period, the tendency is inversed. Rheological studies pointed out that the epoxy resin was no Newtonian material (fixed viscosity), but has an increasing viscosity when sterees are decreasing: this explains the surprising observed result.

These two examples are pointing out that the rheological behaviour of resin material is also to be taken into account to define a "good resin" for the Stereolithography process.

II.1.2 Sources of macroscopic deformations:

One of the essential problems in SPL-L/S, is to avoid part deformations due to resin shrinkage. Work has been done to model mathematically this behaviour for a simple part geometry. Figure 3 shows a part composed of two distinct materials: one is non evolutive material (Young modulus E1, thickness e1, no shrinkage), supposed to be simulating the already created layers, the other represents the new layer in formation, having evoluting parameters (Young modulus: E2= 0 to E1, shrinkage S= 0 to fixed arbitrary value, thickness e2). This very simple situation allowed computation of the evolution of the deformation versus time (arbitrary time scale). Figure 4 shows that different final results were obtained (case I, II and III). In fact, different supposed evolutions of E2 versus S, for the same final values of E2 and S, were

simulated. Those different cases are leading to different time evolution of the deformation, but the most interesting result is to point out that the final deformation value is changing.

So it is clear that part macroscopic deformations are **not only related with resin shrinkage** and final mechanical properties, but also depend on the evolution of mechanical parameters during curing. Some resin manufacturers have worked on convergent problems and have designed resin materials with a special curing mode (Rapid Prototyping, Nottingham 6-7 July, pp 163-182), the objectives being to limit the formation of internal stresses during curing.

Figure 5 shows (simulation) that the non isotropic light absorption leads to spontaneous deformations (due to shrinkage). Rheological tests were also performed on the cured material, in particular to study long periods (several months) evolutions (ENTROPIE n°167-1992, pp 51-61).

II.2 INDUSTRIAL CONSTRAINTS:

For a given resin, it is always possible to improve the quality of the parts. For improving **micro-precision**, you "just" have to take the time necessary to reach complete surface relaxation (vertical precision) and to work with a low scanning speed to avoid the inertia problems relative to the beam deflection device (horizontal precision). **Macro-precision** is more difficult to improve, because of the numerous sources of deformations, and because deformations are varying with the geometry of each part: trial-error sequences and users "feeling" are sometimes necessary ingredients to use before reaching the requested accuracy.

The above "pseudo-solutions" are not proper industrial solutions which would like to ultimately reach::

                - Low cost manufacturing

                - "Press-button" machine and repeatability

We will describe below the industrial solutions adopted in L 3D's new machinery, in terms of:
- **Improving process efficiency**
- **Improving manufacturing speed**
- **Reducing user's training requirements (new software concepts)**
- **Reducing operating costs**

III LASER 3D - SPL 1000 /LSA DESIGN: A NEW STEP IN TECHNOLOGY

As described earlier, the french team used several working prototypes from 1988 to 1992, developing a 5 year-experience with high power Ar Ion UV laser (1988-92), assessing experimentally the importance of all major key variables, before deciding to integrate all the accumulated knowledge (1984-92) into an industrial venture, controlled by LASER 3D S.A. in 1991.The industrial entrepreneur LASER 3D made an extensive study of the SPL/L-S market in the USA in 1990-91, assessing the relative strengths of 3D Systems/ DUPONT /QUADRAX/ LASER FARE first generation technologies, before deciding to buy the french second generation technologies and know-how in order to define a completely new product: the SPL 1000 /LSA,

with a new marketing strategy designed to enter in 1993 the existing market of the "sophisticated SPL" users (100 kg/year potential), whose needs are well defined today (1992).The new second generation SPL 1000 /LSA, based on the liquid-solid technology, was designed in 1992, 1) to take into account the most sophisticated American and European SPL users (above 100 kg / year potential) and 2) to use the french 1984-92 historical work.

We redesigned entirely a new machinery and were forced to solve new problems, keeping in mind two coherent objectives:

- **decrease the process costs**
- **increase technical productivity of each technical function.**

Particular attention was taken to the design of a simple, real industrial working tool which does not necessarily require special knowledge and/or experience (software architecture), in order to facilitate market entry and acceptance of this technology by new "users". In particular, the following new software features are included:

Step 1: STL transition
   - Scanning vectors computed during part manufacturing

   ==>   Slice + Merge = 0

                   No necessity for sliced part memorization
   - Pre-processing:

                   - Part preparation while the machine is working

                   - Possibility to see final aspect of the sliced part before manufacturing

                   - Integrated CAD system (if needed), directly related by native format
                     with the manufacturing machine.

                   - New concept: **"styles"**

No parameters, but style selection which AUTOMATICALLY chooses priorities imposed by the part designer (surface finish, geometrical precision, manufacturing speed, etc...)

Step 2:
                   - No need to use STL interface

                   - Creation of native mode interaction with CATIA (1993) and other major

systems (upon request).

III.1 The advantages of a powerful (>1 Watt) laser:

There are two main reasons for using a powerful laser; both reasons are constrained by resin technology (temperature control of an exothermic chain reaction):

   1   Cost of the UV photon
   2   Speed of the SPL manufacturing process

264

1. As we know, the polymerization reaction is economically efficient (it is a characteristic of most chain reactions) : a few Joules only are necessary to solidify 1 cm^3. The historical first generation SPL process uses today essentially UV lasers, which in turn produce some of the most expensive form of energy (Joules).Technical constraints (of laser manufacturing) impose that the cost of the UV energy (UV photon) is relatively less expensive, if and when one uses the most powerful lasers. There is more than a 10 factor between the 25 mW HeCd lasers and the larger useful (several W) Ar Ion lasers in terms of cost of the UV photon, including the investment cost of the laser, the cost of laser usage, and the replacement cost (statistical data given by laser manufacturers). All decisions leading to diminishing the UV photon cost will directly influence the new SPL machinery economic efficiency.

2. We should now underline that if we divide the effective part manufacturing time by 10 to 50, we will dramatically change current historical users outlook on the SPL technology, compared to other alternative RPT. A new user will not hesitate to make several trials before obtaining an acceptable new SPL product, if it takes only one hour to manufacture as opposed to 2 days ! We think that minimizing manufacturing time is not only important to minimize direct manufacturing cost, but also and most importantly, it is very important for allowing efficient trial/error sequences, which in turn will open faster new markets. In the fall 1992 we are putting on the market the SPL 1000/ LSA which should be around 10 times faster than actual competitors in recoating time (Appendix 1 line 5). Third party users will be able to make parts before the end of 92 on the SPL 1000 /LSA.

We are preparing, for 93 and/or as soon as our patents position is well established worldwide, a much faster version , the SPL 1000/LSB, which will again increase manufacturing speed as per the industry's numerous requests (International Conference on Rapid Prototyping, Dayton OH, pp.191,196).

III.2 Major problems associated with using high power lasers:

Except for the very low 0-10 mW range where inhibition problems occur in the photochemical reaction, the essential parameter governing the solid creation is the ratio laser **power/ scanning speed**. This means that if you increase the laser power you have to increase simultaneously the scanning speed to obtain the same results in terms of geometrical results (for a given spot size: brightness and depth of the polymerized line). In the case of a 1 Watt laser, the speed of the displacement of a typical 150 micrometer spot size required to bring up correct SPL parts is near 20 m/s (10-50 range), depending on the reactivity of the resin. Galvanometric technology is now capable of providing such scanning speeds, keeping proper accuracy in line (two years ago the problem of galvanometric mirrors inertia was drastically limiting the technology). We shall be using a 1 Watt laser this fall in Nancy. New patents have been filed (1992); they will allow the use of the most powerful commercial lasers available today on the market (7 Watts) for our 1993 SPL 1000 /LSB machinery. The increase of scanning speed is of course directly related to the speed of the SPL manufacturing process, but the efficiency of the

process should not be considered only in terms of scanning speed. In fact, the following figures will underline that in the liquid-solid technology, the most important source of inefficiency is linked to the recoating system (new patents pending):
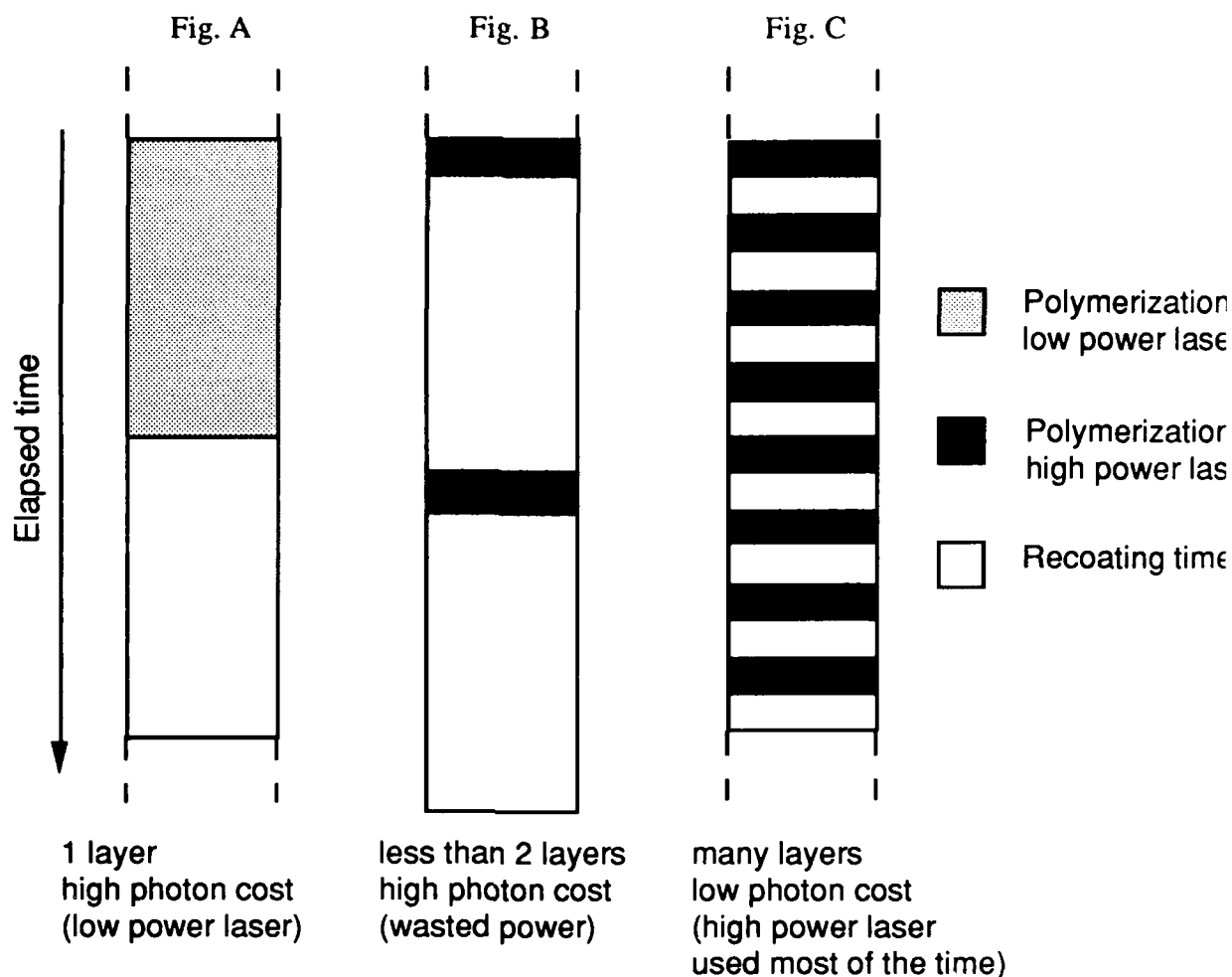

Fig. A   Fig. B   Fig. C

Polymerization low power lase

Polymerizatior high power las

Recoating time

1 layer
high photon cost
(low power laser)

less than 2 layers
high photon cost
(wasted power)

many layers
low photon cost
(high power laser
used most of the time)

Fig. A shows that a small laser is properly dimensioned in the historical first generation SPL technology. One could therefore say that, given the current artificial constraints, first generation machinery is properly (not efficiently) defined.

In Fig. B, one can see that a high power laser (even infinitely powerful !) could only improve actual historical SPL global manufacturing speed by a factor of around 2; hence one could say in that sense (artificial historical constraints) that high power lasers are "inefficient" !

Fig. C is the proper objective for combining A and B: if one wants to obtain the "efficiency" of Fig. A, and the power usage of Fig. B, one must "balance" Tl and Tp durations (Tl: time required to lay an elementary layer, Tp: polymerization time).

That is why, while increasing laser power, one must dramatically diminish the minimum time required to properly lay an elementary layer, and this minimum time must be "almost" independent of layer thickness. The new second generation SPL 1000 LSA does include software adaptations and a new concept for installing properly elementary layers; our new second generation machine is designed as shown in Fig. C.One important additional point is

that the recoating time is "almost" independent of the viscosity of the resin; we can also therefore use low shrinkage viscous resins without being penalized by the recoating process. The use of low shrinkage viscous resins is interesting for limiting MACROSCOPIC deformations.

III.3 Other necessary improvements:

Most software preparation work imposed by the historical first generationSPL systems is in general (exceptions are possible) relatively small, hence not important, when compared to the part global manufacturing time.This "relatively small" preparation time for the historical SPL technology (in absolute terms compared to other RPT) is too high for the new concept SPL technology.

Slice + merge	< 10 %		Slice + merge	> 50 %
Fabrication			Fabrication	
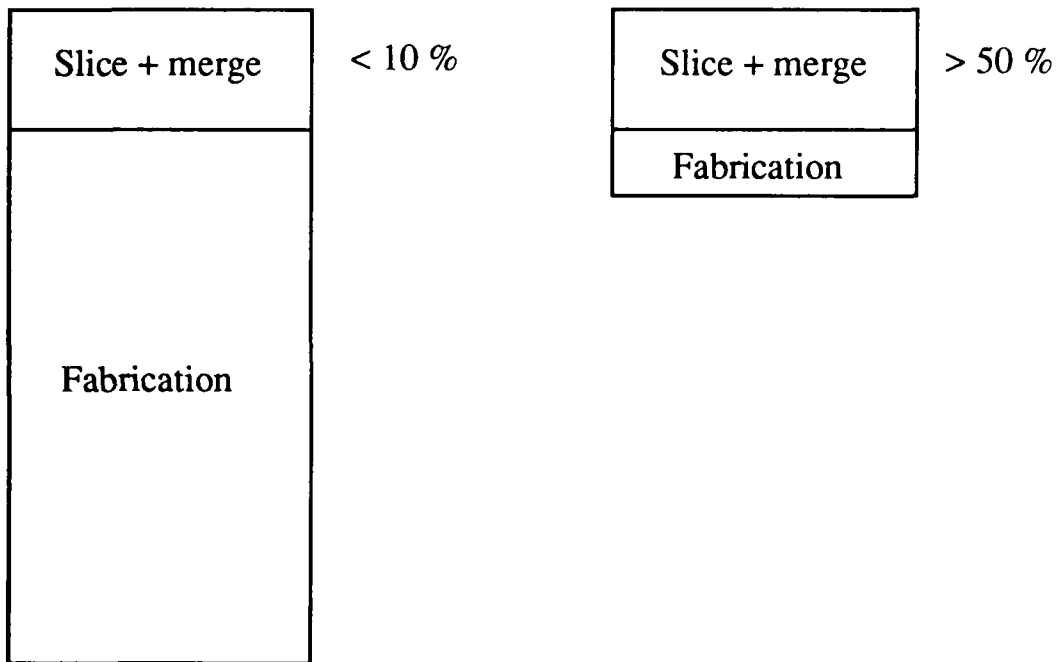
Therefore, if one wants to take advantage of a powerful laser, one must also define a new manufacturing strategy, where the new bottlenecks are properly managed. One must improve all manufacturing sequences by at least the same efficiency factors as the expensive increase in laser power. This imposed very substantial new SPL software design, and explains the reason why the second generation SPL 1000 /LSA is using much more powerful computers than the first generation SPL systems.

III.4 New solutions for the SPL 1000/LSA:

1 Access to efficient mirrors systems which allow the use of high UV laser power currently well above 1 W (up to 7 Watts)

2 A brand new concept (patents pending) for installing properly elementary layers

3 New SPL software (patents pending) allows, in particular, to prepare a new part during the manufacturing sequence of the preceeding one, to see the final aspect of the sliced part, to avoid adjustments of several parameters ("STYLES").

4 The mathematical slicing of the part takes place in parallel with (not before) the manufacturing sequence, which gives two additional advantages :

4.1   slicing time is strictly zero
4.2   No need to store "in advance" all computations necessary to define the SPL part.

Conclusions

The new SPL concept SPL 1000/LSA, integrating the whole knowledge of 5 years of experimentation, using high power lasers (> 1 W), leads to a new step in SPL technology, as can be underlined by comparing the historical (1988-91) and the new (1992) SPL technology :
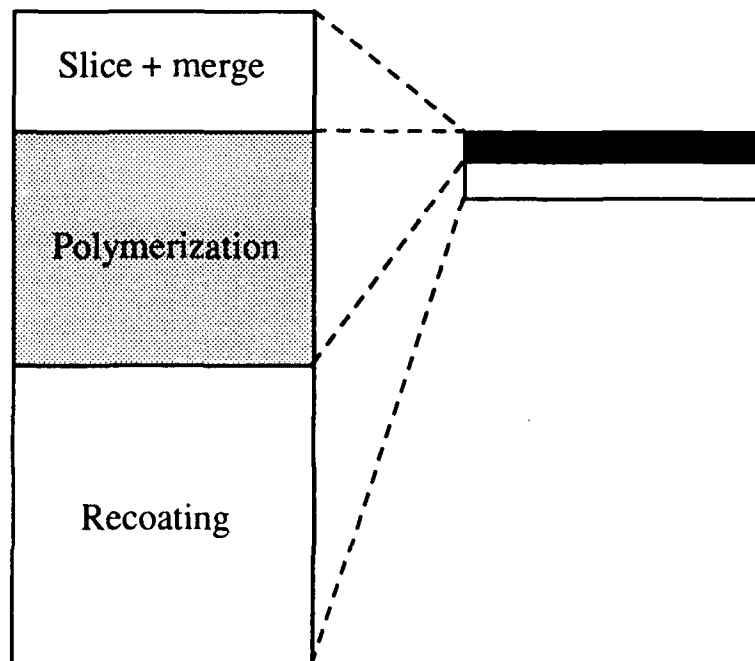
APPENDIX 1: Technical specifications: comparative summary

	EOS 400	SLA 500	SPL 1000 LSA
Laser power (mW) +	25 to 300	200	>1 Watt
Maximal dimensions of the parts (cm3)	40x40x60 *	50x50x60 **	50x55x65 *
Typical scanning speed (m/s) +	1 to 10	2.5	10 to 50 (Typ. 20)
Spot location (micrometer)	±50	±65	±50
Recoating time (s) +	30 to 60	30 to 60	3 to 6
Minimal layer thickness + (micrometers)	100	127	<50
Slicing computer + (Mips/ Mflops/ SPEC)	26/ 4.6/ 20	option	58/ 12/ 50
Graphical performances + (vect. 3D/ s)	<220 000 °	option °	1 150 000 ∞
Sliced parts memorization + (Mbytes available)		40	not necessary
Process control computer	486	386	486/ 33MHZ

*   Removable

**   Not removable

°   No possibility to see the final aspect of the sliced part

∞   Possibility to see the final aspect of the sliced part

+   NEW CHARACTERISTICS: Second generation SPL- 100% improvement or above

FIGURES
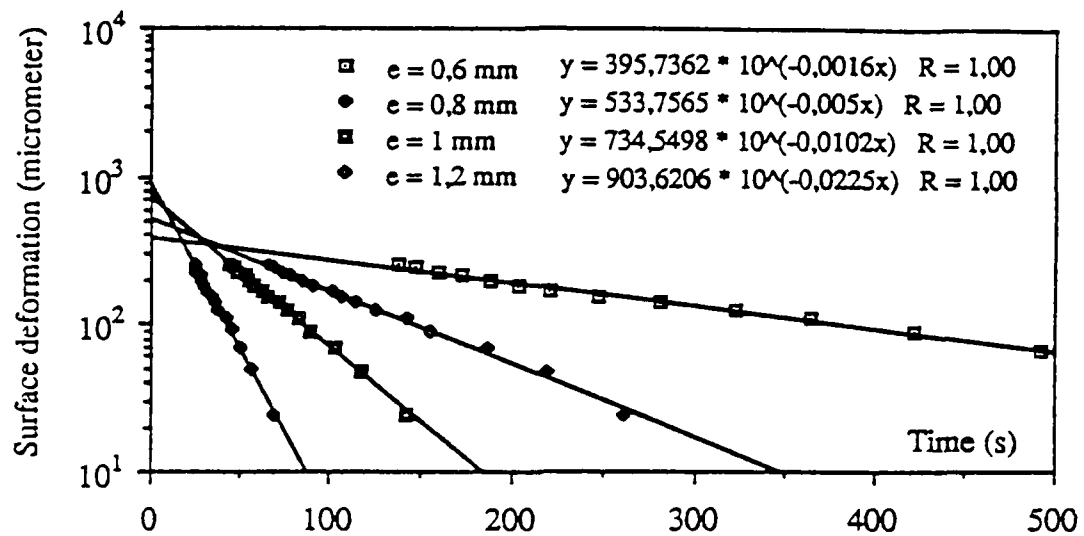
FIG. 1: Surface relaxation versus time for different layer thickness (e)
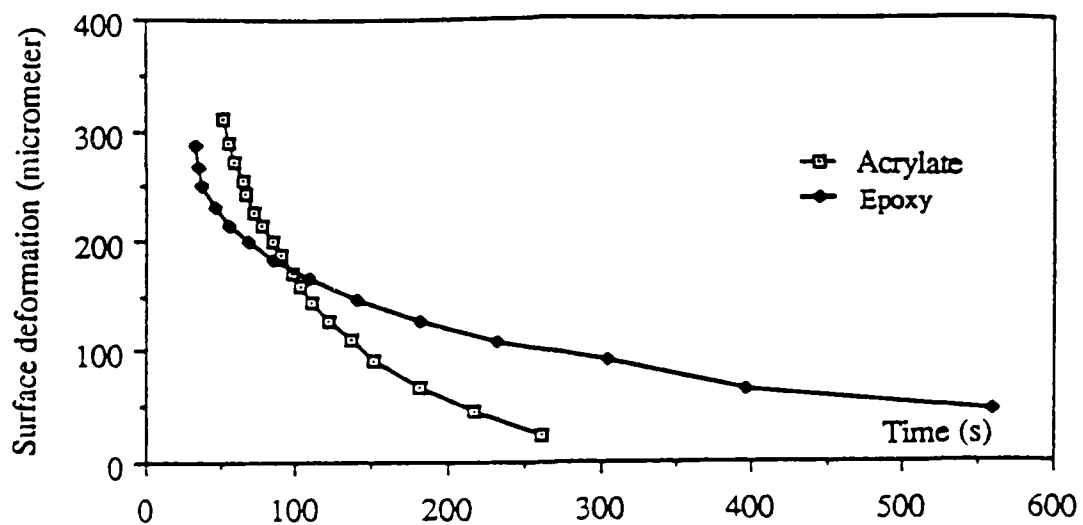
FIG. 2: Surface relaxation for two different resins

— — — — Initial state
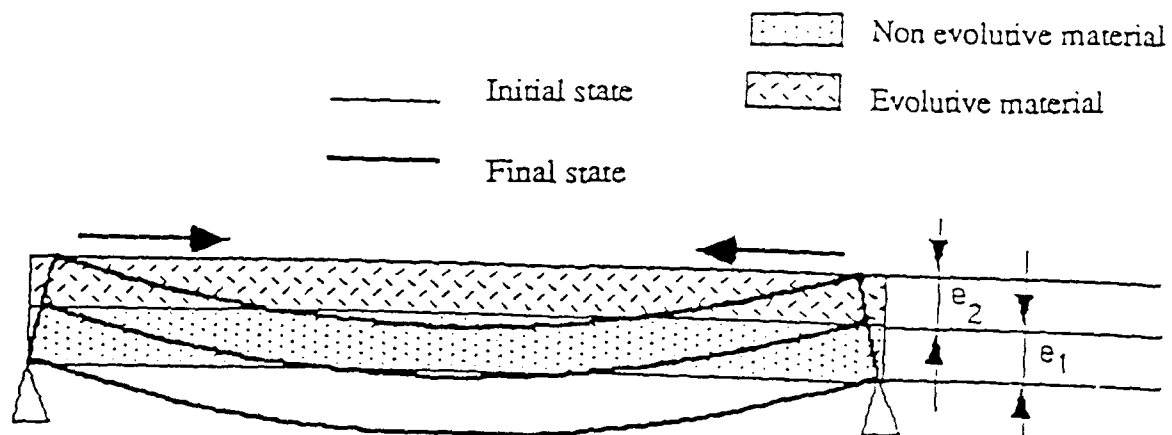
——— Final state

FIG. 3: Deformation induced by resin shrinkage (Simulation)
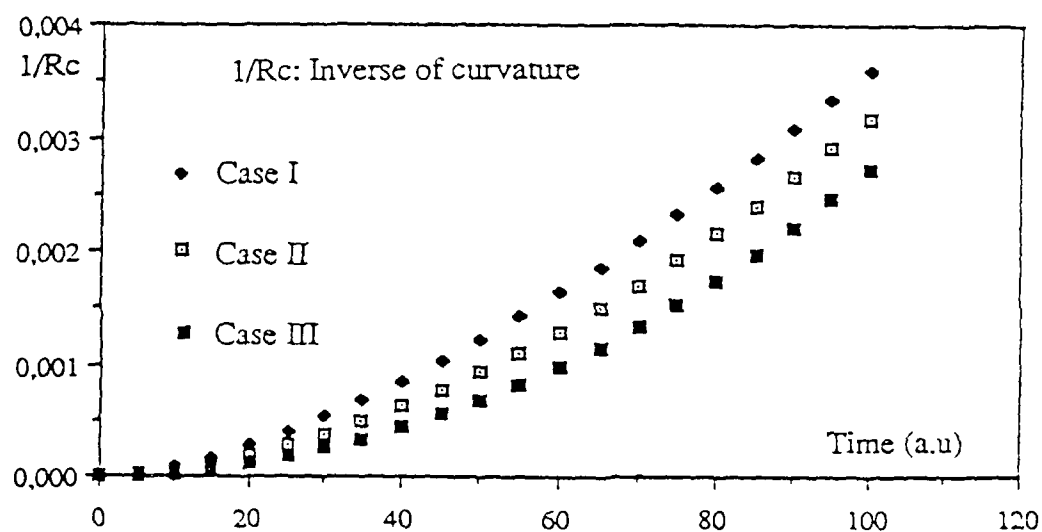

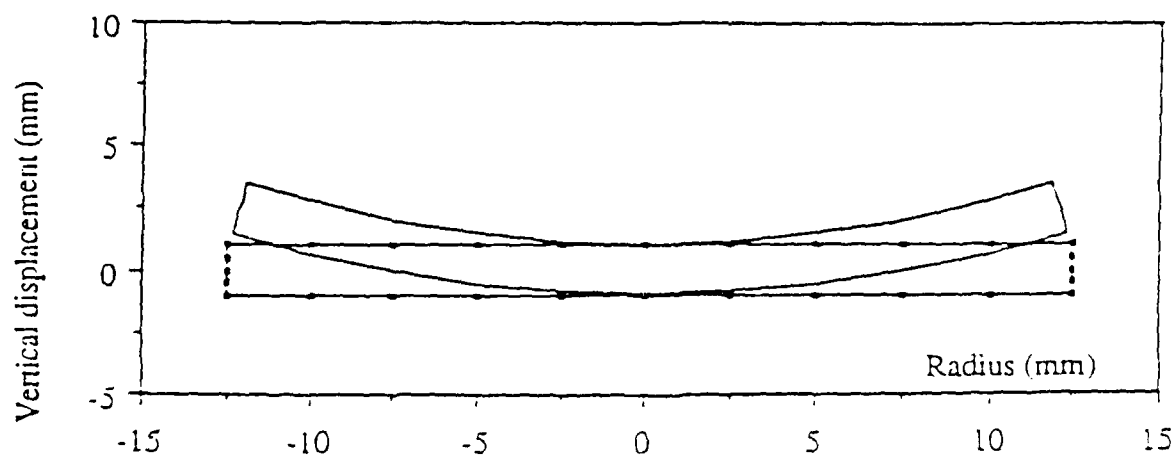
FIG. 4: Different time evolution cf the deformation

FIG. 5: Spontaneous deformation due to gradient effects (circular plate, simulation)

Manufacturing mechatronics using thermal spray shape deposition

James E. Beck, Fritz B. Prinz, Daniel P. Siewiorek, Lee E. Weiss

Engineering Design Research Center
Carnegie Mellon University

Abstract

A new technology for manufacturing mechatronics is described. The technique is based on recursive masking and deposition of thermally sprayed materials. Using these methods, mechanical structures can be created that embed and interconnect electronic components. This results in highly integrated mechatronic devices. A simple, electromechanical artifact was designed and produced to assess the feasibility of these techniques. The details and limitations of this project will be discussed. Areas of future research are identified which are aimed at realizing the full potential of this emerging manufacturing process.

Keywords: Mechatronics, Thermal Spray.

Introduction

The phrases "solid freeform fabrication" and "shape deposition" are synonymous. They refer to the process of creating a physical artifact by incrementally and selectively depositing material in thin, 2-1/2 dimensional layers. Shape deposition can be done in many ways. Most methods, however, have focused on single material applications. The MD* process [1,2,3] is a thermal spray shape deposition system. In this process, thermal spray methods (i.e. plasma, electric arc, or combustion) are used to deposit thin, planar layers of material. Each of these layers is carefully shaped using disposable, laser generated masks. The artifact being produced is grown as a succession of thermally sprayed, cross-sectional layers within a sacrificial support structure.

The MD* process is driven by a 3-D CAD model of the artifact being produced. This model provides a complete spacial representation of the part, and is generated using the NOODLES CAD environment [4]. Next, the CAD model is sliced, and the slices are used to generate files that control the laser mask cutting station [7]. Each mask that is generated corresponds to a slice of the CAD model. A semi-automated version of the MD* process has been implemented which includes two stations: a laser mask cutting station and a thermal (electric arc) spray station. Masks are manually transferred between stations. This system was used to create a prototype turbine blade shape which established these techniques in the mechanical domain.

The MD* masking system also allows selective material deposition within each layer. As a result, multi-material artifacts can be produced in an integrated fashion using a single process. This type of artifact represents a much broader class of applications which is no longer limited to the mechanical

domain. Consequently, a methodology was conceived for manufacturing complete, integrated electromechanical assemblies [1,2]. One possible implementation of an MD* system for manufacturing multi-material, composite parts is shown in figure 1 [1].
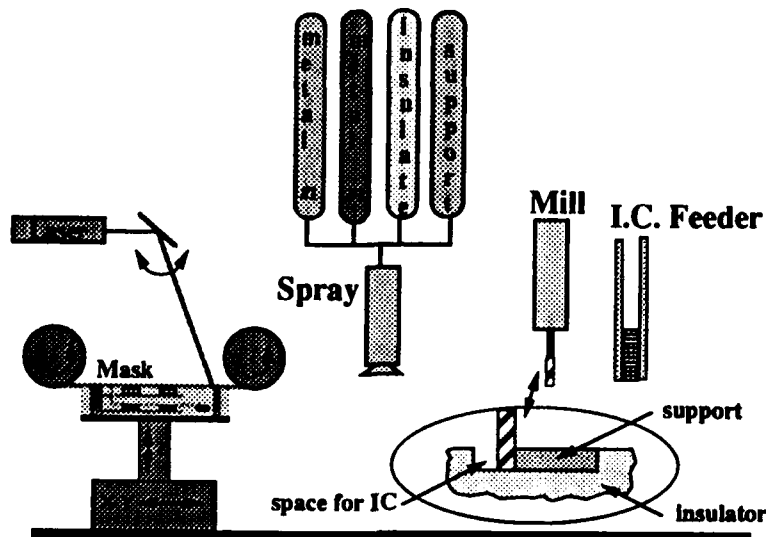

FIGURE 1. Envisioned MD* System

One class of multi-material, composite parts which could be produced with MD* is mechatronics. Mechatronics is a term for a new type of hybrid system component that performs both mechanical and electronic functions [5]. These parts contain embedded electronic components, and have become especially pervasive in the automotive industry. Manufacturing these components traditionally involves separate production of the electronic circuits and the mechanical structures. The electronic and mechanical sub-assemblies are then coupled to form the final part. The research described in this paper is aimed at using MD* to manufacture mechatronics in an integrated way. With this approach, a single manufacturing process is used to perform concurrent fabrication in the mechanical and electronic domains. The direct advantage of this is a high degree of integration not available using the traditional approach. This also accommodates high density, conformable embedded circuitry since three dimensional electronic part placement and interconnection is possible. Furthermore, since a single manufacturing process is used which is driven by a single CAD representation of the composite part, concurrent, multi-domain design is supported.

To demonstrate the feasibility of using MD* to manufacture mechatronics, a simple electromechanical artifact was designed and produced. A version of the familiar, hand-held "simon" electronic game was chosen to be implemented. This game consists of a mechanical housing that contains a reset button, two play buttons and two LEDs. The LEDs are lit in a pseudorandom sequence which must be duplicated by the user via the play buttons. Physically, the device consists of an insulating housing and embedded electronic components that are interconnected using two planar routing layers. This device was ideal for our purposes because of its balanced electrical and mechanical requirements and modest complexity. The "simon" game that was produced is shown in figure 2.
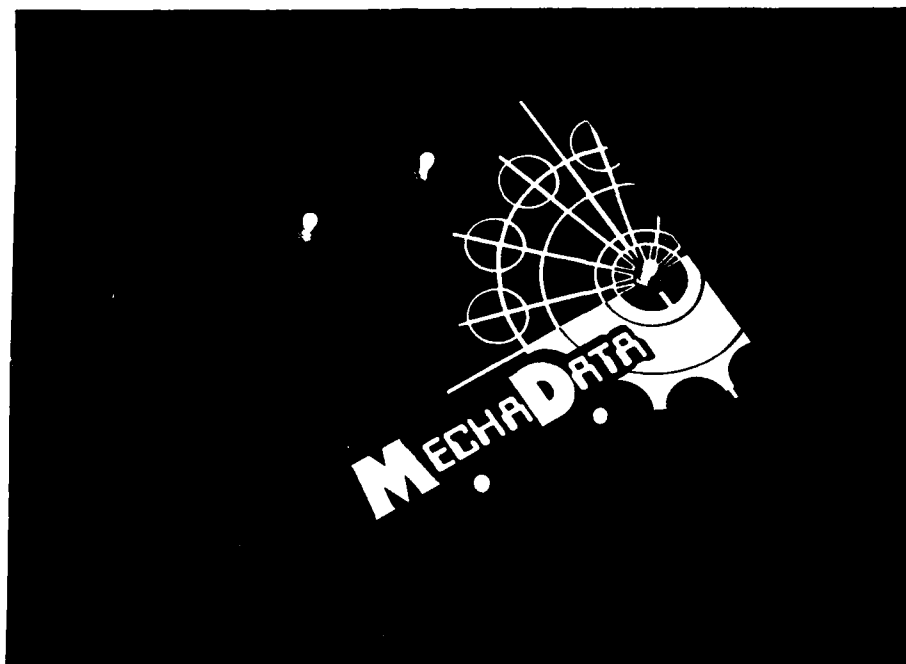
FIGURE 2. "Simon" game

Producing a device of this nature requires design in multiple engineering domains as well as enhancement of the MD* manufacturing process. The manufacturing process was extended to allow electronic components to be embedded and interconnected into a mechanical structure. The multi-domain design effort was largely dominated by design in the electronic domain since this was the first time that the linkage from a physical electronic design to MD* manufacturing had been attempted. These research thrusts proceeded concurrently and are described in detail in this paper.

Fabrication Process Experimentation

Manufacturing the "simon" device required deposition of both metallic and insulating materials. The current spray station, however, is only equipped to perform electric arc and flame spraying. Electric arc spray techniques can only be used to deposit metallics. Insulating materials can be deposited using flame spraying, but the flame destroys the masking material and has a high potential for damaging embedded electronic components. This prompted the decision to use a castable insulator to form the mechanical housing of the "simon" game. In the future, however, the MD* system will be equipped to support plasma spraying which can accommodate a wide range of materials and masks. As another alternative, it may be possible to deposit the castable insulators using non-thermal spray techniques. Castable insulators are formed by combining fast-curing resin and hardener materials. These materials can easily be atomized and mixed in a spray system. Experimentation with these techniques has not yet been completed.

Little information existed concerning the electrical characterization of sprayed conductors. Initial experimentation was done to gauge the feasibility of using sprayed conductors in the "simon" device. Although these experiments were not extensive, preliminary results indicated that thermally sprayed zinc conductors, 0.004 inches thick, 0.10 inches wide and greater than 20 inches in length, were capable of carrying digital signals in excess of 25MHz. Furthermore, these results were robust with respect to

manufacturing process variations such as atomization gasses and particle velocities. Although these results are not conclusive in the absence of a complete characterization, they proved that sprayed zinc interconnections were more than adequate for the "simon" design.

Experimentation was also done to establish a method for embedding electronic components in insulating material and spraying interconnections to the exposed leads. The ability to spray 3-D interconnections was hindered by the absence of a sprayable insulator. The decision was therefore made to only allow planar layers of sprayed interconnections. To provide multiple interconnection layers between components, "vias" were needed to interconnect the planar sprayed layers. These "vias" were inserted as discrete components. On a given plane, sprayed connection was made to an inserted "via" which provided a conduction path to other planar layers. In this way, all intra-layer connections were thermally sprayed and all interlayer connections were formed with inserted "vias". Furthermore, all sprayed connections to the leads of embedded components other than "vias", such as resistors, capacitors and integrated circuits, were restricted to the first planar sprayed layer. All subsequent sprayed layers were used to interconnect vias.

Initial experiments with the use of "vias" showed that shadowing effects degraded the quality of the electrical connection. Inserted "vias" were necessarily longer than the leads of other embedded components, since they must extend through the insulator to the next layer of sprayed interconnections. The length of the exposed "via" impeded the flow of the sprayed material causing a void (i.e. shadow) near the interconnection interface. To combat this, insulator layer thickness (i.e. "via" height) and "via" lead diameter were kept to a minimum.

Design Flow

The primary design goal in the electronic domain was maximum functionality for minimum physical part count. This motivated the decision to use programmable logic devices (PLDs) and a traditional design methodology rather than synthesis tools.

The gate level design was completed first. This provided a baseline for the electronic complexity. At this point the game was pruned from four buttons to two, and the decision to use two, twenty-four macrocell PLDs to implement the logic was made. The selection of the PLDs was also based on assumptions about the manufacturing process. The method developed for interconnecting embedded components restricted the type of integrated circuit packages that could be used.

A commercially available software package was used to generate the programming files for the PLDs. Input files were manually translated from the gate-level design. Test vectors were written and the design was thoroughly simulated. Slight modifications were made in the design between the gate level and the PLD representation. This is largely explained by modifications that were made to fit the design into the two PLDs. Behavioral constructs were favored that closely matched the PLD macrocell architecture.

Functionally, the "simon" circuitry consists of a clock generator, reset circuitry and a clocked, sequential circuit. The sequential circuit was implemented with the PLDs. Specifically, the sequential circuit consists of eight functional blocks controlled by a finite state machine. One of the functional blocks was a linear feedback shift register that was used to generate the pseudorandom lighting sequence. A free-running counter that was enabled during the reset state was used to generate a random seed. Other functional blocks were included to capture button depressions made by the user and compare them to the lighting sequence. Other counters were included to track the

length of the lighting sequence, the state of the current sequence and a visible delay for displaying and blanking the LEDs. The finite state machine was a Mealy type and contained fourteen states.

Because time was an issue and the number of physical parts and signals was small, part placement and routing was done by hand. One layer of planar part placement was assumed. Two levels of planar interconnections were assumed. The first interconnection level consists of electrical signals while the second level includes power, ground and battery cable connections.

The physical design was completed next. This was done by creating 3-D models of the electronic parts and 2-D models of the interconnection layers. These models were constructed using the NOO-DLES user interface DISH. These models were entered into the CAD tool manually, by adding dimensional information to the part placement and routing. The NOODLES models of the two interconnection layers were extracted and sent to the laser mask cutting station. Masks of the interconnection layers were produced that were later used to manufacture the device. NOODLES models of the interconnection layers are shown in figures 3.
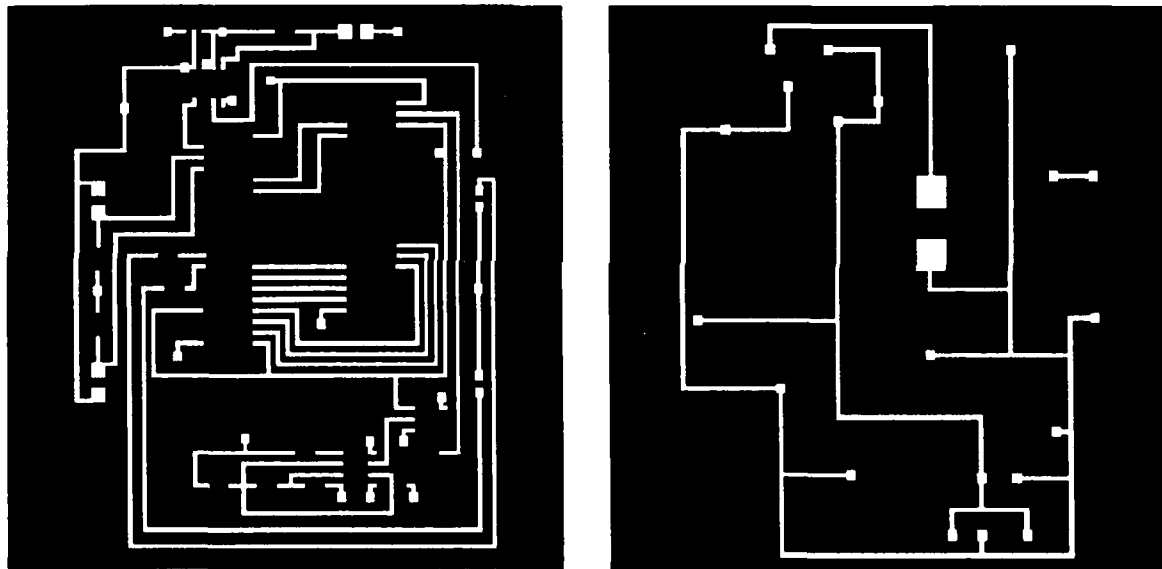

FIGURE 3. NOODLES models of interconnection layers. Left: layer 1. Right: layer 2.

The circuit which implements the simon game is a regulated, 5V digital synchronous circuit with a maximum internal frequency of 2 kHz. Physically, the simon circuit contains the following components:

- One (1) reset button
- Two (2) play buttons
- Two (2) play LEDs
- One (1) voltage regulator (3-pin SIP)
- Two (2) EPLDs (40-pin DIP)
- One (1) "MicorMonitor" IC (8-pin DIP)
- One (1) timer (8-pin DIP)

- One (1) counter (16-pin DIP)
- One (1) 9V battery cable
- Seven (7) resistors
- Three (3) capacitors

The design flow for the simon game was chosen to match the complexity of the device. More complex designs may warrant the use of design synthesis tools, such as MICON [6] rather than traditional, manual design. Automated placement and routing tools would also be a benefit, as well as an enhanced NOODLES interface. The NOODLES representation of the physical design is linked directly to the MD* manufacturing process and provides the final target for design synthesis tools. Once a design has been represented in NOODLES, the manufacturing steps are generated automatically.

With the MD* process, design of the mechanical structure can be done directly in NOODLES. Two factors limited the mechanical structure of the "simon" design. The first was the decision to use a castable insulator for the bulk material, thereby limiting geometries. Secondly, conservative decisions concerning the manufacturing process and placement and interconnection of embedded parts drove physical design in the electronic domain, thereby dictating the rectangular solid shape of the final artifact.

Manufacturing Steps

Once physical design of the "simon" device was completed and MD* had been extended to accommodate embedded electronics, manufacturing commenced. This section will describe the steps used to produce the "simon" game.

First, an aluminum mold was made for the castable insulator. This mold was used to house the growing device and also acted as a support frame for spraying. Next, a thin (1/8") face plate was cast using the mold. Switches and LEDs were mounted to the face plate, and discrete components such as resistors and capacitors were attached to the underside. The mask for the first layer of interconnections was used to determine part placement. Integrated circuit packages and "vias" were also inserted in this manner. A total of twenty-two electronic components and eighteen "vias" were needed for the "simon" circuit. Before proceeding, the circuit was completed using microclips and functionality was verified. All of the circuit components were then embedded by casting another layer of insulating material onto the underside of the faceplate. Only the component leads were visible, and they were trimmed to a uniform height. Again, "vias" were naturally longer; once the first layer of interconnections are complete and embedded, the via leads must still reach through the insulator and be exposed so they can be connected in the next sprayed layer.

To prepare the material for thermal spraying, the insulating material and exposed leads were grit blasted. Initial experimentation showed that grit blasting increased the adhesion strength of the sprayed interconnections. The mask for the first layer of interconnections was then applied over the exposed leads to the grit blasted surface and the first interconnection layer was sprayed (see figure 4). At this point, microclips were again used to complete the circuit and test functionality. Once functionality was verified, another layer of insulator was cast which embedded the sprayed interconnections so that only the "via" leads were exposed. The 9-V battery cable was also inserted at this time.

The second sprayed layer of interconnections was needed to interconnect the exposed "vias" and the battery cable. The surface was once again grit blasted. Care was taken not to damage the battery cable. Next, the mask for the second interconnection layer was set in place and the spray process was repeated. The battery was attached and functionality was confirmed. The final step was another cast layer of insulating material to embed the exposed interconnections. At this point the buttons and LEDs were accessible from the initial, top surface, and the battery cable protruded from the final, bottom surface.
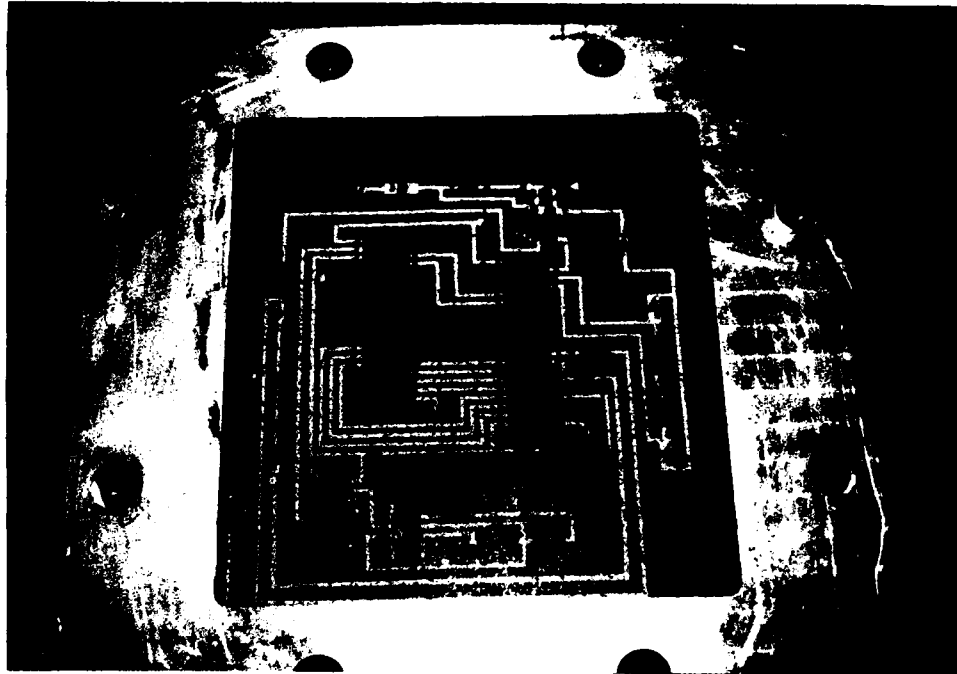
FIGURE 4. Sprayed Interconnections: Layer 1

Conclusions

The simon experiment successfully demonstrated the ability to embed and thermally spray electrical connections between electronic components. Although the insulator that was used was cast and not sprayed, adequate techniques do exist to deposit insulators. Adaptation of the simon manufacturing process to include sprayed insulators will provide a novel, integrated method of manufacturing mechatronics.

To narrow the gap between the vision and reality of MD*, research spanning many disciplines is required. In the material science domain, research is needed to increase and identify the spectrum of sprayable materials for multi-material, composite devices. This should be accompanied by an analysis and taxonomy of material properties that affect thermal spraying.

In the mechanical domain, experimentation with the masking scheme is needed. This would assuage the use of multiple materials per layer, where a planar surface is a concern. Also, finer masking geom-

etries are desirable. This is especially true in the context of embedded electronic circuits, considering the densities afforded by existing electronic packaging techniques. Another issue is thermal properties, including heat dissipation and accommodating the CTE (Coefficient of Thermal Expansion) range of various materials. For more complex devices, the thermal environment of the embedded electronic components must be insured for reliable operation.

In the electronic domain, more thorough characterization of sprayed conductors and connections is warranted. A comparison should also be made to existing approaches such as printed circuit boards and hybrid circuits, which clearly set the standard regarding minimum acceptable circuit density. Ultimately, the MD* approach will allow arbitrary 3-D placement and interconnection of embedded electronic components. This illustrates a potential not inherent in existing approaches. Other areas of research include thermally sprayed circuit components such as high precision resistances and capacitances. The architectural implications of creating fully embedded circuit assemblies should also be explored. These include concerns regarding partitioning, modularity and serviceability.

One of the key advantages of the MD* manufacturing system is that a direct link is provided between a CAD tool design representation and a single, integrated manufacturing process. Software development is needed to strengthen the links between domain-specific CAD tools and the final NOODLES representation.

Acknowledgments

References

[1] L. Weiss and F. B. Prinz. A conceptual framework for a masks and deposits thermal spray shape deposition system. in *DARPA Workshop on Manufacturing*, Univ. of Utah, Feb. 1991

[2] L. Weiss, F. B. Prinz, D. P. Siewiorek. A framework for thermal spray shape deposition: The MD* system. in *Solid Freeform Fabrication Symposium*, Univ. of Texas at Austin, Aug. 1991

[3] L. Weiss, F. Prinz, D. Adams. Solid freeform fabrication by thermal spray shape deposition. in *ASM International Thermal Spray Conference*, Orlando FL, Jun 1992

[4] A. Sudhalkar, R. Bhargava, R. Mattikalli, J. Chen. An Introduction to the NOODLES Geometric Modeling System (Version 7). in *Technical Report*, Carnegie Mellon University, Pittsburgh PA, Oct 1990

[5] L. Berardinis. Mechatronics: A new design strategy. in *Machine Design*, Apr. 26, 1990

[6] W. P. Birmingham, A.P. Gupta, D. P. Siewiorek. *Automating the Design of Computer Systems: The Micon Project.* Jones and Bartlett, 1992.

[7] R. Merz, F.B. Prinz L.E. Weiss. Planning Mask Cutting for Thermal Spray Shape Deposition. in *Technical Report*, EDRC 24-74-91, Carnegie Mellon University, Pittsburgh PA, 1991

RAPID PROTOTYPING USING 3-D WELDING

Dr P M Dickens, Dr M S Pridham, Dr R C Cobb, Dr I Gibson and Mr G Dixon

Department of Manufacturing Engineering and Operations Management,
University of Nottingham, UK.

Introduction

Rapid prototyping systems are based, almost exclusively on polymer, or paper materials. The dimensions of the parts produced are limited by the volume of the processing area within the machine, and parts tend to warp or distort due to shrinkage and lack of support. Also the mechanical properties of the part are restricted to those of the processable materials and thus, in many cases, required 'engineering properties' cannot be obtained.

Various European organisations are undertaking research to produce metal prototypes directly, for example, one project is concerned with a version of Laminated Object Manufacturing where sheets of steel are laser welded together. There are also a number of organisations using laser sintering to produce parts in Mild Steel and Stainless Steel.

At Nottingham, work on Rapid Prototyping systems, based on a 3-D welding system, has been undertaken to try to combat some of the weaknesses of the other processes. There is some history of the use of welding as a means of building up components and parts for salvage and reclamation; thicknesses up to 50mm being typical (1). The use of welding for creating free standing shapes was established in Germany in the 1960's (2). This led to companies such as Krupp, Thyssen and Sulzer developing welding techniques for the fabrication of large components of simple geometry, such as pressure vessels which could weigh up to 500 tonnes (3). The technique was to become known as 'shape welding'.

Other work in this area has been undertaken by Babcock and Wilcox (4) who have been working mainly on large components produced in austenitic material. Also, work by Rolls-Royce (5) has centred on investigating the technique as a means of reducing the wastage levels of expensive high performance alloys which can occur in conventional processing. They have successfully produced various aircraft engine parts in Nickel based and titanium based alloys.

As a production technique, 3-D welding offers significant advantages over conventional processing, these include:

-    The potential for robot control of the welding torch allowing large variation in part dimensions and geometry.

-    A highly automated system.

-    Parts with consistent properties.

-    Rapid processing times, hence vastly reduced development times.

-    Efficient use of materials.

-    Direct production of a metal part - unique amongst current Rapid Prototyping.

3-D Welding Trials

Initial work on 3-D welding, verified the potential of welding as a Rapid Prototyping system. The first parts produced by robot welding were simple unsupported vertical walls in a square box formation (figure 1). The successful completion of these parts led to trials involving the production of sloping walls in the form of a truncated pyramid (figure 2).

Once it was established that more complicated structures were possible, a thermostat housing for a Ford automobile was obtained and the robot programmed to manufacture this shape. Firstly the base and body of the housing was produced and then rotated through 90° to weld the outlet (see figure 3), this required 22 minutes of welding. This proved the ability to manufacture parts that would normally be produced by casting. A sheet metal part was chosen next and figure 4 illustrates the original part with the welded version alongside. As there was more material in this part, the welding time was longer, at approximately 3 hours.

Effect of Welding Parameters on Weld Bead Characteristics

The shape and dimensions of the weld bead are very important in the use of 3-D welding as a Rapid Prototyping system, since these will determine the limits to the wall thickness which may be produced and will also influence the quality of the surface finish.

Numerous trials were undertaken to produce single weld beads for a range of welding conditions. The parameters which were varied included voltage, wire feed rate, wire stickout, wire diameter and welding velocity. The arc voltage and welding current under each condition was monitored and the dimensions of the bead produced (height and width) were subsequently measured using a shadowgraph technique. A vast amount of data was generated in this way, but the general trends are presented in Table 1.

Increasing Variable	Effect on Measured Variable			
	Arc Voltage	Current	Bead Width	Bead Height
Voltage	↑	=/↑	↑	↓
Wire Feed	↓	↑	↑	↑
Stickout	↑	↓	↓	↑
Wire Diameter	↓	↑	↑	↑
Velocity	=	=	↓	↓

Table 1 - Effect on Measured Variables

The shape of the weld bead can be controlled to change it from a wide-flat bead to a more narrow bead with vertical walls (see figure 5). When thin walls are to be produced then the best results are achieved by using a narrow bead, however, there are many situations where beads will need to be placed along side each other and so a variety of bead shapes could be used, depending on the slope of the wall surface (see figure 6).

This work has produced information to start constructing a welding database but further work is required, areas such as the effect of multiple layers on weld bead dimensions, require further investigation, even though wall smoothness has improved (see figure 7).

Materials

As one of the main advantages of this technique is the direct production of a metal part, it is very important to confirm the mechanical and structural properties of parts produced in this way. To do this, a programme of mechanical and microstructural examination was undertaken. Using typical operating parameters and mild steel welding wire based on Fe-C (0.08%) - Si:(0.9%) Mn(1.5%), square box section walls were produced and test-pieces were cut at different positions and orientations within the walls.

Vickers hardness measurements (10kg load) made in a range of positions over the wall surface, showed little variation along the wall length, but a definite increase in hardness from 146.3 VHN at the base to 172.6 VHN at the top of the wall was noted (the height of the wall being approximately 100mm and corresponding to around 70 welding passes).

Tensile tests were carried out on test-pieces cut from various orientations in the wall, with samples being taken:-

(i)   With the tensile axis corresponding to the vertical direction and
(ii)   With the tensile axis corresponding to the horizontal direction, both from the upper and lower part of the wall.

Results were consistant, regardless of orientation, with typical values of 490 MPa measured.

Values obtained from vertical specimens indicated few areas of weakness between adjacent weld layers. Elongation to failure values however, showed a marked difference between horizontal test-pieces cut from the bottom and top of the wall. Typical values for the base of the wall are in excess of 30%, whilst those at the top average 22.5%. The measured mechanical properties are summarised in Table 2.

Specimen Orientation	Ultimate Tensile Strength MPa	Elongation to Failure %
Vertical	489	35.0
Horizontal (Top)	484	22.5
Horizontal (Bottom)	499	33.1

Table 2 - Average Tensile Test Data

Optical microscopy revealed a microstructure in the wall of largely equiaxed ferrite (α) and pearlite ($\alpha +$ Fe_3C) with a grain size of approximately 60μm, see figure 8. There are local regions where the structure is much less equiaxed and more columnar in nature (grain size approximately 600μm x 100μm) as would be expected in an as-cast material, seen in figure 9, These regions, however, are restricted to the very top layers of the wall where the layers have not been subjected to reheating, from the deposition of subsequent weld layers. This accounts for the lower levels of ductility measured in specimens cut from the top of the wall in the horizontal direction. A simple heat treatment procedure could be used to produce a more uniform microstructure throughout the wall.

Microscopy revealed no voids or cavities and the measured density was approximately 99.5% of equivalent wrought material. No indication was found of oxidation between adjacent layers, this is supported by the strength measurements for the vertical test pieces

Results indicate that parts produced by the 3-D welding process have good structural integrity and property levels which would allow them to be exploited in service conditions.

Off-Line Robot Programming

The parts which have been produced and described so far have been produced using a cumbersome and highly time consuming on-line robot programming technique. It is evident that to be a viable process for producing prototype parts in the desired timescale, an efficient off-line programming system is required.

To test the robot welding system for more complex and representative shapes, a CAD system was used to generate welding trajectories. The following procedure was adopted:-

1)   A CAD image of the part to be manufactured was created using the PEPS2 CAD machining package (6). This package does not have a robot post processor but the instructions are similar to those used for milling. The milling process could be considered to be the negative of the welding process.

2)   Once the part has been designed and a simulation of the process has been successfully presented, the post processor generates the spatial positions required for the welding torch along with commands to signify the tool status (torch/gas on/off).

3)   The file of positions is not fully understandable to the robot. A further post processing (written on a PC in the C programming language) is required to include robot command words. This file is then concatenated with an initialisation programme which provides start positions, velocity profiles and signal levels. This concatenated file is then capable of being directly down-loaded to the robot for part fabrication.

A number of limitations to the system can be identified and some modifications need to be made.

As has already been mentioned, there is no feedback loop between the robot controller and the welding system. It is not possible, therefore, to dynamically control the welding quality through the robot system. Sensory feedback would be a requirement for improvement of the system quality through process monitoring and for post inspection purposes. Some of this information could be used to direct any further machining of the part that may be required. Attention must also be given to the use of sensors to prevent possible collapse of the part through temperature build up. The CAD/CAM link and the post processor is only of limited value, allowing only sequential machine operations with no facility for sensory update. The PEPS2 system will only provide code using a cartesian coordinate system for 3 axis machines which is only of limited use for robot systems. The technique used required a substructure that is directly below the current welding path. Part manipulation is therefore required to build up complex shapes (like the thermostat housing in figure 3) by combining simpler ones. The need for extra degrees of freedom and integration of robots with part manipulators (rotary XY tables) requires a software simulation and post processing system beyond the capabilities of PEPS2.

Future Developments

The 3D robot welding system relies as much on CAD/CAM technology as welding and robotic technology. Further development will be linked very strongly with the CAD system used and the manipulator post processor. The fabrication procedure involves the building up of complex geometric shapes from more simple constituent shapes. It has been found that cylinders (for instance) are best built in the form of rings laid on top of each other. It can be seen, therefore, that the layer formation used by conventional rapid prototyping is not wholly appropriate for this technique. Since the constituent shapes can be placed in an infinite number of ways with respect to each other, it is obvious that some form of part manipulation will be required in conjunction with the robot welder. A future system must therefore incorporate both a robot and a 3-axis part manipulator.

The formulation of the geometry will require the adaption of an existing CAD package. This package will be used to design the part and then determine the best geometric procedures required to fabricate it. This information will then be passed onto a robot simulation package (eg GRASP (7)) which will calculate the robot and part manipulator instructions. The post processor within this system will be used to programme the robot once simulation has been shown to adequately construct the part. This whole procedure of design and simulation may require an iterative process with some human intervention.

Initial experiments have already shown that, although complex shapes can be formed, the results are not perfect. There are a number of basic reasons for such imperfections:-

-       Heat build up due to the welding process can cause earlier welding passes to remelt and cause part distortion or collapse of the structure.

-       Inaccuracies in the welding and robot parameters can cause cumulative errors, resulting in the torch being too close or too far away from the surface.

-       Solid layers (ie filling in of outline shapes) cannot be performed sufficiently accurately to form a smooth surface. This means that gaps can occur inside solid objects.

It is evident from these problems that some form of sensing is required to control the process. Real time weld monitoring systems do exist, but it is unlikely that such systems can be used to overcome all of these difficulties. However, it will be necessary to stop welding at intermittent stages to leave the part to cool down and avoid collapse due to heat build up, or to implement forced cooling. Sensors can be used at this time to determine how much cooling is required and to perform post inspection of the welding process. This inspection information can be used to update the robot position to avoid cumulative errors, plot new robot trajectories to avoid gaps and generally control the weld parameters.

Conclusions

The object of this work has been to expand the use of 3-Dimensional Welding from large simple pressure vessels to a wide range of part sizes having much greater geometrical complexity.

There are several targets to aim for in the future:-

- Part Complexity: Parts will be produced such as engine castings, cylinder heads and inlet and exhaust manifolds, in order to demonstrate the capability of the system.

- Part accuracy: At present the part accuracy is about ±0.5mm, but it is expected that eventually this will be reduced to ±0.2mm.

- Surface Roughness: The present poor surface roughness is unacceptable for many situations, but better weld control and appropriate cooling techniques will improve this considerably.

The applications for this technique can be characterised by two main groups:-

- Parts: Prototype parts or small batches can be rapidly produced without any specific tooling. In addition, small modifications could be made to existing components, such as different brackets or lugs on a car chassis.

- Tooling: If it is possible to build a part without tooling then it should also be possible to produce prototype tools, such as press or forge tools, plastic molds and dies.

Further investigation of the welding technology will also be required. As yet, other welding techniques that may result in smoother, more predictable finishes have not been tried. Investigation into this branch of technology may result in the development of new welding based processes. In the past it has usually been more important to develop new welding systems that can lay down as much weld as possible in a short time. The 3-D welding system relies on precision methods and may require development of robotic welding system with very small diameter filler wires.

References

1. American Society for Metals, 1983, "Metals Handbook, 9th Edition, Vol 6: Welding, Brazing and Soldering" prepared under the direction of the ASM Handbook Committee, Ohio, pp771-803.

2. Kassmaul, K.; Schoch, F.W. and Lucknow, H., September 1983, "High Quality Large Components "Shape Welded" by a SAW process", Welding Journal.

3. Piehl, K-H., January 1989, "Formgebendes Schweißen von Schwekomponenten", Company report: Thyssen Aktiengesellschaft, Duisburg.

4. Doyle, T.E. (Babcock & Wilcox), October 1991, "Shape Melting Technology", The Third International Conference on Desktop Manufacturing: Making Rapid Prototyping Pay Back, The Management Round Table.

5. Private Communication with the Manufacturing Technology Section, Rolls-Royce Aerospace Group, Bristol, U.K.

6. Camtek, March 1990, "PEPS2 NC Part Programming System, Version 2.3", Camtek Ltd.

7. Sorenti, P. and Bennaton, J., December 1989, "Off-line programming moves into practice", The Industrial Robot, vol 16(4), pp 205-207.
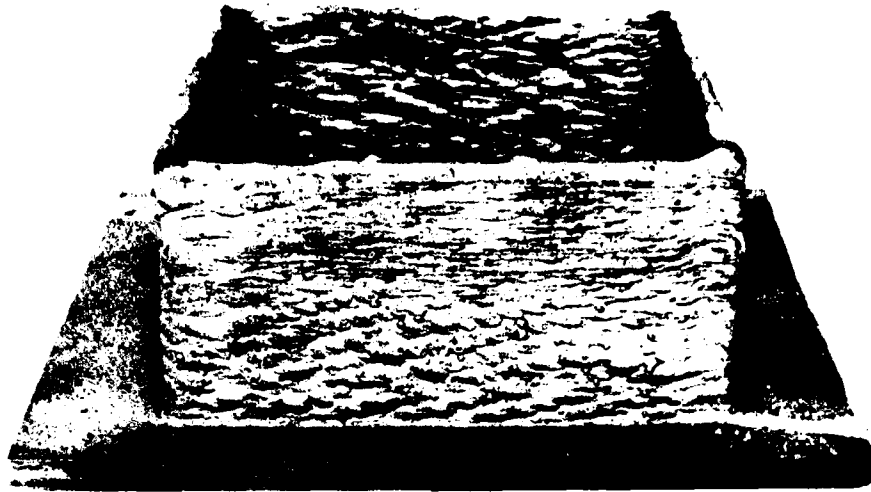
Figure 1 - Square Box Formation
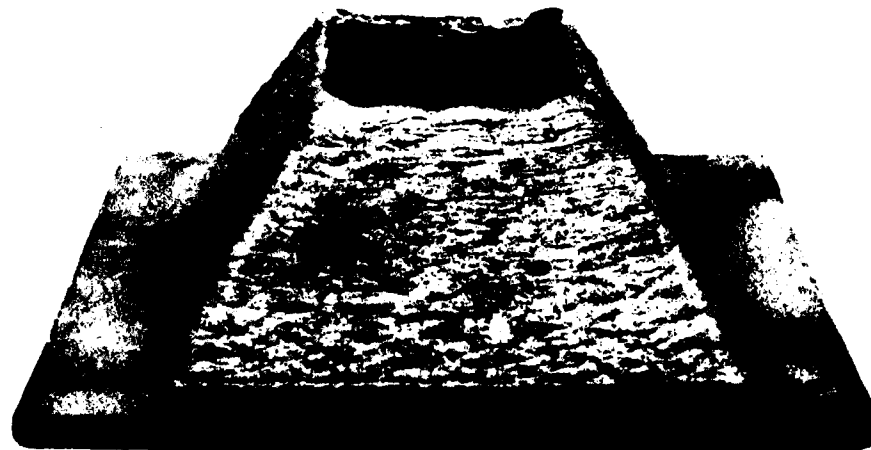
Figure 2 - Truncated Hollow Pyramid
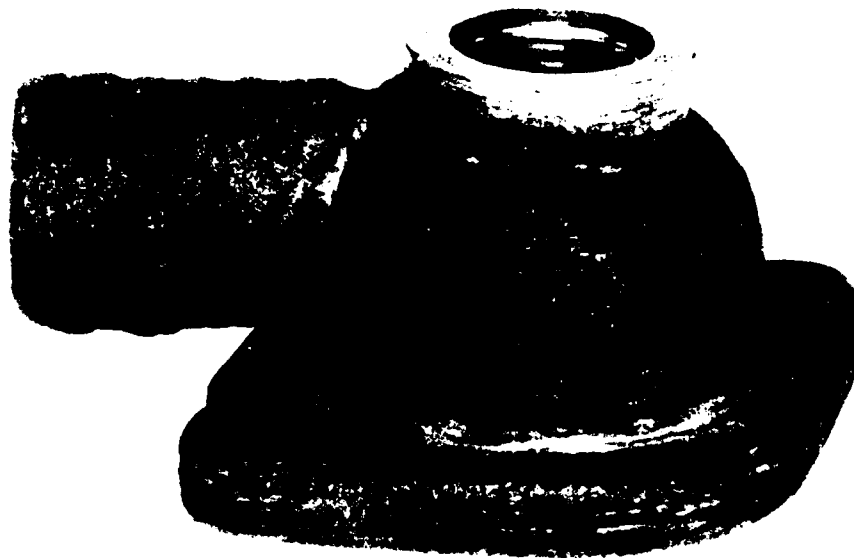
Figure 3 - Welded Thermostat Housing
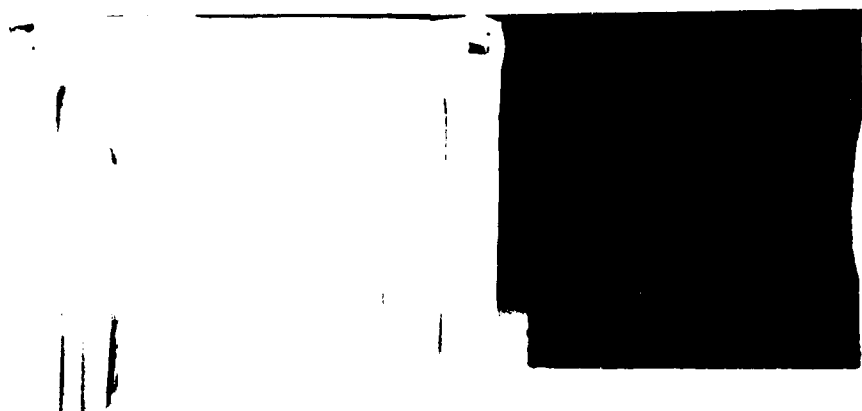
Figure 4 - Sheet Metal Part and Welded Version
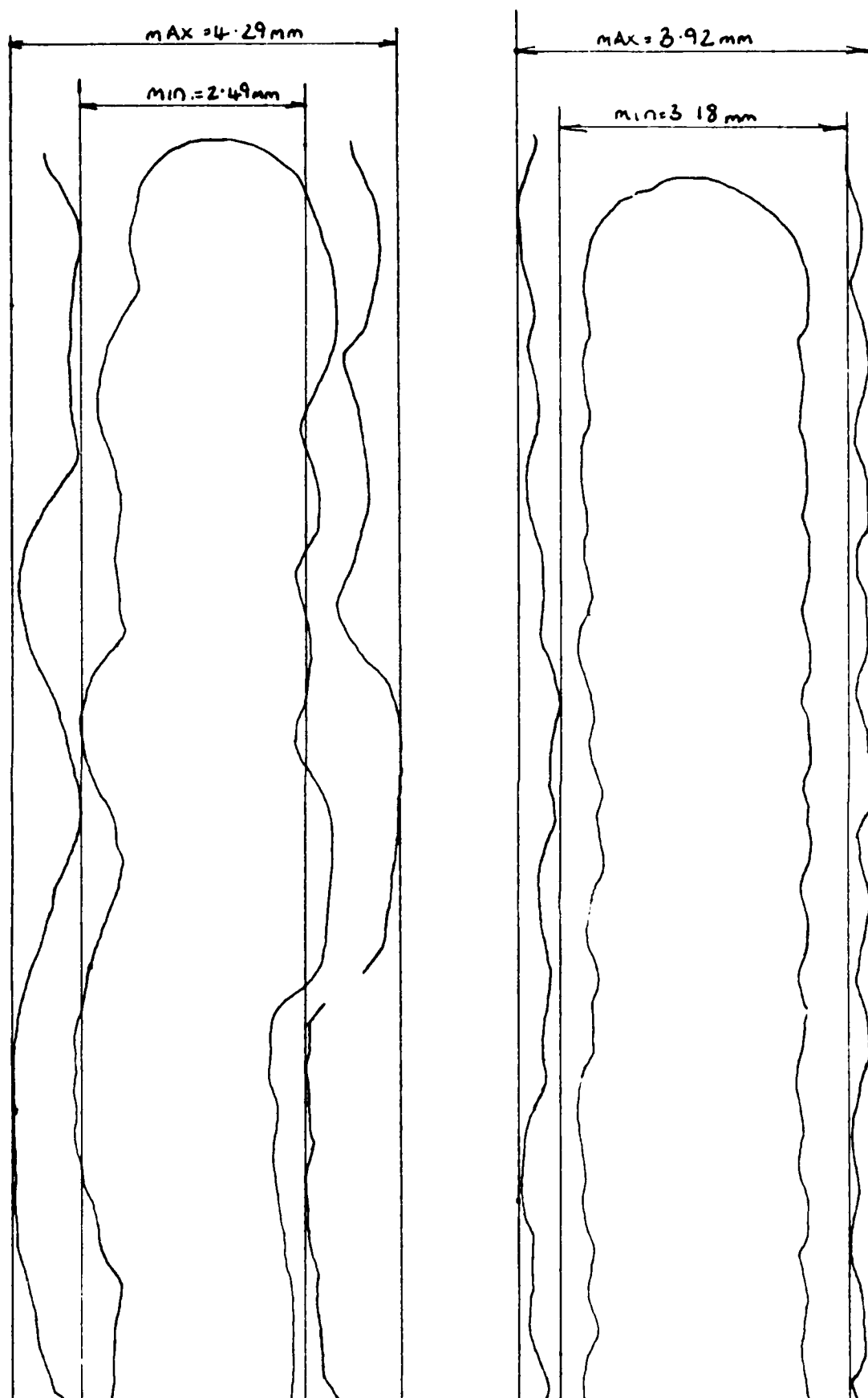
Figure 5 - Cross-section of welded walls before and after investigating the
effect of weld bead parameters

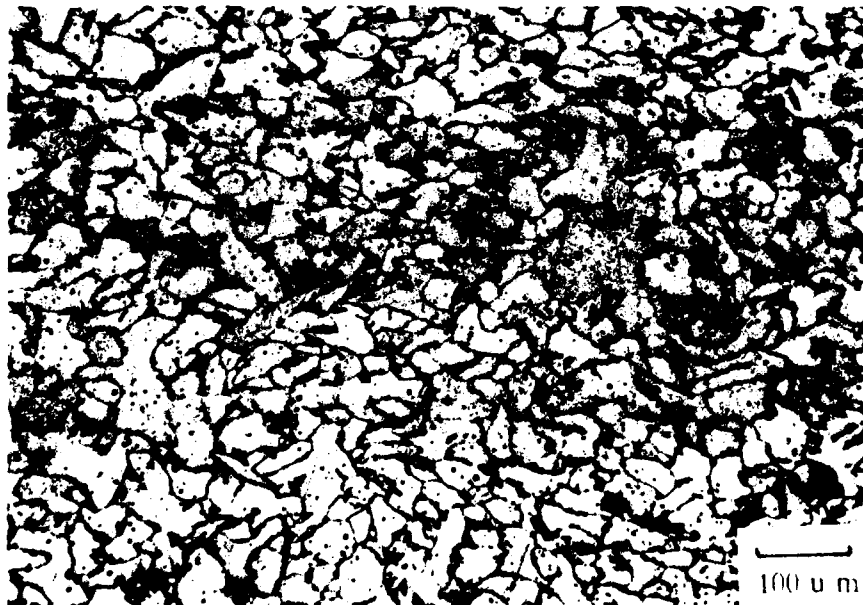Figure 6 - Large equiaxed Ferrite and Pearlite structure

Figure 7 - As-cast type structure

290

ADAPTIVE LAMINATED MACHINING FOR PROTOTYPING OF DIES AND MOLDS

F. A. Vouzelaud and A. Bagchi
Department of Mechanical Engineering
Center for Advanced Manufacturing
Clemson University
Clemson, SC
and
P. F. Sferro
Ford Motor Co.
Dearborn, MI

ABSTRACT

Adaptive laminated machining is the fusion of slicing a solid model into layers and producing parts by CNC milling machines. Unlike other solid freeform fabrication processes which create the part by addition of material, adaptive laminated machining can create solid parts by selectively removing in layers. The research issues and practical limitations on shape and manufacturability are thus different from other processes. However, the biggest advantage is the ability to obtain a solid metal part such as a die or a mold directly. In this paper, the concept of this technique, and initial results and parts produced in Clemson will be presented. In addition, future research needs and issues will be discussed.

INTRODUCTION

The main problem in manufacturing prototypes lies in the control of the delay between design and production. Until recently, a prototype of a new part required weeks or months merely to see if the shape or features would be acceptable or not. With the newer technologies developed in the past four years, a prototype can be created within hours. These new processes are grouped under the generic term free form fabrication (FFF).

FFF techniques can produce parts without any shape restriction because: (i) no tooling is required and (ii) parts are built layer by layer. 3D Systems' StereoLithography, DTM's Solid Laser Sintering, Cubital's Solider, Stratasys' Fused Deposition Molding are some of the commercially available prototyping units. If the slices are thin, texture quality and dimensional accuracy are competitive with more traditional manufacturing processes like milling and turning. However, the materials used by the FFF techniques are limited to polymers (liquid and powder) and ceramic powders, and cannot reach the mechanical properties required for many practical uses, such as dies and molds. Therefore, these processes are limited to the production of smaller parts and those to represent shapes and sizes only.[1]

A recent study presented at an MIT conference on Leadership for Manufacturing in 1991 (Table 1) shows that computer numerical controlled (CNC) machining matches stereolithography in many points. The greatest advantage of FFF over CNC machining is its capacity to produce any intricate shape. However, most, if not all, FFF processes are limited to non-metallic materials or metals with a relatively large void fraction. In addition, due to size limitations, dimensions of parts producible on these FFF units are limited to 20 inch cubed. CNC machining is limited by its programming time needed to convert a three dimension solid model to a machined part. If the programming time for CNC machining can be reduced without affecting other parameters, new applications can be developed for this conventional manufacturing process for both prototyping and limited batch production.

---

[1] Several other processes are being developed using paper, metal and ceramic powders and other materials as of this writing. However, these processes are not commercially available and were not included here.

In this paper, a concept on product realization from a CAD solid model is developed by fusing FFF processes and conventional machining. This concept, called adaptive laminated machining, is based on the integration of slice generation as in FFF technologies and 2½ dimension CNC machining. The overall idea is to decompose a solid model of the part into layers and then to automatically machine each layer to create the finished shape. The final aim is the automation of prototyping of dies and molds from a computer aided design (CAD) model. The approach taken to develop adaptive laminated machining and some results is the subject of this paper.

BACKGROUND

Introduction to FFF

Several techniques can be used to produce prototypes, like stereolithography, solid base curing, selective laser sintering, fused deposition modeling and three dimensional printing [1-6]. All of these techniques decompose the CAD model into a number of layers, called slices. The slices generated by the slicing algorithm comprise of basic entities, such as arcs, circles and straight lines, which are used to reconstruct a solid object. Therefore the first step for all FFF processes is slicing based on the graphical representation of the part. An overall scheme presented in Figure 1 describes the process flow.

The advantages in using an FFF process are:

1. texture quality and dimensional accuracy can compete with conventional machining;
2. no shape constraint comes from the process itself, the only limitation is associated with CAD;
3. the manufacturing process is fully automated, and can be run untended overnight;
4. no tooling or special fixturing is required;
5. the production of several parts at the same time with different geometries is possible;

and

6. the building speed is a function of both process characteristics and dimensions of the part, and it is not affected by the geometrical complexity.

The main drawback of these processes is that because of the materials used to date, the mechanical properties of the parts are insufficient. Hence the applications of the processes are limited to look-alike parts rather than true prototypes with the same strength, stiffness and toughness. Secondly, the initial cost of hardware, software and training is very high when compared with conventional manufacturing techniques. These technologies utilize novel materials and concepts, and thus require the acquisition of knowledge of the materials and familiarization with the concepts (e.g., slicing) and machines (e.g., stereolithography apparatus).

Table 2 compares the characteristics of different FFF processes based on the data obtained from the references. It should be recognized that since all these processes are new, the values are based on few experimental measures, some on theoretical calculations, while those for some others are not available at this time. With time the characteristics of these processes should be better understood and evaluated.

Slicing Algorithms

Slices are 2 dimensional geometrical entities (or cross-sections) assembled sequentially to create a solid object. Since all rapid prototyping technologies fabricate objects out of slices, they are the basic geometrical entities [7]. The general procedure to produce the slices from the CAD representation of the object is shown in Figure 2. Because surface texture, and form and dimensional accuracy are important to the prototype, it is essential to keep the best CAD representation possible to minimize geometrical error.

The first step in Figure 2 shows the transfer of the original CAD file into an STL format, which has become the de facto standard for FFF processes. This new representation approximates the surface of the object by triangles, the vertices of which belong to the original surface. The accuracy of the tessellated file can be improved by increasing the number of facets, requiring greater storage space and computation time. The slicing algorithm then utilizes this STL file and computes the intersection between the object and horizontal planes. The boundaries obtained through such an intersection, represented by polygons, is the cross-section of the object at that layer. The information on the cross-section of the object is utilized to create the part one layer at a time.

At present the concept of slicing is well established. Many commercial CAD packages provide capabilities for slice generation from a solid model to generate the software manually. In addition, researchers at University of Dayton, Carnegie Mellon University and Clemson University [8] have been working independently to automatically convert solid models to slices. The key issue in developing such indigenous software is to provide faster computation, better control over the process and minimize errors due to slicing.

ADAPTIVE LAMINATED MACHINING

Given that it is not possible to produce metal parts with FFF processes, classical techniques like machining need to be developed to reduce the time between design and production. Although computer aided manufacturing systems (CAM) have considerably simplified process planning, they are not adapted to the complex shapes encountered in parts like dies and molds. Such tasks require the knowledge of an experienced operator. The combination of CNC machining and production of parts layer by layer can give a satisfactory answer to this specific problem.

The objective of this research is to develop an integrated design for manufacturing system to prototype dies and molds using adaptive laminated machining as presented in Figure 3. Similar to slicing and cross hatching in stereolithography, tool path planning is of paramount interest in adaptive laminated machining. The core of the study will focus on issues related to tool path generation shown in the highlighted boxes in Figure 3.

Slice controlled machining is based on the decomposition of the solid object into layers, and a contour describing the cross-section of the object at each layer. A complex die or mold can thus be rapidly manufactured for prototyping purposes by breaking it up into simpler three dimensional segments (if necessary), decomposing each of these segments into layers, machining the contour for each layer, and thus creating the die layer by layer. This process thus requires an efficient slicing process for the original solid model and a tool path generation algorithm for both rough machining as well as finish machining.

The objective will be met by addressing three research issues: (i) developing the interface between a CAD system and CNC machining through a slicing algorithm (to be developed for adaptive laminated machining) (ii) developing an integral tool path generator to work with the slicing process and a wide variety of milling machines by using standard commands; and (iii) characterizing the quality of parts obtained by slice controlled machining to produce dies and molds whose quality will be comparable to those obtained using existing manufacturing processes (such as casting and machining).

CONCEPT AND VALIDATION

By selecting machining to fabricate dies and molds, most of the process parameters are already pre-established by the working environment. Examples in point include shape complexity, presence of cooling and/or heating circuits, fixturing constraints, strength and stiffness at critical locations in the die or mold, surface quality obtainable using CNC machining.

In adaptive laminated machining, the process planning and execution of CNC machining will be completely modified. This approach leads to the creation of computer numerical controlled (CNC) machine codes for each slice generated, proceeding one slice at a time from top to bottom. This will permit the handling of any shape of a die surface with the desired texture, and dimensional and form accuracy. Alternatively, in conventional methods, the special features would need to be identified and generated individually utilizing machining rules in an expert system which is being investigated by other researchers [9, 10].

The overall concept of adaptive laminated machining is presented in Figure 4. The sliced boundaries are directly obtained from the original CAD model. Therefore an intermediate file like the STL format, which is a faceted representation of the geometry and used by many other commercially viable rapid prototyping systems, can be avoided. Due to this difference with other rapid prototyping systems' approach, existing slicing algorithms are not applicable any more. However, slicing becomes easier because only the intersecting boundaries of the solid model with the slicing planes are needed, and no post processing of

data to obtain any hatching inside the contour is needed. Therefore, a built-in macro in any CAD package to intersect a plane with a solid model can be used. This implementation inside the CAD environment can benefit from flexibility and diversity of CAD commands. Thus, the algorithms can focus on quality issues instead of trying to solve entity manipulation, intersection, and graphic representation problems.

The object is drawn using AutoCAD AME extension as a solid model. Using the standard AutoCAD plane intersection algorithm the object is divided into different layers. Thus, the slicing is done within AutoCAD using its C libraries. The resultant is a slice containing the boundary of the object due to intersection of the layer with the object. The object is thus broken down into a number of layers, separated by the slice thickness specified by the planner. Each layer boundary is stored in a file, sequentially, utilizing the AutoCAD data exchange format (DXF). This file thus contains line and arc segments corresponding to each layer. Each line or arc segment is then defined in terms of its radius of curvature (if appropriate) and the coordinates of its end points. This data is used in a C program to generate the process plan from layer to layer and subsequently the numerical part program to drive the machine.

The example in Figure 5 illustrates the feasibility of the method with a manually varied z increment. It is possible also to develop the slices with variable z increments to better represent the surfaces [11]. The finished part produced on a desktop 3 axis milling machine using a flat end mill is shown in Figure 6. The work to date clearly shows the feasibility of the process and the ability to produce a large die or mold cavity from a metal block using adaptive laminated machining.

DISCUSSION

Several geometrical limitations are expected using this approach. In addition to machining constraints imposed by the milling machine itself, the slicing process adds new shape restrictions. Feature like threads, grooves or convex shapes are to be machined using a more conventional technique or after refixturing. Figure 7 provides some examples of geometrical constraints in adaptive laminated machining.

Once the undesired features are removed from the CAD model and the pockets are extracted, the minimum number of fixturing has to be determined as a function of the degrees of freedom of the machine tool. If a single fixturing is desired, the solid model can be used directly by slicing program, with no further modification. Parts such as dies and molds have geometrical properties where the positive shape is extractable and these parts do not have any undercut. If the parts need refixturing, only a minimum number of fixturing needs to be used. This is an area of ongoing research and will be discussed in depth in a future paper.

The direction of the slicing and identification of dominant features are two other domains of research in adaptive laminated machining. The choice of the direction of slicing will relate to the minimum number of fixturing needed and thus ultimately to producibility of shapes by machining. Another issue of concern is tool path generation and tool offset necessary for different geometries. These too will be discussed in a future paper.

ACKNOWLEDGEMENT

REFERENCES

1.   E. Sachs, M. Cima, and J. Bredt, "Three Dimensional Printing of Ceramic Shells And Cores For Metal Casting", Intelligent Design and Manufacturing for Prototyping, PED-Volume 50, ASME 1991.
2.   L.L. Kimble, "The Selective Laser Sintering Process: Applications Of A New Manufacturing Technology", Intelligent design and manufacturing for prototyping, PED-Volume 50, ASME 1991.
3.   E.P. Gargiulo, and D.A. Belfiore, "Photopolymer Solid Imaging Process Accuracy", Intelligent design and manufacturing for prototyping, PED-Volume 50, ASME 1991.

4. S. Scott Crump, "Fast, Precise, Safe Prototypes With FDM", Intelligent design and manufacturing for prototyping, PED-Volume 50, ASME 1991.

5. J.M. Pacheco, Rapid Prototyping, MTIAC, Jan. 1991.

6. J.P. Kurth, "Material Incress Manufacturing by Rapid Prototyping Techniques", Annual of the CIRP, 1991 pp 603-614, Katholieke Universiteit Leuven, Belgium.

7. K.L. Chalasani, B. Grogan, A. Bagchi, C.C. Jara-Almonte, A.A. Ogale, and R.L. Dooley, "An Algorithm To Slice 3-D Shapes For Construction In Prototyping Systems", Computers in Engineering volume 1, ASME 1991.

8. K. L. Chalasani, "The Design and Implementation of a Slicing and Hatching Algorithm for Freeform Fabrication", MS Thesis, Clemson University, Clemson, SC, August 1992

9. M. Anjanappa, J.A. Kirk, D.K. Anand, and D.S. Nau, "Automated Rapid Prototyping With Heuristics And Intelligence: Part I- Configuration", Int. J. Computer Integrated Manufacturing volume 4, 1991.

10. J.A. Kirk, D.K. Anand, and M. Anjanappa, "Automated Rapid Prototyping With Heuristics And Intelligence: Part II-Implementation", Int. J. Computer Integrated Manufacturing volume 4, 1991.

11. K. L. Chalasani and A. Bagchi, "Process Planning Issues in Freeform Fabrication", accepted for publication in Quality Assurance through Integration of Manufacturing Processes and Systems, ASME WAM, November 1992, Anaheim, CA.

Table 1: Comparison of Four Prototyping Techniques for Part Representation and Realization

	Computer Aided Design (CAD)	Stereolithography	CNC Machining	Reaction Injection Molding (RIM)
Strength to stiffness ratio[1]	0	0.38	0.80	0.85
Form accuracy[1]	0.83	0.85	0.85	0.95
Appearance[1]	0.50	0.80	0.90	1.0
Shape and texture perception[1]	0.20	0.52	0.98	1.0
Cost to produce a prototype[1]	0.95	0.22	0.5	0
Speed of producing a prototype	Very fast	Fast	Medium	Slow
Overall rank[2]	4	3	2	1

[1] Rated on a scale from 0 to 1, with 1 being the highest possible and 0 the lowest

[2] Ranked between the four techniques considered here

Table 2: Comparison of some of Free Form Fabrication Processes [5, 6].

	Materials	Accuracy	Speed	Remarks
Stereolithography	liquid photopolymer resin	Slice thickness 0.125 – 0.75 mm x/y +/–0.46 mm[1] x/y +/–0.12 mm[2]	Variable with size From 20 s to 3 min/layer	uses toxic polymers needs post curing
Selective Laser Sintering	investment casting wax, polycarbonate, PVC, ABS plastic and nylon.	+/–0.12 – 0.05 mm	Scanning speed .76 to 1. m/s building rate: 12 to 25 mm/h	powdered metals and ceramics are under development
Three Dimensional Printing	alumina powder and colloidal silica binder	+/– 0.05 mm for slow axis	above 30 mm/h with 100 jets (under development)	Used for ceramic shells and cores for metal casting
Ballistic Particle Manufacturing	wax, plastics	+/– 0.1 mm in x/y plane		Under development
Fused Deposition Modeling	nylon like material, investment casting wax	+/–0.12 mm	Scanning speed: 381 mm/s	Capable of a 1 min material changeover
Laminated Object Manufacturing	material in sheets: paper, metal	x/y/z +/– 0.1 mm	Cutting speed: .4 m/s	
Solid Base Curing	photopolymers + wax as support	+/– 0.05 mm	90 s/layer	
Mask (Cubital)	liquid photopolymers	0.1% in all dimensions	110 s/layer	

	Materials	Accuracy	Speed	Remarks
Desktop Machining	Polymers, Light alloys, steels ...	+/– 0.012 mm	0.7 m/min	uses tooling and fixturing

[1] Based on a study from E.I. Du pont de Nemours and Company Wilmington
[2] Claimed by most manufacturers
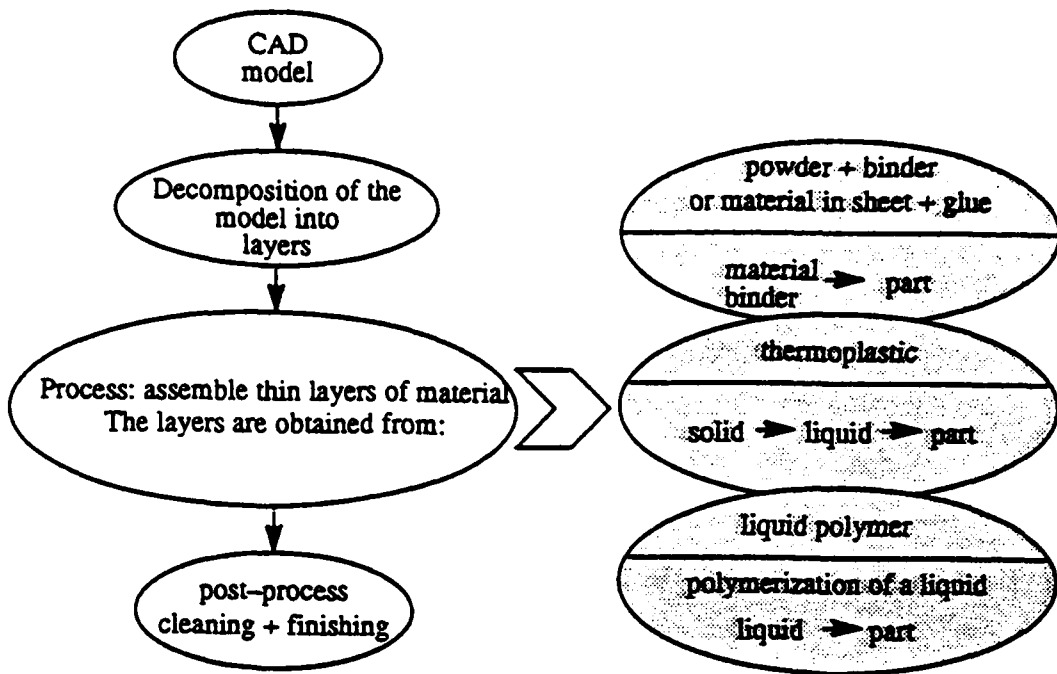
Figure 1: Overview of Free Form Fabrication
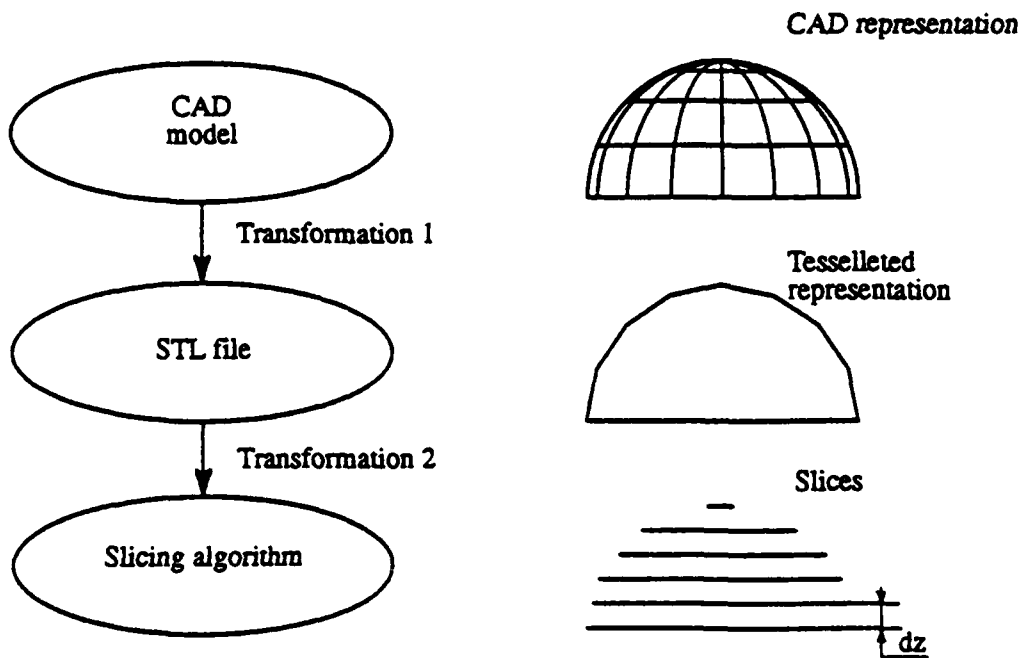
Figure 2: Slicing Procedure

CAD/CAM environment

Display

CAD model — CAD file

Contours — CAD file — Variable slice thickness

Toolpaths — neutral file

Machine codes — NC file

1 — Slicing program — CAD C libraries

2 — Toolpath generation — CAD C libraries

3 — Post-process — Tool type — Machine type

Figure 4: Details of process planning issues necessary in adaptive laminated machining (shown in the highlighted boxes in Figure 3).

Shape, texture and dimension quality

Part — Finishing — Mechanical properties — Error / limitation

Price / time

machine type — fixturing — material — tooling — Toolpaths based on layers

quasi-static parameters

Original CAD Transformation — CAD model

H C M A N

Figure 3: Adaptive Laminated Machining: Environment and Goals

298
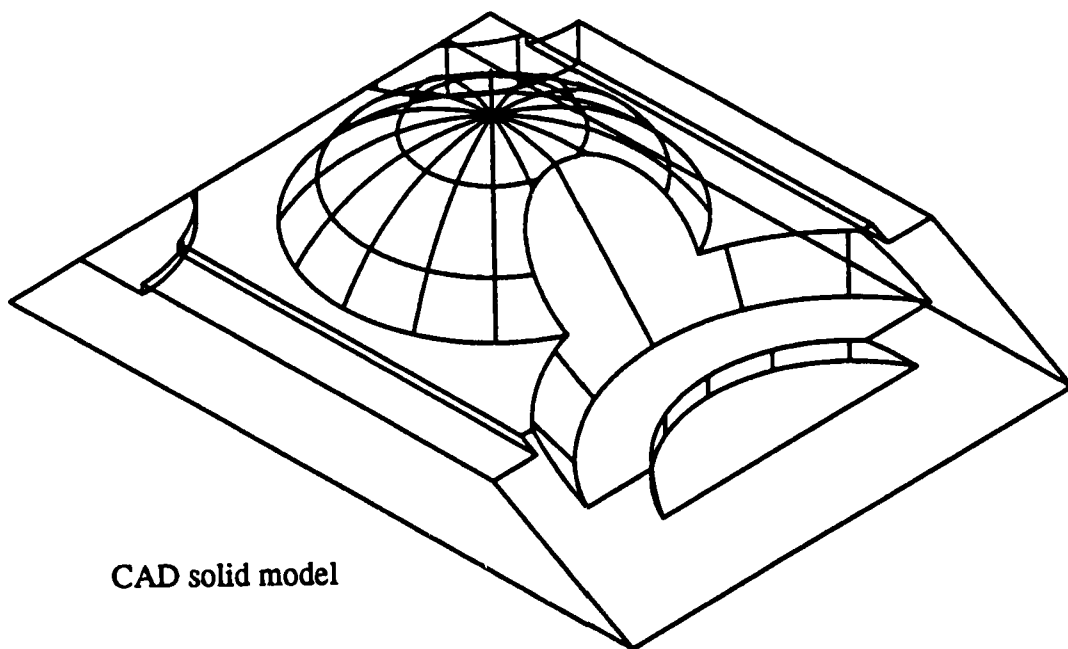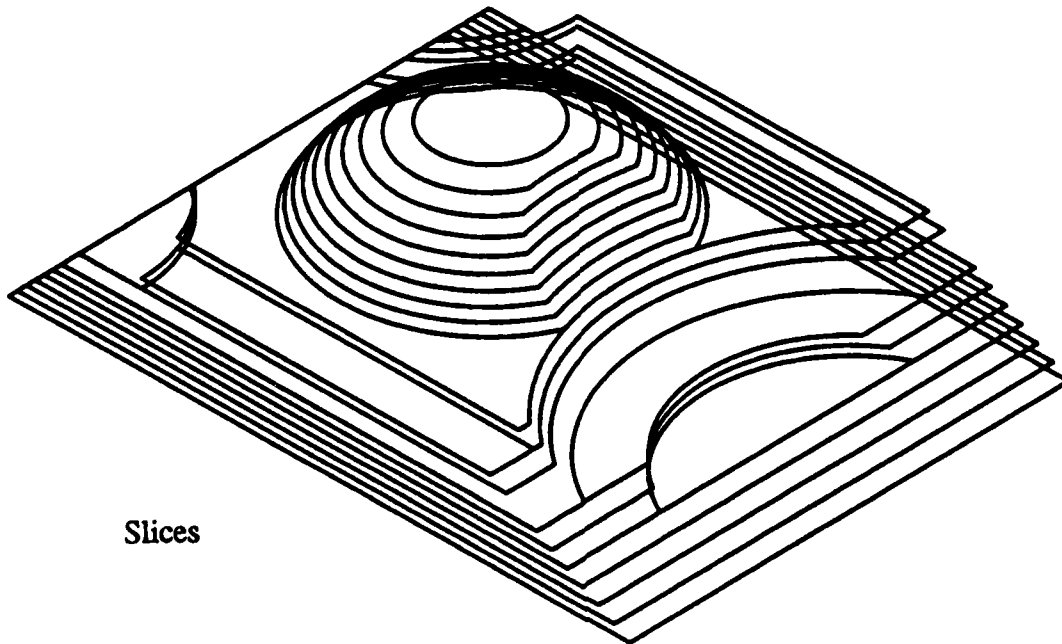
CAD solid model

Slices

Figure 5:   Transformation of a solid model into slices using AutoCAD
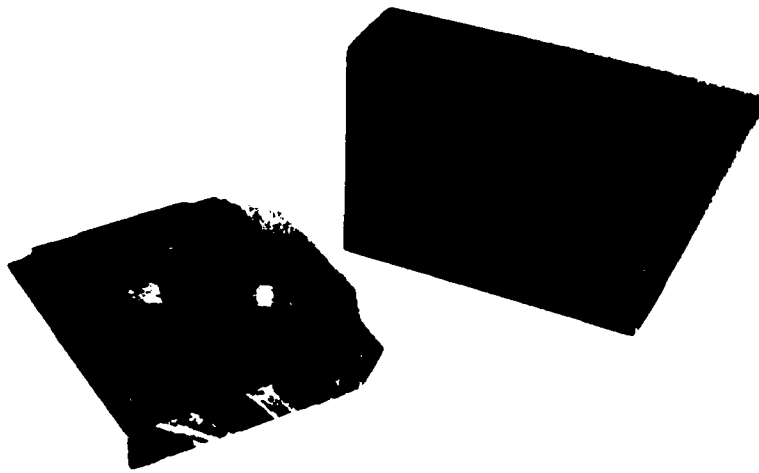
Figure 6: The finished part produced by adaptive laminated machining on a 3 axis milling machine and a flat end milling cutter.

thread

undercut

Ball end mill

cutter

groove
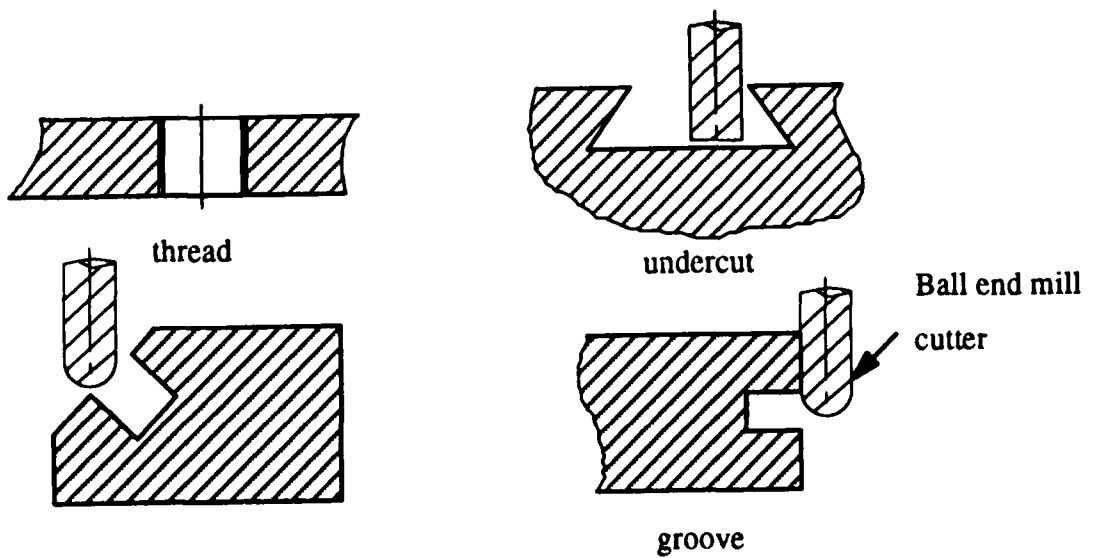
Figure 7: Examples of geometrical constraints in adaptive laminated machining

Rapid Prototyping Using FDM:
A Fast, Precise, Safe Technology

Stratasys, Inc.
7411 Washington Ave. So.
Minneapolis, MN 55439 USA
Phone: 612/941-5607
Fax: 612/944-6741

Introduction

This paper outlines the use of FDM to speed product design and to streamline the manufacturing process.

Time compression, the ability to quickly reduce the time it takes to get new products to market, has increased the pressure on all phases of the manufacturing process. Manufacturers must find and implement time saving systems without sacrificing quality.

Fused Deposition Modeling (FDM) provides a synergistic solution for design and manufac-

An assortment of concept models created on the 3D MODELER showing a variety of geometries, complexities, sizes and materials.

turing engineering: visualization models and part concept designs become accurate physical models leading to final working parts right within the normal engineering office environment.

This clean running, single step operation uses non-toxic, thermoplastic wire-like filaments eliminating liquid photopolymers, powders or lasers from the process.

The current technological quest has been to create a true desktop system suitable for use in an office environment. The FDM process has moved the state of the art beyond lasers, beyond systems that require messy materials and beyond large, cumbersome units to allow for true 3D desktop prototyping.

FDM quickly and safely produces non-toxic physical prototypes from 3D CAD data reducing the time to market, reducing product development costs and allowing verification of production tooling.

Background

In 1988 Scott Crump invented the FDM process (patent pending), an automatic, non-laser based technology using non-toxic materials for rapid part creation. The process builds on early professional experiences with thermofusion control mechanisms and low temperature thermoplastics.

FDM is a unique technology to empower design and manufacturing engineers to be able to quickly produce precise, multi-material models in an engineering environment, right at the CAD workstation.

The Need for Rapid Prototyping

Stratasys, Inc. is a privately held company with partial funding provided by Battery Ventures in Boston. Stratasys, Inc. began shipping 3D MODELERS in the second quarter of 1991.

In today's business environment, manufacturers need every competitive advantage to get a quality product to market as quickly as possible. The ability to rapidly produce 3D models of the images created on CAD workstations has become an additional tool to positively impact both quality and speed (Marks, 1990).

The Stratasys 3D MODELER uses the innovative patented Fused Deposition Modeling (FDM) method to generate three dimensional prototypes and wax patterns from 3D CAD software data.
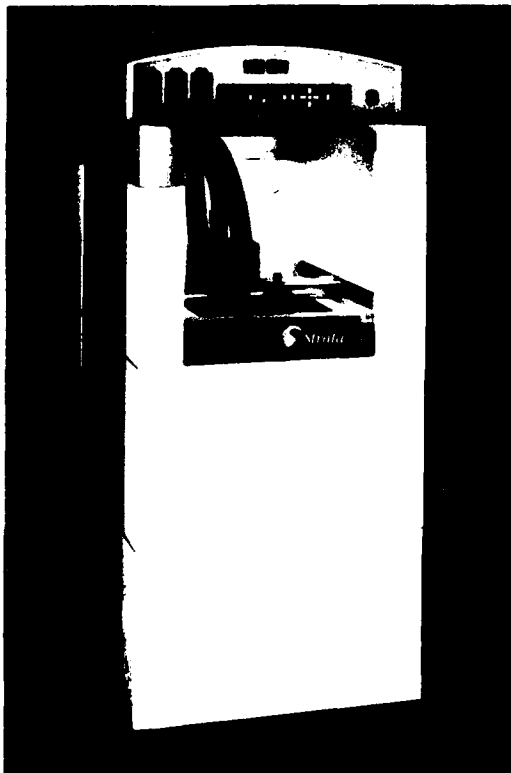
By allowing design and manufacturing engineers to quickly, accurately and efficiently create prototypes, the design process will improve. When an accurate physical model is generated in less than an hour, the designer can economically create multiple iterations prior to final design.

Rapid prototyping gives shape, form and feel to the image on the computer screen by producing 3D models of complex, sculptured-surfaced parts within minutes or a few hours. Rapid prototyping will increase experimentation and allow improvements to be quickly incorporated (Wohlers, 1990).

3D MODELER

The FDM process uses the Stratasys 3D MODELER® in conjunction with a CAD workstation. Stratasys' 3D MODELER is a single step, self-contained modeling system that offers the user several advantages. Speed is an important benefit of this technology; typical models

can be produced in minutes rather than hours or days. As no post curing is required, the FDM technique enables the designer to create multiple versions of a part design within a short time frame.

Elements of the FDM Process

In this process a conceptual geometric model is created on the CAD workstation. It is then imported into a UNIX-based workstation where it is sliced into horizontal layers that are down-loaded to the 3D MODELER.

Liquid thermoplastic material is extruded and then deposited into ultra thin layers from the lightweight FDM head one layer at a time. This builds the model upward off a fixtureless base. The plastic or wax material then solidifies in 1/10 of a second as it is directed into place with an X-Y controlled extrusion head orifice that creates a precision laminate.

A spool of .050 inch diameter modeling filament feeds the FDM head and can be changed to a different material in 1 minute.

Maintaining the liquid modeling material just above the solidification point is fundamental to the FDM process. The thermoplastic melt temperature is controlled to 1 degree Fahrenheit above solidification. The material then solidifies as it is directed into place with an X-Y controlled extruding head nozzle that creates a precision laminate.

Successive laminations, within the 0.001 to 0.030 inch thickness range and a wall thickness of .009 to .250 inch range, adhere to one another through thermal fusion to form the model. Our overall tolerance is ± .005 inches in the X,Y,Z axis over a 12 inch cubed working envelope.

The Fused Deposition Modeling (FDM) process produces safe, accurate 3D models in minutes.

Safety Benefits

The Stratasys 3D MODELER is a stand-alone modeling system that is located next to the CAD workstation. It stands 6 feet tall with a 3' by 2.5' footprint. The system requires no exhaust hood or special facilities, providing a natural extension to the engineering workstation and easily fitting into an office environment.

The process operates at moderate temperatures in the range of 180 to 220 degrees Fahrenheit, making it safe for office use. By comparison, the temperature is similar to that of a hot cup of coffee. There is no worry of possible exposure to toxic chemicals, lasers, or liquid polymer baths. The Stratasys process uses no powders and there is no messy cleanup. Concern over disposal of hazardous materials is eliminated.

303

Materials

The Stratasys technology allows a variety of modeling materials and colors, with new materials continually under development. All are inert, non-toxic materials developed from the range of commercially available thermoplastics and waxes. The ability to use different materials allows the user to match the material to the end use application of the prototype, whether that is a pattern for tooling or as a concept model.

Currently, there are three materials: a machinable wax, a tough plastic polymer and an investment casting wax. These thermoplastics and waxes soften and liquefy when heat is applied.

The Stratasys investment casting wax is an industry standard investment casting material. This wax rapidly dewaxes from the shell using normal investment casting procedures and provides superior surface finishes. Because this is a standard investment casting wax, it can become part of the foundry's normal recycling process.

The machinable wax is primarily used for conceptual modeling and spray metal molding. For instance, the accuracy of the model allows its use in the spray metal process for injection mold prototyping. Both the investment casting wax and the machinable wax can streamline the manufacturing process by allowing the user to go directly to soft tooling using the model as the pattern for investment casting or spray metal injection molding.

The plastic filament is a tough material producing sturdy models suitable for concept models or fit, form and some function applications.

In the three years the FDM technology was in development several obstacles were overcome. A major breakthrough was the decision to settle on a filament system of material media as opposed to a "hopper" system. The spool based filament system has proven to be a significant strength of the 3D MODELER.

The spools give the user the ability to change material in about one minute by threading the desired material into the prototyping unit. There is virtually no waste and no vat to clean.

The materials to produce a part are cost effective, usually under twenty dollars. For example the material for one golf club head costs approximately $9.00 and one spool of material can produce roughly 20 club heads.

The FDM process is not limited by the UV polymers required by many other rapid prototyping systems and new materials are continuously under development.

Supports

The FDM process does not need elaborate supports to produce a part as do some other systems. The 3D MODELER has the ability to create a support in mid-air rather than building the support up from the base in some applications. The system is also capable of extruding plastic into free space depending on the part geometry. When supports are not used, the FDM head forms a precision horizontal support in mid-air as it solidifies.

TABLE OF SUPPORTED IGES ENTITIES

Geometric

100	Circular Arc
102	Composite Curve
104	Conic Arc
106	Copious Data
108	Plane
110	Line
112	Parametric Spline Curve
114	Parametric Spline Surface
116	Point
118	Ruled Surface
120	Surface of Revolution
122	Tabulated Cylinder
124	Transformation Matrix
126	Rational B-Spline Curve
128	Rational B-Spline Surface

140	Offset Surface (limited support)
141	Boundary Surface
142	Curve on a Parametric Surface (limited support)
143	Bounded Surface
144	Trimmed Surface

Annotation Entities

106	Crosshatching (limited support)
202	Angular Dimension
206	Diameter Dimension
210	General Label
212	General Note (limited support)
214	Leader Arrow
216	Linear Dimension
218	Ordinate Dimension
220	Point Dimension

222	Radius Dimension
228	General Symbol

Structure Entities

308	Subfigure Definition
314	Color Definition (limited support)
402	Associate Instance
404	Drawing (limited support)
406	Property
408	Singular Subfigure Instance
410	View (limited support)
412	Rectangular Array Subfigure Instance
414	Circular Array Subfigure Instance

Open Systems

The 3D MODELER imports geometry through standard RS232 serial ports. Either wireframe, surface or solid CAD data from all standard CAD software packages can be imported through IGES running on UNIX workstations.

There are four methods of driving the modeler:

1. Through IGES

A file brought into the CAD software program in an IGES format can be edited, scaled, oriented and even surfaced if the input does not already have surfaces (see table above for supported IGES entities). Supports, if needed, can be added graphically. The 3D MODELER can also import digitized data via IGES. The digitized data can be generated by probe, laser scan, sonic scan, Computed Tomography (CT) scan or Magnetic Resonance Imagining (MRI). This input data can be used as the slices or to define surfaces.

2. Directly from CAD/CAM software that outputs CNC code

A user who already has a CAD/CAM capability that outputs CNC code can use that code to drive the modeler.

3. Through Stratasys' ProtoSlice software

The Stratasys system uses a special packaging of CAD/CAM software and, in fact, delivers a full CAD package as part of its total turnkey system, allowing the user to completely design and build a part from scratch. The capabilities include a full NURBS-based surface modeler for complex or simple shape creation.

4. Through .STL format

It is possible to import an ASCII or binary .STL file and post out NC code to drive the modeler.

Applications

Applications cross a wide spectrum of industries. Any industry that manufactures a tangible product and can benefit from reducing design and manufacturing errors, increasing manufacturing speed or compressing the time to manufacturing has a potential for this technology.

Companies using rapid prototyping are finding the benefits of the technology go beyond the ability to produce more models faster. Once the model has been completed and approved, the prototype may be used in the next step in the manufacturing process.

Ring produced by the Stratasys 3D MODELER in investment casting wax and actual ring investment cast directly from the wax. Model creation time: 35 minutes. Resolution: .002 inches.

Both injection molding and investment casting can use the Stratasys prototype as a direct input master to the manufacturing process.

Investment Casting

Manufacturing complex metal components requires a multi-step investment casting process. As the name implies, the Stratasys investment casting wax is excellent for lost wax investment castings.

The time consuming step of producing a wax replica of the part to be manufactured can be eliminated. The desired part created in Stratasys' investment casting wax can be dipped or invested directly into the ceramic slurry. The wax quickly dewaxes from the ceramic shell.

A report published in INCAST states this about the Stratasys investment casting wax, "For investment casters, these models are an ideal pattern material. They are gated, dewaxed and fired in shell or solid molds exactly as normal wax patterns are processed." (March, 1991)

Investment Casting Examples

The investment casting process is used by a manufacturer of products for the orthopedic surgeon. These products include reconstructive parts such as hip and knee replacement implants as well as shoulder, ankle and other less frequently replaced joints.

In cases where there has been disease or infection, a small implant can be created to attach to the bone (a resurfacing). Pictured above is a resurfacing of a section where the thigh bone connects to the knee.

Typically the parts are machined from solid blocks of titanium. The need for high quality is apparent when considering the part will be a component of someone's leg or knee for life. From a financial aspect the need for quality is

306
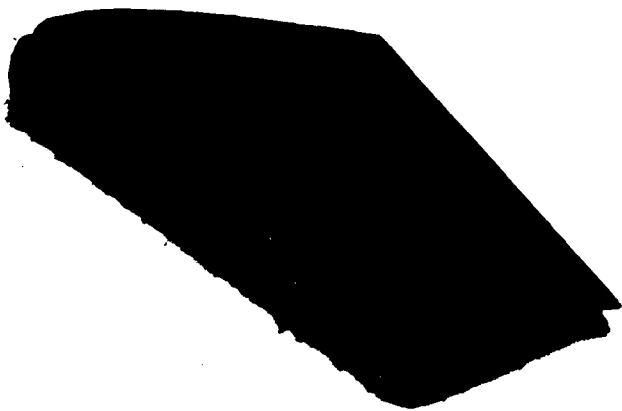
Airfoil part produced in Stratasys machinable wax. Model creation time: 5 hours, 45 minutes. Resolution .010 inches

apparent when considering the expense of the titanium. Precision, quality parts with complex surfaces are an ideal match for the FDM process.

The ability to rapidly produce models allows evaluation by the consulting orthopedic physicians, along with the team members from marketing, design, engineering and manufacturing.

Once a design has been analyzed and consensus is reached the company benefits from the advantages of Stratasys' investment casting wax. By saving steps in the manufacturing process, the company can speed its products into this competitive market.

The jewelry industry is another example where investment casting is used extensively. Although it lacks the emotional impact of a life-changing knee implant, other parallels exist. Certainly the high cost of raw material makes the use of a prototype in a less expensive material desirable.

Injection Molding

The accuracy of the Stratasys model allows the use of the model in the spray metal process for injection molding. The filament materials used by Stratasys have high durability and stability required for a master for spray metal molding.

Using a 3D model produced in the Stratasys machinable wax, allows manufacturers to go directly to the spray metal molding process. Customers create spray metal tooling by spraying the metal onto the model in thin coats.

This technique has been applied across industries from the simple casting of urethane in the shoe industry to injection molding of glass filled resins. These glass filled resins are used for high strength, heat resistant, wear resistant parts such as photo equipment, small power tools and appliances.

Saving steps in the manufacturing process translates into time savings for manufacturers using investment casting or injection molding techniques. These savings allow manufacturers to speed products to market.

Fit, Form and Function Applications

A common frustration in assembled products occurs when interior components are built that will not fit together or do not fit the housing. The ability to rapidly produce prototypes reduces this source of manufacturing error or decreases the time it takes to hand produce prototypes of all components.

The aerospace industry is just one example where fit, form and function are a concern.

Conceptual Modeling

The prototype or model itself can be a marketing tool for the manufacturer. To be able to hand a client a prototype of the proposed part at the final presentation or to include a prototype with the proposal package has strong emotional appeal in the sales process.

Conceptual modeling also enables engineers to quickly produce multiple iterations of a sample part to streamline the design process.

Concept models are important in the shoe industry. One major shoe manufacturer creates hundreds of new shoe heel designs each year. Each heel style is normally produced in one size based on the designer's drawing. After this initial prototype design is verified, models are created for sizes 3 through 12, with the heel dimensions graded for the size.

The ability to quickly and accurately produce the concept model allows this manufacturer to improve quality and productivity in the manufacturing process.

Summary

FDM provides a combination of attractive features to provide true desktop 3D modeling. It is a non-laser based system providing a cost effective, accurate and environmentally safe way to produce 3D models and prototypes.

Reducing time to market by accommodating engineering changes quickly and improving product quality demands state-of-the-art prototyping tools.

References

Kennerknecht, S. and Sifford, D., "New Dimensions in Rapid Prototyping Explored for Aluminum Investment Castings," *INCAST*, March 1990, Vol. IV, Number 3, pp. 5 - 10.

Marks, P., 1990, "The Rapid Prototyping Revolution...Better Products Sooner," *Proceedings, The First International Conference on Desktop Manufacturing*, Cambridge, Massachusetts, October, 1990.

Wohlers, Terry, "Plastic Models in Minutes," *Cadence*, July, 1990.

For more information contact:

Stratasys, Inc.
7411 Washington Avenue South
Minneapolis, MN 55439 USA
Phone: (612) 941-5607
Fax: (612) 944-6741

Trademarks: 3D MODELER, Fused Deposition Modeling (FDM), ProtoSlice, QuickSlice, Models
in Minutes.

Machine Issues Associated with Solid Freeform Fabrication

Joseph J. Beaman
Department of Mechanical Engineering
The University of Texas at Austin

Before we begin a discussion of machine issues it is important that we categorize exactly what we mean. There are differences between the design of a research piece of equipment as compared to a commercial piece of equipment. A research piece of equipment has to have the flexibility to demonstrate a success pattern. A commercial piece of equipment, on the other hand, assumes that you have a stable platform and you are now trying to assess how broad a success path you have (Figure 1). In fact, you are trying to make that path as broad as possible so that the machine will not fail and will always work the same way. This particular talk, and my expertise, is much more along the lines of design of a research piece of equipment. What I will be talking about today are machine issues associated with developing a success path in Solid Freeform Fabrication. The machines we will be talking about have to have the flexibility to operate in a wide variety of ways with a wide variety of experiments.

Given that we are going to talk about machines, we should also discuss what we mean by machines. If we look at the next figure we see that, if we are trying to make a part by Solid Freeform Fabrication which we have defined to be the ability to go directly from the computer rendition of an object directly to the part itself, requires several components. It requires process information which stores the information of the object itself, it requires materials, and it requires process control. All of this sum total is the machine. The point I am trying to make is that it doesn't make sense to talk about a machine without a process (Figure 2). In fact, a machine is nothing more than an embodiment of a process. I am going to be talking about the Selective Laser Sintering process but in such a way to emphasize the general concepts associated with designing and implementing research machines to demonstrate freeform fabrication.

Machines

Research

- Flexibility

- Success Path

Commercial

- Stability

- Width of Path

Figure 1
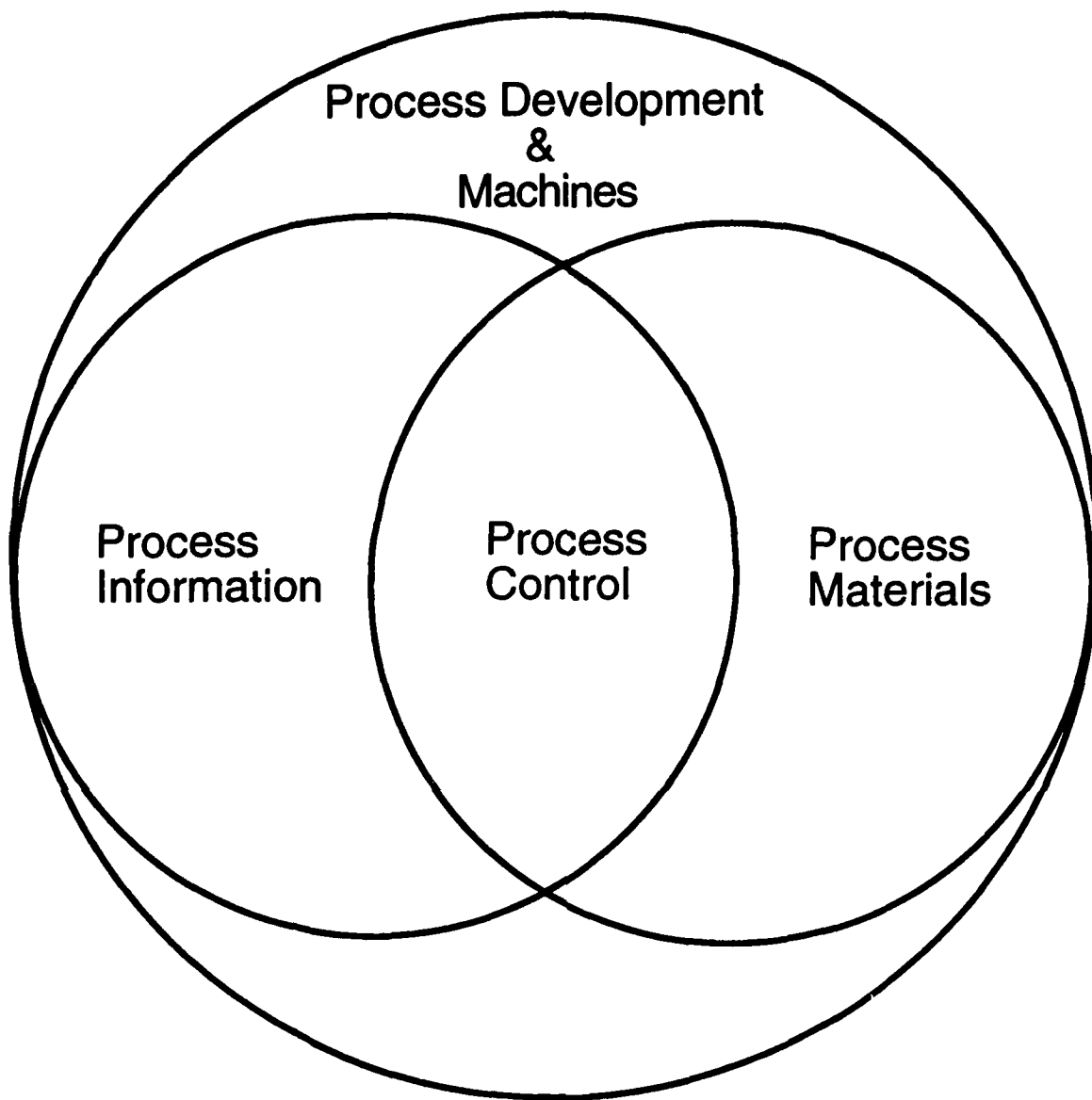
Machines without Process?

Figure 2

In the next figure (Figure 3), we see how we organize our research in Selective Laser Sintering. At the top of this diagram you will see fundamental process understanding. Our process by its very nature is a thermodynamic process. Here we find basic models by which we understand and describe our process. Underneath this we have information processing which includes geometric representation, materials and related microstructures, process control, process development and machines, and finally, parts and applications. I would like to talk about each one of these separately.

At the top of our research hierarchy we included fundamental process understanding. This area contains our thermodynamic models, both written and conceptual that we use to help design our equipment. A particular point I want to make here is that the thermodymics involved, at least in Selective Laser Sintering, includes both macroscopic and microscopic phenomena (Figure 4). What is crucial to Selective Laser Sintering is control not only at the small scale with a laser but also control of the large scale thermodynamics and heat transfer with heaters, either radiant or conduction. If this is not done properly the parts you make can have large amounts of curl or growth. Although I do not want to discuss the details, I do want to make the point that any given process, not just Selective Laser Sintering, will be involved in certain fundamental processes. It is important that we understand what those processes are in order to most effectively optimize the equipment that we design.

Information processing (Figure 5) is one of the processes required for Selective Laser Sintering. We must have a geometric representation of the part. Associated with that we must have a process interface which allows various representations. For example, you have a CAD representation which must effectively talk with the machine slice level. There are other instances where we may not even have a CAD representation. Image data, for example, in scanning where you have data to perform reverse engineering or automatic copying of a part. To achieve this requires a good

312
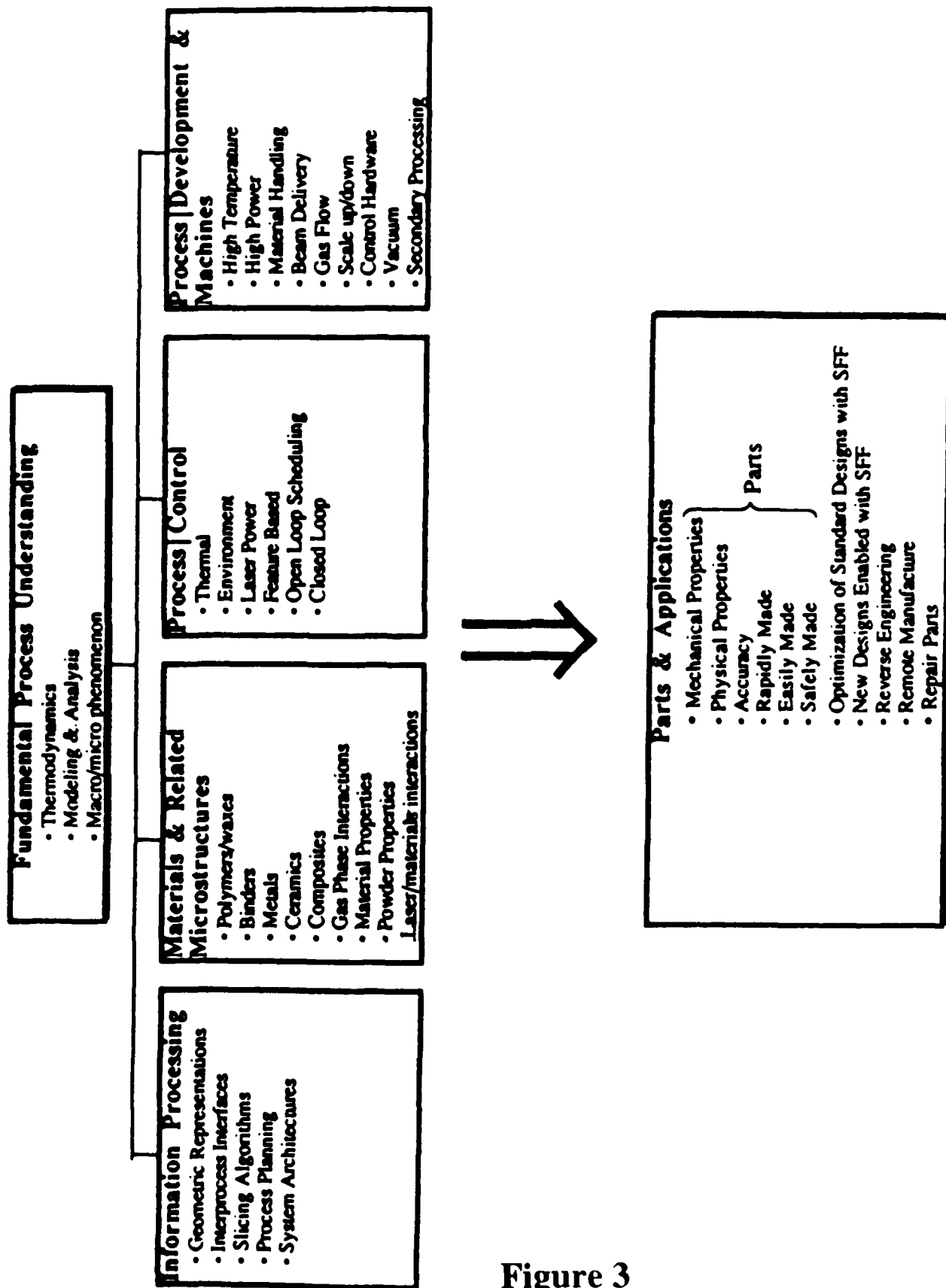
Figure 1: Structure of Overall Solid Freeform Fabrication Research

Figure 3

Fundamental Process Understanding

- **Thermodynamics**
- **Modeling & Analysis**
- **Macro/micro phenomenon**
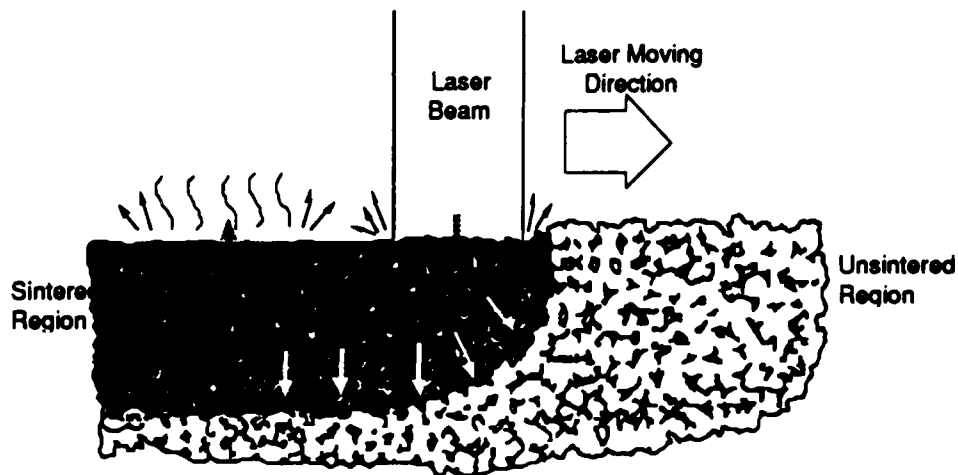
Figure 4

Information Processing

- **Geometric Representations**
- **Interprocess Interfaces**
- **Slicing Algorithms**
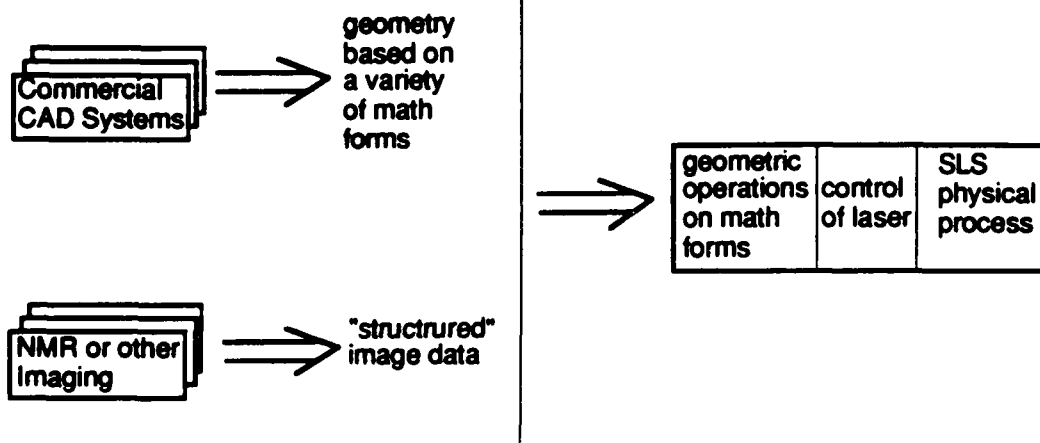- **System Architecture**
- **Artificial Intelligence**

| Commercial CAD Systems | ⟹ | geometry based on a variety of math forms |
| NMR or other Imaging | ⟹ | "structrured" image data |

| geometric operations on math forms | control of laser | SLS physical process |

Figure 5

315

understanding of the data structures themselves and the most efficient way of handling them.

Next we have materials. Materials are particularly important for Selective Laser Sintering. We have both the advantage and the disadvantage of having a lot of different material opportunities. The advantage is an obvious one. The disadvantage is a problem of focus. What are we going to focus on to make the most effective part? At this point we have looked at polymers, binders, metals, ceramics and composites (Figure 6). Each of which has its own idiosyncrasies.

We also have a powder process where we have to concern ourselves with particle size, distribution, density, morphology of the pattern and rheology. Other material properties such as glass transition in polymer melting in crystalline materials, viscosity relationships in polymers, thermal expansions, conductivity and heat capacity.

Process control, our next topic, is an area ripe for improvement in all of these processes (Figure 7). A lot of the improvements which 3-D has done with stereolithography are a direct result from good process control. In Selective Laser Sintering, we are talking about thermal process control, environmental process control, laser power control, both from an open loop and closed loop point of view. Here we can also bring in artificial intelligence techniques and possibly even neural nets. In our basic system, we have a geometric model coming in, from that we have geometry dependent operating conditions which then help control the laser beam, powder delivery, and environment control. We also have process parameter settings and at the same time we measure things that go on in the process. More and more measurements are required as we become more sophisticated. Feedback will be used to a greater extent as compared to feed-forward. Out of this good physical parts are created.

Process development (Figure 8), our last subcategory, is traditionally what you might call machines. This is really, in some ways, just a result of other work. In our particular research we are looking at developing high temperature machines for high

316

Materials

- **Polymers**

- **Binders**

- **Metals**

- **Ceramics**

- **Composites**
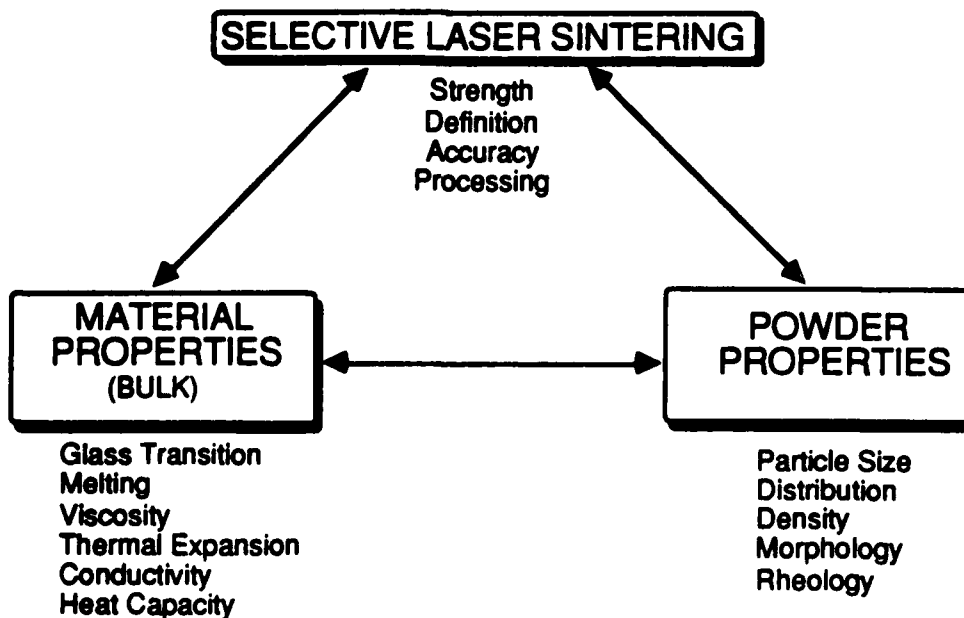
Figure 6

Process Control

- **Thermal**
- **Environment**
- **Laser Power**
- **Open Loop Scheduling**
- **Closed Loop**
- **Artificial Intelligence**
- **Neural Nets**
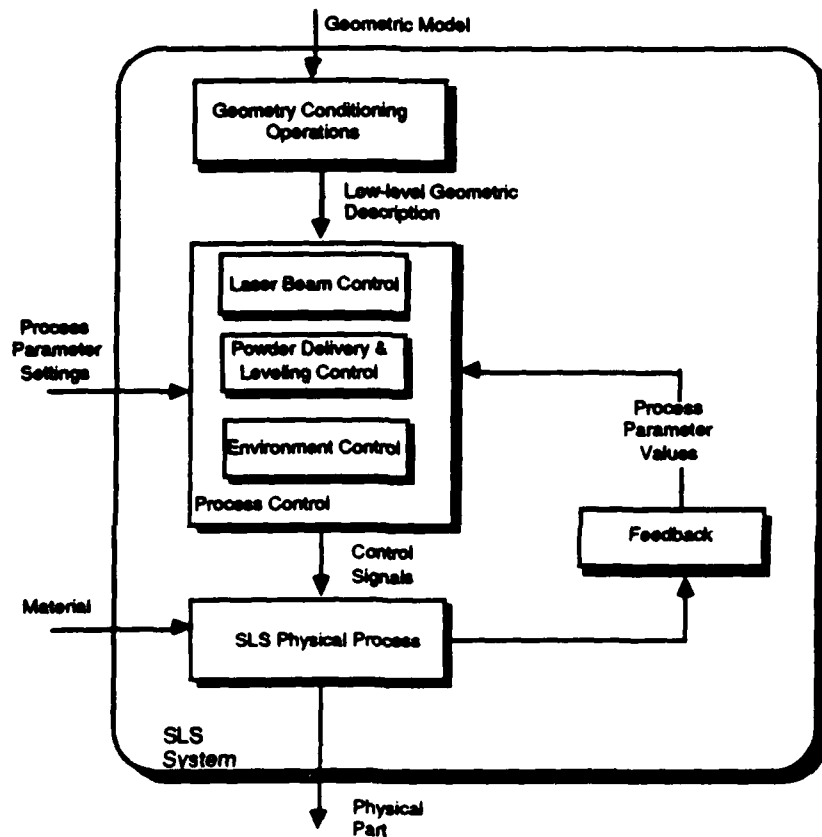
Figure 7

Process Development

- **High Temperature**
- **High Power**
- **Material Handling**
- **Beam Delivery**
- **Scale Up/Down**
- **Hardware**
- **Secondary Processing**
- **Material Processes**

Figure 8

temperature materials, higher power up to kilowatt laser system, different material handling systems, how to handle the beams, and particularly, how to scale up or scale down-both down to the micro and up to very large machines. Given a part we also have to talk about secondary processing in order to best finish this part. We are also concerned with material processes associated with actually making selective sintering specific materials.

Our goal is parts and applications (Figure 9). It is not good enough to say a part just has to be accurate or it just has to be strong. There are a lot of different functions and concerns in a part. For example, if I want a conducting part, the part has to have the right electrical properties. We are also concerned with mechanical and physical properties. In addition, these parts have to be accurate, rapidly and easily made.

What are the applications? One is to optimize standard designs and processes with freeform fabrication. Now that is useful, but what is even more exciting is enablement of new designs and processes. Things that can never be made by any other process can be made with Solid Freeform Fabrication processes. As this technology gets introduced into the market place, we will see more and more designs enabled. Other applications are reverse engineering where items are scanned and then refabricated, remote manufacturing where machines are distributed throughout the world and the information to make parts on those machines is telecommunicated to those locations. Even more exciting, is that once you develop structurally sound parts, inventory can be reduced with machines that make parts on demand.

As a particular example of our research approach consider the design of a high temperature workstation that we are in the process of implementing. Figure 10 is an analysis of our starting point for this workstation design. Basically the state-of-the-art at that point was Selective Laser Sintering for low temperature parts, basically low melting point materials like polymers. We wanted to extend the state-of-the-art to handle high temperature materials with an ultimate goal of being able to sinter fully dense structural

Parts & Applications

- **Mechanical Properties**
- **Physical Properties**
- **Accuracy** } **Parts**
- **Rapidly Made**
- **Easily Made**

- **Optimization of Standard Designs & Processes with SLS**

- **New Designs & Processes Enabled with SLS**

- **Reverse Engineering**

- **Remote Manufacture**

- **Repair Parts**

Figure 9

PROJECT BACKGROUND

- **THE STATE OF THE ART**

  THE SELECTIVE LASER SINTERING PROCESS IS USED TO BUILD PREFORMS AND PROTOTYPE PARTS FROM LOW MELTING POINT MATERIALS

- **EXTENDING THE STATE OF THE ART**

  THE SELECTIVE LASER SINTERING PROCESS WILL BE USED TO DIRECTLY SINTER PARTS FROM HIGH-TEMPERATURE MATERIALS

- **ULTIMATE GOAL**

  THE SELECTIVE LASER SINTERING PROCESS WILL BE USED TO DIRECTLY SINTER FULLY-DENSE STRUCTURAL PARTS

Figure 10

parts in metals and ceramics. We subdivided this into three phases (Figure 11): the first phase being a direct sintering of high temperature materials with just a high laser power sintering. We did not expect full success at this point because we knew from our understanding of the process that you have to elevate the powder temperature to alleviate thermalstresses. Phase two of our process, which we are in the middle of implementing, involves combining a high power laser system with high temperature powder preheating capability for much improved part quality. Phase three of the process will be to get much better control and implementation of our atmosphere, basically to vacuum standards.

Here is a sample of some of the questions we asked ourselves in this design procedure (Figure 12). We looked at the window seal tolerances, maximum obtainable temperatures for representative powders, what kind of temperature distribution you can get, temperature dynamics, what kind of control systems and the effect of chamber walls in designing a higher temperature system. In addition we looked at the effect of powder bed heights, convection effects, temperature measurement calibration, and heater efficiency. For each of these categories we proposed solutions and designs to optimize between the various questions. Out of these discussions in design came a basic configuration which consisted of dual heaters, a laser window, a small powder bed, actually the smallest system we have built to date (Figure 13). We did not want to concern ourselves with building large high temperature systems with uniform temperature distribution. Just recently our first implementation of this design has come into operation. We have achieved powder bed temperatures of 950°C. We have had some problems as well. We were able to melt one of our zinc selenide windows which has now been replaced with a salt window. As testing proceeds we will continue to design and redesign. We have discovered that at full power the chamber becomes too hot and we are going to have to worry about how to take some of the heat away (Figure 14).

In summary, I would like to state that it is our view that machines cannot be designed without a good understanding of the process and that understanding of the

process has to come from fundamental process understanding which then can be reticulated into information processing, control and process development, out of which will flow all the applications and parts that we would all like to see coming out of Solid Freeform Fabrication.

DESIGN STRATEGY

- **PHASE I — HIGH LASER-POWER SINTERING**

  DIRECT SINTERING OF HIGH-TEMPERATURE MATERIALS

- **PHASE II — HIGH TEMPERATURE SINTERING**

  CONTROLLED HIGH-TEMPERATURE POWDER PRE-HEATING CAPABILITY

  FOR IMPROVED PART QUALITY

- **PHASE III — VACUUM SINTERING**

  MEDIUM TO HIGH VACUUM WORKING CHAMBER FOR CREATING HIGH-

  DENSITY SINTERED PARTS

Figure 11

OBJECTIVES

Window Seal Tolerance
• Will the heater window O-ring seals stay at a safe operating temperature?

Maximum Obtainable Temperature (MOT)
• What is the MOT at steady state for some representative powders?

Temperature Distribution
• How does the heat flux distribution compare with the model predictions?
• How does heat flux distribution relate to temperature distribution for powders having different thermal properties?
• How is temperature distribution effected by various parameters?

Temperature Dynamics
• How quickly can we reach steady state operating conditions?
• How does the system respond to a change in heater power?

Temperature Control System Performance
• How precisely can the powderbed temperature be controlled using the IR sensor and PID controller?

Effect of chamber wall reflectivity
• How will chamber wall reflectivity affect thermal performance?

Figure 12

Effect of Powderbed Height
- Is thermal performance an important criteria for selecting powderbed height?

Convection Effects
- How will forced convection affect the thermal performance of the powderbed?

Temperature Measurement Calibration
- The IR sensor must be calibrated to account for attenuation.

Heater Efficiency
- How much of the heater power reaches the powderbed?
- How much reaches the thermal absorbers?

Figure 13
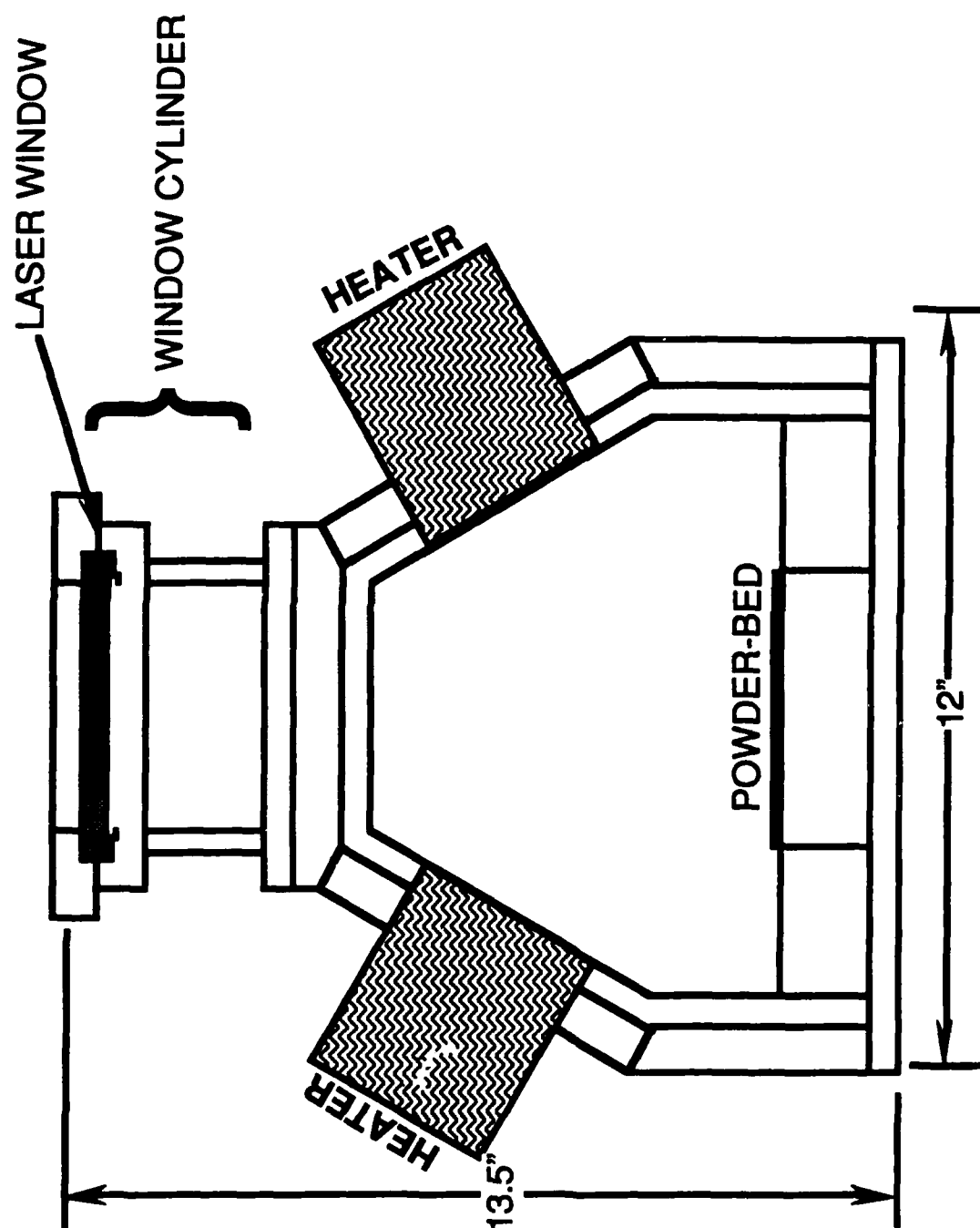
Figure 3: Chamber Configuration

Figure 14

PROJECT STATUS AND FUTURE DEVELOPMENT

- Powder bed temperatures of up to 950°C have been obtained in the high temperature Process Chamber.

- The coating on the zinc selenide laser window was damaged during initial testing. A sodium chloride window is now being tested.

- At full power, the chamber becomes too hot, which may result in damage to the seals. Radiation absorbers were designed to remove excess energy from the chamber. The absorbers will be tested soon.

Figure 15

Figure 16

Key Word Index

Author/Attendee List

Raul Aguinaga
Marquette University
1515 W. Wisconsin Ave.
Milwaukee, WI 53233
414/288-7080
414/288-7082 fax

Mr. Phannara Aing
Center for Materials Science
  and Engineering
The University of Texas
Austin, TX 78712
512/471-1504
512/471-7681 fax

Mark Atkeson
United Technologies
  Research Center
411 Silver Lane, MS 129-48
East Hartford, CT 06108
203/727-7246
203/727-7840 fax

Clinton Atwood
2484-1 Sandia National
  Laboratories
P.O. Box 5800
Albuquerque, NM 87123
505/844-0816
505/844-1110 fax

Richard Aubin
Project Leader
United Technologies
  Pratt and Whitney
400 Main Street, MS 118-38
East Hartford, CT 06108
203/565-9073
203/565-9614 fax

B. Badrinarayan
Dept. of Chemical Engineering
The University of Texas
Austin, TX 78712

Amit Bagchi
Mechanical Engineering Dept.
Clemson University
318 Biggs Hall
Clemson, SC 29634-0921
803/656-5641
803/656-4435 fax

Joel W. Barlow
Dept. of Chemical Engineering
The University of Texas
Austin, TX 78712
512/471-1271

Owen Baumgardner
Texas Instruments
P.O. Box 405
MS 3471
Lewisville, TX 75067
214/462-4462
214/462-5610 fax

Joseph J. Beaman
Dept. of Mechanical Engineering
The University of Texas
Austin, TX 78712
512/471-3058
512/471-8727 fax

James E. Beck
Engineering Design Research
  Center
Carnegie Mellon University
Pittsburgh, PA 15213
412/268-6846

John A. Benda
United Technologies Research
  Center
Silver Lane, MS 129-73
East Hartford, CT 06108
203/727-7215
203/727-7669 fax

Brit Birmingham
Center for Materials Science
  and Engineering
The University of Texas
Austin, TX 78712
512/471-3469
512/471-7681 fax

Paul Blake
Texas Instruments
2501 S. Highway 121
MS 3428
Lewisville, TX 75067
214/462-3015
214/462-2684 fax

Jan Helge Bohn
Rensselaer Design Research
  Center
Rensselaer Polytechnic Institute
110 8th Street
Troy, NY 12180-3590
518/276-6751

William Brower
Department of Mechanical and
  Industrial Engineering
Marquette University
1515 W. Wisconsin Avenue
Milwaukee, WI 53233
414/288-7081
414/288-7082 fax

Robert L. Brown
Advanced Process and Control
The Gillette Company
Gillette Park
Boston, MA 02106-2131

David Bunnell
Center for Materials Science
  and Engineering
The University of Texas
Austin, TX 78712
512/471-3146
512/471-7681 fax

Marshall Burns
Ennex Fabrication Technologies
549 Landfair Avenue
Los Angeles, CA 90024
310/824-5185 (tel. & fax)

Ivo Celi
Fraunhofer-Institut fur
  Produktionstechnologie
Steinbachstrasse 17
D-5100 Aachen
GERMANY
(01149) 241-8904-120
(01149) 241-8904-198 fax

Carlos A. Chacon
Marquette University
1515 W. Wisconsin Avenue
Milwaukee, WI 53233
414/288-7080
414/288-7082 fax

Steve Chang
BDM International
4001 N. Fairfax Drive #750
Arlington, VA 22203
703/351-6900
703/351-6909 fax

Michael J. Cima
Ceramics Processing Research
  Laboratory
M.I.T.
77 Massachusetts Avenue
Room 12-011
Cambridge, MA 02139
617/253-6877
617/258-6936 fax

Richard C. Cobb
Dept. of Manufacturing Eng. &
  Operations Management
The University of Nottingham
University Park
Nottingham, NG7 2RD
UNITED KINGDOM
(01144) 0602 484848

Richard H. Crawford
Dept. of Mechanical Engineering
The University of Texas
Austin, TX 78712
512/471-3030
512/471-8727 fax

Suman Das
Dept. of Mechanical Engineering
The University of Texas
Austin, TX 78712
512/471-5838
512/471-8727 fax

Franco DeAngelis
DTM Corporation
1611 Headway Circle, Bldg. 2
Austin, TX 78754
512/339-2922

Carl Deckard
DTM Corporation
1611 Headway Circle, Bldg. 2
Austin, TX 78754
512/339-2922

Douglas Dickens
BF Goodrich R&D
9921 Brecksville Road
Brecksville, OH 44141
216/447-5266
216/838-4413 fax

Philip M. Dickens
Dept. of Manufacturing Eng. &
    Operations Management
The University of Nottingham
University Park
Nottingham, NG7 2RD
UNITED KINGDOM
(01144) 602 484848 ext 3708
(01144) 602 583015 fax

Charles Dodgen
3M Company
6801 River Place Blvd.
Austin, TX 78726-9000
512/984-6959
512/984-5764 fax

Sam Drake
Department of Computer Sci.
3190 Merrill Engineering Bldg.
University of Utah
Salt Lake City, UT 84112

Deba Dutta
Dept. of Mechanical Engineering
2250 G.G. Brown
University of Michigan
Ann Arbor, MI 48109-2125
313/936-3567
313/764-4256 fax

Paul Forderhase
DTM Corporation
1611 Headway Circle, Bldg. #2
Austin, TX 78754
512/339-2922
512/339-0634 fax

Douglas W. Freitag
LTV Aerospace & Defense Co.
P.O. Box 650003
Dallas, TX 75265-0003
214/266-1632
214/266-9633 fax

Paul S. Fussell
Alcoa Labs
100 Technical Drive
Alcoa Center, PA 15069-0001
412/337-2721
412/337-3043 fax

Martin Geiger
Fraunhofer-Institut fur
    Produktionstechnik
    und Automatisierung
Nobelstrasse 12
D-7000 Stuttgart 80
GERMANY
(01149) 711 970-1835
(01149) 711 970-1004 fax

Ian Gibson
Dept. of Manufacturing Eng. &
    Operations Management
The University of Nottingham
University Park
Nottingham, NG7 2RD
UNITED KINGDOM
(01144) 602 484848

Sashidhar Guduri
Dept. of Mechanical Engineering
The University of Texas
Austin, TX 78712
512/471-5838
512/471-8727 fax

Steven V. Hayes
Program Operations Manager
LTV Aerospace & Defense Co.
P.O. Box 650003
Dallas, TX 75265-0003
214/266-1756
214/266-9633 fax

Mr. Berndt Holmer
The Swedish Institute of
Production Engineering Research
Brinellvagen 81
Stockholm, SWEDEN 10044
(01146) 8 213174
(01146) 8 202227 fax

Robert Hoyt
A.B. Chance
210 N. Allen
Centralia, MO 65240-1395
314/682-8362
314/682-8660 fax

Michael B. Hsu
MARC Analysis Research Corp.
260 Sheridan Avenue, Suite 309
Palo Alto, CA 94306
415/329-6839

Charles Hull
3D Systems Inc.
26081 Avenue Hall
Valencia, CA 91355
805/295-5600
805/295-0249 fax

Christopher Hysinger
Dept. of Mechanical Engineering
The University of Texas
Austin, TX 78712
512/471-8727 fax

Paul F. Jacobs
3D Systems, Inc.
26081 Avenue Hall
Valencia, CA 91355
805/295-5600 ext. 406
805/257-1200 fax

Kevin Jakubenas
Center for Materials Science
    and Engineering
The University of Texas
Austin, TX 78712
512/471-1504
512/471-7681

Anand Jog
400 E. 30th St. #207
Austin, TX 78705

Mary N. Johnson
RPI Design Research Center
Rensselaer Polytechnic Institute
110 8th Street
Troy, NY 12180
518/276-6754
518/276-2702 fax

Bernd Keller
University of Stuttgart
Institut für Kunststoffprüfung
Pfaffenwaldring 32
7000 Stuttgart 80
GERMANY
(01149) 711 685-2667
(01149) 711 685-2066 fax

Luke L. Kimble
Market Development Manager
DTM Corporation
1611 Headway Circle, Bldg. 2
Austin, TX 78754
512/339-2922
512/832-6753 fax

Chuck Kirschman
Clemson University
318 Riggs Hall
Clemson, SC 29634-0921
803/656-2384
803/656-2698 fax

Martin Koch
Industrial Engineering Dept.
Cal. Polytechnic State Univ.
San Luis Obispo, CA 93407
805/756-1114
805/756-5439 fax

Detlef Kochan
Technische Universitat Dresden
Institut für Fertigungsinformatik
Mommsenstrase 13
0-8027 Dresden, GERMANY
(01137) 51 4633339
(01137) 51 4710294 fax

Terry W. Kreplin
Baxter Healthcare Corporation
Route 120 & Wilson Road
RLT-10
Round Lake, IL 60073-0490
708/270-4067
708/270-4008 fax

Uday Lakshminarayan
DTM Corporation
1611 Headway Circle, Bldg. 2
Austin, TX 78754
512/339-2922
512/339-0634 fax

Thomas S. Latham
United Technologies
  Research Center
411 Silver Lane, MS 129-48
East Hartford, CT 06108
203/727-7409
203/727-7840 fax

Richard Levy
Department of Radiology
The University of Michigan
Medical Center
1500 E. Medical Center Drive
Ann Arbor, MI 48109-0030
313/936-9878
313/764-2412 fax

David Lomshek
Pittsburg State University
1701 S. Broadway
Pittsburg, KS 66762
316/235-4114
316/232-8833 fax

Arumugam Manthiram
Center for Materials Science
  and Engineering
The University of Texas
Austin, TX 78712
512/471-1791
512/471-7681 fax

Harris L. Marcus
Center for Materials Science
  and Engineering
The University of Texas
Austin, TX 78712
512/471-3188
512/471-7681 fax

Joe McGrath
Plynetics
627 McCormick
San Leandro, CA 94720
510/613-8300
510/662-6632 fax

John McWilliams
Dept. of Mechanical Engineering
The University of Texas
Austin, TX 78712
512/471-1743
512/471-8727 fax

Dennis Medler
3D Systems
26081 Ave. Hall
Valencia, CA 91355
805/295-5600
805/295-0249 fax

Lawrence S. Melvin III
Dept. of Mechanical Engineering
The University of Texas
Austin, TX 78712
512/471-8727 fax

Steven Michaels
Dept. of Mechanical Engineering
M.I.T.
77 Massachusetts Ave.
Rm. 35-011
Cambridge, MA 01239
617/253-2606
617/253-2123 fax

John F. Miller
EDS
800 Tower Drive, Second Floor
Troy, MI 48098
313/265-8800
313/265-7569 fax

Bob Montague
DTM Corporation
1611 Headway Circle, Bldg. 2
Austin, TX 78754
512/339-2922

Nathan Moore
2800 Barton's Bluff #1106
Austin, TX 78746
512/328-2110

J.C. Nelson
Dept. of Chemical Engineering
The University of Texas
Austin, TX 78712
512/471-7060 fax

Tim Newman
AMP, Inc.
P. O. Box 55
Winston Salem, NC
  27102-0055
919/727-5293
919/727-5151 fax

Hendra Ng
BF Goodrich R&D
9921 Brecksville Road
Brecksville, OH 44141

Kurt O'Connor
Allison Gas Turbine
P.O. Box 420
Speed Code W13
Indianapolis, IN 46206
317/230-6282
317/230-2990 fax

Sean O'Reilly
Ford Motor Company
Manuf. Development Center
Operations Engineering
24500 Glendale Avenue
Detroit, Michigan 48239

335

Panos Papalambros
Dept. of Mechanical Engineering
University of Michigan
Ann Arbor, MI 48109-2125
313/764-8464
313/764-3170 fax

M.S. Pridham
Dept. of Manufacturing Eng. &
   Operations Management
The University of Nottingham
University Park
Nottingham, NG7 2RD
UNITED KINGDOM
(01144) 602 484848

Bill Rafaniello
The Dow Chemical Company
1776 Building
Midland, MI 48674
517/636-1591
517/638-9716 fax

Jim Ramsay
Lanxide Corp.
1300 Marrows Road
Newark, DE 19714-6077
302/456-6508
302/454-1712 fax

R.C. Reuter, Jr.
Manager, Dept. 2984
Sandia National Labs
P.O. Box 5800
Albuquerque, NM 87109
505/845-9200
505/844-1110 fax

Stephen J. Rock
Rensselaer Design
   Research Center
Rensselaer Polytechnic Institute
110 8th Street
Troy, NY 12180-3590
518/276-6754
518/276-2702 fax

Barry Rossing
Lanxide Corp.
1300 Marrows Road
Newark, DE 19714-6077
302/456-6502
302/454-1712 fax

Christine Ryan
B.F. Goodrich
9921 Brecksville Road
Brecksville, OH 44141

Emanuel Sachs
M.I.T.
35-229, 77 Massachusetts Ave.
Cambridge, MA 02139
617/253-5381
617/253-2123 fax

L.E. Salters
Associate Division Head
Code 36401
Naval Air Warfare Center
China Lake, CA 93555
619/939-3705
619/939-2533 fax

Greg Sanders
General Motors Corporation
30300 Mound Road
Mail Drop A/MD36
Warren, MI 48090-9040
313/947-0201
313/947-0200 fax

P. Schaeffer
Laser 3D
6, allée Pelletier Doisy
54603 Villers-les-Nancy
CEDEX-FRANCE
(01133) 83 614476
(01133) 83 440482 fax

Reuven Scharf
Cubital America, Inc.
1307F Allen Drive
Troy, MI 48083
313/585-7880
313/585-7884 fax

Michael Schmerling
Center for Materials Science
   and Engineering
The University of Texas
Austin, TX 78712
512/471-3168
512/471-7681 fax

Don Sifford
Texas Instruments Inc.
P.O. Box 405
MS 3412
Lewisville, TX 75067

Samuel S. Sih
Dept. of Chemical Engineering
The University of Texas
Austin, TX 78712
512/471-6991
512/471-7060 fax

Jim Stewart
Allison Gas Turbine
P.O. Box 420
Speed Code W13
Indianapolis, IN 46206
317/230-4337
317/230-2990 fax

P.K. Subramanian
Center for Materials Science
   and Engineering
The University of Texas
Austin, TX 78712
512/471-3146
512/471-7681 fax

Glenn Taylor
B.F. Goodrich
9921 Brecksville Road
Brecksville, OH 44141

Rich Thissell
Dept. of Mechanical Engineering
The University of Texas
Austin, TX 78712
512/471-3469
512/471-7681 fax

Chuck M. Titus
BF Goodrich R&D
9921 Brecksville Road
Brecksville, OH 44141
216/447-5348
216/838-4413 fax

Jim Tobin
Dept. of Mechanical Engineering
The University of Texas
Austin, TX 78712
512/471-8727 fax

Jim Tompkins
Dept. of Mechanical Engineering
The University of Texas
Austin, TX 78712
512/471-3469
512/471-7681 fax

N.K. Vail
Dept. of Chemical Engineering
The University of Texas
Austin, TX 78712
512/471-6991
512/471-7060 fax

Ralph Wachter
Office of Naval Research
Computer Science Division,
Code 1133
800 N. Quincy Street
Arlington, VA 22217-5000

Craig Wadham
DTM Corporation
1611 Headway Circle, Bldg. #2
Austin, TX 78754
512/339-2922
512/339-0643 fax

William A. Walters
Stratasys, Inc.
7411 Washington Avenue South
Minneapolis, MN 55439
612/941-5607
612/944-6741 fax

Eric M. Weissman
BF Goodrich R&D
9921 Brecksville Road
Brecksville, OH 44141
216/447-5420
216/838-4413 fax

Norman M. Wereley
BDM International
4001 N. Fairfax Drive #750
Arlington, VA 22203
703/351-6900
703/351-6909 fax

Bernd Wiedemann
University of Stuttgart
Institut für Kunststoffprüfung
Pfaffenwaldring 32
7000 Stuttgart 80
GERMANY
(01149) 711 685-2667
(01149) 711 685-2066 fax

Mike Wozny
Rensselaer Design
  Research Center
Rensselaer Polytechnic Institute
110 8th Street
Troy, NY 12180-3590
518/276-6751
518/276-2702 fax

Ying-Jeng Engin Wu
Dept. of Mechanical Eng.
National Yunlin Inst. of Tech.
123 University Road, Section 3
Touliu, Yunlin,
Taiwan 640 ROC
(011-886) 05 5342601 ext. 4101

Yongqiu Wu
Dept. of Mechanical Engineering
The University of Texas
Austin, TX 78712
512/471-5838
512/471-7060 fax

Carolyn Young
DTM Corporation
1611 Headway Circle, Bldg. #2
Austin, TX 78754
512/339-2922

Guisheng Zong
Center for Materials Science
  and Engineering
The University of Texas
Austin, TX 78712
512/471-0967
512/471-7681 fax